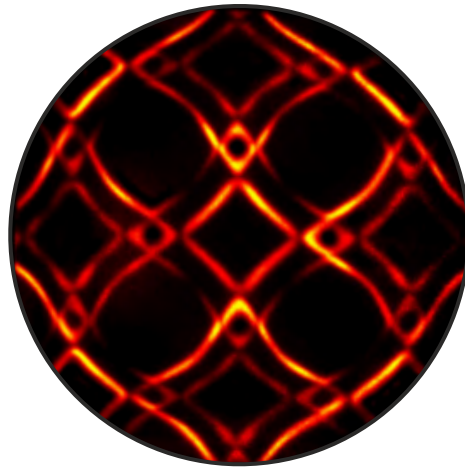# Ultrafast Electron Dynamics in Quasi-two-dimensional Quantum Materials

Dissertation
zur Erlangung des Grades eines
Doktors der Naturwissenschaften

am Fachbereich Physik
der Freien Universität Berlin

vorgelegt von

Julian Maklar

Fritz-Haber-Institut der Max-Planck Gesellschaft
Faradayweg 4-6, 14195 Berlin

Berlin 2022

This work was conducted between October 2018 and July 2022 in the research group *Dynamics of Correlated Materials*, headed by Dr. Laurenz Rettig, at the Department of Physical Chemistry of the Fritz Haber Institute of the Max Planck Society.

Abstract

Quantum materials are solids with tantalizing properties arising from special symmetry, dimensionality, topology, and many-body interactions between elementary degrees of freedom (charge, spin, orbital, and lattice). They are host to fascinating emergent phenomena such as unconventional superconductivity, Mott transitions, charge density waves (CDWs), and topologically-protected electronic states, and hold promise for revolutionizing electricity generation and distribution, (quantum) computing, and data storage. Gaining a microscopic understanding of quantum materials to experimentally realize and control many-body phases is one of the overarching goals of modern condensed-matter physics. A promising pathway to fulfilling this goal are ultrashort optical excitations. Tracking the response of a broken-symmetry state after perturbation by a light pulse grants access to the relevant many-body interactions governing the emergence of equilibrium quantum states. Additionally, the interaction of quantum materials with light can induce novel emergent phenomena by steering a system towards specific transient or metastable states, facilitating control over additional functionalities within the light-enriched phase diagram.

This thesis explores the electronic structure and ultrafast dynamics of several single-layer and layered quasi-2D quantum materials using femtosecond time- and angle-resolved photoemission spectroscopy (trARPES). We first establish a novel time-of-flight-based photoelectron detector for trARPES, a momentum microscope, and benchmark its performance against the widely used hemispherical analyzers. Next, we utilize the complementary nature of both detectors to characterize the electronic nonequilibrium properties of a novel 2D topological insulator, bismuthene. We map the transiently occupied conduction band after photoexcitation, observe faint signatures of topological edge states within the large fundamental bulk band gap, and track the full relaxation pathway of hot photocarriers. Next, using trARPES in combination with a complementary time-resolved structural probe, we investigate the dynamics of a prototypical layered CDW compound, $TbTe_3$, after optical excitation. Tracking the system's order parameter during the photoinduced CDW melting and recovery reveals a surprising reemergence of CDW order at elevated electronic temperatures far greater than the thermal critical temperature, which we attribute to strong nonequilibrium between coupled electronic and lattice degrees of freedom. Additionally, we show how changes of the CDW energy gap during the CDW-to-metal transition can lead to a transient modulation of the relaxation rates of excited high-energy photocarriers. Theoretical calculations based on a nonequilibrium Green's function formalism reveal the critical role of the phase space of electron-electron scattering and the interplay of elementary interactions and the electronic band structure. Lastly, we study the ultrafast nonthermal pathway to a long-lived metastable quantum state in bulk $1T$-TaS_2 after optical excitation. Utilizing a double-pulse excitation of a vibrational CDW coherence, we demonstrate a high degree of control over the phase transition, laying the basis for actively controlling macroscopic material properties on ultrafast timescales. The thesis concludes with an outlook on future research of quantum materials enabled by time-resolved momentum microscopy.

Deutsche Kurzfassung

Quantenmaterialien weisen emergente Phänomene mit faszinierenden Eigenschaften auf, wie beispielsweise unkonventionelle Supraleitung, Mott-Übergänge, Ladungsdichtewellen (CDWs) und topologisch geschützte elektronische Randzustände, welche zukunftsweisende Anwendungen in der Stromerzeugung und -verteilung, dem (Quanten-) Computing und der Datenspeicherung ermöglichen. Die außergewöhnlichen Eigenschaften von Quantenmaterialien resultieren aus einem komplexen Zusammenspiel von Symmetrie, Dimensionalität, Topologie, und Vielteilchen-Wechselwirkungen zwischen elementaren Freiheitsgraden (Ladung, Spin, Orbital und Gitter). Um emergente Phänomene zu realisieren und die makroskopischen Eigenschaften von Quantenmaterialien zu kontrollieren, ist jedoch ein mikroskopisches Verständnis dieses Zusammenspiels erforderlich. Einen vielversprechenden Ansatz hierzu bieten ultrakurze optische Anregungen. Die dynamische Antwort einer geordneten Phase auf eine optische Anregung ermöglicht Rückschlüsse auf fundamentale Wechselwirkungen. Darüber hinaus kann die Manipulation von Quantenmaterialien mit Licht neue Phänomene mit vielversprechenden Eigenschaften hervorrufen, indem Materialien gezielt in transiente oder metastabile Zustände überführt werden.

Die vorliegende Arbeit untersucht die elektronische Struktur und ultraschnelle Dynamik verschiedener Quantenmaterialien mithilfe von zeit- und winkelaufgelöster Photoemissionsspektroskopie (trARPES). Zunächst etablieren wir einen neuartigen Photoelektronendetektor, das sogenannte Flugzeit-Impulsmikroskop, und vergleichen dessen Leistungsfähigkeit mit einem konventionellen Halbkugelanalysator im Rahmen üblicher trARPES Experimente. Anschließend nutzen wir die komplementäre Funktionsweise beider Detektoren um die elektronischen Eigenschaften des neuartigen 2D topologischen Isolators Bismuthen nach optischer Anregung zu charakterisieren. Wir bestimmen den Verlauf des Leitungsbands, beobachten Signaturen topologischer Randzustände innerhalb der Bandlücke und identifizieren den gesamten Relaxationspfad angeregter Elektronen. Daraufhin untersuchen wir mittels trARPES und komplementärer struktureller Messmethoden die Dynamik des quasi-2D CDW-Materials TbTe$_3$ nach optischer Anregung. Der Verlauf des Ordnungsparameters während der photoinduzierten Unterdrückung und Rückkehr der CDW zeigt ein überraschendes Wiederauftreten der CDW-Ordnung bei elektronischen Temperaturen, die weit über der thermischen Übergangstemperatur liegen, was wir auf das Nicht-Gleichgewicht zwischen gekoppelten elektronischen und Gitter-Freiheitsgraden zurückführen. Zudem zeigen wir, wie sich das Schließen der elektronischen CDW-Bandlücke infolge des photoinduzierten Phasenübergangs auf die Relaxationsrate angeregter Elektronen auswirkt, was wir auf ein komplexes Wechselspiel zwischen Elektron-Elektron-Streuung und Bandstruktur zurückführen. Zuletzt untersuchen wir den photoinduzierten Übergang in eine langlebige metastabile Nicht-Gleichgewichtsphase in $1T$-TaS$_2$. Dabei nutzen wir eine Sequenz optischer Pulse zur Anregung einer CDW Kohärenz und erzielen ein hohes Maß an Kontrolle über die Stabilisierung der Nicht-Gleichgewichtsphase. Die Arbeit schließt ab mit einem Ausblick auf zukünftige Forschung an Quantenmaterialien mit einem Fokus auf zeitaufgelöste Impulsmikroskopie.

Publications forming this thesis

[I] J. Maklar, S. Dong, S. Beaulieu, T. Pincelli, M. Dendzik, Y. W. Windsor, R. P. Xian, M. Wolf, R. Ernstorfer, and L. Rettig, "A quantitative comparison of time-of-flight momentum microscopes and hemispherical analyzers for time- and angle-resolved photoemission spectroscopy experiments", Rev. Sci. Instrum. **91**, 123112 (2020)

[II] J. Maklar, Y. W. Windsor, C. W. Nicholson, M. Puppin, P. Walmsley, V. Esposito, M. Porer, J. Rittmann, D. Leuenberger, M. Kubli, M. Savoini, E. Abreu, S. L. Johnson, P. Beaud, G. Ingold, U. Staub, I. R. Fisher, R. Ernstorfer, M. Wolf, and L. Rettig, "Nonequilibrium charge-density-wave order beyond the thermal limit", Nat. Commun. **12**, 2499 (2021)

[III] J. Maklar, M. Schüler, Y. W. Windsor, C. W. Nicholson, M. Puppin, P. Walmsley, I. R. Fisher, M. Wolf, R. Ernstorfer, M. A. Sentef, and L. Rettig, "Coherent modulation of quasiparticle scattering rates in a photoexcited charge-density-wave system", Phys. Rev. Lett. **128**, 026406 (2022)

[IV] J. Maklar, R. Stühler, M. Dendzik, T. Pincelli, S. Dong, S. Beaulieu, A. Neef, G. Li, M. Wolf, R. Ernstorfer, R. Claessen, and L. Rettig, "Ultrafast Momentum-Resolved Hot Electron Dynamics in the Two-Dimensional Topological Insulator Bismuthene", Nano Lett. **22**, 5420–5426 (2022)

Articles [I–IV] form the main part of this cumulative thesis and are reproduced in Chapter 4.

Publications concerning other topics

[V]   S. Beaulieu, J. Schusser, S. Dong, M. Schüler, T. Pincelli, M. Dendzik, J. Maklar, A. Neef, H. Ebert, K. Hricovini, M. Wolf, J. Braun, L. Rettig, J. Minár, and R. Ernstorfer, "Revealing Hidden Orbital Pseudospin Texture with Time-Reversal Dichroism in Photoelectron Angular Distributions", Phys. Rev. Lett. **125**, 216404 (2020)

[VI]   S. Beaulieu, S. Dong, N. Tancogne-Dejean, M. Dendzik, T. Pincelli, J. Maklar, R. P. Xian, M. A. Sentef, M. Wolf, A. Rubio, L. Rettig, and R. Ernstorfer, "Ultrafast dynamical Lifshitz transition", Sci. Adv. **7**, eabd9275 (2021)

[VII]   S. Dong, S. Beaulieu, M. Selig, P. Rosenzweig, D. Christiansen, T. Pincelli, M. Dendzik, J. D. Ziegler, J. Maklar, R. P. Xian, A. Neef, A. Mohammed, A. Schulz, M. Stadler, M. Jetter, P. Michler, T. Taniguchi, K. Watanabe, H. Takagi, U. Starke, A. Chernikov, M. Wolf, H. Nakamura, A. Knorr, L. Rettig, and R. Ernstorfer, "Observation of ultrafast interfacial Meitner-Auger energy transfer in a van der Waals heterostructure", arXiv:2108.06803 (2021)

[VIII] S. Beaulieu, M. Schüler, J. Schusser, S. Dong, T. Pincelli, J. Maklar, A. Neef, F. Reinert, M. Wolf, L. Rettig, J. Minár, and R. Ernstorfer, "Unveiling the orbital texture of 1T-TiTe$_2$ using intrinsic linear dichroism in multidimensional photoemission spectroscopy", npj Quantum Mater. **6**, 93 (2021)

[IX]   A. Neef, S. Beaulieu, S. Hammer, S. Dong, J. Maklar, T. Pincelli, R. P. Xian, M. Wolf, L. Rettig, J. Pflaum, and R. Ernstorfer, "Orbital-resolved Observation of Singlet Fission", arXiv:2204.06824 (2022)

[X]   G. Kremer, J. Maklar, L. Nicolaï, C. W. Nicholson, C. Yue, C. Silva, P. Werner, J. H. Dil, J. Krempaský, G. Springholz, R. Ernstorfer, J. Minár, L. Rettig, and C. Monney, "Field-induced ultrafast modulation of Rashba coupling at room temperature in ferroelectric α-GeTe(111)", arXiv:2204.11630 (2022)

[XI]   J. Maklar, S. Dong, J. Sarkar, Y. A. Gerasimenko, T. Pincelli, S. Beaulieu, P. S. Kirchmann, J. A. Sobota, S.-L. Yang, D. Leuenberger, R. G. Moore, Z.-X. Shen, M. Wolf, D. Mihailovic, R. Ernstorfer, and L. Rettig, "Coherent Light Control of a Metastable Hidden Phase", arXiv:2206.03788 (2022)

The preprint version of Ref. [XI] is reproduced in Appendix B, as the manuscript is currently under review. Note that the listed co-authored articles may be submitted in connection with other dissertations.

Contents

1

Introduction

The 21st century: the age of quantum materials? From the prehistoric age of stone tools and early metallurgy to the information age enabled by zone-refined silicon, the progression of society is intimately linked to its ability to create and utilize new materials. A material class that may facilitate the next societal leap owing to its potential to revolutionize data processing and storage, quantum computing, and energy-related technologies, are quantum materials [1–5]. The term quantum materials unites a vast array of systems whose macroscopic properties are governed by quantum many-body effects and unusual topological properties of the electronic wave function. In this material class, complex interactions between elementary degrees of freedom – electronic, spin, orbital, and lattice – and the geometric and topological aspects of their wave functions manifest over a wide range of energy and length scales. This interplay gives rise to exotic collective phenomena such as unconventional and topological superconductivity, quantum spin liquids, Mott transitions, and topological insulators.

Many fascinating properties of quantum materials derive from a reduced dimensionality, particularly from confinement to two-dimensional sheets. Firstly, dielectric screening is reduced within 2D planes, amplifying the Coulomb interaction between electrons and thus evoking many-body effects. Secondly, as the scattering phase space is strongly reduced in low-dimensional systems, collective excitations and coherences take a leading role. Lastly, confined geometries are host to exotic phenomena such as the massless Dirac energy spectrum in graphene [6] and dissipationless spin currents in 2D materials with a topologically nontrivial band structure [7, 8]. Furthermore, the reduced dimensionality facilitates the formation of charge density waves (CDWs), which is a symmetry-broken phase characterized by a charge superstructure coupled to a periodic lattice deformation [9]. While dimensional confinement effects are particularly pronounced in strictly 2D materials, also the properties of many layered bulk materials are governed by their quasi-2D character, as out-of-plane interactions are generally weak compared to intralayer bonding. Yet, the additional out-of-plane degree of freedom in bulk materials can give rise to a complex interplay of intra- and interlayer interactions, manifesting, for example, in the rich phase diagram of the layered transition metal dichalcogenide (TMD) $1T$-TaS_2 [10–12]. While our understanding of quantum materials has increased dramatically over the last two decades, a microscopic description of their wide array of emergent phases remains a great challenge. Gaining a full understanding of quantum materials, however, is critical as it implies the possibility of designing compounds with desirable

properties.

An established approach to gain a better understanding of quantum materials is to study their dynamical response to a tailored ultrashort optical excitation. In thermal equilibrium, disentangling the interactions between elementary degrees of freedom is hardly possible and their specific coupling can not be accessed due to a lack of directly measurable observables. Time-resolved methods overcome this problem by investigating interactions directly in the time domain on the intrinsic timescale of fundamental scattering processes. This facilitates, for example, a quantitative determination of electron-phonon coupling [13]. Optical excitations can also trigger phase transitions under highly nonequilibrium conditions. Tracking the time- and energy scales of the quench of an ordered state and its recovery allows decoupling of interlinked degrees of freedom, identifying the decisive processes during melting and reformation of order, and disentangling intertwined and competing phases [14–17].

Optically induced phase transitions also provide a promising pathway toward material properties on demand, since, by steering a quantum material into a specific ground, metastable or transient state, desirable functionalities can be realized [18, 19]. Particularly nonequilibrium states that go beyond simple melting of thermal states but are governed by a transient modification of the free energy landscape are promising for solid-state quantum devices. This is because nonequilibrium states are generally switchable on ultrafast timescales and can further expand the functionalities of quantum materials beyond the properties present in the equilibrium phase diagram [20, 21]. Fascinating representatives of such nonequilibrium phases are light-induced superconductivity in organic compounds [22, 23] and the optically or electrically induced metallic hidden phase of $1T$-TaS$_2$ [24]. Yet, so far an understanding of the underlying processes that govern the transition pathways to nonequilibrium states is largely missing.

Time- and angle-resolved photoemission spectroscopy. A powerful technique that allows addressing these questions and plays a key role in the characterization of 2D quantum materials is time- and angle-resolved photoemission spectroscopy (trARPES). This technique directly probes the energy- and momentum-resolved electron dynamics of solids after excitation by ultrashort optical pulses at femtosecond (fs) time resolution. Thus, trARPES directly provides nonequilibrium changes to the electronic band structure during phase transitions and grants access to fundamental interactions on intrinsic timescales, such as electron-electron and electron-phonon scattering. As various phenomena that are not primarily of electronic nature are imprinted on the electronic band structure, trARPES also allows investigating the coupling of electrons to other subsystems, such as electron-phonon coupling through excitation of coherent phonons [13, 25]. Particularly the combination of trARPES with complementary probes, such as time-resolved X-ray diffraction to probe concomitant structural dynamics, is extremely powerful, as it allows for a complete description of various subsystems and their respective couplings. Lastly, due to its extreme surface sensitivity and direct access to the in-plane momentum distribution of photoelectrons, trARPES is ideally suited for the investigation of 2D *all surface* materials, for example, adatom systems.

Focus of this thesis. In this work, we employ trARPES in combination with complementary structural probes to gain a better understanding of nonequilibrium phase

transitions and fundamental interactions in a variety of 2D and layered quasi-2D quantum materials. (i) We first establish a novel time-of-flight-based photoelectron detection scheme for trARPES, that is, a momentum microscope, and benchmark its capabilities against the conventional photoelectron detector system, the hemispherical analyzer [I]. (ii) Combining both detection schemes, we characterize the unoccupied electronic band structure of the 2D topological insulator bismuthene, a graphene analog built from bismuth atoms on a semiconductor substrate, and investigate the scattering channels of hot photocarriers. Remarkably, we observe faint signatures of metallic topological edge states connecting the semiconducting bulk bands, which enable a highly efficient relaxation of hot electrons [IV]. (iii) Next, we explore the ultrafast melting and subsequent recovery of a CDW in the layered quasi-2D system TbTe$_3$ after optical excitation. Tracking the electronic and structural CDW order-parameter dynamics allows us to reconstruct the transient energy landscape governing the nonthermal order-parameter response using a time-dependent extension of Ginzburg-Landau theory. Furthermore, we find a CDW recovery at elevated electronic temperatures, which we ascribe to the nonequilibrium between hot electrons and an initially cold lattice [II]. (iv) Additionally, we observe an unusual transient modulation of the relaxation rates of hot high-energy photocarriers in photoexcited TbTe$_3$. Supported by a theoretical analysis of the electron self-energy, we investigate how an ultrafast CDW-to-metal transition affects fundamental interactions and show how the phase space of electron-electron scattering is critically modulated by a photoinduced collective CDW excitation [III]. (v) Lastly, we study the ultrafast nonthermal pathway to a long-lived metastable phase in bulk $1T$-TaS$_2$ after optical excitation. We present strong evidence for the critical role of the CDW amplitude mode as main driver of the phase transition and demonstrate a high degree of control over the phase transition using a tailored optical multi-pulse sequence [XI].

In the next chapter, we briefly introduce the main phenomena examined in this thesis, followed by an introduction to trARPES. The four publications forming the main part of this cumulative thesis are reprinted in Chapter 4, followed by a discussion of the manuscripts and their connection. The thesis concludes with an outlook toward future research of 2D quantum materials with a focus on time-resolved momentum microscopy.

2

Theoretical background

We first introduce the main phases and material classes discussed in this thesis, that is, charge density waves, Mott insulators, and 2D topological insulators. This chapter aims at providing a summary of the central properties and key concepts of the respective systems. For an extensive review of charge density waves, see Refs. [9, 26], for Mott insulators, see Refs. [27, 28], and for 2D topological insulators, see Refs. [29–31].

2.1 Charge density waves

Below a critical temperature, certain metals are susceptible to the formation of a CDW, that is, a spatial modulation of the electron density accompanied by a periodic distortion of the lattice that breaks the original translational crystal symmetry. Due to the ubiquity of this broken-symmetry state in quantum materials and its proximity to unconventional superconductivity, CDWs continue to attract significant interest for several decades. The following introduction is based on Refs. [9, 26, 32].

Peierls instability. The concept of a CDW was first described by Rudolf Peierls in a 1D atomic chain. Peierls showed that strictly 1D systems are unstable against a periodic charge- and lattice distortion, as sketched in Fig. 2.1a-b). Simply put, CDW formation opens an energy gap at the Fermi level E_F, lowering the electronic energy. As the energy gain overcomes the energy cost of elastic lattice deformation, the CDW is stable. Formally, the Peierls instability is captured by the Lindhard response function, which describes the rearrangement of the charge density in response to a time-independent periodic potential. For a 1D free electron gas at $T = 0$, the Lindhard response diverges at the momentum wave vector $q = 2k_\mathrm{F}$ connecting the electronic states at E_F, implying that the electron gas itself is unstable with respect to the formation of a periodically varying electron charge density.

By introducing a periodic potential with $q = 2k_\mathrm{F}$ the coupled electron-lattice system of the 1D atomic chain exhibits a new periodicity $2a$ and new Brillouin-zone boundaries at $\pm k_\mathrm{F}$. The new periodicity results in spectral-weight transfer from the main bands to replica (or shadow) bands, see the dashed curves in Fig. 2.1b). These replica bands are shifted from the main bands by $2k_\mathrm{F}$ and are most pronounced near their crossings with the main bands. Hybridization between main and replica bands opens an energy gap 2Δ at the Fermi points at the new zone boundaries. This electronic energy gain compen-

sates for the cost of the concomitant structural deformation, which can be thought of as a frozen lattice distortion. The strong interaction between electrons and lattice renormalizes the phonon mode with a wave number close to $2k_F$ to lower energy, termed Kohn anomaly. Below the critical temperature T_c, the phonon dispersion at $q = 2k_F$ dips to zero energy, meaning that a static lattice distortion appears. Thus, upon cooling below T_c, the system undergoes a metal-insulator transition of second order driven by a coupled periodic charge and lattice superstructure.

For a strictly 1D system at $T = 0$, the entire Fermi surface consisting of parallel sheets at $\pm k_F$ can be connected by a single wave vector $q = 2k_F$, termed *perfect* Fermi-surface nesting, see Fig. 2.1c). In this scenario, the introduced CDW periodicity gaps the entire Fermi surface and the gain in energy of occupied electron states always overcomes the energy cost of lattice deformation. However, at elevated temperatures, in quasi-1D or higher-dimensional systems, the Fermi surface may only be partially nested and the singularity is removed from the Lindhard response. The electronic energy gain from nesting is reduced as only a fraction of the Fermi surface may become gapped, and further mechanisms, for example, momentum-dependent electron-phonon coupling, are required to trigger CDW formation.
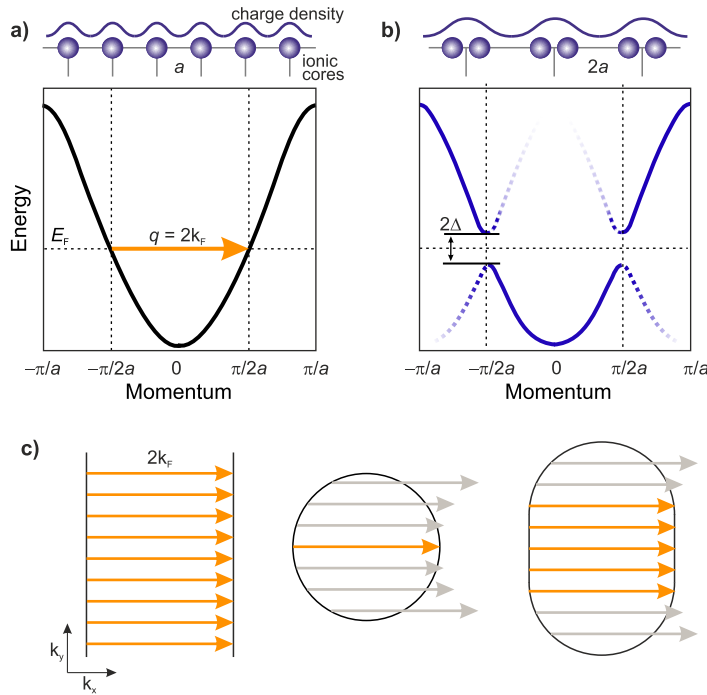
Figure 2.1: Peierls instability and Fermi-surface nesting. a) 1D chain of atoms with lattice constant *a* and corresponding band-structure schematic for the metallic phase above T_c. **b)** Below T_c, a CDW with periodicity 2*a* forms, opening an energy gap 2Δ at E_F and inducing replica bands shifted from the main bands by wave vector *q*. **c)** Fermi-surface topology with nesting wave vectors for a 1D electron gas (left), a 2D free electron gas (center), and an anisotropic 2D system (right). Orange arrows indicate nested Fermi-surface regions.

Mean-field description. In analogy to Bardeen-Cooper-Schrieffer (BCS) supercon-
ductivity, a weak-coupling mean-field treatment based on the Fröhlich Hamiltonian can
be applied to approximate central properties of the CDW state. The benefit of the mean-
field approach is that it captures the average interactions without the need to explicitly
specify the microscopic details of the electron-phonon interaction. The effective CDW
order is parametrized by the complex order parameter $\psi = \Delta e^{i\phi}$ with the deviation of the
charge density from the normal state Δ and the relative phase ϕ of the modulation with
respect to the original lattice. To characterize the amplitude Δ of the CDW, the single
particle gap at E_F is commonly employed. The displacement of the lattice from the nor-
mal state can be used equivalently to the electronic description of the order-parameter
amplitude. While ARPES directly allows to access the electronic order parameter from
the electronic band-gap size, the superlattice Bragg peak intensity measured by x-ray
diffraction may be used as observable of the structural deformation. In the metallic
phase above the transition temperature T_{MF}, the order-parameter amplitude Δ is zero
as no CDW order is established. Below T_{MF} (in the region close to the transition), the
mean-field temperature dependence of the order parameter is given by

$$\Delta = 1.74\Delta_0\sqrt{1 - \frac{T}{T_{\mathrm{MF}}}} \tag{2.1}$$

where Δ_0 is the CDW energy gap at zero temperature. The zero-temperature gap and
mean-field transition temperature are linked by the well-known BCS relation

$$2\Delta_0 = 3.52k_{\mathrm{B}}T_{\mathrm{MF}}\,. \tag{2.2}$$

However, the mean-field approximation neglects fluctuations of the order parameter,
which are particularly important in low-dimensional systems due to the reduced phase
space. In strictly 1D systems, fluctuations even inhibit long-range order above $T = 0$. In
real 3D systems, coupling between neighboring 1D chains leads again to a finite tran-
sition temperature T_{3D} at which long-range 3D order emerges. Yet, the experimentally
observed transition temperatures T_{3D} are significantly smaller than the predictions by
mean-field theory T_{MF}. Upon cooling below T_{MF}, the system does not undergo a phase
transition, as initially only short-range 1D fluctuations arise, which are not correlated to
fluctuations at neighboring chains. Upon further cooling, correlations between neighbor-
ing chains start to develop, until, at T_{3D}, long-range 3D CDW order develops.

Fluctuations in 1D. We briefly introduce the main characteristics of fluctuation effects
using the model system of a 1D chain. Order parameter fluctuations can be described by
the Ginzburg-Landau functional

$$F = F_0 + n(E_{\mathrm{F}})\int dx\left[a|\psi|^2 + b|\psi|^4 + c\frac{|d\psi|^2}{|dx|}\right] \tag{2.3}$$

with the free energy in the metallic phase F_0, the density of states at the Fermi level
$n(E_{\mathrm{F}})$, and the complex order parameter ψ. The shape of the energy landscape is defined
by the first two terms inside the integral and is illustrated for $T \ll T_{\mathrm{MF}}$ in Fig. 2.2a). The

last term describes spatial fluctuations of the order parameter, which were neglected in the mean-field approximation discussed above. As ψ is complex, amplitude and phase fluctuations have to be considered. The dispersion relations in the long-wavelength limit and sketches of amplitude and phase excitations, so-called amplitudons and phasons, are shown in Fig. 2.2b-c). The amplitude- and phase branches are reminiscent of optical and acoustic phonons and often emerge as additional phonon modes once a material enters the CDW phase. While amplitudons dominate near the transition temperature, their contribution is progressively removed upon cooling. At $T \ll T_{\mathrm{MF}}$, the amplitude is approximately at the $T = 0$ value, while phasons rotate the order-parameter phase in the bottom of the Mexican-hat potential.
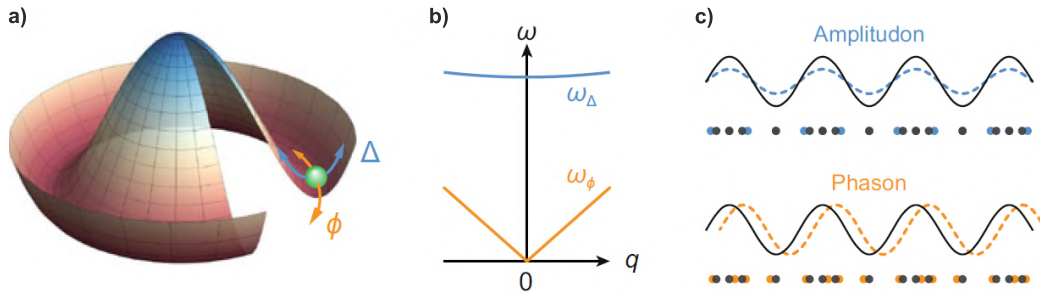
Figure 2.2: Elementary excitations in a 1D chain. a) Ginzburg-Landau potential of a complex order parameter $\psi = \Delta e^{i\phi}$ near $T = 0$. The arrows indicate amplitude- and phase excitations. **b)** Dispersion of the amplitude- and phase excitations near $q = 0$. **c)** Illustration of amplitude- and phase excitations in the $q \rightarrow 0$ limit. Dashed curves indicate a change in electron density, while circles show the atomic displacement. *Reprinted with permission from Ref. [32]. Copyright 2021 Springer Nature.*

Application to real materials. While the Peierls picture provides an intuitive understanding of CDW physics in strictly 1D systems, most real materials are only partially consistent with this model, as interactions between neighboring quasi-1D chains, higher-dimensional CDW formation, momentum-dependent electron-phonon coupling, and electronic correlations have to be considered. One of the few materials that features all main characteristics of the Peierls transition – a charge- and lattice superstructure, a metal-insulator transition, a dip in the phonon spectrum, and a clear peak in the Lindhard function – is the quasi-1D system TTF-TCNQ [26]. In contrast, in many quasi-2D CDW systems, such as the rare-earth tritellurides, momentum-dependent electron-phonon coupling drives the CDW formation while Fermi-surface nesting takes a secondary role [33–35]. To describe the CDW formation in several layered TMD compounds, such as $1T$-TaS$_2$ and $2H$-TaSe$_2$, the Peierls model has to be extended to a strong-coupling regime, as the electronic band-energy lowering that stabilizes the broken-symmetry state does not result from the opening of a uniform gap at the Fermi vector, but from sub-band splittings and shifts over extended parts of the Brillouin zone (BZ) [36]. Intriguingly, while the CDW state in $1T$-TaS$_2$ does not fully gap the entire Fermi surface, it facilitates charge localization at the superstructure centers resulting in strong electronic correlations, which leads us to the phenomenon of Mott insulators discussed in the following.

2.2 Mott insulators

The band theory of non-interacting electrons developed by Bethe, Sommerfeld and Bloch distinguishes between metals and insulators based on band filling. For insulators, the Fermi level is situated inside the band gap, while it is located inside the highest filled band for metals. Although this theory was a great success, its basic prediction fails for a variety of materials such as the TMD $1T$-TaS$_2$ [37] and the triangular tin (Sn) adatom lattice on a semiconductor substrate Sn/Si(111)-($\sqrt{3} \times \sqrt{3}$) [38, 39], which we will both investigate in the context of this thesis. The deviation from band theory stems from electronic correlation effects, that is, purely electronic phenomena that cannot be understood within the independent-electron Hartree-Fock approximation. Mott suggested that Coulomb repulsion between electrons in the same orbital may lead to insulating behavior despite partially filled bands, which laid the foundation for the Hubbard model. The following introduction to Mott insulators is based on Refs. [27, 40, 41].

The Hubbard model. The Hubbard model is an intriguingly simple Hamiltonian based on two opposing tendencies: Electron hopping and on-site Coulomb repulsion. The kinetic energy (electron hopping) term facilitates metallic behavior by delocalization of electrons into Bloch states, while the electron-electron interaction by Coulomb repulsion induces localization onto atomic sites. The main ingredients of this model for a 2D triangular lattice with lattice constant a and one electron per lattice site are visualized in Fig. 2.3a). The tight-binding matrix element t describes the overlap integral between atomic orbitals of adjacent atoms, corresponding to the probability of hopping between nearest-neighbor sites. Double occupancy of a single orbital by electrons with opposite spins at site i leads to the intra-atomic Coulomb energy

$$U = \int dr_1 \int dr_2 \, |\Theta(r_1 - R_i)|^2 \frac{e^2}{|r_1 - r_2|} |\Theta(r_2 - R_i)|^2 \tag{2.4}$$

where r_1 and r_2 are the electron positions with respect to the lattice site R_i in the Wannier state Θ. These two competing principles are the basis of the Hubbard Hamiltonian

$$\mathcal{H} = -t \sum_{\langle ij \rangle, \sigma} \left(c_{i\sigma}^\dagger c_{j\sigma} + \text{h.c.} \right) + U \sum_i n_{i\uparrow} n_{i\downarrow} \tag{2.5}$$

describing interacting electrons on a lattice. Here, $c_{i\sigma}^\dagger$ ($c_{i\sigma}$) creates (annihilates) an electron in the Wannier state $\Theta(r - R_i)$, i and j are lattice sites, $\sigma = \uparrow, \downarrow$ denotes the spin, the sum $\langle ij \rangle$ runs over nearest neighbors, and $n_{i\sigma} \equiv c_{i\sigma}^\dagger c_{i\sigma}$ is the density of electrons at site i with spin σ.

The zero-temperature properties of the Hubbard model are governed by the relative interaction strength U/t and the electron density $n = N/L$ with the total number of electrons N and the number of lattice sites L. Let us reconsider a half-filled 2D atomic lattice, which, in the single-orbital model, corresponds to $n = 1$ (same number of electrons as lattice sites). The following thought experiment where we change the lattice constant a, thus varying the overlap integral, illustrates the three regimes of the Hubbard model depicted in Fig. 2.3b).
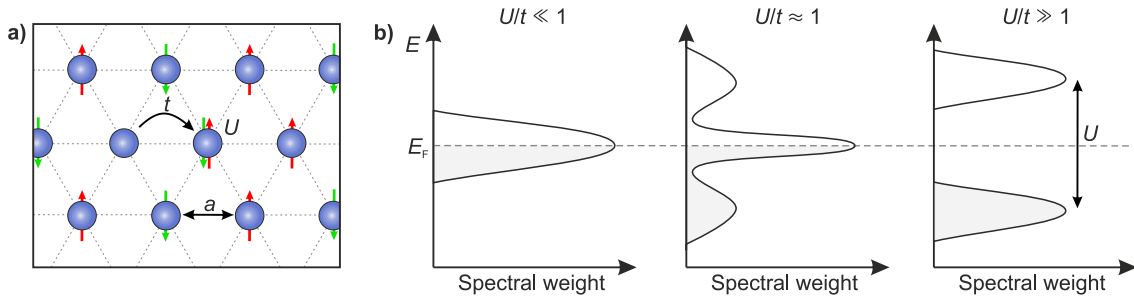
Figure 2.3: Regimes of the Hubbard model. a) Illustration of a 2D triangular lattice with lattice constant *a*, inter-site hopping *t*, and intra-site Coulomb repulsion *U* at half filling. Spin-up (spin-down) electrons are indicated by red (green) arrows. **b)** Spectral weight distribution for the metallic, intermediate, and strongly correlated Mott-insulating regime of the Hubbard model for increasing ratios of *U/t* at half filling.

- $U \ll t$: By decreasing the atomic spacing *a*, hopping becomes the dominant term of the Hamiltonian due to high orbital overlap between neighboring sites – the system turns metallic as the electrons become highly delocalized. Even in the presence of weak correlations, the system can be classified as a Fermi liquid with metallic spectral weight around E_F.

- $U \gg t$: Increasing *a* to a value where *t* becomes insignificant removes charge fluctuations from the system. This corresponds to the limit of extremely strong interactions, which can be thought of as a set of isolated atoms, where double occupancy is prohibited due to strong Coulomb repulsion. The system is in a Mott insulating state where each lattice site is occupied by a single spin-up or spin-down electron. The spectral weight at E_F vanishes and is redistributed into a lower Hubbard band (LHB) and upper Hubbard band (UHB), separated by *U*. This gap corresponds to the energy cost of electron removal from a single occupied site and subsequent double occupancy of a neighboring orbital. Although the density of states may appear similar to a semiconductor, its nature is very different, as the splitting into two Hubbard bands is purely a correlation effect. The density of states is occupation-dependent, as the UHB only exists due to double occupancy. Each sub-band cannot contain more than *L* electrons, in contrast to ordinary bands that can hold up to 2*L* electrons.

- $U \approx t$: As we have derived insulating behavior in the atomic limit and a metallic Fermi liquid for weak correlations, the intermediate must feature a phase transition, the so-called Mott metal-insulator-transition. Starting from the metallic case, an increase in correlation strength results in a redistribution of spectral weight into precursors of the Hubbard sub-bands. Additionally, electronic correlations trigger the formation of a metallic quasiparticle, that is, electrons dressed by excited states, that can be treated similarly to non-interacting electrons but with renormalized energy, mass, and finite lifetime. With increasing *U*, charge fluctuations are suppressed, the quasiparticle peak narrows due to an enhancement of effec-

tive mass, and spectral weight is gradually transferred to the incoherent part of the spectrum. At a critical value of U, the effective mass diverges associated with a vanishing width of the peak at E_F; the metallic quasiparticle disappears and the system becomes insulating.

Application to real materials. As illustrated above, in materials with strongly localized electronic states, a Mott-insulating ground state may form at low temperatures despite partial band filling. Most prominently, material systems with open d and f electron shells such as transition metal oxides are subject to strong correlations, as electrons experience strong Coulomb repulsion due to the spatial confinement and small overlap of such orbitals. Low-dimensional systems with large inter-site spacing and a reduced number of neighboring hopping sites (resulting from the dimensional confinement) may also show electronic correlation effects. Prominent representatives of such low-dimensional Mott insulators are dilute 2D adatom systems on semiconductor surfaces such as K/Si(111)-($\sqrt{3} \times \sqrt{3}$) and Sn/Si(111)-($\sqrt{3} \times \sqrt{3}$) [38, 39, 42]. For a quantitative description of real materials, the introduced single-band Hubbard model generally has to be extended to a multi-band theory and to higher-order hopping terms and inter-site Coulomb repulsion [43, 44]. Furthermore, Mott transitions in real systems are often accompanied by a structural transition, which may substantially alter the atomic distances and therefore the U/t ratio. Thus, for a realistic treatment of phase transitions in quantum materials, not only correlated electrons, but also their coupling to structural degrees of freedom has to be considered. Note that most Mott insulators also feature a wide array of magnetic orderings [27], which, however, goes beyond the scope of this introduction.

2.3 Quantum spin Hall insulators

A breakthrough in condensed matter physics was Landau's approach to characterize distinctive phases in terms of spontaneous breaking of underlying symmetries, such as the breaking of translational symmetry in CDWs and gauge symmetry in superconductors. The discovery of the quantum Hall (QH) effect in 1980 led to a different classification scheme based on a system's topological order. The topological order does not break any symmetries, but rather defines a topological phase that is insensitive to a smooth variation of material parameters and can only be changed by crossing through a topological quantum phase transition. A remarkable and for prospective device applications critical consequence of a nontrivial bulk topology of insulators is the presence of metallic edge or surface states. An intuitive argument for the existence of such gapless states is as follows. Most insulators (such as vacuum) are topologically trivial. At the interface between a conventional and a topological insulator (TI), the band structure cannot be interpolated continuously without closing the energy gap – forcing the appearance of metallic states of topological origin at the interface [45]. The following introduction is based on Refs. [30, 31, 46, 47].

From quantum Hall to quantum spin Hall. In the QH state, the bulk of a 2D sample forms Landau levels under strong external magnetic fields, while the sample edge carries
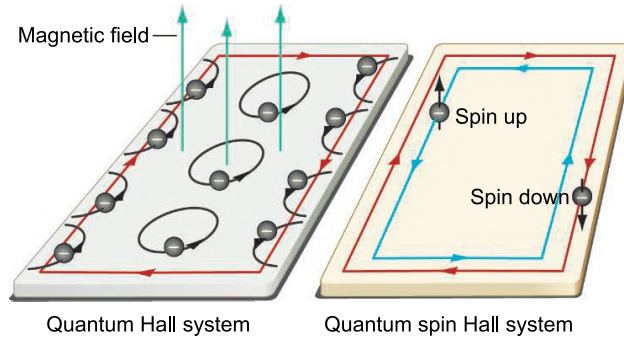
Figure 2.4: Quantum Hall and quantum spin Hall effect. In a QH system (left), an applied magnetic field causes electrons to bounce off the sample edges in circular orbits, resulting in a unidirectional net flow of charge along the boundary of the material. In a QSH system (right), spin-up and spin-down carriers flow in opposite directions in edge channel states, and no magnetic field is needed. *Reprinted with permission from Ref. [47]. Copyright 2007 AAAS Science.*

a one-directional electric current, see Fig. 2.4. The Hall conductance transverse to the electric current takes on quantized values of $\sigma_{xy} = Ce^2/h$ (where e is the electron charge and C is an integer), as σ_{xy} is a topological invariant that is independent of the specific material details. The edges of a QH insulator allow for dissipationless flow, as electrons, which are deflected into circular paths by the magnetic field, bounce back from the edges, resulting in a unidirectional net 1D motion. As the 1D counterflows at the left and right edges of the sample are spatially separated, backscattering is forbidden given the absence of the counterpropagating state, and dissipation is fully suppressed even in the presence of impurities.

A more recent class of topological systems are quantum spin Hall (QSH) insulators, synonymously called 2D TIs[1], where intrinsic spin-orbit (SO) coupling takes the role of the magnetic field, which is particularly pronounced in heavy elements. The QSH effect can be roughly understood as two copies of the QH state. While the 2D bulk again has an insulating gap, the sample edge features two gapless counterpropagating states with opposite spin, as the SO coupling effectively acts as a spin-dependent magnetic field of opposite direction for spin-up and spin-down electrons, see Fig. 2.4. As the spin is directly related to the direction of motion, they are called helical edge states. Since no external magnetic field is required, the QSH state is invariant under time reversal (TR) and can be classified by a $\mathbb{Z}_2$ topological order parameter, that is, a mathematical classification of the Bloch wave function discriminating between topologically trivial and non-trivial phases of TR-invariant systems. The helical edge states are time-reversed partners of each other

---

[1]The topological characterization of QSH insulators can be generalized in three dimensions [48, 49]. The resulting material class, termed 3D TIs, is insulating in the 3D bulk and features unique conducting states on the surface in which the electron's spin and linear momentum are locked. Following the theoretical prediction and experimental verification of a 3D TI state in $Bi_{1-x}Sb_x$, a variety of 3D TIs have been identified [50]
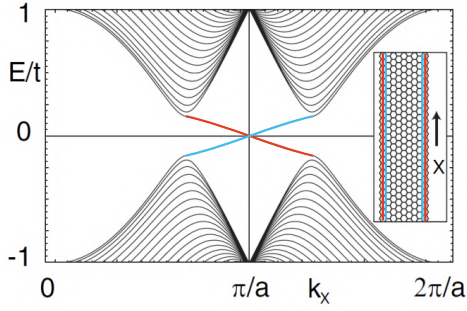
Figure 2.5: Band structure for a strip of graphene. The insulating bulk bands (black) are connected by 1D gapless spin-polarized edge states (red, blue) with $t_2/t = 0.03$. The inset illustrates the graphene strip with edge states along the zig-zag edges. *Adapted with permission from Ref. [7]. Copyright 2005 American Physical Society.*

and form a Kramers doublet[2]. Thus, the crossing of their energy-momentum dispersions at special points in the BZ is ensured by TR symmetry and the degeneracy point cannot be removed by any TR-invariant perturbation. Hence, the helical edge states are *topologically protected* by TR symmetry. Although edge states are available in both directions in QSH insulators, scattering between the counterpropagating channels is forbidden unless TR symmetry is broken. Thus, edge-state transport in QSH insulators is dissipationless.

Kane-Mele model. The QSH effect was first predicted by Kane and Mele in two seminal articles in 2005 [7, 51], where they investigated the effect of SO coupling on the low-energy electronic structure of graphene and introduce the $\mathbb{Z}_2$ topological invariant to classify graphene's nontrivial topology. Graphene consists of a 2D honeycomb lattice of carbon atoms with two sublattices. The low-energy band structure is defined by p_z orbitals that give rise to π-bands forming Dirac cones at the K and opposite K' corners of the hexagonal BZ. In the absence of SO coupling, the system features gapless states with linear dispersion $E(\mathbf{k}) = \pm \hbar v_\mathrm{F} |\mathbf{k}|$. Without doping, the Fermi level is situated at the Dirac point and the system is semimetallic. Adding a SO-coupling term to the system respects all of the symmetries of graphene and introduces an energy gap $2\Delta_\mathrm{SO}$ with $E(\mathbf{k}) = \pm \sqrt{(\hbar v_\mathrm{F} \mathbf{k})^2 + \Delta_\mathrm{SO}^2}$. The distinctive feature of SO coupling is that it produces gaps with opposite signs at the K and K' points. This state can not be adiabatically connected to a conventional insulating phase – it is topologically nontrivial. The edge states can be seen explicitly in a simple tight-binding model with Hamiltonian

$$\mathcal{H} = t \sum_{\langle ij \rangle \alpha} c_{i\alpha}^\dagger c_{j\alpha} + t_2 \sum_{\langle\langle ij \rangle\rangle \alpha\beta} i \nu_{ij} s_{\alpha\beta}^z c_{i\alpha}^\dagger c_{j\beta} \tag{2.6}$$

where the first term is the nearest neighbor hopping with hopping amplitude t and the second term arises from SO coupling and represents spin-dependent next-nearest neighbor hopping with $\Delta_\mathrm{SO} = 3\sqrt{3} t_2$ at low energy. $\nu_{ij} = -\nu_{ji} = \pm 1$ depends on the orientation of the two nearest-neighbor bonds the electrons traverses and s^z is the Pauli matrix representing the electron's spin. Solving this Hamiltonian for a strip geometry yields bulk band gaps at K and K' points and two gapless bands connecting K and K', see the 1D projected band structure in Fig. 2.5.

---

[2]Kramers theorem states that each energy level of a TR symmetric quantum mechanical system with half-integer spin is at least double degenerate.

Realizations of QSH insulators. As shown above, Kane and Mele proposed graphene as a QSH candidate. However, as intrinsic SO coupling of graphene is small and only emerges due to SO coupling between next-nearest neighbors (Eq. 2.6) at the level of second-order perturbation theory, the QSH effect is expected to occur only below 0.01 K [52]. The QSH effect was first experimentally observed in HgTe/CdTe quantum wells [53], following the theoretical prediction by Bernevig et al. [54] where the central feature is band inversion. The barrier material CdTe has a normal band progression, whereas, for a certain thickness, the well material HgTe has an inverted band progression, resulting in a single pair of helical edge states at the interfaces. Also certain monolayer TMDs with $1T'$ structure, namely $1T'$-MX$_2$ with M=(W, Mo) and X=(Te, Se, S), may give rise to the QSH effect due to an inverted band structure [8]. While quantized conduction through edge states remains to be confirmed for this material class, scanning tunneling microscopy (STM) measurements have demonstrated gapless edge states at up to ~ 100 K in monolayer $1T'$-WTe$_2$ [55, 56]. A further promising QSH material class are graphene analogs built from heavier atomic species. The basic idea is to apply the Kane-Mele model to an element with increased SO coupling, thereby increasing the band gap to a more practical regime. A prominent representative of this material class is bismuthene, which we will investigate further within this thesis. Bismuthene is a planar bismuth monolayer arranged in a honeycomb geometry on a semiconducting silicon carbide substrate. It is insulating in the 2D bulk and shows gapless 1D states at substrate step edges, which act as sample boundaries [57]. In contrast to graphene, the low-energy physics are governed by on-site SO coupling of p_x and p_y orbitals, as the p_z orbitals are shifted to higher energies due to interaction with the SiC substrate. This *orbital filtering* by the substrate is a critical ingredient, as the band gap is generated from huge on-site atomic SO coupling [58], resulting in a topological gap of ~ 0.8 eV at the Dirac points – the largest band gap of any QSH system. In Chapter 5, we will further explore the electronic band structure of bismuthene using trARPES and investigate the role of edge states in the relaxation of excited photocarriers.

3

Time- and angle-resolved photoemission spectroscopy

Time-resolved ARPES is at the forefront of current condensed-matter research and is the main technique employed in this thesis. It is based on angle-resolved photoemission spectroscopy (ARPES), which is a powerful tool to access the electronic structure and many-body effects of solids with momentum resolution. Utilizing a pump-probe approach, trARPES extends the capabilities of ARPES to the time domain, granting access to out-of-equilibrium processes and properties of solids on fs timescales. This chapter introduces the fundamentals of photoemission as well as the basic concepts and experimental considerations of trARPES based on Refs. [4, 41, 59–63]. The chapter closes with a technical overview of the XUV trARPES setup at the Fritz Haber Institute, Berlin.

3.1 Basic principles of ARPES

Photoemission spectroscopy is one of the most direct methods to investigate the electronic structure of atoms, molecules, and solids. Incident light at a photon energy above the work function[3] Φ is absorbed by electrons which are released from the material, as described by the photoelectric effect. This simple principle is the basis of ARPES, which has become a standard technique in materials science. In the simplest sense, ARPES directly provides the occupied momentum-resolved electronic band structure of a solid by measuring the energy spectrum and angular distribution of emitted photoelectrons. Monochromatic radiation of frequency ν is used to excite electrons to a kinetic energy

$$E_{\mathrm{kin}} = h\nu - \Phi - |E_{\mathrm{B}}| \tag{3.1}$$

(where h is Planck's constant) and provides access to the binding energy E_{B} of electronic states inside a solid. The energetics of the photoemission process and the ARPES measurement geometry are sketched in Fig. 3.1.

The general aim in ARPES is the determination of the electronic dispersion relation $E(\mathbf{k})$ inside the solid, that is, the relation between binding energy E_{B} and crystal momentum $\mathbf{k}$, from the kinetic energy E_{kin} and the momentum $\mathbf{K} = \mathbf{p}/\hbar$ of the photoelectrons

---

[3]The work function is a material-specific potential barrier hindering the valence electrons from escaping the surface. It is typically on the order of 3 to 5 eV.
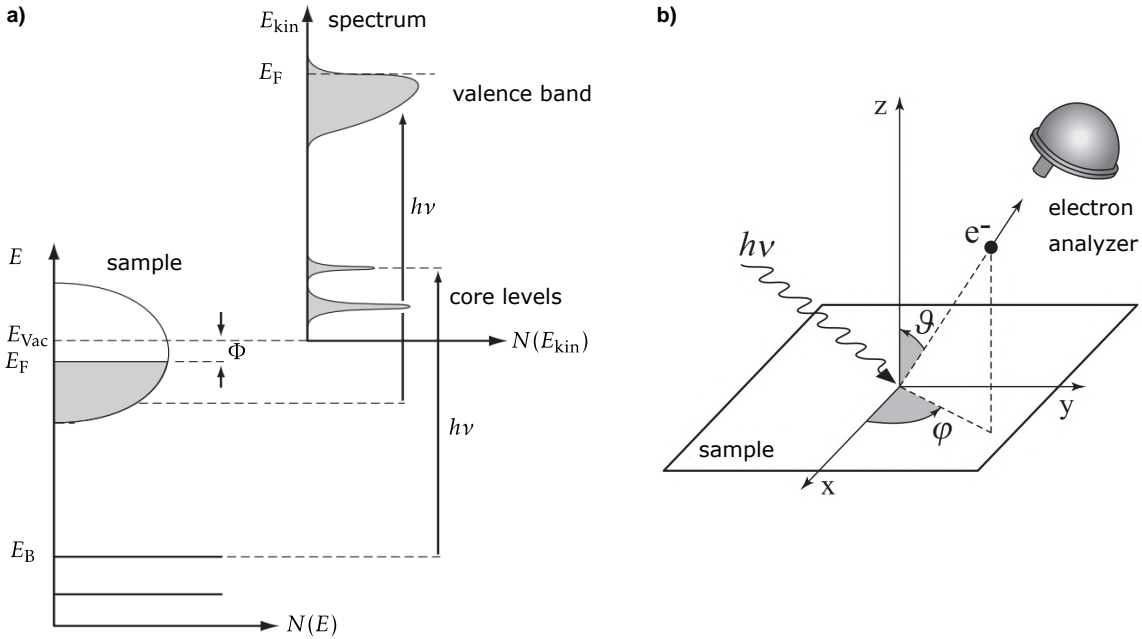
Figure 3.1: Energetics of the photoemission process and ARPES geometry. a) Energy diagram of photoemission from a metal. In the photoemission process, a replica of the electronic distribution of the solid is created outside of the sample. **b)** Illustration of the geometry of an ARPES experiment with incoming light $h\nu$ and the photoelectron path specified by angles ϑ and φ. *Adapted with permission from Ref. [59]. Copyright 2003 Springer.*

in vacuum. The wave vector $\mathbf{K}$ with $K_{x,y}$ parallel and K_z perpendicular to the sample surface is completely determined by the emission angles ϑ (polar, out-of-plane) and φ (azimuthal, in-plane):

$$\mathbf{K} = \begin{pmatrix} K_x \\ K_y \\ K_z \end{pmatrix} = \frac{1}{\hbar} \sqrt{2mE_{\mathrm{kin}}} \begin{pmatrix} \sin\vartheta\cos\varphi \\ \sin\vartheta\sin\varphi \\ \cos\vartheta \end{pmatrix} \tag{3.2}$$

Three-step model. The phenomenological three-step model provides an intuitive understanding of the photoemission process, dividing the process into three independent sequential steps. (i) The first step is the optical excitation of electrons inside the solid from the initial to final bulk Bloch states. Note that for determining the wave vector $\mathbf{k}$ inside the crystal, the photon momentum transfer can be neglected for the XUV photon energies utilized in this work, as it is insignificant compared to the typical BZ dimensions. (ii) Next, the photoelectrons propagate to the surface. During this step, photoexcited electrons may scatter inelastically with other electrons, phonons, or defects, which may alter their energy or momentum and give rise to an incoherent background. As the average path between scattering events, termed inelastic mean free path, is on the order of 1 to 10 nm in the relevant energy range of 5 to 1000 eV for most solids, ARPES
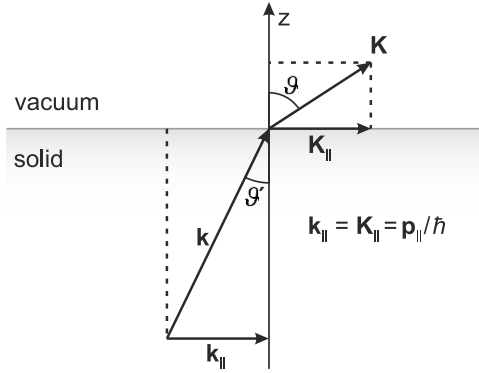
Figure 3.2: Momentum relations at the solid-vacuum interface. The parallel component of the crystal momentum inside the solid $\mathbf{k}_\parallel$ is conserved when transversing the solid-vacuum interface, while the perpendicular component is altered by the abrupt potential change. *Adapted with permission from Ref. [59]. Copyright 2003 Springer.*

is extremely surface sensitive. Particularly in the energy range of 10-100 eV most relevant for trARPES, electrons originating from the topmost atomic layer dominate the photoemission signal. (iii) Last, the photoelectrons penetrate the surface potential barrier and escape into vacuum. Conveniently, the translational symmetry in the $x-y$ plane is maintained during this step, resulting in the conservation of the parallel momentum component

$$|\mathbf{k}_\parallel| = |\mathbf{K}_\parallel| = \frac{1}{\hbar}\sqrt{2mE_{\text{kin}}} \cdot \sin\vartheta. \tag{3.3}$$

The momentum relations at the solid-vacuum interface are illustrated in Fig. 3.2. Complexity arises from the fact that the perpendicular momentum $\mathbf{k}_\perp$ is not conserved during the emission process due to the abrupt potential change along the z-direction when transmitting through the surface. Thus, (quasi-) 2D materials represent an ideal platform to be studied by ARPES, as, for low-dimensional structures, the perpendicular momentum is less relevant due to the negligible dispersion along the z direction. Additionally, ARPES is ideally suited for the investigation of monolayer samples and surface states due to its surface sensitivity.

Photoemission intensity. The formal, quantum-mechanical description of the photoemission process is based on Fermi's Golden Rule, characterizing the transition probability between initial and electron final states upon perturbation by a light field. Based on this approach, the photoemission intensity can be written as

$$I(\mathbf{k},\omega) = |M^{\mathbf{k}}_{f,i}|^2 f(\omega) A(\mathbf{k},\omega) * R(\Delta k, \Delta\omega) \tag{3.4}$$

where $\mathbf{k} = \mathbf{k}_\parallel$ is the electron momentum parallel to the sample surface and ω is the electron energy with respect to E_{F}. The transition matrix element $|M^{\mathbf{k}}_{f,i}|^2$ depends largely on extrinsic factors such as light polarization, photon energy, and experimental geometry but also carries information on the material's orbital texture [64]. The Fermi-function term $f(\omega) = (e^{\omega/k_B T} + 1)^{-1}$ originates from the fact that only occupied electronic states at temperature T can be probed. The one-particle spectral function $A(\mathbf{k},\omega)$ defines the one-electron removal spectra based on the Green's function formalism, describing the propagation of a single electron in a many-body environment. For a non-interacting system, $A(\mathbf{k},\omega) = \delta(\omega - \epsilon_{\mathbf{k}})$ with electron band energy $\epsilon_{\mathbf{k}}$ directly represents the single-particle

band structure. In the presence of electronic correlations, $A(\mathbf{k}, \omega)$ contains renormalization effects due to interactions in the underlying many-body system and the lifetime of the photohole created by the excitation. The last term accounts for the broadening introduced by a finite experimental resolution $R(\Delta k, \Delta \omega)$.

The energy of an electron interacting with the surrounding many-body environment is defined as the complex self-energy

$$\Sigma(\mathbf{k}, \omega) = \Sigma^{'}(\mathbf{k}, \omega) + i\Sigma^{''}(\mathbf{k}, \omega) \tag{3.5}$$

where the real part gives the deviation between the one-electron and the dressed quasiparticle state and the imaginary part accounts for the inverse lifetime of the quasiparticle. The spectral function in terms of the complex self-energy is the basis of interpreting ARPES spectra of correlated materials and can be written as

$$A(\mathbf{k}, \omega) = -\frac{1}{\pi} \frac{\Sigma^{''}(\mathbf{k}, \omega)}{[\omega - \epsilon_{\mathbf{k}} - \Sigma^{'}(\mathbf{k}, \omega)]^2 + [\Sigma^{''}(\mathbf{k}, \omega)]^2} \, . \tag{3.6}$$

Effectively, $\Sigma^{'}(\mathbf{k}, \omega)$ offsets the band energy with respect to the non-interacting case, while the quasiparticle peak width broadens with $\Sigma^{''}(\mathbf{k}, \omega)$, which, for 2D systems, can be directly associated with the lifetime of the photohole. In sum, ARPES is the most direct probe of the momentum-resolved electronic band structure and intrinsic many-body effects and is particularly suited to investigate low-dimensional systems.

3.2 Basic principles of time-resolved ARPES

Combining ARPES with a pump-probe approach extends the study of electronic states in solids to the time domain. In trARPES, an ultrashort pump pulse excites the sample, followed by a probe pulse generating the photoemission signal of the nonequilibrium state, as illustrated in Fig. 3.3a). Recording the ARPES spectra for a series of temporal delays between the pump- and probe pulses Δt grants access to the dynamical evolution of the out-of-equilibrium state with fs resolution. The trARPES signal recorded for each time delay can be generally treated equivalently to a single-photon photoemission process as introduced above. Hence, the expression of the photoemission intensity in equilibrium (Eq. 3.4) can be readily extended to the time domain, $I(\mathbf{k}, \omega, \Delta t)$. We briefly examine the time dependence of the individual terms. The photoemission matrix elements are generally considered to remain constant with Δt, although in certain cases, time-dependent matrix elements may transiently affect the photoemission signal [65, 66]. Next, the generation of hot electrons by the pump pulse and subsequent cooling dynamics lead to a strongly time-dependent electronic occupation function. In metals, after an initial electron-electron thermalization time (typically $\Delta t \lesssim 100\,\mathrm{fs}$), the occupation can be approximated by a Fermi-Dirac distribution with a time-dependent electronic temperature. Lastly, also the spectral function may feature a time dependence, as, for example, during a nonthermal phase transition, the electronic structure and complex self-energy may evolve with Δt. Thus, a vast amount of information is encoded in the trARPES signal

$I(\mathbf{k}, \omega, \Delta t)$, facilitating access to the dynamical band structure, elementary excitations, and energy flow.
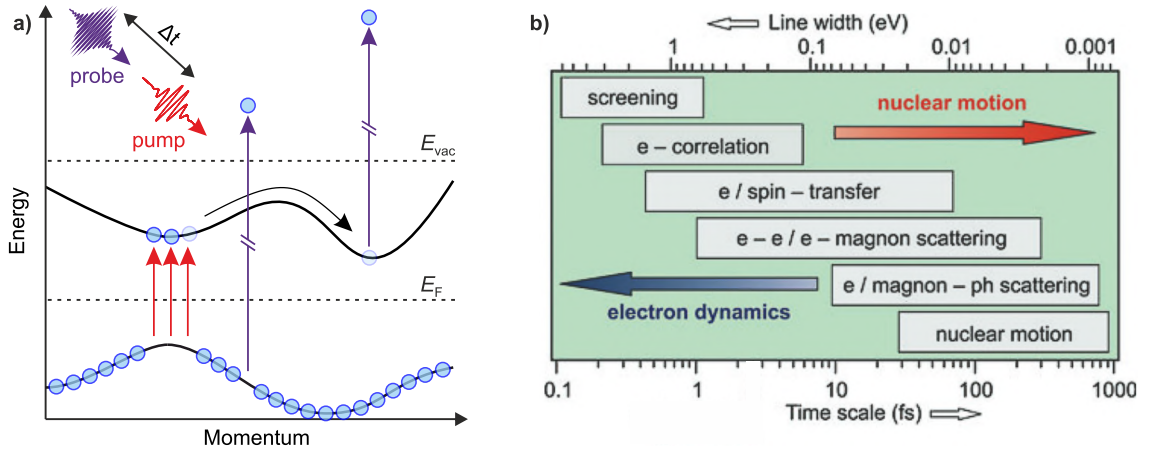
Figure 3.3: trARPES schematic and elementary excitations. a) Schematic band-structure diagram showing vertical transitions (red arrows) induced by an optical pump pulse in a semiconductor. Subsequent photoemission of a valence electron and a scattered conduction electron by a time-delayed probe pulse are indicated (purple arrows). **b)** Time scales and corresponding line widths of fundamental excitations and decay processes in solids. *Adapted panel b with permission from Ref. [61]. Copyright 2012 WILEY-VCH.*

Common excitation themes. We introduce the five most relevant excitation themes and experimental approaches employed in trARPES. (i) Through vertical optical transitions states far above E_F can be transiently populated. Probing such excited states has been critical for the determination of quasiparticle band gaps of semiconductors and for mapping the thermally unoccupied band structure of quantum materials [67–72]. (ii) Investigating the relaxation dynamics of the nonequilibrium state prepared by the pump pulse provides insights into fundamental processes in solids on intrinsic scattering timescales, see Fig. 3.3b). Tracking the transient evolution of excited-carrier populations in energy-momentum space allows identifying and disentangling elementary excitations by their respective time- and energyscales [61, 73–77]. (iii) Ultrashort optical excitations can perturb ordered states and drive nonthermal phase transitions. trARPES has been a vital tool to study the dynamical destruction and recovery of ordered states such as CDWs, Mott-insulating, and superconducting phases [78–84]. (iv) Ultrashort excitations may also launch coherent modes such as coherent phonons. Through electron-phonon coupling, such modes can be imprinted on the electronic structure, manifested in a coherent oscillation of the electronic band energy with pump-probe delay [14, 85–88]. Remarkably, by exploiting coherent modes, recent trARPES-based methods allow quantifying the electron-phonon coupling strength of specific bands with momentum resolution [13, 25]. (v) Lastly, trARPES has been key for understanding the coherent dressing of electronic states by a periodic light field, as described by Floquet theory [19, 89, 90]. Note that these excitation themes are not mutually exclusive. Tailoring the polarization, fluence, wavelength, and pulse length of the pump pulses provides a tuning knob to

specify the desired type of excitation.

Experimental considerations. As trARPES requires a narrow-bandwidth, pulsed fs light source for probing electrons, ultrashort laser radiation is a natural choice. Since the photoelectrons must overcome the material's work function Φ (typically 4 to 5 eV), up-conversion of the laser's fundamental frequency is required. A common approach is to generate the fourth harmonic of a Ti:sapphire laser at $h\nu \sim 6$ eV using nonlinear optical crystals [91–95]. However, the accessible in-plane momentum range is directly linked to the kinetic energy of the photoelectrons (Eq. 3.3) and thus depends on the applied photon energy. For this reason, 6 eV setups are limited to probing the momentum region close to the center of the BZ. To access the full first BZ of most materials, a photon energy $\gtrsim 15$ eV is required, which can be achieved by frequency up-conversion using high-harmonic generation (HHG) in noble gases [96–103]. For completeness, we note that also free-electron lasers may serve as a versatile light source for trARPES experiments [104].

An important consideration in trARPES is the Coulomb repulsion between electrons within a photoelectron cloud traveling from the sample surface to the detector unit, termed space charge. Minimizing space-charge effects is critical, as they can modify the photoelectron energy- and momentum distribution and may significantly deteriorate momentum and energy resolution. A key factor to mitigate space charge is a high laser repetition rate to distribute the total acquired photoemission signal over many pulses, limiting the number of electrons within each photoelectron cloud. Recent progress in laser science allows the generation of sufficient XUV photon flux using HHG at repetition rates beyond 10 MHz [105, 106], de facto eliminating space-charge effects. Yet, at such high repetition rates, samples may not entirely relax to equilibrium between consecutive pump pulses. Thus, during experimental design, a trade-off assessment between repetition rate and sample equilibration time is critical.

A further critical consideration is the uncertainty relation of the spectral and temporal full-width at half-maximum (FWHM) of the probe pulses,

$$\Delta E \Delta t \geq 4\hbar \ln 2 \approx 1825 \, \text{meV fs} \tag{3.7}$$

for Gaussian pulses. Effectively, the time-bandwidth product sets the boundaries for the best achievable energy and time resolution in trARPES experiments. However, most trARPES setups operate at an energy- and temporal resolution significantly above the transform limit, with typical resolution values ranging from 20 to 200 meV and 30 to 300 fs, respectively [95].

The pump pulses in trARPES experiments are most commonly the fundamental laser output of $h\nu \sim 1.5$ eV or frequency-doubled 3 eV at incident fluences in the range of few $10 \, \mu\text{J cm}^{-2}$ to few mJ cm^{-2}. Though, a wide range of excitation parameters has been combined with trARPES, ranging from resonant excitations in the visible regime [107, 108] to the mid-infrared and THz range [89, 109].

As ARPES only probes the topmost atomic layers, the sample-detector environment must be kept in ultra-high vacuum (UHV) to prevent contamination of the sample surface. Samples are either cleaved directly in the UHV setup or may be prepared and transferred to the analysis chamber without breaking vacuum. The samples are mounted

on a 6-axis manipulator that allows for alignment of the sample surface with respect to the detector along all spatial and rotational degrees of freedom. Emitted photoelectrons are recorded by either a hemispherical analyzer (HA), which is the most common electron spectrometer in trARPES, or a momentum microscope (MM), a more recent time-of-flight-based detection scheme. The HA is a 2D detector that allows for parallel detection of the energy spectrum and angular distribution along a certain in-plane momentum direction defined by the sample-detector geometry. Reconstructing larger regions of the 3D photoelectron distribution can be achieved by subsequently recording 2D energy-momentum scans for various sample rotations. The MM allows for parallel acquisition of both in-plane momentum directions and the energy spectrum, providing the 3D photoelectron distribution in a large energy- and momentum range. An in-depth discussion of both detection schemes for trARPES experiments is presented in Ref. [I].

3.3 trARPES setup at the Fritz Haber Institute

The experimental apparatus at the Fritz Haber Institute in Berlin combines a table-top high-repetition-rate XUV source and a UHV end-station with a HA and a time-of-flight MM, as illustrated in Fig. 3.4. Based on Refs. [I, 101, 110], this section will briefly describe the optical parametric chirped-pulse amplification (OPCPA) system, the XUV generation, and the end-station.

OPCPA system. A mode-locked Ytterbium fiber oscillator provides optical pulses at a central wavelength of 1030 nm and 25 MHz. In a dual-stage fiber preamplifier followed by a Yb:YAG rod-type photonic crystal fiber, the pulses are amplified to an average output of 9 W, while the repetition rate is reduced to 500 kHz using an acousto-optic modulator. 40% of the power is used to seed a Yb:YAG slab amplifier, outputting 200 W at 1030 nm, which is frequency-doubled in a beta barium borate (BBO) crystal and subsequently used as pump for the OPCPA. The remaining output is used for white-light generation in a YAG crystal, providing the seeding for the OPCPA. The pump and seed pulses are spatially and temporally overlapped in a non-collinear geometry in a 4 mm thick BBO, resulting in an average OPCPA output of 15 W at 800 nm. Using a prism compressor, the pulses are recompressed to a temporal FWHM of 35 fs. While for most experiments, the high repetition rate of 500 kHz is desirable to maximize counting statistics, an electro-optical pulse picker allows reducing the repetition rate to study materials with extended re-equilibration times. Finally, the OPCPA output is split into two arms. The main portion of the output serves to drive the XUV generation, while ~ 1 W is used as an optical pump for trARPES experiments. Using a delay stage to control the length of the pump beam path allows varying the pump-probe delay for time-resolved measurements. An optional BBO for frequency-doubling in the pump arm facilitates optical excitation at 400 nm. For experiments requiring two separate optical pump pulses, the pump arm can be further split into two beams with individually tunable temporal delay, power, and linear polarization.

XUV generation. Before up-conversion to the XUV regime, the OPCPA output is first frequency-doubled in a BBO to 400 nm, as this increases the conversion efficiency and simplifies selection of a single harmonic compared to directly using 800 nm pulses [97].
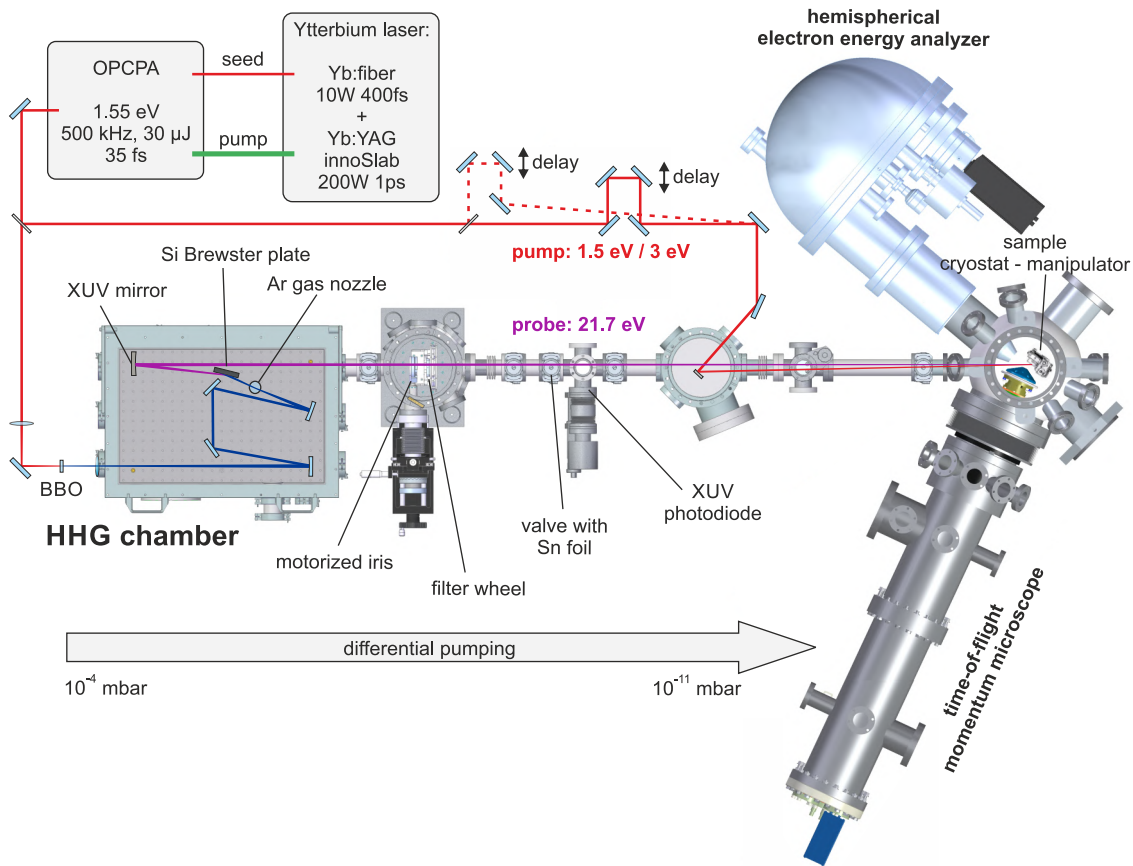
Figure 3.4: Schematic of the XUV trARPES setup at the Fritz Haber Institute. See the text for details.

The second harmonic of the laser pulses is then focused onto a dense Argon gas jet above a thin gas nozzle for HHG upconversion. This yields a frequency comb of odd harmonics of the fundamental photon energy up to the 11th harmonic that co-propagates the driving laser. As ARPES requires monochromatized radiation, a combination of a Si Brewster plate, absorbing most of the fundamental driving power, an XUV multilayer mirror and ~400 nm thick Sn foil are employed to isolate the 7th harmonic (21.7 eV, 110 meV FWHM), which is used as probe beam. At the sample position, a photon flux of up to 10^{11} photons/s is obtained. Using a motorized filter wheel, additional metallic filters can be used to reduce the XUV intensity and enhance the spectral contrast relative to unwanted harmonics. To minimize absorption losses, the XUV generation is enclosed in a high-vacuum environment.

trARPES end-station. Employing a differential pumping scheme and using an Sn window to isolate the HHG chamber from the ARPES end-station, the XUV beamline is directly connected to the UHV analysis chamber ($p < 10^{-10}$ mbar). The pump and probe beams are focused onto the sample, which is mounted on a 6-axis manipulator (SPECS GmbH) with cryostat ($T < 15$ K). The analysis chamber also includes a He dis-

charge lamp for static ARPES characterization at high energy resolution (not shown in the illustration). For photoelectron detection, a HA (Phoibos 150, SPECS GmbH) and a time-of-flight MM (METIS 1000, SPECS GmbH) are available. During standard operation, experimental energy and time resolutions are 150 meV and 35 fs, respectively. The ARPES end-station also includes a state-of-the-art UHV preparation chamber for in-situ sample growth. It includes multiple Knudsen cell evaporators, an Ar sputter gun, a stage for direct-current substrate heating, and a low-energy electron diffraction system.

Data treatment and calibration. The detection unit of the HA consists of a micro-channel plate (MCP), multiplying the photoelectrons, which are subsequently accelerated onto a phosphor screen that is imaged by a CCD camera. First, the raw camera images are frequency Fourier filtered to remove inhomogeneities introduced by a wire mesh in front of the MCP. Next, the acquired kinetic energy and angular distribution are converted to binding energy and in-plane momentum. For that, the energy- and momentum conservation laws can be employed. Empirically, often a fit of E_F and identification of dominant features at high-symmetry points of the BZ are more practical for axis calibration.

The detection unit of the time-of-flight MM consists of an MCP followed by a delay-line detector. Each registered event directly corresponds to a single photoelectron. Saving this data stream at a single-event level permits event-wise correction and calibration and selective binning during the analysis [I, 104, 111, 112]. First, spherical timing aberrations, symmetry distortions within the momentum plane, and space-charge warping are corrected for each recorded event. Next, the momentum axis is calibrated from positions of known high-symmetry points, and the arrival time of photoelectrons is converted to photoelectron energy with the help of calibration data acquired for different bias voltages applied between the sample and ground. Finally, the corrected and calibrated events are binned to a multidimensional data hypervolume, usually a 4D dataset $I(k_x, k_y, E, \Delta t)$. For both detector systems, temporal pump-probe overlap is generally calibrated by fitting the transient pump-pulse induced population of states significantly above E_F by a Gaussian distribution convolved with an exponential decay.

4

Articles as published

In this chapter, the four scientific articles forming the main part of this thesis are reproduced.

4.1 Rev. Sci. Instrum. 91, 123112 (2020): A quantitative comparison of time-of-flight momentum microscopes and hemispherical analyzers for time- and angle-resolved photoemission spectroscopy experiments

J. Maklar, S. Dong, S. Beaulieu, T. Pincelli, M. Dendzik, Y.W. Windsor, R.P. Xian, M. Wolf, R. Ernstorfer, and L. Rettig

The publication Maklar et al., Rev. Sci. Instrum. 91, 123112 (2020) presents a systematic comparison of conventional HAs and novel time-of-flight MMs for trARPES experiments and highlights the advantages of combining both photoelectron detection schemes in a single setup. The associated raw data is publicly available at the Zenodo data repository, doi 10.5281/zenodo.4067968.

Author contributions

J.M., S.D., S.B., T.P., M.D. and L.R. carried out the trARPES experiments; **J.M.** analyzed the data; R.P.X. developed the data analysis framework with support from M.D. and L.R.; **J.M.** wrote the manuscript with support from L.R.; M.W., R.E. and L.R. provided the research infrastructure; all authors commented on the paper.

A quantitative comparison of time-of-flight momentum microscopes and hemispherical analyzers for time- and angle-resolved photoemission spectroscopy experiments

J. Maklar, S. Dong, S. Beaulieu, T. Pincelli, M. Dendzik, Y. W. Windsor, R. P. Xian, M. Wolf, R. Ernstorfer, and L. Rettig

View Online   Export Citation   CrossMark

ARTICLES YOU MAY BE INTERESTED IN

A quantitative comparison of time-of-flight momentum microscopes and hemispherical analyzers for time- and angle-resolved photoemission spectroscopy experiments

View Online   Export Citation   CrossMark

J. Maklar, [ID] S. Dong, [ID] S. Beaulieu, T. Pincelli, M. Dendzik,[a] Y. W. Windsor, [ID] R. P. Xian,[b] M. Wolf, R. Ernstorfer, [ID] and L. Rettig[c] [ID]

AFFILIATIONS

Fritz-Haber-Institut der Max-Planck-Gesellschaft, Faradayweg 4-6, D-14195 Berlin, Germany

[a]Current address: Department of Applied Physics, KTH Royal Institute of Technology, SE-16440 Stockholm, Kista, Sweden.
[b]Current address: Department of Neurobiology, Northwestern University, Evanston, Illinois 60208, USA.
[c]Author to whom correspondence should be addressed: rettig@fhi-berlin.mpg.de

ABSTRACT

Time-of-flight-based momentum microscopy has a growing presence in photoemission studies, as it enables parallel energy- and momentum-resolved acquisition of the full photoelectron distribution. Here, we report table-top extreme ultraviolet time- and angle-resolved photoemission spectroscopy (trARPES) featuring both a hemispherical analyzer and a momentum microscope within the same setup. We present a systematic comparison of the two detection schemes and quantify experimentally relevant parameters, including pump- and probe-induced space-charge effects, detection efficiency, photoelectron count rates, and depth of focus. We highlight the advantages and limitations of both instruments based on exemplary trARPES measurements of bulk WSe_2. Our analysis demonstrates the complementary nature of the two spectrometers for time-resolved ARPES experiments. Their combination in a single experimental apparatus allows us to address a broad range of scientific questions with trARPES.

I. INTRODUCTION

Angle-resolved photoemission spectroscopy (ARPES) is a key technique to investigate the electronic structure of solids. By extracting the kinetic energy and angular distribution of emitted photoelectrons, one gains direct access to the spectral function and, in particular, the quasiparticle band structure.[1] Combining this technique with a pump–probe approach allows for studying the electron dynamics after optical excitation on a femtosecond timescale. In recent years, time-resolved ARPES (trARPES) has been successfully applied to many fields in materials science, such as control of quantum matter,[2–6] photo-induced phase transitions,[7–13] and the investigation of electronic states and phases not accessible in equilibrium.[14–17] Advances in laser-based extreme ultraviolet (XUV) sources using

high harmonic generation in noble gases[18–20] now enable space-charge free photoemission up to MHz repetition rates at high time and energy resolution (10 s of fs/meV) and at photon energies up to far XUV.[21–30]

The most commonly used electron spectrometer in trARPES is the hemispherical analyzer (HA).[31] Here, the photoelectrons enter an electrostatic lens system followed by two hemispherical deflector electrodes acting as a dispersive bandpass energy filter, as sketched in Fig. 1(a). Subsequently, the electrons are projected onto a 2D multichannel plate (MCP) detector, which allows for the parallel detection of kinetic energy and emission angle. This detection scheme is rather inefficient, as only a single two-dimensional (2D) cut in a narrow energy and momentum window of the 3D photoelectron distribution can be simultaneously captured.
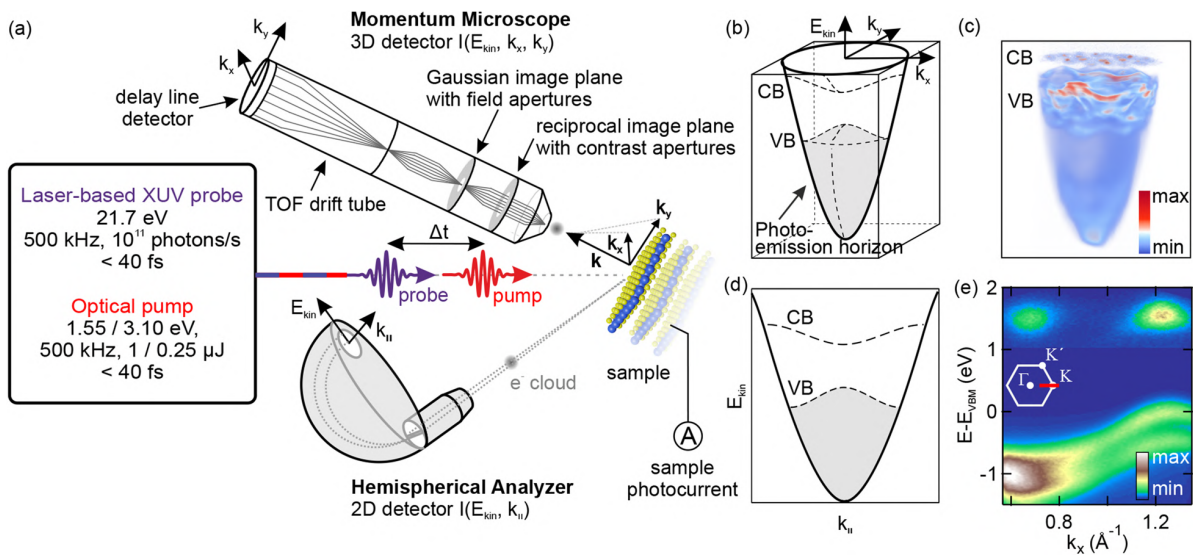
FIG. 1. (a) Schematic layout of the setup. Note that in the real experiment, the angle of incidence for measurements with the MM is fixed at 65°. (b) Illustration and (c) experimental data of a 3D dataset of WSe_2 acquired with the MM. (d) Sketch and (e) data of a 2D energy–momentum cut acquired with the HA. The momentum direction within the hexagonal BZ of WSe_2 is indicated in red. The excited-state signal above the valence band maximum of the exemplary datasets (pump–probe delay t = 0 fs, absorbed fluence F_{abs} = 150 $\mu J/cm^2$) is enhanced by a factor of (c) 100 and (e) 75. In all MM measurements, the extractor voltage is V_{extr} = 6 kV and the sample-extractor distance is 4 mm with the sample surface aligned perpendicular to the optical axis of the instrument.

The more recent detection scheme based on a time-of-flight (TOF) energy analyzer overcomes this limitation but requires a pulsed light source with an appropriate repetition rate.[32] The momentum microscope (MM) is based on a cathode-lens electron microscope.[33–36] By applying a high positive voltage to an electrostatic objective lens placed close to the sample surface, all emitted photoelectrons are steered into the lens system, resulting in an acceptance of the complete 2π solid angle. In analogy to optical microscopy, a reciprocal image is generated in the back focal plane of the objective lens, corresponding to the surface-projected band structure. Next, the photoelectrons pass through a field-free TOF drift tube. Finally, their 2D momentum distribution and kinetic energy (encoded in the arrival time) are detected at a single-electron level using an MCP stack combined with a position-sensitive delay-line detector (DLD). Ultimately, the TOF-MM enables parallel acquisition of the 3D photoelectron distribution $I(E_{kin}, k_x, k_y)$ across the full accessible in-plane momentum range (at low kinetic energies limited by the parabola of the photoemission horizon) and within a large energy range from the threshold energy to the hard x-ray regime,[36–38] as illustrated in Fig. 1(b).

In principle, trARPES is expected to benefit greatly from the improved parallelization in data acquisition of the TOF-MM for several reasons: (i) The excited-state signal is usually orders of magnitude lower than that of the occupied states in equilibrium,[4,12,16,39,40] which necessitates efficient detection. (ii) Prediction of the relevant energy–momentum regions of photoexcited states can be difficult, and a time-resolved mapping of the entire first Brillouin zone (BZ) with a HA is typically not feasible. (iii) Various photoinduced electronic processes can occur simultaneously and spread

over a large energy–momentum range, which are now accessible within a single measurement. However, while the MM theoretically constitutes the ultimate photoelectron detector, certain limitations, such as increased space-charge effects[38,41] and constraints of the DLD detection rate, compromise the experimental practicability, in particular, for pump–probe experiments. Therefore, a detailed benchmark of these two photoelectron detection schemes is of great interest.

In this article, we present a table-top XUV trARPES setup that combines a TOF-MM and a conventional HA and investigate their respective operational capabilities. We quantify critical parameters, such as depth of focus, experimental count rates, acquisition times, and space-charge effects. By two exemplary trARPES experiments—excited-state band structure mapping at a fixed time delay and tracking of the excited population dynamics—we demonstrate the advantages and limitations of both instruments and illustrate the benefits of combining both types of analyzers. After an overview of our experimental setup in Sec. II, we will introduce some important aspects specific to the MM in Sec. III. In Sec IV, we finally compare the two spectrometers based on our experimental data, followed by a discussion in Sec. V.

II. DESCRIPTION OF THE EXPERIMENTAL SETUP

The table-top XUV light source consists of an optical parametric chirped pulse amplifier (OPCPA) generating fs light pulses at 1.55 eV and 500 kHz at an average power of 20 W (40 μJ pulse energy).[42] A beam splitter at the exit of the OPCPA extracts a portion of the pulse energy as a 1.55 eV or frequency-doubled

3.1 eV synchronized optical pump. The probe pulses are frequency-doubled in a beta barium borate crystal and focused onto a high-pressure argon jet for an up-conversion to XUV via high harmonic generation. By a combination of a multilayer mirror and metallic (Sn) filters, only the seventh harmonic (21.7 eV) is transmitted to the analysis chamber.[27] Then, the pump and probe beams are focused onto the sample in a near-collinear geometry, and the emitted photoelectrons are detected with a HA (SPECS PHOIBOS 150 2D-CCD) or a TOF-MM (SPECS METIS 1000). The MM is mounted on a linear translation stage connected to the analysis chamber with a vacuum bellow and can be retracted to avoid collision with the cryogenic six-axis carving manipulator when using the HA.

For time-resolved studies with the HA, measurements are performed for a series of pump–probe delays. When using the MM, we continuously scan a defined pump–probe delay window, whereas the current delay is stored for each measurement event by an analog-to-digital conversion of the delay stage position. The detection unit of the MM features an MCP followed by a DLD. Each registered event directly corresponds to a single photoelectron. Saving this data stream at a single-event level permits event-wise correction and calibration and selective binning later during the analysis.[38,43,44] The operating principle of the DLD limits the count rate to a single electron per pulse,[45,46] resulting in maximum rates of $\sim5 \times 10^5$ cts/s, corresponding to the repetition rate of the laser system. For the case of the HA, the photoelectrons are first multiplied in an MCP and subsequently accelerated onto a phosphor screen, which is imaged by using a CCD camera. Thus, a single photoelectron generates several counts spread over adjacent pixels. To obtain an estimate of the actual photoelectron count rate, we calibrated the CCD response in the regime of distinct single-electron events. To quantify relevant experimental parameters of both spectrometers (see Sec. IV), we introduce the metrics *emitted electrons per pulse* e_{tot}, i.e., the total photoelectron yield per pulse obtained from the sample photocurrent, and *detected electrons per pulse* cts_{MM} and cts_{HA}, corresponding directly to the count rate of the MM and to the rescaled CCD count rate of the HA, respectively.

The material used for the benchmark study is bulk tungsten diselenide (2H–WSe$_2$). This layered semiconductor exhibits an indirect bandgap,[47] a sharp electronic band structure, and a distinct electronic response upon near-infrared optical excitation.[4] Exemplary datasets acquired with both detectors on WSe$_2$ at a temporal pump–probe overlap are shown in Figs. 1(c) and 1(e). The MM captures the entire photoemission horizon (momentum disk with radius $k_{\parallel,max} \approx 2.15$ Å^{-1}), exceeding the first BZ of WSe$_2$, and the full energy range from the pump-pulse-induced population in the conduction band (CB) to the secondary electron cutoff. In contrast, the HA covers an energy window of a few electron volts (at a reasonable energy resolution) and a narrow momentum range, resulting from the limited acceptance angle of $\pm15°$ (wide angle mode). The momentum resolution orthogonal to the dispersing direction is determined by the width of the slit located at the entrance of the spherical deflector. All HA data were recorded with a slit width of 0.5 mm, corresponding to a momentum integration of ≈0.04 Å^{-1}, and a pass energy of 30 eV.

Using the MM, the angle between the pump and probe beams and the sample surface normal is fixed at 65°. For comparability between the detectors, we align the sample in a similar geometry

in the HA measurements, which yields the Σ–K momentum cut shown in Fig. 1(e). All samples are cleaved at room temperature in ultra-high vacuum ($<1 \times 10^{-10}$ mbar).

Whereas the energy resolution of our trARPES setup is limited by the bandwidth of the XUV probe pulses to ~150 meV, the HA offers an improved momentum resolution over the MM. Based on band structure data, we estimate an effective momentum resolution of the MM and the HA of 0.08 Å^{-1} and 0.04 Å^{-1} (~1°), respectively. The ultimate instrument resolution is reported as $<4 \times 10^{-3}$ Å^{-1} ($<0.1°$) for the HA and $<5 \times 10^{-3}$ Å^{-1} for the MM.[35,36,48] However, achieving such optimal conditions with the MM requires very high extractor voltages and tedious optimization of the lens settings and corrector elements.

III. DEPTH OF FOCUS IN MOMENTUM MICROSCOPY

Before starting our systematic comparison of the two spectrometers, we further introduce features of the MM arising from the similarity to optical microscopy. First, both a reciprocal and a Gaussian real-space image plane form consecutively in the electron-optical lens column, which can be selectively projected onto the DLD. Thus, by the choice of lens settings, the instrument can be used either for band structure mapping or to investigate the real-space distribution of photoelectrons via photoemission electron microscopy (PEEM).[49] Second, apertures can be inserted in both image planes, which enables trARPES at high spatial selectivity and time- and momentum-resolved PEEM.

We first focus on the use of field apertures inserted into the Gaussian image plane, which can be used to study the electronic band structure of spatially inhomogeneous or small samples below the size of the probe spot down to the micrometer range; see Fig. 2(a). The electron transmission T_{FA} for various field apertures and for various probe spot sizes is shown in Fig. 2(b).
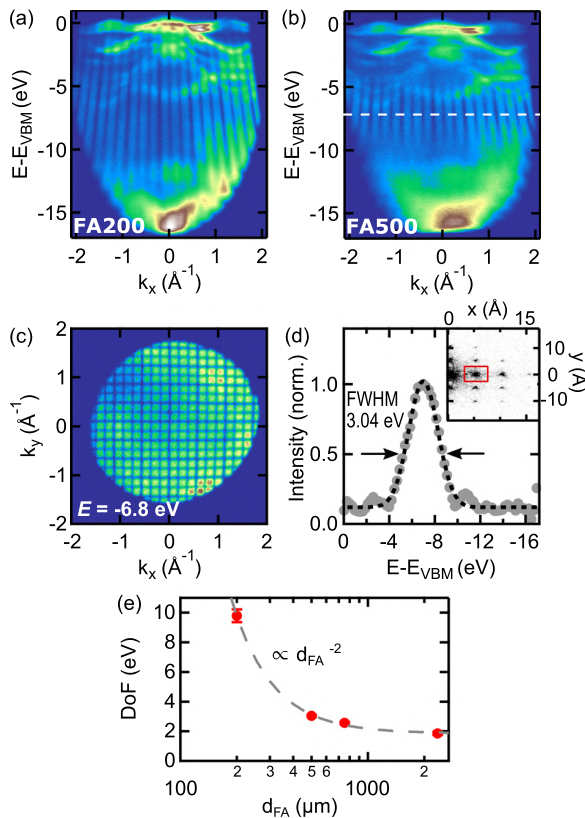
The effective source size, defined by the field aperture or the spot size, also determines the depth of focus (DoF), i.e., the energy window with sharp momentum resolution, resulting from the chromatic aberrations of the electron lenses. To investigate the DoF, we insert a grid in the momentum image plane and analyze the sharpness of the resulting grid lines as a function of kinetic energy
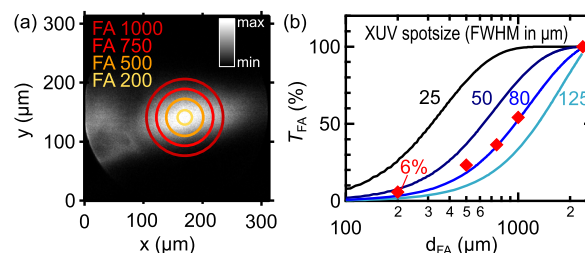
FIG. 2. (a) PEEM image of the elongated XUV beam footprint (a focal diameter of ≈80 μm) at an incidence angle of 65° on a WSe$_2$ sample at a magnification of 7.6. Projected field aperture sizes are illustrated in color (diameters in μm). (b) Calculated transmission as a function of field aperture diameter for selected probe spot sizes, taking into account the angle of incidence. Experimentally determined values, corresponding to the apertures indicated in panel (a), are marked by red diamonds.

for various field apertures, shown in Fig. 3. For the aperture diameter $d_{FA} = 200 \, \mu m$, we observe sharp grid lines superimposed on the band structure of WSe_2 reaching from the valence band (VB) down to almost the entire secondary electron tail. However, with an increase in the aperture size, the energy window of sharp momentum imaging narrows. To quantify this trend, we perform a 2D Fourier transform of the iso-energy contours and analyze the magnitude of the spatial frequency peaks corresponding to the grid periodicity as a function of energy, shown in Figs. 3(c) and 3(d). Similar to the depth of field in optical imaging,[50] we find that the DoF follows an inverse square dependence of the aperture diameter; see Fig. 3(e).

To achieve a uniform performance in a typical range of interest of few eV, it is necessary to have a DoF of ~10 eV. For this, the effective source size has to be reduced to ~25 μm, which corresponds to a field aperture diameter of 200 μm for the chosen magnification settings. At the given spot size of $80 \times 80 \, \mu m^2$, this reduces the photoelectron transmission to $T_{FA} = 6\%$ of the total yield, as shown in

Fig. 2(b). However, to compensate for transmission losses, the XUV flux and, thereby, the total number of emitted electrons cannot be arbitrarily increased. Here, space-charge effects have to be considered, as discussed in Sec. IV. Thus, for high spatial selectivity and a large DoF without significant transmission losses, the size of the XUV spot is an important parameter to consider.
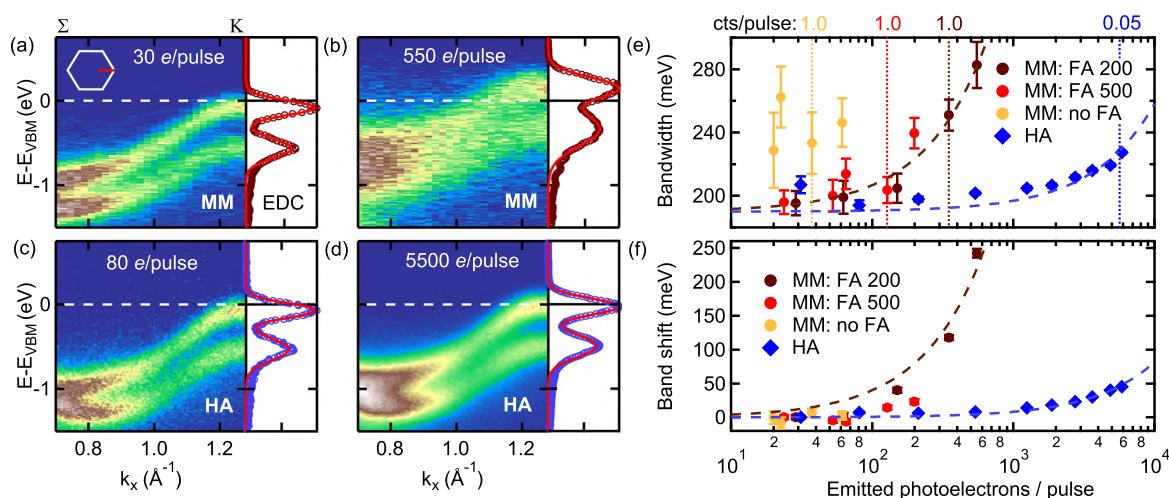
IV. QUANTITATIVE COMPARISON OF THE MM AND THE HA

A. XUV-induced space charge

A fundamental limitation of photoemission with ultrashort light pulses is space charge. The Coulomb repulsion within a dense photoelectron cloud can modify the electrons' angular and energy distribution and can significantly deteriorate momentum and energy resolution. Space charge and its dependence on source parameters, such as pulse duration, flux, and spot size, have already been studied extensively.[51–56] Here, we compare the space-charge effects for both detection schemes using the energy shift and broadening of the energy dispersion curve (EDC) of the spin–orbit split VBs at the K point of WSe_2; see Fig. 4. In the regime of few emitted photoelectrons per pulse, the band structure measurements of both detectors are in excellent agreement; see panels (a) and (c). When increasing the XUV source flux (and thereby the density within the photoelectron cloud), the MM spectrum rapidly shifts toward higher energies and becomes drastically broadened, while the HA spectrum is only weakly affected; see panels (b) and (d).

For the MM, detectable energy distortions (shift and additional broadening ≳10 meV) arise above ~100 emitted electrons per pulse, roughly one order of magnitude before distortions appear in HA measurements; see Figs. 4(e) and 4(f) and the discussion below. While the transmission and, thereby, the effective count rate decrease for a smaller field aperture size, we find that space charge is rather independent of the apertures. This demonstrates that its major contribution stems from the Coulomb interaction of photoelectrons on their trajectories prior to the Gaussian image plane, in agreement with simulation results for the case of hard x-ray ARPES.[41] In other words, to employ the MM at a reasonable resolution, the source flux and the resulting number of emitted photoelectrons per pulse have to be chosen carefully. For instance, when using the aperture $d_{FA} = 200 \, \mu m$ (allowing for a large DoF), ~350 emitted photoelectrons per pulse are required to reach the instrumental limit of a single event per pulse due to transmission losses and an imperfect detection efficiency. However, in this regime, the spectrum is already significantly shifted and broadened.

These observations demonstrate that space-charge effects can be a major limitation of the MM compared to HAs when using fs pulses, as illustrated in Fig. 5. In the field-free region in front of the HA, the emitted photoelectron disk spreads over the complete 2π solid angle, while it simultaneously broadens along the direction of propagation due to the high relative energy difference between the primary (fast) and inelastically scattered, secondary (slow) electrons. In contrast, the high extractor field of the MM guides the entire electron cloud into the lens column, leading to increased electron densities, and accelerates it to few keV. Therefore, before discrimination in the TOF-tube, the primary and secondary electrons propagate at

FIG. 3. 2D cut of a MM measurement along the K–Γ–K direction with a square grid in the momentum image plane for field apertures of diameters (a) 200 μm and (b) 500 μm. (c) Iso-energy contour at the focus energy (sharpest momentum image), see the white dashed line in panel (b), for $d_{FA} = 500 \, \mu m$. (d) Intensity of the Fourier transform peak corresponding to the grid spacing, see the red box in the inset, as a function of energy. The FWHM of the peak is extracted from a Gaussian fit (black dashed curve). The inset shows the Fourier transform of the iso-energy contour in c. (e) Depth of focus (FWHM) vs aperture diameter with an inverse quadratic fit.

FIG. 4. (a) and (b) False-color plots of MM cuts (d_{FA} = 200 μm) and (c) and (d) HA measurements along the Σ–K direction at selected photoelectron emission rates. The EDCs at the K point (0.09 Å^{-1} integration window) are shown with a fit by two Gaussians (red curve). (e) FWHM and (f) energy shift extracted from the fit to the upper band at the K point as a function of emitted photoelectrons per pulse (obtained from the sample photocurrent). The MM bandwidth values without an aperture deviate from the other curves, as the spectra are already significantly blurred due to the low DoF. Linear fits (dashed lines) serve as guides to the eye. Selected photoelectron detection rates are indicated by vertical lines. The effective electron detection rate of the HA is orders of magnitude below the MM since a drastically smaller energy–momentum window is covered in a single measurement.

comparable velocities and spread only marginally along the direction of propagation. As a result, the effective interaction travel length and interaction time between fast electrons of the primary spectrum and secondary electrons are significantly higher in the MM.
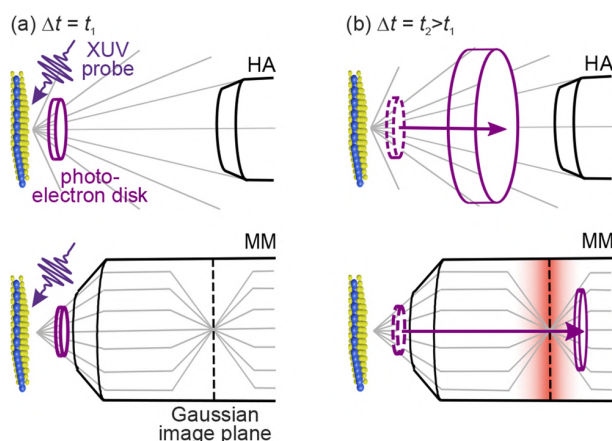
FIG. 5. (a) Schematic of the emitted photoelectron disk shortly after the arrival of the XUV pulse for the HA (top) and MM (bottom). (b) Photoelectron disk at a later time. In the HA, the electron disk spreads over the complete 2π solid angle and broadens along the direction of propagation. In the MM, all photoelectrons are guided into the lens column. Due to the high acceleration voltage, the relative energy difference between the primary and secondary electrons is small, and the photoelectrons remain confined to a thin, dense disk. Focal planes (indicated in red) further increase the electron–electron interaction.

Refocusing of the photoelectron disk at several focal planes of the lens column further increases these space-charge effects. Since the secondary electrons travel close to the optical axis, the primary electron spectrum features a Lorentzian profile of iso-energy surfaces, with space-charge distortions most pronounced at the Γ point. Note that these deterministic energy shifts can be compensated by numerical correction,[41] in contrast to the space-charge-induced energy broadening.

For illustration, we estimate the involved time and length scales of the spread of the photoelectron cloud along its trajectory for both instruments. In the HA, it takes $\approx$90 ps to separate electrons of highest kinetic energy (corresponding to the VB maximum, $E_{kin} \approx 17$ eV) from the secondary electron tail (exemplary energy $E_{kin} \approx 5$ eV) by 100 μm, during which the fast electrons have traveled 220 μm. In the MM (at an approximate average potential within the initial lens elements of 2 kV after acceleration), it takes $\approx$1.3 ns to achieve the same distance spread between the fast and slow electrons, during which the primary electrons have traveled several centimeters, reaching already into the lens column. Note that when using the MM in the regime of the soft/hard x-ray PES, the relative velocity difference of primary and secondary electrons is increased, which reduces the space-charge interaction between the two electronic species. Detailed simulations of the space-charge effects in momentum microscopy can be found elsewhere.[41]

In summary, in our experimental configuration (an XUV spot diameter of 80 μm), we apply a small FA to reach a sufficient DoF in typical band mapping experiments. While the resulting transmission losses can be partially compensated by increasing the number of total emitted photoelectrons per pulse, space-charge effects ultimately constrain the operating conditions to a regime significantly

below the detector saturation. A reduction in the spot diameter below 25 μm would allow to omit field apertures in most experiments. Due to the increased transmission, only few emitted photoelectrons per pulse are required to reach the limit of detector saturation, and space-charge effects would be negligible with respect to the typical energy resolution in time-resolved experiments. However, most current trARPES setups work at spot diameters in the range of 80 μm to few hundred μm,[23,25–27,29] as reducing the focus size below few 10 μm in the XUV regime is difficult to achieve with conventional beamline layouts.

B. Count rates

Next, we discuss the total count rate of both instruments achievable under these space-charge restrictions. For the MM, the detected counts per pulse cts_{MM} are given by the product of the total emitted counts per pulse, the transmission of the FA, and the quantum efficiency of the DLD/MCP stack,

$$cts_{MM} = e_{tot} \cdot T_{FA} \cdot QE_{MM}. \tag{1}$$

We estimate $QE_{MM} \approx 5\%$ from measurements without an FA ($T_{FA} \approx 1$). Combined with the transmission losses at the FA in typical experiments ($T_{200\,\mu m} \approx 6\%$), roughly 0.3% of the total emitted photoelectrons are detected.

For the HA, the detected counts per pulse are given by

$$cts_{HA} = e_{tot} \cdot f \cdot QE_{HA}, \tag{2}$$

with the fraction of the electron distribution sampled in a single HA measurement f and the quantum efficiency of the MCP $QE_{HA} \approx 10\%$. For our settings of a slit width of 0.5 mm and a pass energy of 30 eV centered on the upper valence band region, we estimate $f \approx 0.03\%$. Therefore, 0.003% of the total emitted photoelectrons are detected, which is roughly two orders of magnitude below the MM. Note that the relatively low quantum efficiency of the detectors in both instruments could be related to detector aging and the comparably low impact energy of the photoelectrons.[57]

In our measurement configuration, the space-charge limit of $e_{tot} \approx 100$ emitted photoelectrons per pulse restricts the MM count rate to $cts_{MM} \approx 0.3$ cts/pulse. However, a substantial portion of these electrons originates from the secondary electron tail and deep-lying VBs. Focusing only on the topmost VB region from the VB maximum to 1.5 eV below, which is typically of most interest in time-resolved studies, yields 0.006 cts/pulse or 3000 cts/s at a repetition rate of 500 kHz. In contrast, when using the HA, the XUV flux can be increased by approximately an order of magnitude to $e_{tot} \approx 1000$ photoelectrons per pulse before critical space-charge effects emerge. For a typical cut, such as shown in Fig. 1(e), we detect ~15 000 cts/s. In comparison, when extracting a comparable cut from the MM dataset, the count rate is roughly 40 cts/s, which is a factor of $\approx$350 below the rate of the HA, resulting from the reduced XUV source flux (~10×), transmission losses at the aperture (~17×), and a lower detection efficiency (~2×). Nevertheless, when the total photoelectron distribution is of interest, the MM outperforms the HA by a factor of $cts_{MM}/cts_{HA} \approx 10$.

In an optimal scenario (small XUV spot, $T_{FA} \approx 1$, $QE_{MM} \approx 1$), only few emitted photoelectrons per pulse are required, and the count rate of the MM cts_{MM} is only limited by the detector

saturation of ~1 cts/pulse. However, compared to the experimental scenario discussed above (0.3 cts/pulse), this increases the total count rate only by a factor of $\approx$3. Thus, also under optimized conditions, our conclusions still hold true. Another approach to improve the MM count rate is by increasing the repetition rate of the laser system. However, in pump–probe experiments, re-equilibration of the sample within the laser's duty cycle has to be considered, which, at multi-MHz repetition rates, critically limits the applicable excitation fluences. While, in the regime of very weak excitation, repetition rates of several 10 MHz allow to mitigate space-charge effects and to substantially reduce acquisition times,[23,24] the TOF of slow electrons further limits the maximum applicable repetition rate (typically <10 MHz).[32]
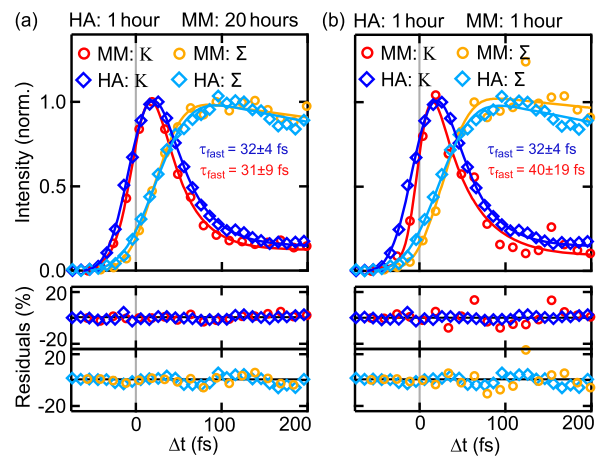
C. Experimental scenarios

Next, we discuss common trARPES scenarios to highlight the advantages of each instrument and the benefit of combining both detectors in a single setup. As a first use case, we show the (excited-state) band mapping of bulk WSe$_2$ upon excitation with near-infrared optical pulses ($\lambda_{pump} = 800$ nm). Using the MM, we acquire the quasiparticle dispersion across the full photoemission horizon in a single measurement at a fixed sample geometry. We gain access to the band structure of the first projected BZ up to 1.55 eV above the VB; see the transient occupation of the CB at the K and Σ points in Figs. 6(b) and 6(c). For static 3D band mapping using the MM, typically 10^7–10^8 total events are required, as a large portion of the intensity originates from secondary electrons, achievable in ~1 min to 10 min at a typical count rate of $\approx 1.5 \cdot 10^5$ cts/s [Fig. 6(a)]. In order to accurately resolve the much weaker signal of excited states, typically, ~10^9 events are detected within ~2 h, producing data as shown in Figs. 6(b) and 6(c). For comparison, the energy–momentum window covered in a single HA measurement along the Σ–K direction is shown in panel (d) of Fig. 6, recorded within ~10 min. Mapping the full irreducible part of the BZ with the HA (by sample rotation or by using a deflector arrangement) requires at a comparable momentum resolution ~60 sequential scans. This procedure is further complicated by the fact that high emission angles are difficult to access and spectra have to be merged and mapped from angle to momentum space. In addition, light polarization, fluence, and photoemission matrix elements might change during such a mapping procedure using a sample manipulator. Thus, to get an overview of the full (excited-state) dispersion relation, band mapping with the MM is highly advantageous.

Another typical use case of trARPES is the investigation of the transient carrier relaxation dynamics along certain pathways in momentum space. In bulk WSe$_2$, electrons are initially excited into the conduction band (CB) at the K valley, followed by a relaxation into the global CB minimum at the Σ point. Note that while we study a bulk sample, the dominant fraction of the photoemission intensity originates from the topmost WSe$_2$ layer due to the limited photoelectron escape depth in the XUV regime. A detailed discussion of the relaxation dynamics in bulk and monolayer WSe$_2$ can be found elsewhere.[4,59,60] As such relaxation dynamics are often highly localized in momentum space, information on selective regions in momentum space is sufficient to study the temporal evolution. Measuring such dynamics with the MM results in a 4D dataset (3D + time) of the full energy-, momentum-, and time-dependent band
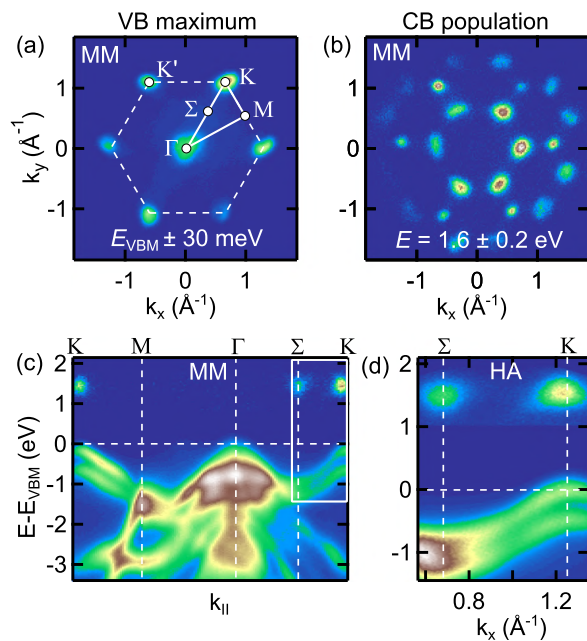
FIG. 6. MM iso-energy contours of (a) the VB maximum and (b) the transiently excited CB population. Asymmetries between equivalent points result from orbital interference effects in photoemission.[58] Minor symmetry distortions were corrected using symmetry-guided registration.[44] (c) Extracted energy–momentum cuts along the high-symmetry directions. (d) Data acquired with the hemispherical analyzer, corresponding to the energy–momentum window indicated by the white box in panel (c). The intensity of the CBs is enhanced by a factor of 75 in both datasets to achieve a comparable intensity of the CB signal and the topmost VBs at K ($t = 0 \pm 50$ fs, $h\nu = 1.55$ eV, $F_{abs} = 150$ μJ/cm^2). For comparability, the momentum integration orthogonal to the plotted direction of the MM cuts in (c) is matched to the HA measurements.


FIG. 7. Time traces of the integrated excited-state signal at the K and Σ valleys for acquisition times of (a) 1 h (HA) and 20 h (MM), and (b) an equal acquisition time of 1 h for both instruments. The excited-state signal of the MM data is extracted from an energy–momentum plane corresponding to the HA measurement. The time traces are fitted with a single-exponential (Σ) and double-exponential (K) decay curve convolved with a Gaussian, respectively. The fit results are shown as solid curves, along with the time constants (standard deviation as uncertainty) of the fast decay component of the transient population at K. While the residuals in panel (a) show similar levels of noise for both instruments, the MM time traces in (b) feature substantial scatter.

structure, which requires ~10^{10} events and an acquisition time of 20 h or more, depending on the sample characteristics, the required statistics, and the pump–probe delay range. In contrast, using the HA, only the relevant energy–momentum region is recorded, and we can utilize the higher photon flux and larger transmission within this window, yielding an acquisition time in the range of 1 h–2 h for a time trace. To illustrate these differences, Fig. 7(a) shows the time traces of the conduction band population at the K and Σ points for both spectrometers, measured for 1 h (HA) and 20 h (MM), respectively. Both datasets show similar statistics and scatter, as visible from the residuals of the exponential fits. In contrast, comparing the data for similar acquisition times [Fig. 7(b)] shows much larger scatter in the MM traces due to the lower number of acquired events. This is also represented in the accuracy of the fit parameters. Even if we sum the symmetry-equivalent locations in the Brillouin zone that the MM data cover, the HA still permits much faster data acquisition of a limited energy–momentum region. This allows for a time-dependent systematic variation of external parameters (e.g., temperature and pump fluence)—challenging with the MM. However, if the electron dynamics over an extended momentum–space region are of interest[61] or

comparing different momentum points not simultaneously accessible within the angular range of the HA is required,[4] the MM is clearly advantageous.

D. Optical pump-induced space charge

A further critical aspect in trARPES is the space-charge effects induced by electrons emitted by the pump pulses. Multi-photon photoemission and emission at surface inhomogeneities can generate a significant number of low-energy electrons. Depending on the pump–probe time delay, this can lead to complex interactions with the probe–pulse-induced electron cloud.[38,62,63] While this phenomenon plays a secondary role when exciting WSe$_2$ at $h\nu = 1.55$ eV, it becomes increasingly important as the photon energy of the pump pulses approaches the material's work function since the order of the nonlinearity needed for multiphoton ionization decreases. In the following, we systematically study the pump-induced space-charge effects at $h\nu = 3.1$ eV, utilizing the metrics introduced in Sec. IV A, i.e., the energy shift and broadening of the VB at the K point.

Already at moderate excitation densities ($F_{abs} = 20$ μJ/cm^2), the MM spectra exhibit a severe non-uniform broadening and shift most pronounced at the Γ point; see Fig. 8. In this fluence regime, the low-energy electrons released by the pump pulses greatly outnumber probe-pulse-induced photoelectrons, shown in panel (e). The pump-pulse-induced space-charge effects strongly depend on delay[38] and extend over several ps around the temporal pump–probe overlap; see panel (d). Here, one has to carefully distinguish the true temporal overlap from the space-charge maximum at positive delays. Space-charge interaction is particularly critical at positive
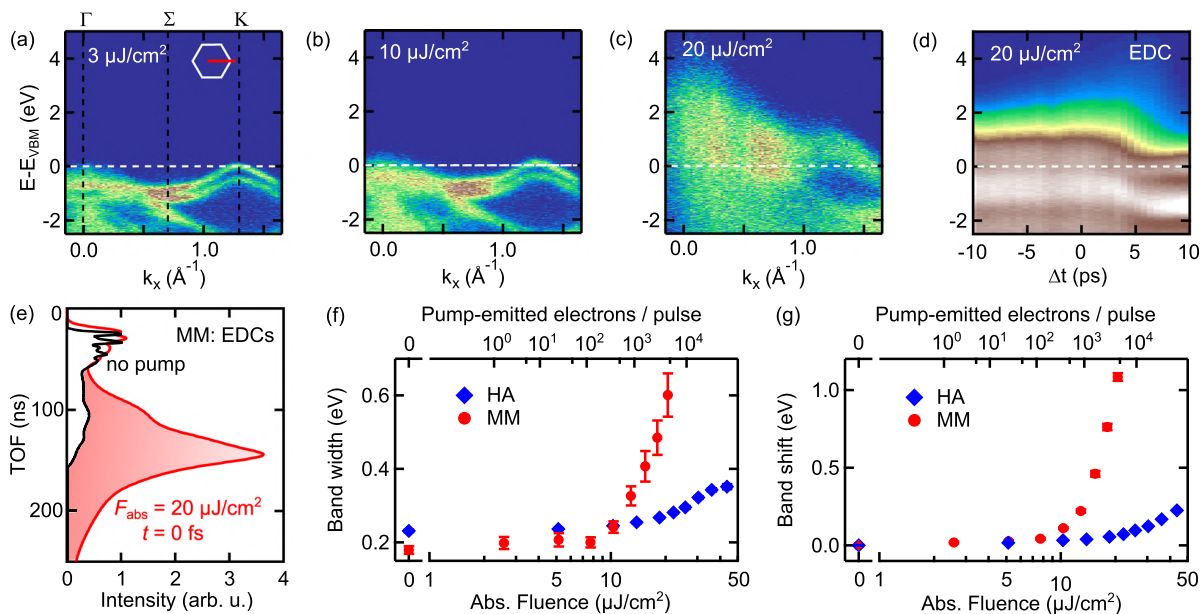
FIG. 8. (a)–(c) False-color plots of 2D MM cuts along the momentum direction indicated by the red line in panel (a) for various pump fluences ($h\nu$ = 3.1 eV, t = 0 fs). (d) Total momentum-integrated EDC as a function of time delay. (e) Total intensity vs TOF at equilibrium (black) and with an optical pump at t = 0 fs (red). (f) and (g) Fit results (analogous to Fig. 4) of width and shift of the VB at the K point as a function of absorbed fluence ($t \approx 0$ fs, d_{FA} = 200 μm) and of pump-laser-emitted electrons per pulse. The sharp onset of the space-charge effects in the MM measurements demonstrates the high nonlinearity of the pump–pulse-induced photoemission.

delays (pump pulse precedes the XUV probe) since the fast probe photoelectron cloud traverses through the cloud of slow, pump-pulse-emitted electrons on its path to the detector. In the MM, the relative difference between the velocities of the two electron species is minute due to the high acceleration field of the extractor, similar to the interaction between the primary and secondary electrons within the probe-pulse electron cloud discussed in Sec. IV A. As a result, the critical interaction region extends far into the lens column. Moreover, also the low-energy electrons emitted by the pump pulses travel along the optical axis, which enhances the energy shift and broadening at the Γ point. In contrast, in the field-free region between the sample and the HA, the relative speeds of both electron clouds differ strongly, so the interaction region is limited to a small region close to the sample. Thus, pump-pulse-induced space-charge effects completely blur the band dispersion already at several 100 pump-emitted electrons per pulse when using the MM, while distinct bands can be discerned with the HA above 10 000 electrons per pulse, as shown in Figs. 8(f) and 8(g), in agreement with XUV-induced space-charge discussed in Sec. IV A.

Ultimately, this significantly limits the experimental flexibility of the MM with regard to excitation wavelengths approaching the sample work function and strongly restricts the applicable excitation fluences. For our test case of $h\nu$ = 3.1 eV, two-photon processes dominate the pump-induced photoemission from WSe$_2$. Here, pump-induced space charge strongly shifts and distorts the spectra near the Γ point and, at the same time, heavily blurs the dispersion at K, which makes it difficult to discern the excited-state signal at 10^{-3} of the level of the VB. In contrast, at comparable excitation densities,
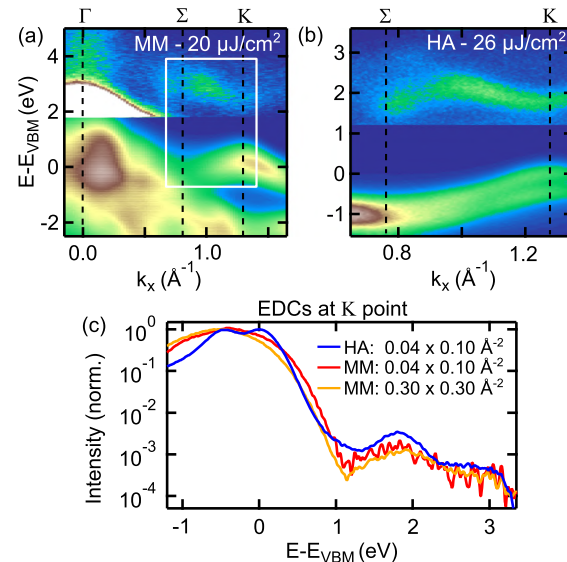
FIG. 9. Excited-state band mapping along the $\Gamma - \Sigma - K$ direction (t = 0 fs, $h\nu$ = 3.1 eV) using (a) the MM (20 h acquisition) and (b) the HA (4 h). The CB intensity is enhanced by a factor of 250 to improve visibility. The white box in panel (a) indicates the area covered by the HA measurement. (c) EDCs extracted at the K point. Despite similar excitation densities, the excited-state signal at 1.8 eV of the MM traces shows significant scatter, for both a small (red) and an extended momentum integration (orange curve) around the K point.

the HA delivers a sharp band dispersion, a well-resolved spin–orbit splitting of the VB, and a clear excited-state signal within reasonable integration times, illustrated in Fig. 9. In addition, the HA permits significantly increased excitation fluences, creating a larger excited-state population without considerable distortions, and it allows even higher excitation photon energies, providing a larger window into the conduction band dispersion.

V. DISCUSSION

Our case studies show that for trARPES studies, despite the parallel detection of the full energy and momentum range, the TOF-MM in its current state does not replace but rather complements the HA. Moreover, the combination of the two complementary detection schemes in a single setup allows us to address a broad variety of scientific questions. To illustrate the complementary role of both instruments, let us consider the scenario of studying a novel material. For an initial characterization, the MM is best suited, as it permits an efficient mapping of the full band structure and gives an overview of all relevant carrier relaxation pathways within the entire projected BZ. After identifying central energy–momentum regions with the MM, the HA can be used to quickly analyze the dynamics within specific energy–momentum regions at high momentum resolution and to systematically explore the experimental parameter space (e.g., fluence and temperature dependence) in a time-resolved fashion. Moreover, the HA can provide access to experimental parameter ranges, e.g., excitation wavelengths, fluences, and polarizations, that are not feasible using the MM due to space-charge restrictions or the experimental geometry (grazing-incidence illumination).

A complementary advantage of the MM is the possibility to measure samples that are susceptible to XUV beam damage, as only a very limited XUV exposure is required due to the efficient simultaneous detection of the full photoemission horizon. In addition, we also note here a few additional experimental difficulties connected with the MM. First, flat sample surfaces are needed to prevent field emission, resulting from the high extractor voltage. Second, a flat and isotropic sample holder is required to prevent distortions of the extractor fields. Third, acquisition with the MM requires processing and storage of large datasets (~100 GB for a typical dataset of 10^{10} events) and involves complex data binning and analysis procedures.[43,44]

We demonstrated that space-charge effects and the detector saturation critically limit the experimental count rates of the MM, in particular, for time-resolved studies. Future developments of high-pass filtering of secondary and pump-emitted photoelectrons close to the sample are expected to mitigate these limitations. Combining such filtering techniques and DLDs with improved multi-hit capabilities would be necessary to exploit all benefits of the MM also under experimental conditions comparable to the HA.

Determination of the complete (time-resolved) electronic band structure dynamics with the MM bears an enormous potential. Most directly, it allows us to track complex momentum- and energy-dependent scattering phenomena, shines light on quasiparticle lifetimes,[64] and permits for a benchmark comparison to band structure theory.[65] As the MM measurements are performed at a fixed sample geometry, it allows us to investigate higher-order modulation effects of the photoemission intensity, such as orbital interference.[58] In addition to comprehensive band structure mapping, the MM further bears conceptually new measurement configurations. The use of apertures in the real-space image plane permits for the spatial selectivity of band structure measurements down to the micrometer scale. Furthermore, the use of apertures in the reciprocal image plane allows us to extract the real-space photoelectron distribution at high momentum-selectivity via PEEM. This novel technique allows us to study spatial inhomogeneities that involve subtle momentum variations, such as the formation of domain boundaries of symmetry-broken states, the impact of defects on ordering phenomena, and the spatial distribution of intertwined complex phases after photoexcitation.[66,67]

VI. CONCLUSION

We have demonstrated a dual-detector XUV time-resolved ARPES setup and benchmarked the characteristics of a time-of-flight electron momentum microscope and a hemispherical analyzer, using metrics such as depth of focus, pump- and probe-pulse-induced space-charge effects, and experimental acquisition times. The unique combination of analyzers enables for a full view of the band structure dynamics across the entire photoemission horizon using the momentum microscope and a rapid data acquisition across a limited energy–momentum region at high momentum resolution using the hemispherical analyzer. Furthermore, the possibility to achieve high spatial selectivity and the option of mapping the (time-dependent) real-space photoelectron distribution of confined spectral features via momentum-resolved photoemission electron microscopy allow for entirely new perspectives.

SUPPLEMENTARY MATERIAL

See the supplementary material for a video of the temporal evolution of the excited-state signal in WSe_2 acquired with the MM (iso-energy contour at 1.6 ± 0.2 eV) and the HA (cut along the Σ–K direction, CB signal enhanced).

DATA AVAILABILITY

The data that support the findings of this study are publicly available in Zenodo, at https://doi.org/10.5281/zenodo.4067968.[68]

REFERENCES

[1] A. Damascelli, "Probing the electronic structure of complex systems by ARPES," Phys. Scr. **2004**, 61.

[2] S. Ulstrup, A. G. Čabo, J. A. Miwa, J. M. Riley, S. S. Grønborg, J. C. Johannsen, C. Cacho, O. Alexander, R. T. Chapman, E. Springate et al., "Ultrafast band structure control of a two-dimensional heterostructure," ACS Nano **10**, 6315–6322 (2016).

[3] F. Mahmood, C.-K. Chan, Z. Alpichshev, D. Gardner, Y. Lee, P. A. Lee, and N. Gedik, "Selective scattering between Floquet-Bloch and Volkov states in a topological insulator," Nat. Phys. **12**, 306 (2016).

[4] R. Bertoni, C. W. Nicholson, L. Waldecker, H. Hübener, C. Monney, U. De Giovannini, M. Puppin, M. Hoesch, E. Springate, R. T. Chapman et al., "Generation and evolution of spin-, valley-, and layer-polarized excited carriers in inversion-symmetric WSe$_2$," Phys. Rev. Lett. **117**, 277201 (2016).

[5] J. Reimann, S. Schlauderer, C. P. Schmid, F. Langer, S. Baierl, K. A. Kokh, O. E. Tereshchenko, A. Kimura, C. Lange, J. Güdde, U. Höfer, and R. Huber, "Subcycle observation of lightwave-driven Dirac currents in a topological surface band," Nature **562**, 396–400 (2018).

[6] S. Beaulieu, S. Dong, N. Tancogne-Dejean, M. Dendzik, T. Pincelli, J. Maklar, R. P. Xian, M. A. Sentef, M. Wolf, A. Rubio et al., "Ultrafast light-induced Lifshitz transition," arXiv:2003.04059 (2020).

[7] F. Schmitt, P. S. Kirchmann, U. Bovensiepen, R. G. Moore, L. Rettig, M. Krenz, J.-H. Chu, N. Ru, L. Perfetti, D. H. Lu et al., "Transient electronic structure and melting of a charge density wave in TbTe$_3$," Science **321**, 1649–490 (2008).

[8] T. Rohwer, S. Hellmann, M. Wiesenmayer, C. Sohrt, A. Stange, B. Slomski, A. Carr, Y. Liu, L. M. Avila, M. Kalläne et al., "Collapse of long-range charge order tracked by time-resolved photoemission at high momenta," Nature **471**, 490–493 (2011).

[9] R. Cortés, L. Rettig, Y. Yoshida, H. Eisaki, M. Wolf, and U. Bovensiepen, "Momentum-resolved ultrafast electron dynamics in superconducting Bi$_2$Sr$_2$CaCu$_2$O$_8$+δ," Phys. Rev. Lett. **107**, 097002 (2011).

[10] C. L. Smallwood, J. P. Hinton, C. Jozwiak, W. Zhang, J. D. Koralek, H. Eisaki, D.-H. Lee, J. Orenstein, and A. Lanzara, "Tracking Cooper pairs in a cuprate superconductor by ultrafast angle-resolved photoemission," Science **336**, 1137–1139 (2012).

[11] S. Mathias, S. Eich, J. Urbancic, S. Michael, A. Carr, S. Emmerich, A. Stange, T. Popmintchev, T. Rohwer, M. Wiesenmayer et al., "Self-amplified photoinduced gap quenching in a correlated electron material," Nat. Commun. **7**, 12902 (2016).

[12] C. W. Nicholson, A. Lücke, W. G. Schmidt, M. Puppin, L. Rettig, R. Ernstorfer, and M. Wolf, "Beyond the molecular movie: Dynamics of bands and bonds during a photoinduced phase transition," Science **362**, 821– 825 (2018).

[13] P. Tengdin, W. You, C. Chen, X. Shi, D. Zusin, Y. Zhang, C. Gentry, A. Blonsky, M. Keller, P. M. Oppeneer et al., "Critical behavior within 20 fs drives the out-of-equilibrium laser-induced magnetic phase transition in nickel," Sci. Adv. **4**, eaap9744 (2018).

[14] J. A. Sobota, S. Yang, J. G. Analytis, Y. Chen, I. R. Fisher, P. S. Kirchmann, and Z.-X. Shen, "Ultrafast optical excitation of a persistent surface-state population in the topological insulator Bi$_2$Se$_3$," Phys. Rev. Lett. **108**, 117403 (2012).

[15] I. Gierz, J. C. Petersen, M. Mitrano, C. Cacho, I. C. E. Turcu, E. Springate, A. Stöhr, A. Köhler, U. Starke, and A. Cavalleri, "Snapshots of non-equilibrium Dirac carrier distributions in graphene," Nat. Mater. **12**, 1119–1124 (2013).

[16] M. Ligges, I. Avigo, D. Golež, H. Strand, Y. Beyazit, K. Hanff, F. Diekmann, L. Stojchevska, M. Kalläne, P. Zhou et al., "Ultrafast doublon dynamics in photoexcited 1T-TaS$_2$," Phys. Rev. Lett. **120**, 166401 (2018).

[17] X. Shi, W. You, Y. Zhang, Z. Tao, P. M. Oppeneer, X. Wu, R. Thomale, K. Rossnagel, M. Bauer, H. Kapteyn et al., "Ultrafast electron calorimetry uncovers a new long-lived metastable state in 1T-TaSe$_2$ mediated by mode-selective electron-phonon coupling," Sci. Adv. **5**, eaav4449 (2019).

[18] A. McPherson, G. Gibson, H. Jara, U. Johann, T. S. Luk, I. A. McIntyre, K. Boyer, and C. K. Rhodes, "Studies of multiphoton production of vacuum-ultraviolet radiation in the rare gases," JOSA B **4**, 595–601 (1987).

[19] M. Ferray, A. L'Huillier, X. F. Li, L. A. Lompre, G. Mainfray, and C. Manus, "Multiple-harmonic conversion of 1064 nm radiation in rare gases," J. Phys. B: At., Mol. Opt. Phys. **21**, L31 (1988).

[20] R. Haight and D. R. Peale, "Tunable photoemission with harmonics of subpicosecond lasers," Rev. Sci. Instrum. **65**, 1853–1857 (1994).

[21] S. Eich, A. Stange, A. V. Carr, J. Urbancic, T. Popmintchev, M. Wiesenmayer, K. Jansen, A. Ruffing, S. Jakobs, T. Rohwer et al., "Time- and angle-resolved photoemission spectroscopy with optimized high-harmonic pulses using frequency-doubled ti: Sapphire lasers," J. Electron Spectrosc. Relat. Phenom. **195**, 231–236 (2014).

[22] G. Rohde, A. Hendel, A. Stange, K. Hanff, L.-P. Oloff, L. X. Yang, K. Rossnagel, and M. Bauer, "Time-resolved ARPES with sub-15 fs temporal and near fourier-limited spectral resolution," Rev. Sci. Instrum. **87**, 103102 (2016).

[23] C. Corder, P. Zhao, J. Bakalis, X. Li, M. D. Kershis, A. R. Muraca, M. G. White, and T. K. Allison, "Ultrafast extreme ultraviolet photoemission without space charge," Struct. Dyn. **5**, 054301 (2018).

[24] A. K. Mills, S. Zhdanovich, M. X. Na, F. Boschini, E. Razzoli, M. Michiardi, A. Sheyerman, M. Schneider, T. J. Hammond, V. Süss et al., "Cavity-enhanced high harmonic generation for extreme ultraviolet time- and angle-resolved photoemission spectroscopy," Rev. Sci. Instrum. **90**, 083001 (2019).

[25] J. H. Buss, H. Wang, Y. Xu, J. Maklar, F. Joucken, L. Zeng, S. Stoll, C. Jozwiak, J. Pepper, Y.-D. Chuang et al., "A setup for extreme-ultraviolet ultrafast angle-resolved photoelectron spectroscopy at 50-kHz repetition rate," Rev. Sci. Instrum. **90**, 023105 (2019).

[26] R. Cucini, T. Pincelli, G. Panaccione, D. Kopic, F. Frassetto, P. Miotti, G. M. Pierantozzi, S. Peli, A. Fondacaro, A. De Luisa et al., "Coherent narrowband light source for ultrafast photoelectron spectroscopy in the 17-31 eV photon energy range," Struct. Dyn. **7**, 014303 (2020).

[27] M. Puppin, Y. Deng, C. W. Nicholson, J. Feldl, N. B. M. Schröter, H. Vita, P. S. Kirchmann, C. Monney, L. Rettig, M. Wolf, and R. Ernstorfer, "Time- and angle-resolved photoemission spectroscopy of solids in the extreme ultraviolet at 500 kHz repetition rate," Rev. Sci. Instrum. **90**, 023104 (2019).

[28] E. J. Sie, T. Rohwer, C. Lee, and N. Gedik, "Time-resolved XUV ARPES with tunable 24-33 eV laser pulses at 30 meV resolution," Nat. Commun. **10**, 3535 (2019).

[29] M. Keunecke, C. Möller, D. Schmitt, H. Nolte, G. M. Jansen, M. Reutzel, M. Gutberlet, G. Halasi, D. Steil, S. Steil et al., "Time-resolved momentum microscopy with a 1 MHz high-harmonic extreme ultraviolet beamline," Rev. Sci. Instrum. **91**, 063905 (2020); arXiv:2003.01602.

[30] S. Peli, D. Puntel, D. Kopic, B. Sockol, F. Parmigiani, and F. Cilento, "Time-resolved VUV ARPES at 10.8 eV photon energy and MHz repetition rate," J. Electron Spectrosc. Relat. Phenom. **243**, 146978 (2020).

[31] S. Hüfner, *Photoelectron Spectroscopy: Principles and Applications* (Springer Science & Business Media, 2003).

[32] C. Tusche, P. Goslawski, D. Kutnyakhov, M. Ellguth, K. Medjanik, H. J. Elmers, S. Chernov, R. Wallauer, D. Engel, A. Jankowiak et al., "Multi-MHz time-of-flight electronic bandstructure imaging of graphene on ir (111)," Appl. Phys. Lett. **108**, 261602 (2016).

[33] M. Kotsugi, W. Kuch, F. Offi, L. I. Chelaru, and J. Kirschner, "Microspectroscopic two-dimensional Fermi surface mapping using a photoelectron emission microscope," Rev. Sci. Instrum. **74**, 2754–2758 (2003).

[34] B. Krömker, M. Escher, D. Funnemann, D. Hartung, H. Engelhard, and J. Kirschner, "Development of a momentum microscope for time resolved band structure imaging," Rev. Sci. Instrum. **79**, 053702 (2008).

[35] C. Tusche, A. Krasyuk, and J. Kirschner, "Spin resolved bandstructure imaging with a high resolution momentum microscope," Ultramicroscopy **159**, 520–529 (2015).

[36] G. Schönhense, K. Medjanik, and H.-J. Elmers, "Space-, time- and spin-resolved photoemission," J. Electron Spectrosc. Relat. Phenom. **200**, 94–118 (2015).

[37] K. Medjanik, S. V. Babenkov, S. Chernov, D. Vasilyev, B. Schönhense, C. Schlueter, A. Gloskovskii, Y. Matveyev, W. Drube, H. J. Elmers et al., "Progress in HAXPES performance combining full-field k-imaging with time-of-flight recording," J. Synchrotron Radiat. **26**, 1996–2012 (2019).

[38] D. Kutnyakhov, R. P. Xian, M. Dendzik, M. Heber, F. Pressacco, S. Y. Agustsson, L. Wenthaus, H. Meyer, S. Gieschen, G. Mercurio et al., "Time- and momentum-resolved photoemission studies using time-of-flight momentum microscopy at a free-electron laser," Rev. Sci. Instrum. **91**, 013109 (2020).

[39] A. Grubisic Cabo, J. A. Miwa, S. S. Grønborg, J. M. Riley, J. C. Johannsen, C. Cacho, O. Alexander, R. T. Chapman, E. Springate, M. Grioni et al., "Observation of ultrafast free carrier dynamics in single layer MoS$_2$," Nano Lett. **15**, 5883–5887 (2015).

[40] F. Liu, M. E. Ziffer, K. R. Hansen, J. Wang, and X. Zhu, "Direct determination of band-gap renormalization in the photoexcited monolayer MoS$_2$" Phys. Rev. Lett **122**, 246803 (2019).

[41] B. Schönhense, K. Medjanik, O. Fedchenko, S. Chernov, M. Ellguth, D. Vasilyev, A. Oelsner, J. Viefhaus, D. Kutnyakhov, W. Wurth et al., "Multidimensional photoemission spectroscopy- the space-charge limit," New J. Phys. **20**, 033004 (2018).

[42] M. Puppin, Y. Deng, O. Prochnow, J. Ahrens, T. Binhammer, U. Morgner, M. Krenz, M. Wolf, and R. Ernstorfer, "500 kHz OPCPA delivering tunable sub-20 fs pulses with 15 W average power based on an all-ytterbium laser," Opt. Express **23**, 1491–1497 (2015).

[43] R. P. Xian, Y. Acremann, S. Y. Agustsson, M. Dendzik, K. Bühlmann, D. Curcio, D. Kutnyakhov, F. Pressacco, M. Heber, S. Dong, T. Pincelli, J. Demsar, W. Wurth, P. Hofmann, M. Wolf, M. Scheidgen, L. Rettig, and R. Ernstorfer, "An open-source, end-to-end workflow for multidimensional photoemission spectroscopy," arXiv:1909.07714v2 (2020).

[44] R. P. Xian, L. Rettig, and R. Ernstorfer, "Symmetry-guided nonrigid registration: The case for distortion correction in multidimensional photoemission spectroscopy," Ultramicroscopy **202**, 133–139 (2019).

[45] S. E. Sobottka and M. B. Williams, "Delay line readout of microchannel plates," IEEE Trans. Nucl. Sci. **35**, 348–351 (1988).

[46] A. Oelsner, O. Schmidt, M. Schicketanz, M. Klais, G. Schönhense, V. Mergel, O. Jagutzki, and H. Schmidt-Böcking, "Microspectroscopy and imaging using a delay line detector in time-of-light photoemission microscopy," Rev. Sci. Instrum. **72**, 3968–3974 (2001).

[47] S. Manzeli, D. Ovchinnikov, D. Pasquier, O. V. Yazyev, and A. Kis, "2D transition metal dichalcogenides," Nat. Rev. Mater. **2**, 17033 (2017).

[48] C. Tusche, Y.-J. Chen, C. M. Schneider, and J. Kirschner, "Imaging properties of hemispherical electrostatic energy analyzers for high resolution momentum microscopy," Ultramicroscopy **206**, 112815 (2019).

[49] J. Feng and A. Scholl, "Photoemission electron microscopy," in *Springer Handbook of Microscopy*, edited by P. W. Hawkes and J. C. H. Spence (Springer International Publishing, Cham, 2019), p. 2.

[50] D. B. Murphy, *Fundamentals of Light Microscopy and Electronic Imaging* (John Wiley & Sons, 2002).

[51] X. J. Zhou, B. Wannberg, W. L. Yang, V. Brouet, Z. Sun, J. F. Douglas, D. Dessau, Z. Hussain, and Z.-X. Shen, "Space charge effect and mirror charge effect in photoemission spectroscopy," J. Electron Spectrosc. Relat. Phenom. **142**, 27–38 (2005).

[52] S. Passlack, S. Mathias, O. Andreyev, D. Mittnacht, M. Aeschlimann, and M. Bauer, "Space charge effects in photoemission with a low repetition, high intensity femtosecond laser source," J. Appl. Phys. **100**, 024912 (2006).

[53] S. Hellmann, K. Rossnagel, M. Marczynski-Bühlow, and L. Kipp, "Vacuum space-charge effects in solid-state photoemission," Phys. Rev. B **79**, 035402 (2009).

[54] J. Graf, S. Hellmann, C. Jozwiak, C. L. Smallwood, Z. Hussain, R. A. Kaindl, L. Kipp, K. Rossnagel, and A. Lanzara, "Vacuum space charge effect in laser-based solid-state photoemission spectroscopy," J. Appl. Phys. **107**, 014912 (2010).

[55] E. Rotenberg and A. Bostwick, "microARPES and nanoARPES at diffraction-limited light sources: opportunities and performance gains," J. Synchrotron Radiat. **21**, 1048–1056 (2014).

[56] M. Plötzing, R. Adam, C. Weier, L. Plucinski, S. Eich, S. Emmerich, M. Rollinger, M. Aeschlimann, S. Mathias, and C. M. Schneider, "Spin-resolved photoelectron spectroscopy using femtosecond extreme ultraviolet light pulses from high-order harmonic generation," Rev. Sci. Instrum. **87**, 043903 (2016).

[57] R. R. Goruganthu and W. G. Wilson, "Relative electron detection efficiency of microchannel plates from 0-3 keV," Rev. Sci. Instrum. **55**, 2030–2033 (1984).

[58] S. Beaulieu, J. Schusser, S. Dong, T. Pincelli, M. Dendzik, J. Maklar, A. Neef, H. Ebert, K. Hricovini, M. Wolf et al., "Signature of hidden orbital-texture in photoemission time-reversal dichroism," Phys. Rev. Lett. **125**, 216404 (2020); arXiv:2006.01657.

[59] M. Puppin, "Time- and angle-resolved photoemission spectroscopy on bidimensional semiconductors with a 500 kHz extreme ultraviolet light source," Ph.D. thesis, Freie Universität Berlin, 2017.

[60] J. Madéo, M. K. Man, C. Sahoo, M. Campbell, V. Pareek, E. L. Wong, A. A. Mahboob, N. S. Chan, A. Karmakar, B. M. K. Mariserla et al., "Directly visualizing the momentum forbidden dark excitons and their dynamics in atomically thin semiconductors," arXiv:2005.00241 (2020).

[61] L. Rettig, R. Cortés, J.-H. Chu, I. R. Fisher, F. Schmitt, R. G. Moore, Z.-X. Shen, P. S. Kirchmann, M. Wolf, and U. Bovensiepen, "Persistent order due to transiently enhanced nesting in an electronically excited charge density wave," Nat. Commun. **7**, 10459 (2016).

[62] R. Al-Obaidi, M. Wilke, M. Borgwardt, J. Metje, A. Moguilevski, N. Engel, D. Tolksdorf, A. Raheem, T. Kampen, S. Mähl et al., "Ultrafast photoelectron spectroscopy of solutions: space-charge effect," New J. Phys. **17**, 093016 (2015).

[63] L.-P. Oloff, K. Hanff, A. Stange, G. Rohde, F. Diekmann, M. Bauer, and K. Rossnagel, "Pump laser-induced space-charge effects in HHG-driven time- and angle-resolved photoelectron spectroscopy," J. Appl. Phys. **119**, 225106 (2016).

[64] F. Haag, T. Eul, P. Thielen, N. Haag, B. Stadtmüller, and M. Aeschlimann, "Time-resolved twophoton momentum microscopy—A new approach to study hot carrier lifetimes in momentum space," Rev. Sci. Instrum. **90**, 103104 (2019).

[65] R. P. Xian, V. Stimper, M. Zacharias, S. Dong, M. Dendzik, S. Beaulieu, B. Schölkopf, M. Wolf, L. Rettig, C. Carbogno et al., "A machine learning route between band mapping and band structure," arXiv:2005.10210 (2020).

[66] E. Fradkin, S. A. Kivelson, and J. M. Tranquada, "Colloquium: Theory of intertwined orders in high temperature superconductors" Rev. Mod. Phys. **87**, 457 (2015).

[67] S. Wandel, F. Boschini, E. Neto, L. Shen, M. Na, S. Zohar, Y. Wang, G. Welch, M. Seaberg, J. Koralek et al., "Light-enhanced charge density wave coherence in a high-temperature super-conductor," arXiv:2003.04224 (2020).

[68] J. Maklar, S. Dong, S. Beaulieu, T. Pincelli, M. Dendzik, Y. W. Windsor, R. P. Xian, M. Wolf, R. Ernstorfer, and L. Rettig (2020). "Time-resolved ARPES data of bulk WSe2 for a quantitative comparison of time-of-flight momentum microscopes and hemispherical analyzers," Zenodo. https://doi.org/10.5281/zenodo.4067968.

4.2 Nat. Commun. 12, 2499 (2021): Nonequilibrium charge-density-wave order beyond the thermal limit

J. Maklar, Y. W. Windsor, C. W. Nicholson, M. Puppin, P. Walmsley, V. Esposito, M. Porer, J. Rittmann, D. Leuenberger, M. Kubli, M. Savoini, E. Abreu, S. L. Johnson, P. Beaud, G. Ingold, U. Staub, I. R. Fisher, R. Ernstorfer, M. Wolf, and L. Rettig

The publication Maklar et al., Nat. Commun. 12, 2499 (2021) reports on the ultrafast electronic and structural CDW order parameter dynamics of the prototypical CDW compound $TbTe_3$ upon photoexcitation. The associated supplementary information is reprinted below the main article. The associated raw data is publicly available at the Zenodo data repository, doi 10.5281/zenodo.4106272.

Author contributions

Y.W.W, L.R., M.Pu., C.W.N. and **J.M.** carried out the trARPES experiments; L.R., V.E., M.Po., J.R., D.L., M.K., M.S., E.A., S.L.J., P.B., G.I. and U.S. carried out the trXRD experiments; P.W. and I.R.F. provided the samples; **J.M.** analyzed the data with support from L.R; **J.M.** wrote the manuscript with support from L.R., R.E. and M.W.; all authors commented on the paper.

Reprinted with permission from Ref. [II]. Copyright 2021 Springer Nature.

ARTICLE

Check for updates

Nonequilibrium charge-density-wave order beyond the thermal limit

J. Maklar [1✉], Y. W. Windsor [1], C. W. Nicholson [1,7], M. Puppin [1,8], P. Walmsley [2,3], V. Esposito [3,4], M. Porer[4], J. Rittmann[4], D. Leuenberger[5], M. Kubli[6], M. Savoini[6], E. Abreu[6], S. L. Johnson[4,6], P. Beaud [4], G. Ingold[4], U. Staub [4], I. R. Fisher [2,3], R. Ernstorfer [1], M. Wolf[1] & L. Rettig [1✉]

The interaction of many-body systems with intense light pulses may lead to novel emergent phenomena far from equilibrium. Recent discoveries, such as the optical enhancement of the critical temperature in certain superconductors and the photo-stabilization of hidden phases, have turned this field into an important research frontier. Here, we demonstrate nonthermal charge-density-wave (CDW) order at electronic temperatures far greater than the thermo-dynamic transition temperature. Using time- and angle-resolved photoemission spectroscopy and time-resolved X-ray diffraction, we investigate the electronic and structural order parameters of an ultrafast photoinduced CDW-to-metal transition. Tracking the dynamical CDW recovery as a function of electronic temperature reveals a behaviour markedly different from equilibrium, which we attribute to the suppression of lattice fluctuations in the transient nonthermal phonon distribution. A complete description of the system's coherent and incoherent order-parameter dynamics is given by a time-dependent Ginzburg-Landau framework, providing access to the transient potential energy surfaces.

[1] Fritz-Haber-Institut der Max-Planck-Gesellschaft, Berlin, Germany. [2] Geballe Laboratory for Advanced Materials and Department of Applied Physics, Stanford University, Stanford, CA, USA. [3] Stanford Institute for Materials and Energy Sciences, SLAC National Accelerator Laboratory, Menlo Park, CA, USA. [4] Swiss Light Source, Paul Scherrer Institut, Villigen PSI, Switzerland. [5] Department of Physics, University of Zürich, Zürich, Switzerland. [6] Institute for Quantum Electronics, Physics Department, ETH Zürich, Zürich, Switzerland. [7] Present address: Department of Physics and Fribourg Center for Nanomaterials, University of Fribourg, Fribourg, Switzerland. [8] Present address: Laboratory of Ultrafast Spectroscopy, ISIC, Ecole Polytechnique Fédérale de Lausanne (EPFL), Lausanne, Switzerland. ✉email: maklar@fhi-berlin.mpg.de; rettig@fhi-berlin.mpg.de

Complex solids exhibit a multitude of competing and intertwined broken symmetry states originating from a delicate interplay of different degrees of freedom and dimensionality. Among these states, charge-density-waves (CDWs) are a ubiquitous phase characterized by a cooperative periodic modulation of the charge density and of the crystal lattice, mediated by electron-phonon coupling[1–3]. While lattice and charges are intrinsically coupled in equilibrium, ultrafast optical excitation allows to selectively perturb each of these subsystems and to probe the melting of order and its recovery as a real-time process. This approach grants access to the relevant interactions of CDW formation[4–15], to out-of-equilibrium and metastable states[16–19] and elucidates competing orders[20–22].

In close analogy to superconductivity, the formation of a CDW broken symmetry ground state can be described by an effective mean field that serves as an order parameter, which is governed in equilibrium by a static free energy surface. While mean field theory captures the phase transition on a qualitative level, thermal lattice fluctuations reduce the critical temperature T_c of long-range 3D order significantly below the predicted mean field value T_{MF}[1,2]. It is of strong interest how our understanding of phase transitions in the adiabatic limit can be adapted to a nonequilibrium, dynamical setting induced by an impulsive excitation[11,23–27]. It remains an open question whether the thermal transition temperature is still a relevant quantity in the description of such an out-of-equilibrium state, and which parameters permit transient control of T_c[20,28–32].

Symmetry-broken phases also allow for collective excitations of the order parameter, as observed in a variety of systems, including CDW compounds, superconductors and atoms in optical lattices[33–35]. Two types of modes emerge in the symmetry-broken ground state, related to a variation of the amplitude and the phase of the complex order parameter, i.e., the Higgs amplitude mode (AM) and the Nambu-Goldstone phase mode. In CDW compounds, upon impulsive excitation, the AM manifests as coherent oscillations of the electronic and structural order-parameter amplitudes[4,6,36]. However, recent studies investigating the structural dynamics of various CDW compounds upon strong perturbation hint towards collective modes at increased frequencies far beyond the intrinsic AM[11,26,37].

To address these issues, we investigate the electronic and structural order of optically excited bulk TbTe₃, a prototypical CDW compound of the rare-earth tritelluride family[38,39]. Using time- and angle-resolved photoemission spectroscopy (trARPES) in combination with time-resolved X-ray diffraction (trXRD), schematically depicted in Fig. 1a, we extract the amplitude of the electronic and structural order parameters and the electronic temperature as functions of pump-probe delay t. This reveals CDW formation at electronic temperatures substantially above the thermal critical temperature. We attribute this transient stabilization to a reduced contribution of lattice fluctuations in the out-of-equilibrium state due to a nonthermal phonon population. Furthermore, with increasing excitation density, the coherent order parameter dynamics indicate a transition from the AM regime to a high-frequency regime, driven by a modification of the underlying potential energy surface. We model the order-parameter dynamics in a time-dependent Ginzburg–Landau framework, which further supports the scenario of a nonthermal stabilization of the CDW order.

Results

Electronic and structural CDW signatures. First, using ARPES, we analyze the Fermi surface (FS) of TbTe₃ at $T = 100$ K, well below $T_c = 336$ K, the transition temperature of the unidirectional CDW phase[40]. The electronic properties near E_F are governed by
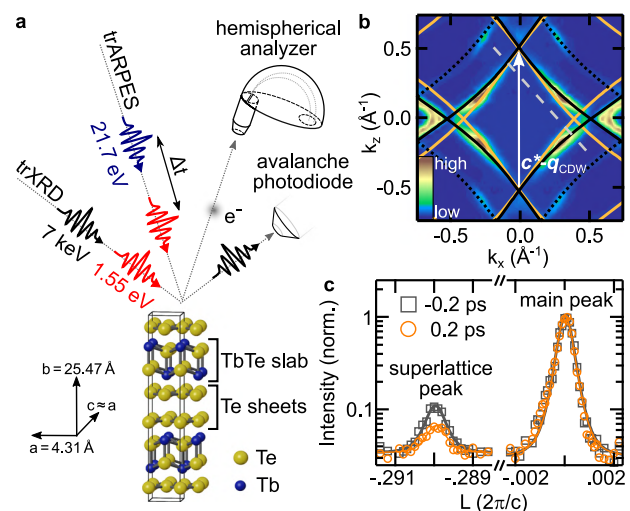

Fig. 1 Experimental scheme. a Schematic of the trARPES and grazing-incidence trXRD experiments. TbTe₃ is a quasi-2D compound consisting of a stack of Te sheets and TbTe slabs. **b** Symmetrized FS of TbTe₃ ($T = 100$ K, $t = 0$ fs). Below T_c, the spectral weight within the nested FS regions connected by the CDW wave vector $\mathbf{c}^* - \mathbf{q}_{CDW}$ vanishes[39]. The black solid and dotted lines correspond to Te $5p_x/5p_z$ bands from tight-binding calculations. FS nesting also leads to the formation of shadow bands (orange lines). The gray dashed line indicates the momentum-direction analyzed in Fig. 2a-c. **c** Representative X-ray Bragg peaks with Voigt fits along the (3 7 L) direction before and after optical excitation (absorbed fluence $F = 1.35$ mJ cm⁻²).

the Te sheets (Fig. 1a), which give rise to the diamond-shaped bands shown in Fig. 1b. Strongly wave-vector dependent electron-phonon coupling[41], in conjunction with a moderately well-nested Fermi surface[42], lead to a unidirectional CDW in which some portions of the Fermi surface are gapped while others remain metallic[39]. To study the effect of the CDW on the lattice, we investigate the intensity of superlattice (SL) Bragg peaks using trXRD. These SL peaks arise from the periodic lattice distortion associated with the CDW, and are displaced by the CDW wave vector $\pm \mathbf{q}_{CDW}$ from the main peak positions[40,43]. As Fig. 1c shows, photoexcitation strongly suppresses the SL peak corresponding to a rearrangement of the atomic mean positions towards the trivial metallic phase, while the main lattice peak reflecting the average crystal structure shows only minor changes.

Next, we investigate the electron dynamics associated with the CDW upon photoexcitation. We focus on an energy-momentum cut that contains the electronic signatures of the CDW, namely the energy gap at E_F in the nested regions and the backfolded shadow bands[44], shown in Fig. 2a, b. At temporal pump-probe overlap ($t = 0$ fs), the interacting tight-binding model introduced by Brouet et al.[39] is in excellent agreement with the observed quasiparticle dispersion: In the nested region (left side of Fig. 2a, b), we observe a pronounced hybridization energy gap at E_F. In the imperfectly nested region (right side), the Te band exhibits metallic behavior, as the energy gap is located above E_F. Furthermore, we observe faint shadow bands in the vicinity of the energy gaps (boxes 2 and 3 in Fig. 2b). Within 120 fs, the system undergoes a photo-induced CDW-to-metal transition[6], as apparent from the transient suppression of the energy gap and the shadow bands, see Fig. 2c–e.

CDW order-parameter dynamics. The CDW-to-metal transition can be described by an order parameter ψ, with $|\psi| = 0$ in the metallic and $0 < |\psi| \leq 1$ in the CDW phase. Due to the coupling
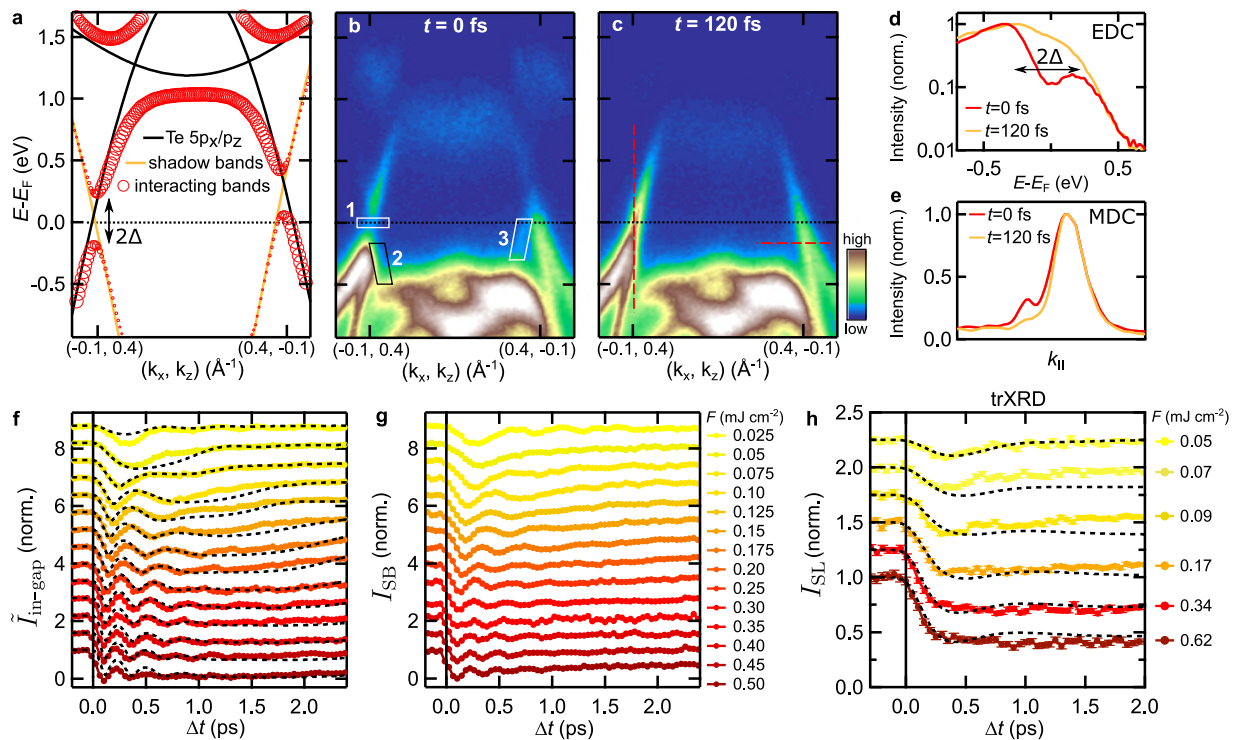
Fig. 2 CDW band structure dynamics. a Tight-binding bands along the momentum-direction indicated by the dashed gray line in Fig. 1b. The black and orange curves correspond to the non-interacting Te main and shadow bands, respectively. The red circles mark the hybridized bands with interaction potential Δ. The circle size illustrates the spectral weight. **b**, **c** trARPES measurements ($F = 0.45$ mJ cm^{-2}) along the momentum direction shown in **a**. At $t = 0$ fs, the energy gap at E_F (box 1) and shadow bands (boxes 2, 3) indicate the CDW order. After 120 fs, the CDW vanishes, and the energy gap and shadow band intensity are strongly suppressed. **d**–**e** Energy and momentum distribution curves along the dashed vertical and horizontal lines in **c**, respectively. **f** Inverted in-gap intensity $\tilde{I}_{in-gap} = 1 - I_{in-gap}$ with in-gap intensity I_{in-gap} (box 1 in **b**, normalized by the respective pre-excitation values) as function of pump-probe delay for various fluences (displaced vertically). Normalized time-dependent Ginzburg–Landau simulations are shown in black. For details of the model, see main text and Supplementary Note 1. **g** Normalized shadow band intensity extracted from box 2. The shadow band intensity obtained from box 3 is shown in Supplementary Fig. 1. **h** Time evolution of the (2 10 1 + q_{CDW}) SL peak intensity for various fluences (displaced vertically) with layered Ginzburg–Landau simulations, see Supplementary Note 3. The curves are normalized by their respective pre-excitation values. The error bars correspond to one standard deviation from photon counting statistics.

between charges and lattice, the transition can be characterized by an electronic (ψ_e) or a structural (ψ_s) order parameter. We utilize trARPES to access the amplitude of the electronic order parameter $|\psi_e|$. Most directly, $|\psi_e|$ can be extracted by tracking the energy gap 2Δ at E_F[13,45]. However, this method faces practical limitations due to the vanishing occupation of bands above E_F after a few 100 fs and due to the limited experimental energy resolution. Therefore, we choose two alternative metrics to quantify the CDW order: We introduce the inverted in-gap intensity $\tilde{I}_{in-gap} = 1 - I_{in-gap}$ with normalized in-gap intensity I_{in-gap}, extracted from box 1 in Fig. 2b. We find that this metric – for the chosen region of interest and our experimental resolution – follows a BCS-like temperature dependence in equilibrium, as confirmed by static measurements (black markers in Fig. 3b), and thus is considered equivalent to $|\psi_e|$. Further, as the inverted in-gap intensity is derived from a region where the gap is centered around E_F, it is unaffected by thermal changes to the distribution function. As a second metric, we extract the shadow band intensity $I_{SB} \propto |\psi_e|$[30,44] from box 2 in Fig. 2b.

Using these equivalent metrics, we investigate the photo-induced CDW suppression and recovery over a wide range of fluences, as shown in Fig. 2f–g. For a low absorbed fluence of 0.025 mJ cm^{-2} below the CDW melting threshold, we observe a weak modulation of the CDW gap and SB intensity corresponding to the AM of the CDW at $\omega_{AM}/2\pi = 2.2$ THz (see

Supplementary Fig. 2). At the CDW melting threshold ≈ 0.05 mJ cm^{-2}, the AM softens and becomes overdamped, while the CDW melting time t_{melt} slows down, and the energy gap and SB intensity vanish almost completely. Upon crossing the melting threshold, we observe a fast initial quench of the CDW within $t_{melt} \approx 100$ fs (see Supplementary Fig. 8), followed by few damped coherent oscillations that exhibit a pronounced frequency reduction with pump-probe delay (down-chirp). Interestingly, the initial frequency of the collective excitation increases with fluence, doubling at the highest accessible fluences. Concurrently, the time required to restore the ground state after perturbation steadily increases with fluence, leading to a persistent suppression of the CDW for a few ps at the highest excitation densities we used.

To gain a complementary view of the photo-induced phase transition, we use trXRD to extract the structural order parameter from the normalized SL peak intensity upon optical excitation[11,23,37], which, in first approximation, is given by $I_{SL}(t) \propto |\psi_s(t)|^2$. As Fig. 2h shows, the SL response qualitatively resembles the dynamical quench and recovery of the extracted electronic order parameter. In the low-fluence regime, a weak initial suppression is followed by a quick recovery of the SL structure, on top of which a faint modulation can be identified (see Supplementary Fig. 3). In the high-fluence regime, the SL peak intensity is strongly quenched, and, with increasing fluence,
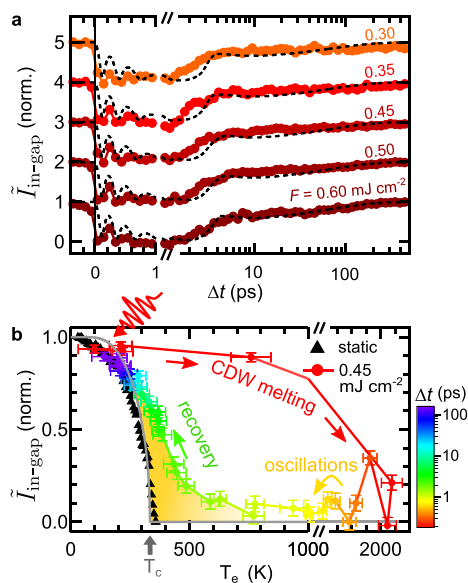
Fig. 3 CDW recovery dynamics. a Time evolution of the inverted in-gap intensity in the high-fluence regime (displaced vertically). Normalized time-dependent Ginzburg–Landau simulations are shown in black. **b** Inverted in-gap intensity versus extracted electronic temperatures. One standard deviation of the T_e fit (horizontal error bars) and one standard deviation derived from electron counting statistics (vertical error bars) are given as uncertainty. $\tilde{I}_{\text{in-gap}}$ extracted from a static temperature series (black markers, T values from heater setpoints, curve normalized to the lowest accessible T value) is in general agreement with the BCS-type T-dependence of the order parameter (gray curve). The dynamic trace shows the full cycle of laser-heating and CDW melting, coherent oscillations and CDW recovery (delay encoded in the color code). The yellow shaded area marks the region of dynamical CDW formation at electronic temperatures above T_c. The pre-excitation value of the dynamic trace ($T = 100$ K) is normalized to the corresponding value of the static T-dependence.

the time required to recover diverges. In contrast to the electronic response, we do not observe clear coherent oscillations of the SL peak intensity upon strong excitation. This originates most likely from the lower temporal resolution of the trXRD setup and the contribution of sub-surface crystal layers with varying, lower excitation densities (see Supplementary Note 3). Recent trXRD experiments with improved temporal resolution have revealed fluence-dependent collective excitations of the SL peak intensity in a closely related tritelluride[37] – in agreement with our observations for ψ_e. Furthermore, while the SL intensity I_{SL} drops linearly with excitation density shortly after excitation, this behavior plateaus after crossing a fluence of ≈ 0.1 mJ cm^{-2}. This results in a residual SL intensity of 35% even after strong excitation of up to 1.35 mJ cm^{-2}. We assign this persisting SL background to a contribution of unexcited sample volumes due to surface steps caused by crystal cleaving[11]. Nonetheless, the trXRD data clearly shows that not only the electronic, but also the lattice superstructure is melted upon strong photoexcitation. The qualitative agreement of the electronic and structural response demonstrates a strong coupling between electronic and lattice degrees of freedom on ultrafast timescales, and suggests an equivalent treatment of $|\psi_s|$ and $|\psi_e|$ within the experimental time resolution.

Diffraction also probes the long-range coherence of the SL phase. While phase coherence plays a secondary role in the low-fluence regime, it becomes increasingly important during the CDW recovery after strong perturbation due to the creation of

topological defects. These dislocation-type defects broaden the SL peaks, locally decrease the amplitude of the periodic lattice modulation, and can persist long after the CDW amplitude has recovered[46–48]. Therefore, rather than trXRD, we employ trARPES to access the amplitude of the order parameter throughout the full recovery to equilibrium. As shown in Fig. 3a, in the high-fluence regime, the majority of the CDW order is restored after ≈ 5 ps, followed by a complete recovery on a 100 ps timescale.

Transient electronic temperature. Time-resolved ARPES allows to extract the transient electronic temperatures from Fermi–Dirac fits to the energy distribution of metallic regions of the FS (see Supplementary Note 2), and thereby to compare the nonequilibrium CDW melting and recovery to the mean field behavior upon thermal heating. Remarkably, in the dynamic case, the electronic order parameter does not follow the mean field dependence governed by T_c. In the low-fluence regime below the CDW melting threshold, electronic temperatures reach up to 500 K, far above $T_c = 336$ K (see Supplementary Fig. 7). Yet, photo-excitation causes only a minor initial suppression of the energy gap and of the periodic lattice distortion, and initiates a collective AM oscillation – a hallmark of the CDW state.

In the high-fluence regime, the CDW is fully suppressed ($\tilde{I}_{\text{in-gap}} = I_{SB} = 0$) as initial electronic temperatures exceed 2000 K. However, recovery of the CDW order already sets in when the electronic system is still at elevated temperatures $T_e \gg T_c$. To illustrate this dynamic behavior, Fig. 3b presents the inverted in-gap intensity of the melting and the recovery cycle as a function of extracted electronic temperatures. In the out-of-equilibrium setting, CDW order reappears below $T_e \approx 600$ K (yellow shaded area), indicating an increased effective critical temperature T_c^*. At delay times of several ps, corresponding to electronic temperatures of $T_e \lesssim T_c$, the dynamic behavior converges to the equilibrium T-dependence. This trend of nonthermal CDW recovery is consistent over a wide range of fluences (see Supplementary Fig. 4).

Time-dependent Ginzburg–Landau theory. Near the transition temperature, the order parameter can be approximated by the Landau theory of second-order phase transitions[2]. Thus, to simulate the dynamics of the order parameter in TbTe$_3$, we make the following ansatz for the effective potential energy surface (in dimensionless units) based on time-dependent Ginzburg–Landau (tdGL) theory[11,27,37,49,50]:

$$V(\psi, t) = -\frac{1}{2}\left(1 - \eta(t)\right)\psi^2 + \frac{1}{4}\psi^4 . \quad (1)$$

Upon perturbation, the dynamics of the order parameter are determined by the equation of motion derived from Eq. (1) (see Supplementary Note 1). The transient modification of the potential, resulting from the laser excitation and subsequent relaxation, is modeled by the ratio of the electronic temperature and the critical temperature $\eta(t) = T_e/T_c$. Motivated by the increased transient ordering temperature discussed above, we replace the static T_c by a phenomenological time-dependent critical temperature

$$T_c^*(t) = T_c(1 + H(t) \cdot s \cdot \exp(-t/\tau_{\text{ph-ph}})) , \quad (2)$$

with Heavyside step function H. It captures the enhanced critical temperature in the nonthermal regime, given by the temperature scaling s, and converges to T_c at late times. This leaves us with only two global fit parameters for the simulations: damping γ and scaling s in the nonthermal regime (see Supplementary Note 1 for details of the model). For the timescale connecting both regimes,
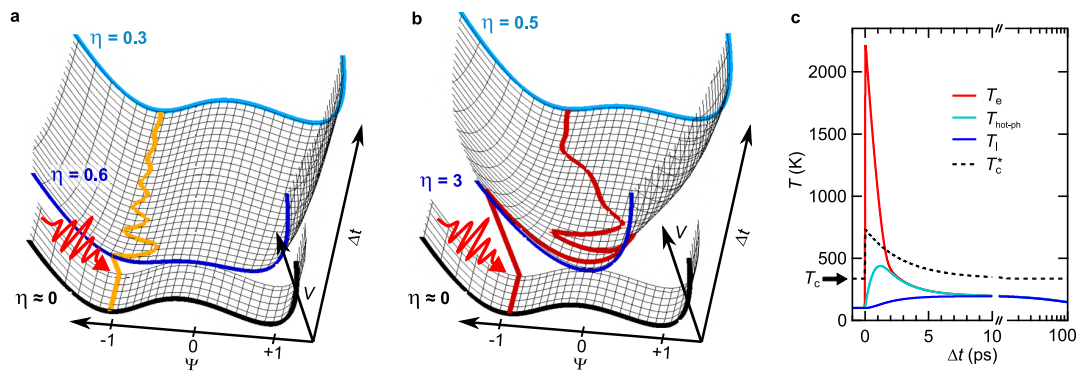
Fig. 4 Simulated order-parameter dynamics and 3TM. Transient potential energy surface and order-parameter pathway upon **a** weak and **b** strong optical excitation. The potential shapes before excitation (black curve), at 0 ps (dark blue) and 3.5 ps (light blue) are highlighted. **a** In the AM regime, the double-well potential is weakly modified, while in **b** the overshoot regime, the CDW melting threshold is reached, resulting in a single-well shaped potential, followed by a relaxation to the double-well ground state. **c** 3TM of electronic, hot phonon and lattice temperatures T_e, T_{hot-ph} and T_l in the regime of strong perturbation ($F = 0.35$ mJ cm^{-2}). In the 3TM, the optical excitation of the electronic system is followed by an energy transfer to certain strongly coupled optical phonons, widely observed in materials with selective electron-phonon coupling[27,51,52,61-63]. Subsequently, this hot phonon subset equilibrates with the remaining lattice phonon bath on a ps timescale (τ_{ph-ph}). To account for the recovery of the base temperature via heat diffusion on a 100 ps timescale, the lattice is coupled to an external heat sink. The black dashed line indicates the rescaled critical temperature T_c^*. In the 3TM simulations, material properties of the related compound LaTe$_3$[27] were used.

we find a good description of the data by choosing the lattice thermalization time $\tau_{ph-ph} = 2.2$ ps reported for the closely related compound LaTe$_3$[27]. Energy redistribution processes within the electron and lattice systems are often modeled by a three temperature model (3TM)[51,52], as presented in Fig. 4c. Here, τ_{ph-ph} corresponds to the timescale of energy transfer between strongly coupled optical phonon modes (T_{hot-ph}) with the remaining cold lattice modes (T_l). The choice of the parameter τ_{ph-ph} is further motivated in the following discussion. In this description, CDW order emerges when the electronic temperature T_e falls below the introduced dynamic effective T_c^* (black dashed curve in Fig. 4c). During the thermalization process, the estimated lattice temperatures T_l stay below the thermal critical temperature for all applied fluences.

Given the complexity of the system, this model with its minimal amount of free parameters is in remarkable agreement with the electronic order parameter extracted directly from the trARPES data throughout the CDW melting and full recovery over a large fluence range, as shown in Figs. 2f and 3a. It captures (i) the AM in the low-fluence regime, (ii) the CDW melting time after arrival of the pump, (iii) the coherent oscillations and the down-chirp in the high-fluence regime, and (iv) the full CDW recovery to equilibrium. The fit yields a nonthermal critical temperature of $T_c^*(t = 0$ fs$) \approx 745$ K, i.e., more than double of the equilibrium T_c. Remarkably, this value is similar to the electronic temperature where the onset of CDW recovery is observed in Fig. 3b. To illustrate the necessity of a transiently enhanced T_c^* to describe the data, we perform tdGL simulations keeping the critical temperature fixed at the equilibrium value, which, however, leads to a severe deviation from the experimental oscillations and CDW recovery, see Supplementary Fig. 5. Next, we illustrate the characteristic regimes of the tdGL simulations based on the extracted transient potential energy surfaces $V(\psi, t)$ in Fig. 4.

AM regime: Before excitation, the system is in the CDW ground state ($\eta \approx 0$), corresponding to an underlying double-well potential with minima at $|\psi| \approx 1$. Upon weak excitation (Fig. 4a), the potential surface is barely altered and maintains its double-well shape. This launches a damped oscillation of the order parameter around the marginally shifted potential minimum at frequency ω_{AM}, i.e., the AM.

Overshoot regime: Upon strong excitation (Fig. 4b), the underlying potential transforms to a single-well shape, corresponding to the metallic phase. The order parameter overshoots to the opposite side of the potential, and oscillates around the new potential minimum at $|\psi| = 0$ at frequency $\omega \gg \omega_{AM}$. Relaxation of the system leads to a transient flattening of the potential, resulting in the observed frequency down-chirp. At $\eta < 1$, the CDW order finally recovers, and the order parameter relaxes into one of the minima of the emerging double-well potential.

A minor deviation of the fit from the data occurs at the dynamical slowing-down of the CDW melting in the vicinity of the melting threshold, as observed in the curve at fluence 0.05 mJ cm^{-2} in Fig. 2f. For an initial perturbation in the range $\eta_{init} \approx 0.5...1$, the system gains just enough energy to reach the local maximum of the double-well potential at $|\psi| = 0$. Close to this metastable point, the potential is rather flat, leading to a critical slowing-down of the order-parameter dynamics[53], discussed in detail in Supplementary Note 4. A similar critical behavior is expected during the recovery of the CDW order. In the overshoot regime, after dampening of the initial oscillations, the order parameter can get trapped at the metastable local maximum despite an incipient recovery of the double-well ground state. However, in real systems, several microscopic processes, such as local modification of T_c by crystal defects[54,55], CDW nucleation and creation of topological defects[47] and coupling of the collective excitation to other phonons[36], will screen against a pronounced critical slowing-down. However, such effects go beyond our current model.
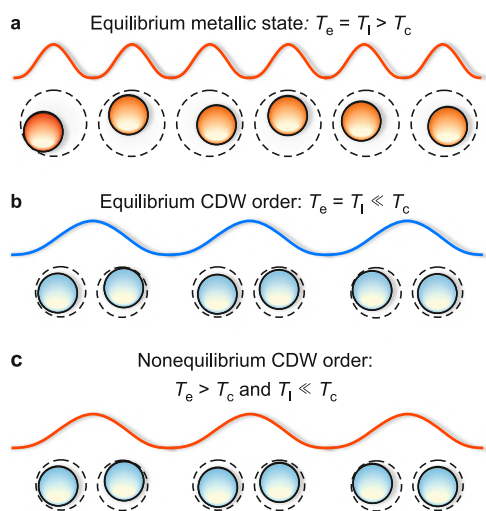
To reproduce the main observations of the extracted structural order parameter, we extend this model to a layered description (see Supplementary Note 3), as shown in Fig. 2h. However, the absence of clear coherent modulations in the time evolution of the SL peak intensity and the additional contribution of the SL phase coherence prohibit a reliable fit of $I_{SL}(t)$. Nonetheless, we conclude that this model captures all key features of the structural and electronic order parameters within a unified framework.

Discussion

We unambiguously demonstrate a transient CDW behavior distinct from equilibrium, as evidenced by the CDW AM

modulations after weak excitation despite electronic temperatures exceeding thermal T_c, and from the CDW recovery at elevated electronic temperatures after strong excitation. The qualitative correspondence of charge and structural features of the CDW excludes a scenario in which only the electronic superstructure is destroyed while the lattice distortion remains intact, which could facilitate such a nonthermal behavior. So what causes this enhanced transient stability of CDW order far beyond the equilibrium T_c? In equilibrium, lattice fluctuations induced by thermally populated phonons, accompanied by fluctuations of the charge density, reduce T_c significantly below the mean-field value T_{MF}. Especially in low-dimensional systems, these fluctuation effects become increasingly important, such that long-range order and phase transitions cannot occur at finite temperatures in strictly 1D systems[1,2]. However, in real materials, coupling between neighboring chains stabilizes the CDW order, resulting in short-range correlations at high-temperatures and long-range 3D order below T_c[2,3].

Ultrafast optical perturbation breaks the thermal equilibrium between charges and lattice. Initially, electrons and certain optical phonons are strongly excited, while the overall vibrational population of the lattice – determined by acoustic modes that account for the majority of the lattice heat capacity – is still close to its pre-excitation value corresponding to an effective lattice temperature significantly below T_c. In this out-of-equilibrium regime, the average displacement of the ionic cores around their mean positions (mean-squared displacement) is small, as the nonthermal phonon population is dominated by high-frequency, low-amplitude optical phonons[56]. Thus, initially after excitation, lattice fluctuations are strongly suppressed and counteract a mean-field long-range ordering only weakly, which facilitates CDW formation even at electronic temperatures far beyond T_c, illustrated in Fig. 5. In this nonthermal regime, T_c is replaced by the effective electronic critical temperature T_c^*, which is

renormalized towards the mean field value depending on the transient lattice temperature and concomitant fluctuations. Over the course of several ps, depending on the lattice thermalization time τ_{ph-ph}, energy is transferred from the strongly coupled optical hot phonons to the remaining phonon modes. This defines the crossover from the nonthermal to the quasi-thermal regime, at which electrons and lattice locally reach thermal equilibrium. As the lattice temperature rises, acoustic (high-amplitude) fluctuations and CDW phase fluctuations increase, which impedes long-range 3D CDW order, and T_c^* consequently converges towards the equilibrium T_c. The increasing occupation of lattice vibrations also increases the lattice entropy, and thus modifies the underlying free energy surface. In this picture, the changing lattice entropy plays the analogous part to the time-dependent critical temperature introduced within our tdGL expansion.

The agreement of the Ginzburg–Landau simulations with the extracted order parameters further underlines this scenario. The initial oscillation frequency of the electronic order parameter, the down-chirp as well as the recovery are reproduced by simulations with an enhanced T_c^*, that converges towards the equilibrium T_c on the lattice thermalization time. In addition, since the initial lattice temperature is close to its equilibrium value also after strong excitation to the overshoot regime, the contribution of thermal fluctuations is expected to be rather independent of fluence. This is in agreement with our model, which captures the experimental data over a wide fluence range with a fluence-independent description of T_c^*. Our simulations yield a transient critical temperature of ≈ 750 K at early times, which is still considerably below the mean field transition temperature $T_{MF} \approx 1600$ K estimated from the electronic energy gap in the nested regions via the well-known BCS expression[2]. However, because of the imperfect nesting of large segments of the FS, a significant reduction of T_{MF} is expected[40,57], and remaining fluctuations at the initial lattice temperature of $T_l \approx 100$ K are further expected to lead to a lower T_c^*.

The CDW order above T_c may be further stabilized by transiently enhanced FS nesting. A previous trARPES study has demonstrated an improved nesting condition in rare-earth tritellurides upon optical excitation[13], caused by a transient modification of the FS. Consequently, the CDW-gapped area at E_F expands and the critical temperature transiently increases. However, the photo-induced enhanced nesting significantly increases with excitation density[13], which would result in a strongly fluence-dependent nonthermal critical temperature. As we find a good description of the data by T_c^* independent of fluence, we assign a suppression of lattice fluctuations in the out-of-equilibrium state as the dominant effect stabilizing the transient CDW. Several studies suggest similar nonthermal behavior in other CDW materials. The commensurate CDW phase of 1T-TaS_2 exhibits an exceptionally robust AM after strong perturbation, with initial electronic temperatures exceeding 1300 K[5]. In elemental Chromium, trXRD measurements of the SL peak indicate a persisting CDW state above the thermal transition temperature[29].

In summary, we experimentally track the structural and electronic order parameters of a photo-induced CDW-to-metal transition in the rare-earth tritelluride TbTe$_3$, and reveal a close correspondence of the charge and lattice components of the CDW phase throughout the melting and initial recovery of order. By extracting the time-dependent electronic temperature, we demonstrated nonthermal CDW formation at electronic temperatures significantly above the thermodynamic transition temperature T_c. We attribute the dominating role of this behavior to reduced lattice fluctuations compared to a scenario in which charges and lattice are in equilibrium above T_c. Since lattice

Fig. 5 Illustration of nonthermal CDW order. a In equilibrium at elevated temperatures, the system is in a trivial metallic phase. The charge density (wavy line) and the mean positions of the ionic cores (circles) are spaced evenly, as strong thermal lattice fluctuations prevent long-range CDW order. **b** In equilibrium at low temperatures, the system features an ordered charge- and lattice superstructure. **c** Photoexcitation of the CDW ground state ($T_{pre-exc.} \ll T_c$) generates a hot electron distribution, while the lattice initially remains cold. In this out-of-equilibrium state, thermal lattice fluctuations are weak and barely hinder long-range CDW ordering. Hence, the charge and lattice superstructure is stabilized at electronic temperatures beyond T_c.

fluctuations play a universal role in the CDW formation, the observed nonthermal stabilization mechanism should also apply to other material families. Moreover, we observed excitation-dependent collective dynamics of the charge order, closely connected to a coherent modulation of the periodic lattice distortion. We applied a tdGL framework to model the order-parameter dynamics and to describe the underlying transient potential energy surface, which governs the collective behavior. Despite its simplicity of using a single degree of freedom, this phenomenological model reproduces all key observations. This suggests that mode-coupling[36] and inhomogeneities (defects) play only a secondary role in the dynamical melting and recovery of the CDW amplitude.

As any memory device relies on nonequilibrium properties, our results have strong implications for applications involving charge-ordering phenomena. A key parameter defining the persistence of the nonthermal stabilization is phonon-phonon coupling, as it dictates the lattice thermalization and thus the timescale on which the fluctuation background rises. Therefore, minimizing phonon-phonon coupling may be critical in the design of switchable CDW devices operating in nonequilibrium conditions[58].

Methods

trARPES. Single crystals of TbTe$_3$ samples were grown by slow cooling of a binary melt[38]. All experiments were carried out at $T = 100$ K. The ARPES measurements were performed in ultra-high vacuum $< 1 \times 10^{-10}$ mbar (samples cleaved in-situ), using a laser-based higher-harmonic-generation trARPES setup[59] ($h\nu_{probe} = 21.7$ eV, $h\nu_{pump} = 1.55$ eV, 500 kHz repetition rate, $\Delta E \approx 175$ meV, $\Delta t \approx 35$ fs) and a SPECS Phoibos 150 hemispherical analyzer. The pump and probe spot sizes (FWHM) are $\approx 230 \times 200\ \mu m^2$ and $\approx 70 \times 60\ \mu m^2$. All discussed fluence values refer to the absorbed fluence F_{abs}. To estimate F_{abs}, the complex refractive index was determined via optical reflectivity measurements at $\lambda = 800$ nm to $n = 0.9$ and $k = 2.6$.

trXRD. The trXRD measurements were carried out at the FEMTO hard X-ray slicing source (X05LA) at the Swiss Light Source, Paul Scherrer Institut, Villigen, Switzerland[60]. The utilized laser-sliced X-ray pulses ($h\nu_{X-ray} = 7$ keV, $\Delta t \approx 120$ fs) feature the high stability of conventional synchrotron radiation and do not exhibit any relevant jitter in position, angle or wavelength. The diffracted X-ray intensity was recorded with an avalanche photodiode in an asymmetric diffraction geometry. A synchronized optical pump laser (10° angle of incidence, $h\nu_{pump} = 1.55$ eV, $\Delta t \approx 110$ fs) was used to excite the system. The pump and probe spot sizes (FWHM) were $\approx 600 \times 600\ \mu m^2$ and $\approx 250 \times 5\ \mu m^2$. The X-ray extinction length was matched to the pump penetration depth of 25 nm by using a grazing angle of incidence of 0.5°.

Data availability

The data that support the findings of this study are publicly available in Zenodo[64] with the identifier https://doi.org/10.5281/zenodo.4106272.

References

1. Motizuki, K. *Structural phase transitions in layered transition metal compounds* (Springer Science & Business Media, 1986).
2. Gruner, G. *Density waves in solids* (CRC press, 1994).
3. Pouget, J.-P. The peierls instability and charge density wave in one-dimensional electronic conductors. *Comptes Rendus Physique* **17**, 332–356 (2016).
4. Demsar, J., Biljakovic, K. & Mihailovic, D. Single particle and collective excitations in the one-dimensional charge density wave solid K$_{0.3}$MoO$_3$ probed in real time by femtosecond spectroscopy. *Phys. Rev. Lett.* **83**, 800 (1999).
5. Perfetti, L. et al. Time evolution of the electronic structure of 1T-TaS$_2$ through the insulator-metal transition. *Phys. Rev. Lett.* **97**, 067402 (2006).
6. Schmitt, F. et al. Transient electronic structure and melting of a charge density wave in TbTe$_3$. *Science* **321**, 1649–1652 (2008).
7. Eichberger, M. et al. Snapshots of cooperative atomic motions in the optical suppression of charge density waves. *Nature* **468**, 799–802 (2010).
8. Möhr-Vorobeva, E. et al. Nonthermal melting of a charge density wave in TiSe$_2$. *Phys. Rev. Lett.* **107**, 036403 (2011).
9. Hellmann, S. et al. Time-domain classification of charge-density-wave insulators. *Nat. Commun.* **3**, 1069 (2012).
10. Sohrt, C., Stange, A., Bauer, M. & Rossnagel, K. How fast can a peierls–mott insulator be melted? *Faraday Discuss.* **171**, 243–257 (2014).
11. Huber, T. et al. Coherent structural dynamics of a prototypical charge-density-wave-to-metal transition. *Phys. Rev. Lett.* **113**, 026401 (2014).
12. Porer, M. et al. Non-thermal separation of electronic and structural orders in a persisting charge density wave. *Nat. Mater.* **13**, 857–861 (2014).
13. Rettig, L. et al. Persistent order due to transiently enhanced nesting in an electronically excited charge density wave. *Nat. Commun.* **7**, 10459 (2016).
14. Monney, C. et al. Revealing the role of electrons and phonons in the ultrafast recovery of charge density wave correlations in 1T- TiSe$_2$. *Phys. Rev. B* **94**, 165165 (2016).
15. Yang, L. et al. Bypassing the structural bottleneck in the ultrafast melting of electronic order. *Phys. Rev. Lett.* **125**, 266402 (2020).
16. Tsuji, N., Eckstein, M. & Werner, P. Nonthermal antiferromagnetic order and nonequilibrium criticality in the hubbard model. *Phys. Rev. Lett.* **110**, 136404 (2013).
17. Stojchevska, L. et al. Ultrafast switching to a stable hidden quantum state in an electronic crystal. *Science* **344**, 177–180 (2014).
18. Zhang, J. et al. Cooperative photoinduced metastable phase control in strained manganite films. *Nat. Mater.* **15**, 956–960 (2016).
19. Gerasimenko, Y. A., Karpov, P., Vaskivskyi, I., Brazovskii, S. & Mihailovic, D. Intertwined chiral charge orders and topological stabilization of the light-induced state of a prototypical transition metal dichalcogenide. *npj Quantum Mater.* **4**, 32 (2019).
20. Fausti, D. et al. Light-induced superconductivity in a stripe-ordered cuprate. *Science* **331**, 189–191 (2011).
21. Wandel, S. et al. Light-enhanced charge density wave coherence in a high-temperature superconductor. Preprint at https://arxiv.org/abs/2003.04224 (2020).
22. Kogar, A. et al. Light-induced charge density wave in LaTe$_3$. *Nat. Phys.* **16**, 159–163 (2020).
23. Beaud, P. et al. A time-dependent order parameter for ultrafast photoinduced phase transitions. *Nat. Mater.* **13**, 923–927 (2014).
24. Wall, S. et al. Ultrafast disordering of vanadium dimers in photoexcited VO$_2$. *Science* **362**, 572–576 (2018).
25. Nicholson, C. W. et al. Beyond the molecular movie: dynamics of bands and bonds during a photoinduced phase transition. *Science* **362**, 821–825 (2018).
26. Neugebauer, M. J. et al. Optical control of vibrational coherence triggered by an ultrafast phase transition. *Phys. Rev. B* **99**, 220302 (2019).
27. Dolgirev, P. E. et al. Amplitude dynamics of the charge density wave in LaTe$_3$: theoretical description of pump-probe experiments. *Phys. Rev. B* **101**, 054203 (2020).
28. Mitrano, M. et al. Possible light-induced superconductivity in K$_3$C$_{60}$ at high temperature. *Nature* **530**, 461–464 (2016).
29. Singer, A. et al. Photoinduced enhancement of the charge density wave amplitude. *Phys. Rev. Lett.* **117**, 056401 (2016).
30. Nicholson, C. et al. Ultrafast spin density wave transition in chromium governed by thermalized electron gas. *Phys. Rev. Lett.* **117**, 136801 (2016).
31. Cavalleri, A. Photo-induced superconductivity. *Contemp. Phys.* **59**, 31–46 (2018).
32. Tengdin, P. et al. Critical behavior within 20 fs drives the out-of-equilibrium laser-induced magnetic phase transition in nickel. *Sci. Adv.* **4**, 9744 (2018).
33. Endres, M. et al. The 'higgs' amplitude mode at the two-dimensional superfluid/mott insulator transition. *Nature* **487**, 454–458 (2012).
34. Matsunaga, R. et al. Higgs amplitude mode in the BCS superconductors Nb$_{1-x}$Ti$_x$N induced by terahertz pulse excitation. *Phys. Rev. Lett.* **111**, 057002 (2013).
35. Torchinsky, D. H., Mahmood, F., Bollinger, A. T., Božović, I. & Gedik, N. Fluctuating charge-density waves in a cuprate superconductor. *Nat. Mater.* **12**, 387–391 (2013).
36. Yusupov, R., Mertelj, T., Chu, J.-H., Fisher, I. & Mihailovic, D. Single-particle and collective mode couplings associated with 1-and 2-directional electronic ordering in metallic RTe$_3$ (R= Ho, Dy, Tb). *Phys. Rev. Lett.* **101**, 246402 (2008).
37. Trigo, M. et al. Coherent order parameter dynamics in SmTe$_3$. *Phys. Rev. B* **99**, 104111 (2019).
38. Ru, N. & Fisher, I. Thermodynamic and transport properties of YTe$_3$, LaTe$_3$, and CeTe$_3$. *Phys. Rev. B* **73**, 033101 (2006).
39. Brouet, V. et al. Angle-resolved photoemission study of the evolution of band structure and charge density wave properties in RTe$_3$ (R= Y, La, Ce, Sm, Gd, Tb, and Dy). *Phys. Rev. B* **77**, 235104 (2008).
40. Ru, N. et al. Effect of chemical pressure on the charge density wave transition in rare-earth tritellurides RTe$_3$. *Phys. Rev. B* **77**, 035114 (2008).
41. Maschek, M. et al. Wave-vector-dependent electron-phonon coupling and the charge-density-wave transition in TbTe$_3$. *Phys. Rev. B* **91**, 235146 (2015).

42. Laverock, J. et al. Fermi surface nesting and charge-density wave formation in rare-earth tritellurides. *Phys. Rev. B* **71**, 085114 (2005).

43. Overhauser, A. Observability of charge-density waves by neutron diffraction. *Phys. Rev. B* **3**, 3173 (1971).

44. Voit, J. et al. Electronic structure of solids with competing periodic potentials. *Science* **290**, 501–503 (2000).

45. Rettig, L., Chu, J.-H., Fisher, I., Bovensiepen, U. & Wolf, M. Coherent dynamics of the charge density wave gap in tritellurides. *Faraday Discus.* **171**, 299–310 (2014).

46. Vogelgesang, S. et al. Phase ordering of charge density waves traced by ultrafast low-energy electron diffraction. *Nat. Phys.* **14**, 184–190 (2018).

47. Zong, A. et al. Evidence for topological defects in a photoinduced phase transition. *Nat. Phys.* **15**, 27–31 (2019).

48. Trigo, M. et al. Ultrafast formation of domain walls of a charge density wave in SmTe$_3$. *Phys. Rev. B* **103**, 054109 (2021).

49. Yusupov, R. et al. Coherent dynamics of macroscopic electronic order through a symmetry breaking transition. *Nat. Phys.* **6**, 681–684 (2010).

50. Schaefer, H., Kabanov, V. V. & Demsar, J. Collective modes in quasi-one-dimensional charge-density wave systems probed by femtosecond time-resolved optical studies. *Phys. Rev. B* **89**, 045106 (2014).

51. Perfetti, L. et al. Ultrafast electron relaxation in superconducting Bi$_2$Sr$_2$CaCu$_2$O$_{8+\delta}$ by time-resolved photoelectron spectroscopy. *Phys. Rev. Lett.* **99**, 197001 (2007).

52. Johnson, S. L. et al. Watching ultrafast responses of structure and magnetism in condensed matter with momentum-resolved probes. *Struct. Dyn.* **4**, 061506 (2017).

53. Zong, A. et al. Dynamical slowing-down in an ultrafast photoinduced phase transition. *Phys. Rev. Lett.* **123**, 097601 (2019).

54. Arguello, C. et al. Visualizing the charge density wave transition in 2H-NbSe$_2$ in real space. *Phys. Rev. B* **89**, 235115 (2014).

55. Fang, A., Straquadine, J. A., Fisher, I. R., Kivelson, S. A. & Kapitulnik, A. Disorder-induced suppression of charge density wave order: STM study of Pd-intercalated ErTe$_3$. *Phys. Rev. B* **100**, 235446 (2019).

56. Waldecker, L., Bertoni, R., Ernstorfer, R. & Vorberger, J. Electron-phonon coupling and energy flow in a simple metal beyond the two-temperature approximation. *Phys. Rev. X* **6**, 021003 (2016).

57. Yamaji, K. First-order phase transition boundary between superconducting and SDW phases in the bechgaard salts. *J. Phys. Soc. Jpn* **52**, 1361–1372 (1983).

58. Vaskivskyi, I. et al. Controlling the metal-to-insulator relaxation of the metastable hidden quantum state in 1T-TaS$_2$. *Sci. Adv.* **1**, e1500168 (2015).

59. Puppin, M. et al. Time-and angle-resolved photoemission spectroscopy of solids in the extreme ultraviolet at 500 kHz repetition rate. *Rev. Sci. Instrum.* **90**, 023104 (2019).

60. Ingold, G. et al. Technical report: Femto: A sub-ps tunable hard x-ray undulator source for laser/x-ray pump-probe experiments at the sls. *Synchrotron Radiat. News* **20**, 35–39 (2007).

61. Tao, Z., Han, T.-R. T. & Ruan, C.-Y. Anisotropic electron-phonon coupling investigated by ultrafast electron crystallography: three-temperature model. *Phys. Rev. B* **87**, 235124 (2013).

62. Nicholson, C. W. et al. Excited-state band mapping and momentum-resolved ultrafast population dynamics in In/Si (111) nanowires investigated with XUV-based time-and angle-resolved photoemission spectroscopy. *Phys. Rev. B* **99**, 155107 (2019).

63. Storeck, G. et al. Structural dynamics of incommensurate charge-density waves tracked by ultrafast low-energy electron diffraction. *Struct. Dyn.* **7**, 034304 (2020).

64. Maklar, J. et al. Time- and angle-resolved photoemission spectroscopy data and time-resolved X-ray diffraction data of TbTe$_3$. *Zenodo* https://doi.org/10.5281/zenodo.4106272 (2020).

Author contributions

Y.W.W., L.R., M.Pu., C.W.N. and J.M. carried out the trARPES experiments; L.R., V.E., M.Po., J.R., D.L., M.K., M.S., E.A., S.L.J., P.B., G.I. and U.S. carried out the trXRD experiments; P.W. and I.R.F. provided the samples; J.M. analyzed the data with support from L.R.; J.M. wrote the manuscript with support from L.R., R.E. and M.W.; all authors commented on the paper.

Competing interests

The authors declare no competing interests.

Additional information

Supplementary information The online version contains supplementary material available at https://doi.org/10.1038/s41467-021-22778-w.

Correspondence and requests for materials should be addressed to J.M. or L.R.

Peer review information *Nature Communications* thanks the anonymous reviewers for their contribution to the peer review of this work. Peer reviewer reports are available.

Reprints and permission information is available at http://www.nature.com/reprints

Publisher's note Springer Nature remains neutral with regard to jurisdictional claims in published maps and institutional affiliations.

Supplementary Information for "Nonequilibrium Charge-Density-Wave Order Beyond the Thermal Limit"

J. Maklar[1,*], Y. W. Windsor[1], C. W. Nicholson[1,†], M. Puppin[1,‡], P. Walmsley[2,3], V. Esposito[3,4], M. Porer[4], J. Rittmann[4], D. Leuenberger[5], M. Kubli[6], M. Savoini[6], E. Abreu[6], S. L. Johnson[6], P. Beaud[4], G. Ingold[4], U. Staub[4], I. R. Fisher[2,3], R. Ernstorfer[1], M. Wolf[1], and L. Rettig[1,*]

[1] *Fritz-Haber-Institut der Max-Planck-Gesellschaft, Faradayweg 4-6, D-14195 Berlin, Germany*
[2] *Geballe Laboratory for Advanced Materials and Department of Applied Physics, Stanford University, CA 94305, USA*
[3] *Stanford Institute for Materials and Energy Sciences, SLAC National Accelerator Laboratory, 2575 Sand Hill Road, Menlo Park, CA 94025, USA*
[4] *Swiss Light Source, Paul Scherrer Institut, CH-5232 Villigen PSI, Switzerland*
[5] *Department of Physics, University of Zürich, CH-8057 Zürich, Switzerland*
[6] *Institute for Quantum Electronics, Physics Department, ETH Zürich, CH-8093 Zürich, Switzerland*
[*] *Correspondence should be addressed to J.M. (maklar@fhi-berlin.mpg.de) or L.R. (rettig@fhi-berlin.mpg.de)*
[†] *Current address: Department of Physics and Fribourg Center for Nanomaterials, University of Fribourg, Chemin du Musée 3, CH-1700 Fribourg, Switzerland*
[‡] *Current address: Laboratory of Ultrafast Spectroscopy, ISIC, Ecole Polytechnique Fédérale de Lausanne (EPFL), CH-1015 Lausanne, Switzerland*

March 17, 2021

Supplementary Figures
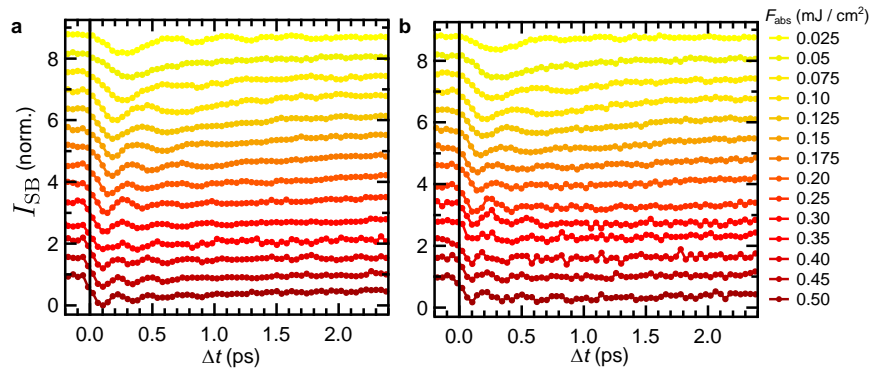
Supplementary Fig. 1: Shadow band intensity dynamics. Shadow band intensities extracted from (**a**) the nested (gapped) region of the FS, see box 2 in Fig. 2b, and (**b**) from the imperfectly nested (metallic) region, see box 3. Despite a slightly lower data quality in **b**, both shadow bands exhibit identical behaviour over the entire fluence range. The curves are vertically offset for clarity. For each curve, an intensity background extracted from a box slightly horizontally offset from the shadow band position is subtracted. Further, all curves are normalized by their respective intensities before excitation.
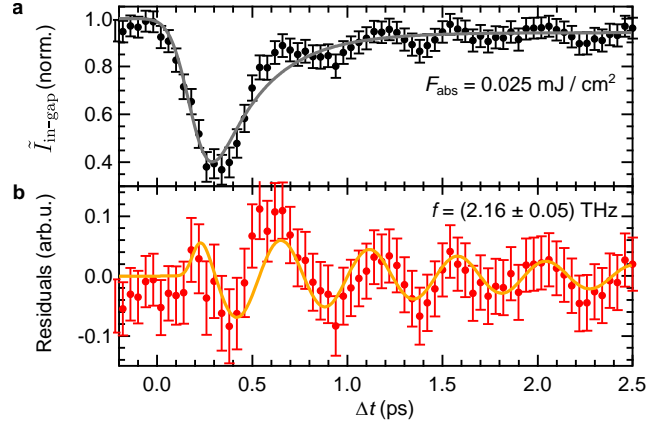
Supplementary Fig. 2: Electronic AM dynamics. (**a**) Time evolution of the inverted in-gap intensity after weak excitation. The grey line marks a double-exponential fit convolved with a Gaussian. (**b**) Fit residuals showing a pronounced amplitude mode in agreement with previous trARPES experiments[1,2], with a damped sinusoidal fit (orange curve). The error bars correspond to one standard deviation from electron counting statistics.
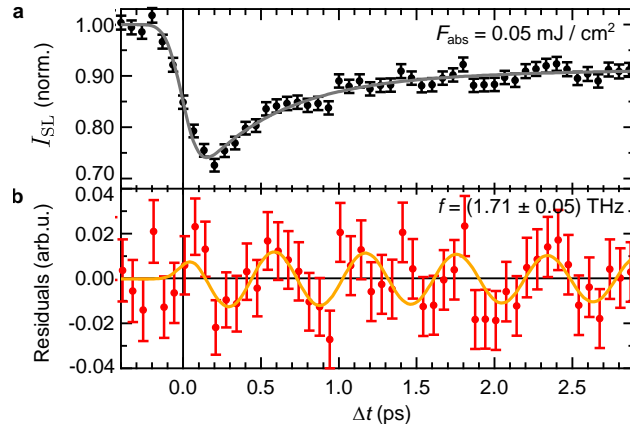
Supplementary Fig. 3: Structural AM dynamics. (**a**) Time evolution of the normalized $(2\,10\,1+q_{CDW})$ SL peak intensity after weak excitation. The grey line marks a double-exponential fit convolved with a Gaussian. The error bars correspond to one standard deviation from photon counting statistics. (**b**) The fit residuals indicate weak oscillations superimposed on the exponential decay, corresponding to a phonon mode that strongly couples to the CDW amplitude mode at $100\,K$, in agreement with previous optical and trXRD studies[3–6], with a damped sinusoidal fit (orange curve).
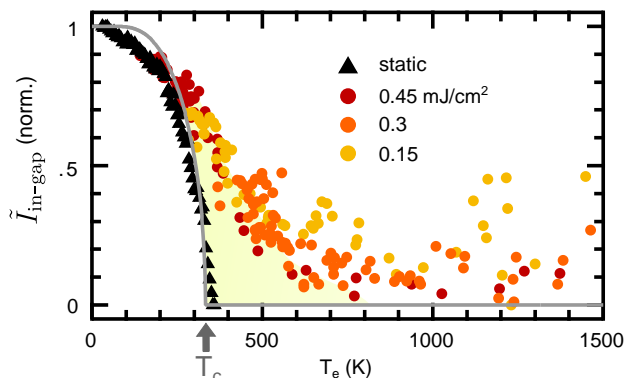
Supplementary Fig. 4: *T*-dependent CDW recovery dynamics. Inverted in-gap intensity of the dynamic CDW recovery versus extracted electronic temperatures for selected fluences. For reference, the static *T*-dependence is shown (black) with the BCS-like mean-field curve (grey). For clarity, the values of the dynamic traces for $t < 200\,\mathrm{fs}$ (initial CDW melting) are omitted. The dynamic curves follow a universal recovery behaviour over a wide range of fluences. The region of nonthermal CDW order above the thermal critical temperature is shaded yellow. Normalization of the dynamic traces according to Fig. 3b.

Supplementary Note 1: Details of the tdGL simulations of the electronic order parameter

To simulate the observed electron dynamics, we solve the following equation of motion based on the transient potential energy surface (Eq. 1)

$$\frac{\partial^2}{\partial t^2}\psi = \frac{\omega_{\mathrm{AM}}^2}{2}\Big(\big(1 - \eta(t)\big)\psi - \psi^3\Big) - \gamma\frac{\partial}{\partial t}\psi\,,\tag{3}$$

which yields the order parameter $\psi(t)$ used to simulate the diffracted intensities and the in-gap photoemission intensities. The initial conditions are chosen as

$$\psi = \sqrt{1 - \frac{T_{\mathrm{base}}}{T_{\mathrm{c}}}} \approx 0.84\,,$$

i.e., the static Ginzburg-Landau value corresponding to the temperature before excitation, and

$$\frac{\delta\psi}{\delta t} = 0\,.$$

We perform a global fit of the electronic in-gap dynamics $\tilde{I}_{\mathrm{in\text{-}gap}}(t)$ over the full accessible fluence range (Fig. 2f) with the free parameters damping γ and scaling factor s of the nonthermal critical temperature, see Eq. 2, while the remaining input parameters are fixed (Supplementary Table 1). In order to fit the inverted in-gap intensity, the order-parameter simulations are normalized. To model the transient potential energy surface, see Eq. 1, we use the extracted electronic temperatures in a parametrized form, see Supplementary Note 2. We find that the maximum electronic temperature yields a good description of the initial excited potential energy shape. This is evident from the saturation of $T_{\mathrm{e,max}}$ in the high-fluence regime (see Supplementary Fig. 7c) that is accompanied by an upper limit of the initial coherent modulation frequency of the electronic order parameter. This also implies that the potential energy surface does not directly scale with the absorbed fluence $\eta \not\propto F$.

We aim to define the fit parameters as simple as possible; however, we can not reproduce the experimental data over the entire fluence- and temporal range with a single global damping constant. While γ correctly captures the initial damped modulations, a constant damping results in the reappearance

of coherent oscillations in the high-fluence regime, when the potential transforms back from the high-symmetry to the double-well shape. To prevent this, we use an alternative global fit parameter $\gamma_{\rm rec}$ during the recovery ($> 2\,\mathrm{ps}$) in the high-fluence regime ($\geq 0.3\,\mathrm{mJ\ cm^{-2}}$). In real systems, dephasing prevents the reappearance of coherent oscillations during the recovery.

We account for the inhomogeneous excitation profile, corresponding to the pump and probe spot sizes (FWHM) of $\approx 230 \times 200\,\mathrm{\mu m^2}$ and $\approx 70 \times 60\,\mathrm{\mu m^2}$, respectively, by averaging over multiple simulations with varying fluences (up to $\pm 7.5\,\%$ around the centre value). Finally, to account for the temporal resolution of the experiment, the simulations are convolved with a Gaussian (FWHM $= 35\,\mathrm{fs}$).

Supplementary Table 1: Parameters of the tdGL simulations

Parameter	Value	Physical meaning
$\omega_{\rm AM}/2\pi$	$2.2\ \mathrm{THz}^3$	AM at $100\,\mathrm{K}$
γ	$4.4\ \mathrm{THz}$	Damping
$\gamma_{\rm rec}$	$11.3\ \mathrm{THz}$	Damping during the recovery $> 2\,\mathrm{ps}$ in the overshoot regime
$T_{\rm c}$	$336\ \mathrm{K}^7$	Critical temperature of the CDW
s	1.22	Scaling factor of the rescaled critical temperature $T_{\rm c}^*$
$\tau_{\rm ph-ph}$	$2.2\,\mathrm{ps}^8$	Decay constant of the rescaled critical temperature $T_{\rm c}^*$

As illustrated in Fig. 3b, the transient CDW recovery strongly deviates from static (thermal) behaviour, which necessitates the introduction of a transiently increased critical temperature T_c^* in the tdGL simulations. To highlight the requirement of a transiently increased T_c^*, we perform additional simulations employing the constant equilibrium critical temperature $T_{\rm c}$, while keeping the remaining parameters fixed as described above. As Supplementary Fig. 5 shows, this does not reproduce the experimental data, as (i) the simulated oscillation frequencies are strongly overestimated due to the increased slope of the underlying potential energy landscape (determined by $\eta(t)$) and (ii) the simulated recovery sets in only at $T_{\rm e} < T_c$ – at a significant delay with respect to the experimental data.
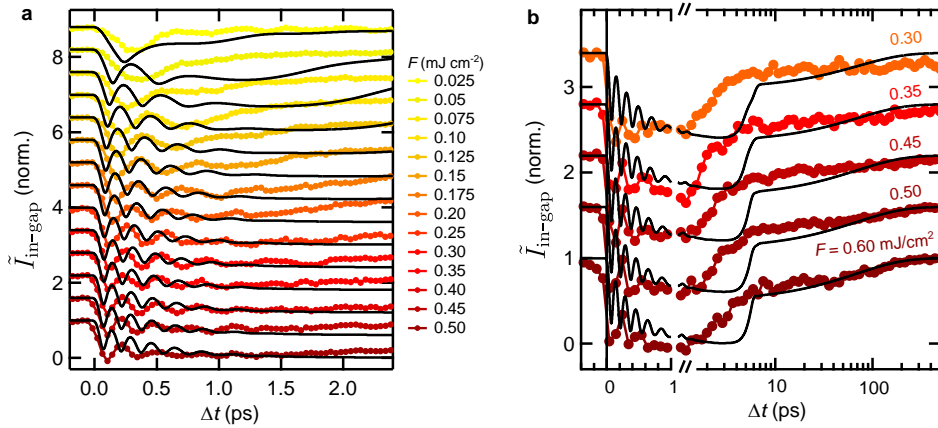

Supplementary Fig. 5: tdGL simulations using the constant equilibrium critical temperature $T_{\rm c}$. (**a**) Experimental data analog to Fig. 2f and (**b**) to Fig. 3a of the main manuscript. The tdGL simulations are performed using the parameters as described above, however, using a fixed critical temperature of $T_{\rm c} = 336\,\mathrm{K}$.

Supplementary Note 2: Parametrization of the electronic temperatures

In the tdGL simulations, the electronic temperature $T_e(t)$ enters as an input parameter that determines the underlying potential shape. Thus, we extract the transient electronic temperatures from Fermi-Dirac fits of the quasiparticle energy distribution of the metallic region of the FS[8,9], as these values are more reliable than the approximation by the 3TM. For each dataset, the energy resolution ($\Delta E \approx 175$ meV) is determined from a fit to energy distribution curves (EDCs) before the arrival of the pump pulse, fixing the base temperature to $T_{base} = 100$ K. Then, the electronic temperature is extracted for varying delays, keeping the energy resolution fixed while using the position of the Fermi level and temperature as free fit parameters. Exemplary fits are shown in Supplementary Fig. 6a. A deviation from a thermal distribution appears for EDCs close to temporal pump-probe overlap, resulting in a large standard deviation of the extracted temperatures. Figure 6b depicts the electronic temperature evolution in the high-fluence regime. The relaxation of T_e features two distinct timescales, which we assign to the initial energy transfer from the electrons to specific optical phonons and a subsequent cooling of the thermalized system via diffusion.
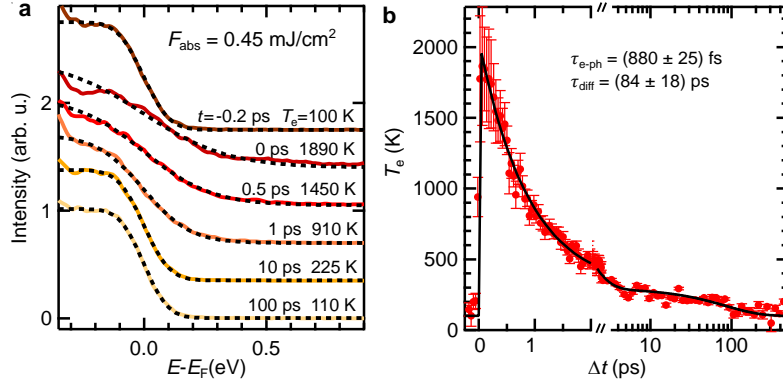

Supplementary Fig. 6: Time-dependent Fermi-Dirac fits. (a) EDCs extracted from the metallic region of the FS with Fermi-Dirac fits for selected pump-probe delays. (b) Extracted electronic temperature as function of delay with biexponential decay fit (black curve). One standard deviation of the temperature fits are given as uncertainty.

This fitting routine has been performed for all measured fluences in order to parametrize the fluence and time dependence of T_e, shown in Supplementary Fig. 7. The temporal evolution is approximated by a double-exponential decay:

$$T_e(t, F) = T_{base} + H(t) \cdot T_{sat}(F) \left[A_0 \cdot \exp(-t/\tau_{e\text{-}ph}) + (1 - A_0) \cdot \exp(-t/\tau_{diff}) \right] \qquad (4)$$

with Heaviside step function $H(t)$, the excitation-dependent temperature increase T_{sat} discussed below, and the amplitude ratio between the fast ($\tau_{e\text{-}ph}$) and slow (τ_{diff}) decay components. The values of the temperature parametrization are listed in Supplementary Table 2.

In the regime of strong excitation, the maximum electronic temperatures saturate at $T_{e,max}(t \approx 0\,\text{fs}) \approx 2300$ K (see Supplementary Fig. 7c). While the electronic system has not fully thermalized close to pump-probe overlap (and therefore electronic temperatures are ill-defined), we find that this saturation trend is also evident at later pump-probe delays. This saturation effect can be either due to a highly nonlinear electronic heat capacity or due to photobleaching. As the FS of TbTe$_3$ consists of metallic and CDW-gapped regions, the electronic heat capacity is expected to follow a linear metal-like temperature dependence with an additional nonlinear increase resulting from the redistribution of spectral weight due
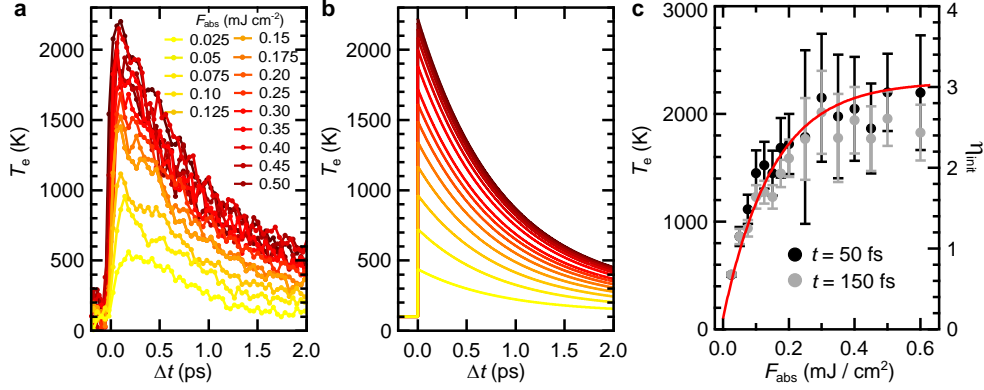
Supplementary Fig. 7: Electronic temperature parametrization. (**a**) Extracted temporal evolution of electronic temperatures and (**b**) parametrization by Supplementary Eq. 4. (**c**) Extracted electronic temperatures close to temporal pump-probe overlap versus fluence. The saturation model of the maximum electronic temperatures (Supplementary Eq. 6) is shown in red. One standard deviation of the temperature fits are given as uncertainty.

to the phase transition[8,10]. Furthermore, our observations agree with the saturation plateau of excited quasiparticle intensity in the related compound $LaTe_3$[11]. Such a fluence saturation trend of the electronic excitation level has also been observed in Blue Bronze[12].

We model the fluence-dependence of the temperature saturation as

$$T_{sat}(F) = T_0 \cdot [1 - \exp(-F/f)], \tag{5}$$

with the upper temperature limit T_0 and the fluence scaling factor f. The maximum electronic temperature is therefore given by

$$T_{e,max}(F) = T_{base} + T_{sat}. \tag{6}$$

Supplementary Table 2: Parametrization values of the electronic temperature.

Parameter	Value	Physical meaning
T_{base}	100 K	Base temperature of the sample
T_0	2200 K	Temperature limit of the saturation model
f	0.15 mJ cm^{-2}	Fluence scaling factor
$\tau_{e\text{-}ph}$	0.85 ps	Fast decay constant of the electronic temperature evolution
τ_{diff}	85 ps	Slow decay constant of the electronic temperature evolution
A_0	0.92	Amplitude ratio between the two components of the biexponential decay

Supplementary Note 3: tdGL simulations of the structural order parameter

To simulate the trXRD measurements of the SL peak intensity, we have to account for the contribution of sub-surface layers of varying excitation densities due to the finite pump and probe beam penetration depths. We introduce a layered model, in which the tdGL equation of motion is solved for each individual layer. The diffracted X-ray beam corresponding to the (2 10 1+q_{CDW}) SL reflection leaves the sample

6

at an exit angle of $\theta \approx 35°$. As the lateral CDW correlation length L_{coh}[7] is significantly larger than the effective penetration depth of the X-ray field $L_{\mathrm{coh}} \gg 2\delta_{\text{X-ray}}/\sin\theta$, interference of different layers has to be considered[13,14]. Thus, the total intensity is given by the coherent sum of all layers j of thickness d

$$I_{\mathrm{SL}}(t) \propto \left(\sum_{j=0}^{\infty} \exp\left(-jd/2\delta_{\text{X-ray}}\right) \cdot \psi_j(t) \right)^2, \tag{7}$$

whereas the first term weights the contribution of each layer according to the X-ray penetration depth $\delta_{\text{X-ray}} = 25\,\mathrm{nm}$. The initial excitation level of the first layer $\eta_{0,\mathrm{init}}$ is calculated from the fluence-to-electronic-temperature calibration obtained from the trARPES data (see Supplementary Note 2). The attenuation of the excitation of burried layers is given by Lambert-Beer's law $\eta_{j,\mathrm{init}} = \eta_{0,\mathrm{init}} \cdot \exp(-jd/\delta_{\mathrm{pump}})$, with the penetration depth of the optical pulses $\delta_{\mathrm{pump}} = 25\,\mathrm{nm}$. We choose a layer thickness of $d = 1\,\mathrm{nm}$ and sum the 250 topmost layers. To account for the temporal resolution of the experimental setup, the simulated intensity is convolved with a Gaussian (FWHM of 160 fs). In the regime of very weak excitation, the introduced model leads to artifacts, as the rescaling of T_c^* causes an initial increase of $\psi(t)$ in cases where the electronic temperature barely increases. To avoid these simulation artifacts from buried layers at very low excitation densities, the order parameter $\psi_j(t)$ of layers j with excitation levels $\eta_{j,\mathrm{init}} < 0.25$ is fixed at the pre-excitation value $\psi_j(t < 0)$.

As we do not observe clear oscillations of I_{SL} upon strong excitation, we do not include the trXRD data in the global fitting procedure. Rather, we apply the parameters of the simulations of the electronic order parameter to the layered model. In agreement with previous studies, we find that the dominant oscillatory component of the SL peak intensity after weak excitation is a $\approx 1.7\,\mathrm{THz}$ mode[4,6]. As the AM softens upon cooling, it crosses the energy of this additional mode, leading to an anti-crossing behaviour. Due to their coupling, this phonon mode appears at the same wave vector as the CDW[3,5], see Supplementary Fig. 3. Thus, we use $\omega_{\mathrm{AM}} = 1.7\,\mathrm{THz}$ to simulate $|\psi_s|$. Further, we omit the averaging over varying fluences, used in the simulations of the electronic order parameter. The remaining parameters are adopted from Supplementary Note 1.

As discussed in the main text, surface steps may lead to unexcited sample areas. Therefore, a SL background persists even after strong excitation. To account for this, we rescale all structural intensity simulations by a global factor according to the maximum suppression of I_{SL} at the highest fluences.

This layered model captures all main experimental features of I_{SL}, see Fig. 2h. The absence of the oscillatory component in the high-fluence regime is well reproduced by the simulations, and results from the limited temporal resolution and the superposition of layers with varying excitation densities. Further, the absence of a recovery after strong excitation for several ps is in agreement with the simulations, and results from a destructive interference of the contributions of different layers with opposite sign of ψ, corresponding to opposite sides of the underlying potential[15]. In the low-fluence regime, the absolute intensities slightly deviate from the simulations. The absorbed fluence (determining the initial electronic temperature) is a highly sensitive input parameter of this model. Minor deviations between the fluence calibration of the trARPES and the trXRD setup have a major impact on the simulations. In addition, small uncertainties of the angle of incidence of the X-ray beam affect the penetration depth, a further sensitive parameter of this model.

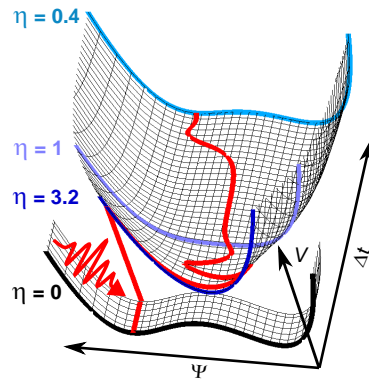# Supplementary Note 4: Critical slowing-down of the CDW melting and recovery

Critical slowing-down is a ubiquitous signature of phase transitions close to equilibrium[16], and can also occur in a dynamical setting upon perturbation[17]. For several CDW systems, a dynamical slowing-down of the CDW melting after optical excitation in the regime of the threshold fluence has been observed[11,18]. Here, we present a further instance of a dynamical slowing-down, which we discuss within the tdGL framework.

First, we utilize the tdGL formalism to study t_{melt}, i.e., the CDW melting time, as function of excitation density, shown in Supplementary Fig. 8b. For clarity, we turn off the relaxation of the potential energy surface after excitation ($\eta = $ const), fix the critical temperature T_c^*, and suppress damping. In the regime of weak perturbation, the first minimum appears at half the period of the AM. With increasing fluence, the CDW melting time increases and finally diverges at $\eta = 0.5$. In the divergent case, see Supplementary Fig. 8a, the energy gain of the excitation is just enough so that the order parameter approaches the local maximum $|\psi| \approx 0$. Close to this metastable point, the potential energy surface is fairly flat, which leads to a dynamical slowing-down. However, when using realistic simulation parameters, such as a relaxing potential energy surface, and taking into account an inhomogeneous excitation profile, the divergence is strongly reduced, and the simulated melting time agrees with the experimental data (see Supplementary Fig. 8c).
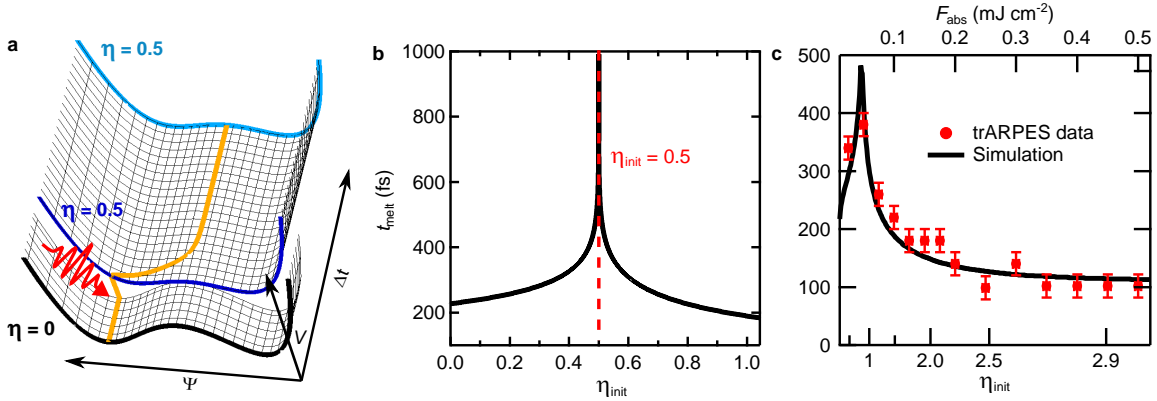
Supplementary Fig. 8: Dynamic slowing-down of the CDW melting. (**a**) Transient potential and simulated order parameter (orange line) upon excitation corresponding to $\eta = 0.5$. (**b**) Time to reach the first local minimum as function of initial excitation η_{init}. Simulation parameters of a and b: $\gamma = 0\,\mathrm{THz}$, $T_c^* = \mathrm{const} = 336\,\mathrm{K}$ and $\tau_{e\text{-}ph} = \tau_{diff} = \infty$. (**c**) Initial minima of the inverted in-gap intensity, see Fig. 2f, versus absorbed fluence and initial excitation η_{init}. Results of the tdGL simulations with realistic model parameters (see Supplementary Note 1) are shown in black. The error bars of the experimentally extracted melting times represent the temporal width (FWHM) of the XUV probe pulses.

A further dynamical slowing-down can occur during the recovery of the CDW. At specific fluences, when $|\psi| \approx 0$ and $\delta\psi/\delta t \approx 0$ at the same time as the potential regains the double-well shape ($\eta = 1$), the order parameter gets frozen, illustrated in Supplementary Fig. 9. Due to the weak curvature in the vicinity of $|\psi| = 0$, the system is trapped in a metallic phase, despite an emerging double-well potential. However, this divergence is difficult to observe experimentally, as it occurs at narrow fluence windows, and is, similar to the slowing-down of the CDW melting, suppressed by crystal defects, coupling to other phonon modes and an inhomogeneous excitation profile. This critical behaviour leads to a delayed onset of CDW recovery in the simulations as compared to the electronic CDW dynamics for certain fluences, see Fig. 2f (curve $F = 0.1\,\mathrm{mJ\ cm^{-2}}$) and Fig. 3a.

Supplementary Fig. 9: Dynamic slowing-down of the CDW recovery. Transient potential and simulated order-parameter pathway of the dynamical slowing-down during the CDW recovery. For specific excitation conditions, the order-parameter dynamics critically slow down during recovery of the CDW double-well potential. Despite the appearance of the double-well shape for $\eta < 1$ (purple line), the order parameter can get trapped at the metastable point $|\psi| \approx 0$, before it relaxes into one of the global minima. Model parameters are chosen analogous to Supplementary Note 1. To demonstrate a pronounced slowing-down, the averaging over multiple curves with varying fluences is omitted.

Supplementary References

1. Schmitt, F. *et al.* Transient electronic structure and melting of a charge density wave in TbTe$_3$. *Science* **321,** 1649–1652 (2008).

2. Schmitt, F. *et al.* Ultrafast electron dynamics in the charge density wave material TbTe$_3$. *New Journal of Physics* **13,** 063022 (2011).

3. Yusupov, R., Mertelj, T., Chu, J.-H., Fisher, I. & Mihailovic, D. Single-Particle and Collective Mode Couplings Associated with 1-and 2-Directional Electronic Ordering in Metallic RTe$_3$ (R= Ho, Dy, Tb). *Physical review letters* **101,** 246402 (2008).

4. Moore, R. *et al.* Ultrafast resonant soft x-ray diffraction dynamics of the charge density wave in TbTe$_3$. *Physical Review B* **93,** 024304 (2016).

5. Maschek, M. *et al.* Competing soft phonon modes at the charge-density-wave transitions in DyT e 3. *Physical Review B* **98,** 094304 (2018).

6. Trigo, M. *et al.* Coherent order parameter dynamics in SmTe$_3$. *Physical Review B* **99,** 104111 (2019).

7. Ru, N. *et al.* Effect of chemical pressure on the charge density wave transition in rare-earth tritel-lurides RTe$_3$. *Physical Review B* **77,** 035114 (2008).

8. Dolgirev, P. E. *et al.* Amplitude dynamics of the charge density wave in LaTe$_3$: Theoretical description of pump-probe experiments. *Physical Review B* **101,** 054203 (2020).

9. Wang, Y. *et al.* Measurement of intrinsic Dirac fermion cooling on the surface of the topological insulator Bi$_2$Se$_3$ using time-resolved and angle-resolved photoemission spectroscopy. *Physical Review Letters* **109,** 127401 (2012).

10. Lin, Z., Zhigilei, L. V. & Celli, V. Electron-phonon coupling and electron heat capacity of metals under conditions of strong electron-phonon nonequilibrium. *Physical Review B* **77,** 075133 (2008).

11. Zong, A. *et al.* Dynamical slowing-down in an ultrafast photoinduced phase transition. *Physical review letters* **123,** 097601 (2019).

12. Neugebauer, M. J. *et al.* Optical control of vibrational coherence triggered by an ultrafast phase transition. *Physical Review B* **99,** 220302 (2019).

13. Beaud, P. *et al.* A time-dependent order parameter for ultrafast photoinduced phase transitions. *Nature materials* **13,** 923–927 (2014).

14. Rettig, L. *et al.* Itinerant and localized magnetization dynamics in antiferromagnetic Ho. *Physical review letters* **116,** 257202 (2016).

15. Trigo, M. *et al.* Ultrafast formation of domain walls of a charge density wave in SmTe$_3$. *Physical Review B* **103,** 054109 (2021).

16. Goldenfeld, N. *Lectures on phase transitions and the renormalization group* (CRC Press, 1992).

17. Dolgirev, P. E., Michael, M. H., Zong, A., Gedik, N. & Demler, E. Self-similar dynamics of order parameter fluctuations in pump-probe experiments. *Physical Review B* **101,** 174306 (2020).

18. Tomeljak, A. *et al.* Dynamics of photoinduced charge-density-wave to metal phase transition in K$_{0.3}$MoO$_3$. *Physical review letters* **102,** 066404 (2009).

4.3 Phys. Rev. Lett. 128, 026406 (2022): Coherent modulation of quasiparticle scattering rates in a photoexcited charge-density-wave system

J. Maklar, M. Schüler, Y. W. Windsor, C. W. Nicholson, M. Puppin, P. Walmsley, I. R. Fisher, M. Wolf, R. Ernstorfer, M. A. Sentef, and L. Rettig

The publication Maklar et al., Phys. Rev. Lett. 128, 026406 (2022) presents a combined experimental and theoretical investigation on the impact of a coherent CDW excitation on the relaxation rate of hot photocarriers in the CDW compound $TbTe_3$ upon optical excitation. The associated supplementary information is reprinted below the main article. The associated raw data is publicly available at the Zenodo data repository, doi 10.5281/zenodo.4106272.

Author contributions

Y.W.W., L.R., M.P. and C.W.N. carried out the trARPES experiments; P.W. and I.R.F. provided the samples; **J.M.** analyzed the data; M.Sc. performed the simulations with guidance from M.Se.; **J.M.** and M.Sc. wrote the manuscript with support from L.R. and M.Se.; M.W., R.E. and L.R. provided the research infrastructure; all authors commented on the paper.

Coherent Modulation of Quasiparticle Scattering Rates in a Photoexcited Charge-Density-Wave System

J. Maklar[1], M. Schüler[2], Y. W. Windsor[1], C. W. Nicholson[1,*], M. Puppin,[1,†] P. Walmsley,[2,3]
I. R. Fisher[2,3], M. Wolf,[1] R. Ernstorfer[1,4], M. A. Sentef[5], and L. Rettig[1,‡]

[1]*Fritz-Haber-Institut der Max-Planck-Gesellschaft, Faradayweg 4-6, 14195 Berlin, Germany*
[2]*Stanford Institute for Materials and Energy Sciences, SLAC National Accelerator Laboratory,
2575 Sand Hill Road, Menlo Park, California 94025, USA*
[3]*Geballe Laboratory for Advanced Materials and Department of Applied Physics, Stanford University,
Stanford, California 94305, USA*
[4]*Institut für Optik und Atomare Physik, Technische Universität Berlin, Straße des 17. Juni 135, 10623 Berlin, Germany*
[5]*Max Planck Institute for the Structure and Dynamics of Matter, Luruper Chaussee 149, 22761 Hamburg, Germany*

We present a complementary experimental and theoretical investigation of relaxation dynamics in the charge-density-wave (CDW) system $TbTe_3$ after ultrafast optical excitation. Using time- and angle-resolved photoemission spectroscopy, we observe an unusual transient modulation of the relaxation rates of excited photocarriers. A detailed analysis of the electron self-energy based on a nonequilibrium Green's function formalism reveals that the phase space of electron-electron scattering is critically modulated by the photoinduced collective CDW excitation, providing an intuitive microscopic understanding of the observed dynamics and revealing the impact of the electronic band structure on the self-energy.

A defining feature of metals is that they feature electronic states around the Fermi level E_F, allowing for low-energy excitations and thus enabling efficient electronic transport. A central quantity that encodes such quasiparticle excitations is the electron self-energy $\Sigma(E, \boldsymbol{k})$, which describes all interactions with the electronic quasiparticle at energy E and momentum $\boldsymbol{k}$. In simple metals, the self-energy is dominated by electron-electron (e-e) scattering and is well-described by Fermi-liquid theory [1]. However, in more complex materials, an interplay between e-e, electron-phonon (e-ph), electron-impurity scattering, and the electronic band structure, governing the available phase space for particular quasiparticle excitations, has to be considered [2]. Thus, for most materials, a quantitative theoretical treatment proves challenging [3,4], and a detailed understanding of the self-energy—essential for disentangling the intricate interactions in complex solids—is still missing.

A key technique to investigate quasiparticle interactions in solids directly on their intrinsic timescales is time- and angle-resolved photoemission spectroscopy (trARPES) [5], in which a femtosecond (fs) optical pump pulse generates

an excited-carrier population. Probing the transient quasiparticle band structure by a time-delayed UV/XUV pulse during the subsequent recovery elucidates charge- and energy redistribution processes and allows disentangling competing contributions to the self-energy [6–13]. Additionally, optical excitation allows for transient manipulation of specific material properties with high selectivity by tailoring the excitation wavelength, polarization, pulse energy, and length. Prominent examples of this rapidly growing research field include photostabilization of superconductivity [14–16], dynamical modification of the band structure due to the formation of photon-dressed states [17,18], and stabilization of nonequilibrium metastable states [19–21]. However, the microscopic processes underlying such transitions and the properties of light-induced states often lack a clear understanding. Intriguingly, time-domain studies offer a natural route to access the transient quasiparticle interactions during the optical control of condensed matter properties, providing an understanding on the microscopic level of the self-energy. As most (photoinduced) phase transitions in complex solids involve an insulator-to-metal transition, it is of special interest how a modification of the low-energy electronic states impacts the electron self-energy and which particular scattering channels are affected.

An ideal testbed to apply this approach of studying quasiparticle interactions upon optical control are charge density waves (CDWs). This ubiquitous symmetry-broken ground state is characterized by a periodic charge- and
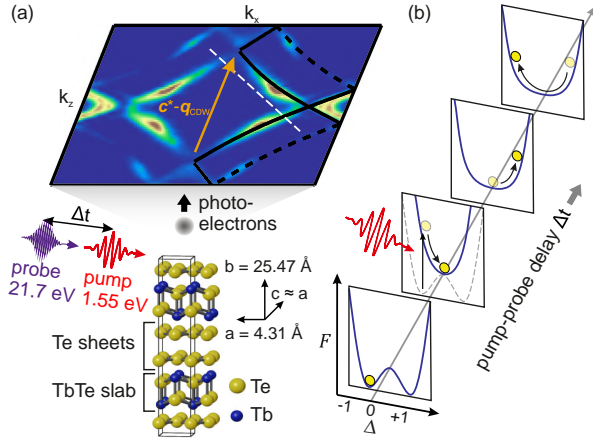
FIG. 1. Experimental scheme. (a) Top: Symmetrized FS of TbTe$_3$ ($T = 100$ K) with tight binding calculations of main (solid) and 3D-backfolded (dashed) bands. Spectral weight along the segments connected by the nesting wave vector $\mathbf{c}^* - \mathbf{q}_{\mathrm{CDW}}$ is strongly reduced. The white dashed line marks the momentum cut discussed in Fig. 2. Bottom: Quasi-2D atomic structure of TbTe$_3$ consisting of TbTe slabs and Te sheets. By convention, the in-plane crystal directions are along the a and c (k_x and k_z) axes. (b) Schematic PES as a function of pump-probe delay after photoexcitation. The yellow circle indicates the system's order parameter, a metric for the degree of symmetry-breaking of the CDW-to-metal transition, with $|\Delta| = 0$ in the metallic and $0 < |\Delta| \leq 1$ in the CDW phase. Photoexcitation transforms the ground-state double-well potential into a high-symmetry state, launching an oscillation between the metallic and CDW phase.

lattice superstructure that opens up an electronic energy gap at E_F. Photoexcitation allows manipulating the system's underlying potential energy surface (PES), which triggers a transient melting of the CDW, i.e., a photoinduced insulator-to-metal transition [22], and thus allows studying the impact of the low-energy band structure on the self-energy.

Here, we use trARPES to investigate the electron dynamics of a prototypical CDW compound of the rare-earth tritelluride family, TbTe$_3$, after ultrafast near-infrared excitation, as illustrated in Fig. 1(a). In this material class, strong photoexcitation transforms the ground-state double-well PES to a single-well shape, sketched in Fig. 1(b). This initiates a melting of the CDW, as the system relaxes towards the new minimum corresponding to the metallic phase. However, for sufficiently strong excitation, the system overshoots across the minimum to the other side of the potential, leading to a reemergence of the CDW, followed by several damped oscillation cycles between metallic and CDW order [23–25], evident from a transient modulation of the CDW energy gap [26]. Besides the collective CDW excitation, we track the photocarrier population of high-energy states and discover a concurrent oscillation of scattering rates at the frequency of the CDW modulation. We find that relaxation of hot photocarriers

accelerates when the system is in the metallic phase and slows down when the CDW gap reopens. To understand the underlying microscopic scattering processes, we employ a time-dependent nonequilibrium Green's function formalism (td-NEGF) [27–29], which reveals that the CDW gap opening critically reduces the phase space of e-e scattering. Additional simulations taking into account e-ph coupling demonstrate that phonon scattering remains unaffected by the CDW gap modulation in the examined energy range.

We perform trARPES measurements on single crystals of TbTe$_3$ as described earlier [26]. The setup includes a tabletop fs XUV source ($h\nu_{\mathrm{probe}} = 21.7$ eV) with a synchronized optical pump laser ($h\nu_{\mathrm{pump}} = 1.55$ eV), using a hemispherical analyzer for photoelectron detection [30]. The ultimate time and energy resolutions are ∼35 fs and ∼150 meV, respectively. All measurements were carried out in $p < 1 \times 10^{-10}$ mbar and at $T = 100$ K, well below the transition temperature $T_c = 336$ K of the unidirectional CDW phase of TbTe$_3$ [31]. Note that in rare-earth tritellurides strongly wave-vector dependent e-ph coupling [32], in conjunction with a moderately well-nested Fermi surface (FS) [33], leads to a unidirectional CDW in which some parts of the FS become gapped while others remain metallic [34], see Fig. 1(a).

We investigate the electron dynamics after photoexcitation in the energy-momentum cut shown in Fig. 2(a). This allows us to simultaneously track the CDW energy gap $\Delta_{\mathrm{CDW}}(\Delta t)$ at E_F (red arrow), the replica bands (yellow arrow), and the population lifetimes of several distinct high-energy states that are transiently populated upon photoexcitation (regions of interest (ROIs) 1 and 2). As Figs. 2(b)–2(c) show, within 140 fs after optical excitation, the system undergoes a transition from the CDW to the metallic phase and the CDW gap closes. Concomitantly, the replica bands vanish, as their spectral weight is transferred back to the main bands. However, due to substantial perturbation of the PES, the system subsequently overshoots beyond the metallic phase, followed by several weakly damped oscillations between metallic and CDW order [schematic Fig. 1(b)], evinced by a transient modulation of the energy gap and replica band intensity [26].

To quantify the CDW dynamics, we estimate the transient energy gap Δ_{CDW} from the energy distribution curves (EDCs) shown in Fig. 2(c), using a leading-trailing edges approach, as discussed in the Supplemental Material [35]. The extracted transient Δ_{CDW} shown in Fig. 2(d) features damped oscillations at a frequency far beyond the intrinsic CDW amplitude mode—a signature of the overshoot regime [26]. Concomitantly, we track the transient photoemission intensities I at ∼1.2 eV [ROI 1 in Fig. 2(a)] and ∼0.8 eV above E_F (ROI 2), see Figs. 2(e)–2(f). Intriguingly, the dynamics of these excited-state populations display a clear correlation with the CDW dynamics, as they feature an exponential decay, on which weak oscillations are imprinted at the frequency of the collective
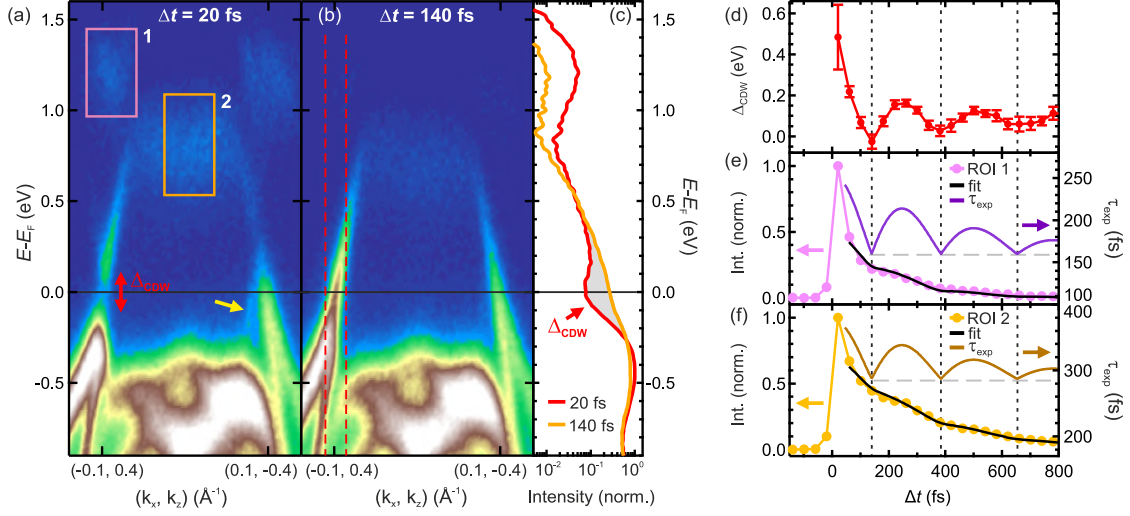
FIG. 2. Experimental band structure dynamics. (a) Energy-momentum cut along the dashed white line in Fig. 1(a) at $\Delta t = 20$ fs and (b) at $\Delta t = 140$ fs for an absorbed fluence of 0.45 mJ/cm². The yellow arrow indicates a replica band arising from the CDW potential. (c) EDCs of the momentum region marked by red lines in panel (b), featuring the CDW gap at E_F at $\Delta t = 20$ fs and subsequent metallization within $\Delta t = 140$ fs. (d) Extracted transient CDW energy gap with 1 standard deviation as uncertainty. Details of the analysis are presented in the Supplemental Material [35]. (e)–(f) Transient photoemission intensities of the ROIs indicated in panel (a) with a single-exponential decay fit (solid black line) using a time-dependent oscillatory lifetime τ_{exp} (right axis). The data point near $\Delta t = 0$ fs is excluded from the fit, as the electrons have not yet reached a thermal distribution, see Supplemental Material [35] for details. The dashed lines serve as guides to the eye.

CDW modulation. This oscillatory component directly reflects a modulation of the relaxation rate of the transient population [48]. In contrast, most previously investigated materials exhibit constant relaxation rates. We quantify the experimental relaxation rates employing a single-exponential decay fit, whereby we use a time-dependent $1/e$ lifetime $\tau_{\mathrm{exp}}(\Delta t)$ with a damped sinusoidal contribution to account for the observed modulations [49], which yields an excellent description of the experimental data. The deviation from a bare exponential decay is emphasized by the extracted lifetimes τ_{exp}, see Figs. 2(e)–2(f), as they feature considerable modulations that coincide with the CDW gap dynamics: Whenever the system becomes metallic ($\Delta_{\mathrm{CDW}} \sim 0$ eV), τ_{exp} reaches its minimum; the high-energy population relaxes faster. Conversely, when the CDW gap opens, the relaxation of the high-energy population slows down, indicated by local maxima of τ_{exp}. While it seems natural to assign the observed modulations to a transfer of spectral weight between main bands [captured by the ROIs in Fig. 2(a)] and replica bands (yellow arrow), this would yield the opposite effect: A reduction of intensity in the CDW phase due to spectral weight transfer from main to replica bands, and an intensity increase in the metallic phase due to spectral weight transfer back to the main bands [50]. Hence, a different explanation needs to be invoked.

To elucidate this dynamical modulation of the relaxation, a microscopic perspective onto the scattering channels is required. To this end we employ microscopic simulations based on the td-NEGF formalism, which allows for explicit treatment of e-e interaction and scattering effects beyond mean field. The relevant bands are captured by the tight binding (TB) model from Ref. [34]. We consider the lesser Green's function $G^<_{(m\nu),(m'\nu')}(\boldsymbol{k}; t, t') = i\langle \hat{c}^\dagger_{km'\nu'}(t)\hat{c}_{km\nu}(t')\rangle$, where m, m' corresponds to the $p_{x,z}$ orbitals and $\nu = -1, 0, +1$ to the nesting index with respect to the CDW wave vector $\mathbf{q}_{\mathrm{CDW}}$. Computing the Green's function provides a direct link to the trARPES intensity [29,51]:

$$I(\boldsymbol{k}, \omega, \Delta t) \propto \mathrm{Im} \sum_m \int dt \int dt'\, s(t)s(t')$$
$$\times e^{i\omega(t-t')} G^<_{(m0),(m0)}(\boldsymbol{k}; t, t'). \quad (1)$$

Here, ω is the binding energy and Δt denotes the pump-probe delay, which enters the shape functions $s(t)$. While the inequivalence of single-particle and population lifetimes prohibits a direct assignment of experimental relaxation rates to quasiparticle lifetimes [9–11,52], extracting the population dynamics from the simulated spectra (1) treats experiment and theory on equal footing and naturally includes population effects and quasiparticle decay [53,54]. A subsequent detailed analysis of the self-energy (which determines the Green's function) allows connecting the microscopic quasiparticle picture to the experimentally observed dynamics.

The model parameter controlling the CDW state is the CDW potential V_{CDW} (which corresponds to $\Delta_{CDW} \approx 2V_{CDW}$). Varying V_{CDW} leads to only minimal changes of the band structure outside of the gapped regions [50]. Hence, the observed slowdown of the relaxation dynamics must be caused by (dynamical) interaction effects. To test this hypothesis, we include e-e scattering by considering a Hubbard model with weak interaction U, which is supported by the sharpness of the bands and the rather long lifetimes observed in the experiment [55]. We treat the e-e self-energy on the level of the second-Born approximation and employ the generalized Kadanoff-Baym ansatz (GKBA) [56]. Details are presented in the Supplemental Material [35].

With these ingredients, we obtain a microscopic description that captures the main features observed in the experiment. However, in contrast to the experiments, we keep the transient gap size constant during relaxation by fixing V_{CDW} to highlight the influence of the CDW on the relaxation and to disentangle it from other effects. We simulate the GKBA time evolution upon excitation by a two-cycle pulse with $h\nu_{pump} = 1.5$ eV and calculate the trARPES signal in the full Brillouin zone (1). A typical spectrum along the same path as in Fig. 2 is shown in Fig. 3(a).

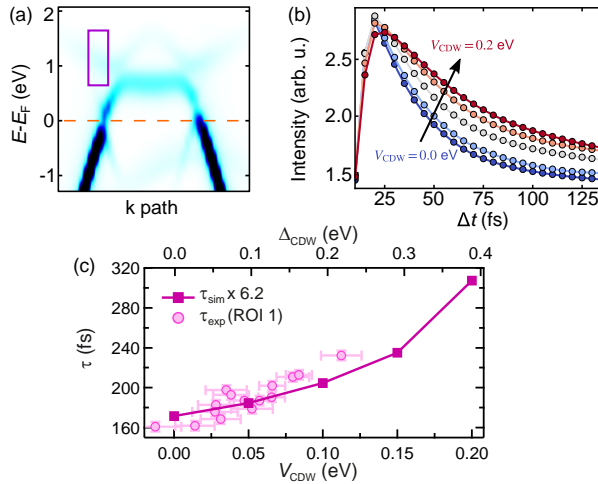Similar to the experimental spectra we have integrated the intensity in the indicated ROI [57]. The transient

photoemission intensity as function of Δt is presented in Fig. 3(b) for different values of $V_{CDW} = 0, \ldots, 0.2$ eV (equidistant steps). For small Δt the intensity is only weakly affected by the CDW, while the long-time relaxation exhibits a pronounced dependence on V_{CDW}. In particular, the decay of intensity in the ROI is significantly faster in the metallic state ($V_{CDW} = 0$ eV). The data fit well to an exponential decay for $\Delta t > 50$ fs. Extracting the respective lifetime τ_{sim} confirms a monotonic dependence of τ_{sim} on V_{CDW}, see Fig. 3(c). For a quantitative comparison to the experimentally observed dynamical modulation of the lifetime, Fig. 3(c) also shows the experimental transient lifetime τ_{exp} of the same ROI as a function of the extracted energy gap Δ_{CDW}, which follows a similar monotonic trend. Remarkably, although the absolute simulated values are significantly shorter due to technical constraints [58], the relative change of the experimental and simulated lifetimes with Δ_{CDW} is in solid agreement.

The dependence of the lifetime τ_{sim} on V_{CDW} explains the superimposed oscillatory component of the relaxation observed in the experiment. Thermalization processes due to e-e scattering in the considered ROI are enhanced in the metallic phase, whereas the presence of the CDW gap renders scattering processes less efficient. To gain intuition on this behavior, we have analyzed the self-energy Σ^{e-e} entering the simulations in detail. In essence, the second-Born approximation captures the relaxation of an excited electron into an unoccupied lower state upon particle-hole (p-h) excitation from a lower energy to an unoccupied higher state while obeying momentum and energy conservation. A gap near E_F suppresses the latter particle-hole transitions, hence reducing the scattering channels of highly excited electrons [Fig. 4(a)]. Note that the CDW gap at E_F is only present at momentum points connected by $\mathbf{q}_{CDW}$; p-h excitations at E_F are still possible in other parts of the Brillouin zone. The relaxation in the upper band is thus not completely suppressed but reduced. In contrast, all p-h channels are available in the metallic phase, which increases the phase space for e-e scattering and thus enhances the relaxation rate [Fig. 4(b)].

This phase-space picture directly enters the Feynman diagrams for Σ^{e-e} [Fig. 4(c)]. For an excited electron to lose the energy $\hbar\omega$ and change its momentum by $\mathbf{q}$, a corresponding p-h excitation obeying energy and momentum conservation is required. The phase-space availability of p-h processes with energy (momentum) transfer ω ($\mathbf{q}$) is captured by the p-h susceptibility $P(\mathbf{q}, \omega)$, also termed polarization in the context of many-body methods [59], illustrated in Fig. 4(c). Since small momentum transfer dominates the relaxation dynamics, we focus on the polarization $\bar{P}(\omega)$ averaged over small momenta $\mathbf{q}$. The scattering phase space of the charges is directly reflected by the retarded component $\bar{P}^R(\omega)$, presented in Fig. 4(d). Comparing the metallic and the CDW phase, the CDW gap opening reduces the available phase space for p-h
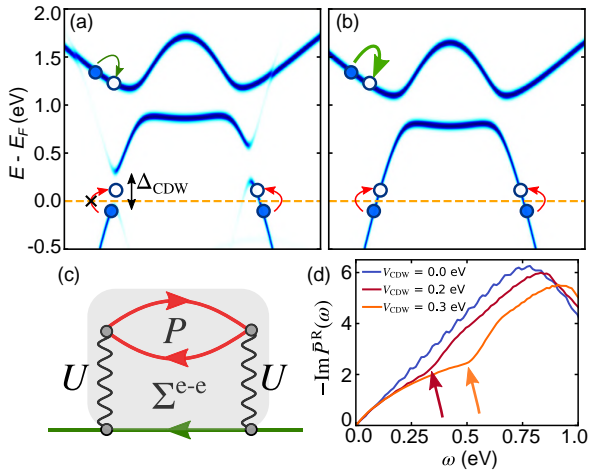
FIG. 3. td-NEGF simulations. (a) Simulated trARPES spectrum in the CDW state ($V_{CDW} = 0.2$ eV) after arrival of the pump pulse along the same momentum direction as in the experiment. (b) Intensity integrated over the ROI indicated in (a) as function of Δt for varying values of the CDW potential V_{CDW}. (c) Rescaled simulated lifetimes τ_{sim} versus V_{CDW} extracted from (b) using exponential decay fits. For direct comparison to the experiment, the transient lifetimes $\tau_{exp}(\Delta t)$ from Fig. 2(e) as function of the extracted $\Delta_{CDW}(\Delta t)$ from Fig. 2(d) are superimposed. The error bars correspond to 1 standard deviation of the respective fits of τ_{exp} and Δ_{CDW}.

FIG. 4. Theoretical investigation of *e-e* scattering. Illustration of the relaxation processes by *e-e* scattering in (a) the CDW, and (b) in the metallic phase. The presence of a gap Δ_{CDW} in (a) suppresses *p-h* excitations close to the FS, limiting scattering processes in the upper band. (c) Sketch of the self-energy Σ^{e-e} diagram within the second-Born approximation. The colors are consistent with the scattering processes in (a),(b). (d) Particle-hole polarization averaged over small momentum transfer $|\mathbf{q}| < 0.05$ a.u. for different values of V_{CDW}.

excitations at lower energy transfer ω. Hence, corresponding relaxation processes with energy transfer ω are increasingly reduced with V_{CDW}. Consistent with experimental observations, we thus demonstrate how the photoinduced modulation of the CDW gap affects the relaxation dynamics of high-energy photocarriers.

We have also inspected *e-ph* scattering as a possible explanation for the observed modulation of the relaxation dynamics, calculating the *e-ph* self-energy Σ^{e-ph} up to second order in *e-ph* coupling strength assuming a Holstein model. However, there is no noticeable effect of V_{CDW} on Σ^{e-ph} in the relevant high-energy ROI [35]. The intuitive explanation is that only *e-ph* scattering processes close to the CDW gap are affected. Thus, an energy gap opening near E_F does not influence *e-ph* scattering of high-energy electrons. Additional GKBA simulations underpin this picture [35]. Hence, we identify *e-e* scattering as the major relaxation mechanism in the high-energy bands.

In conclusion, we presented a complementary experimental and theoretical study of the electron dynamics in a photoexcited charge-density-wave system, TbTe$_3$. We demonstrated how the CDW state affects the electron self-energy, resulting in a decreased relaxation rate of hot photocarriers, as the energy gap at E_F critically restricts the phase space of electron-electron scattering. For this, we employed a combined theoretical approach, simulating population lifetimes that allow a quantitative comparison to the experimental photoelectron intensities, and scrutinizing single-particle lifetimes to gain insight into the

microscopic details of the interactions, which allows us to link the experimental observations to fundamental interactions. While the examined setting of a collective CDW excitation is rather unique, our conclusions are independent of the details of the CDW mechanism and can be directly transferred to a broad range of materials that feature an insulator-to-metal transition. Furthermore, the array of properties that can be controlled by light is expanding rapidly. Ultrashort optical pulses allow modifying the shape of the Fermi surface [60,61], triggering collective modes that are imprinted on the electronic band structure [62,63], and coherently modulating *e-ph* coupling [64]. Hence, the applied approach of tracking the fundamental interactions upon transient optical tuning may facilitate a deeper understanding of a plethora of materials.

The experimental data that support the findings of this study are publicly available [65].

---

*Present address: Department of Physics and Fribourg Center for Nanomaterials, University of Fribourg, Chemin du Musée 3, CH-1700 Fribourg, Switzerland.
†Present address: Laboratory of Ultrafast Spectroscopy, ISIC, Ecole Polytechnique Fédérale de Lausanne (EPFL), CH-1015 Lausanne, Switzerland.
‡rettig@fhi-berlin.mpg.de

[1] M. Bauer, A. Marienfeld, and M. Aeschlimann, Prog. Surf. Sci. **90**, 319 (2015).
[2] E. V. Chulkov, A. G. Borisov, J. P. Gauyacq, D. Sánchez-Portal, V. M. Silkin, V. P. Zhukov, and P. M. Echenique, Chem. Rev. **106**, 4160 (2006).
[3] M. Calandra and F. Mauri, Phys. Rev. B **76**, 205411 (2007).
[4] P. D. C. King, S. M. Walker, A. Tamai, A. de la Torre, T. Eknapakul, P. Buaphet, S.-K. Mo, W. Meevasana, M. S.

Bahramy, and F. Baumberger, Nat. Commun. **5,** 3414 (2014).

[5] U. Bovensiepen and P. S. Kirchmann, Laser Photonics Rev. **6,** 589 (2012).

[6] L. Perfetti, P. A. Loukakos, M. Lisowski, U. Bovensiepen, H. Eisaki, and M. Wolf, Phys. Rev. Lett. **99,** 197001 (2007).

[7] P. S. Kirchmann, L. Rettig, X. Zubizarreta, V. M. Silkin, E. V. Chulkov, and U. Bovensiepen, Nat. Phys. **6,** 782 (2010).

[8] S. Hellmann, T. Rohwer, M. Kalläne, K. Hanff, C. Sohrt, A. Stange, A. Carr, M. M. Murnane, H. C. Kapteyn, L. Kipp, M. Bauer, and K. Rossnagel, Nat. Commun. **3,** 1069 (2012).

[9] I. Gierz, S. Link, U. Starke, and A. Cavalleri, Faraday Discuss. **171,** 311 (2014).

[10] S.-L. Yang, J. A. Sobota, D. Leuenberger, Y. He, M. Hashimoto, D. H. Lu, H. Eisaki, P. S. Kirchmann, and Z.-X. Shen, Phys. Rev. Lett. **114,** 247001 (2015).

[11] J. D. Rameau, S. Freutel, A. F. Kemper, M. A. Sentef, J. K. Freericks, I. Avigo, M. Ligges, L. Rettig, Y. Yoshida, H. Eisaki, J. Schneeloch, R. D. Zhong, Z. J. Xu, G. D. Gu, P. D. Johnson, and U. Bovensiepen, Nat. Commun. **7,** 13761 (2016).

[12] S. Ulstrup, J. C. Johannsen, F. Cilento, J. A. Miwa, A. Crepaldi, M. Zacchigna, C. Cacho, R. Chapman, E. Springate, S. Mammadov, F. Fromm, C. Raidel, T. Seyller, F. Parmigiani, M. Grioni, P. D. C. King, and P. Hofmann, Phys. Rev. Lett. **112,** 257401 (2014).

[13] E. Pomarico, M. Mitrano, H. Bromberger, M. A. Sentef, A. Al-Temimy, C. Coletti, A. Stöhr, S. Link, U. Starke, C. Cacho, R. Chapman, E. Springate, A. Cavalleri, and I. Gierz, Phys. Rev. B **95,** 024304 (2017).

[14] D. Fausti, R. I. Tobey, N. Dean, S. Kaiser, A. Dienst, M. C. Hoffmann, S. Pyon, T. Takayama, H. Takagi, and A. Cavalleri, Science **331,** 189 (2011).

[15] M. Mitrano, A. Cantaluppi, D. Nicoletti, S. Kaiser, A. Perucchi, S. Lupi, P. Di Pietro, D. Pontiroli, M. Riccò, S. R. Clark, D. Jaksch, and A. Cavalleri, Nature (London) **530,** 461 (2016).

[16] M. Budden, T. Gebert, M. Buzzi, G. Jotzu, E. Wang, T. Matsuyama, G. Meier, Y. Laplace, D. Pontiroli, M. Riccò, F. Schlawin, D. Jaksch, and A. Cavalleri, Nat. Phys. **17,** 611 (2021).

[17] Y. H. Wang, H. Steinberg, P. Jarillo-Herrero, and N. Gedik, Science **342,** 453 (2013).

[18] F. Mahmood, C.-K. Chan, Z. Alpichshev, D. Gardner, Y. Lee, P. A. Lee, and N. Gedik, Nat. Phys. **12,** 306 (2016).

[19] M. Rini, R. Tobey, N. Dean, J. Itatani, Y. Tomioka, Y. Tokura, R. W. Schoenlein, and A. Cavalleri, Nature (London) **449,** 72 (2007).

[20] L. Stojchevska, I. Vaskivskyi, T. Mertelj, P. Kusar, D. Svetin, S. Brazovskii, and D. Mihailovic, Science **344,** 177 (2014).

[21] J. Zhang, X. Tan, M. Liu, S. W. Teitelbaum, K. W. Post, F. Jin, K. A. Nelson, D. N. Basov, W. Wu, and R. D. Averitt, Nat. Mater. **15,** 956 (2016).

[22] F. Schmitt, P. S. Kirchmann, U. Bovensiepen, R. G. Moore, L. Rettig, M. Krenz, J.-H. Chu, N. Ru, L. Perfetti, D. H. Lu, M. Wolf, I. R. Fisher, and Z.-X. Shen, Science **321,** 1649 (2008).

[23] T. Huber, S. O. Mariager, A. Ferrer, H. Schäfer, J. A. Johnson, S. Grübel, A. Lübcke, L. Huber, T. Kubacka,

C. Dornes, C. Laulhe, S. Ravy, G. Ingold, P. Beaud, J. Demsar, and S. L. Johnson, Phys. Rev. Lett. **113,** 026401 (2014).

[24] P. Beaud *et al.*, Nat. Mater. **13,** 923 (2014).

[25] M. Trigo, P. Giraldo-Gallo, M. E. Kozina, T. Henighan, M. P. Jiang, H. Liu, J. N. Clark, M. Chollet, J. M. Glownia, D. Zhu, T. Katayama, D. Leuenberger, P. S. Kirchmann, I. R. Fisher, Z. X. Shen, and D. A. Reis, Phys. Rev. B **99,** 104111 (2019).

[26] J. Maklar, Y. W. Windsor, C. W. Nicholson, M. Puppin, P. Walmsley, V. Esposito, M. Porer, J. Rittmann, D. Leuenberger, M. Kubli, M. Savoini, E. Abreu, S. L. Johnson, P. Beaud, G. Ingold, U. Staub, I. R. Fisher, R. Ernstorfer, M. Wolf, and L. Rettig, Nat. Commun. **12,** 2499 (2021).

[27] K. Balzer and M. Bonitz, *Nonequilibrium Green's Functions Approach to Inhomogeneous Systems* (Springer, New York, 2012).

[28] H. Aoki, N. Tsuji, M. Eckstein, M. Kollar, T. Oka, and P. Werner, Rev. Mod. Phys. **86,** 779 (2014).

[29] M. Sentef, A. F. Kemper, B. Moritz, J. K. Freericks, Z.-X. Shen, and T. P. Devereaux, Phys. Rev. X **3,** 041033 (2013).

[30] M. Puppin, Y. Deng, C. W. Nicholson, J. Feldl, N. B. M. Schröter, H. Vita, P. S. Kirchmann, C. Monney, L. Rettig, M. Wolf, and R. Ernstorfer, Rev. Sci. Instrum. **90,** 023104 (2019).

[31] N. Ru, C. L. Condron, G. Y. Margulis, K. Y. Shin, J. Laverock, S. B. Dugdale, M. F. Toney, and I. R. Fisher, Phys. Rev. B **77,** 035114 (2008).

[32] M. Maschek, S. Rosenkranz, R. Heid, A. H. Said, P. Giraldo-Gallo, I. R. Fisher, and F. Weber, Phys. Rev. B **91,** 235146 (2015).

[33] J. Laverock, S. B. Dugdale, Z. Major, M. A. Alam, N. Ru, I. R. Fisher, G. Santi, and E. Bruno, Phys. Rev. B **71,** 085114 (2005).

[34] V. Brouet, W. L. Yang, X. J. Zhou, Z. Hussain, R. G. Moore, R. He, D. H. Lu, Z. X. Shen, J. Laverock, S. B. Dugdale, N. Ru, and I. R. Fisher, Phys. Rev. B **77,** 235104 (2008).

[35] See Supplemental Material at http://link.aps.org/supplemental/10.1103/PhysRevLett.128.026406 which includes additional Refs. [36–47] for the determination of the experimental CDW gap and transient lifetimes, and details on the simulations.

[36] H. Ding, T. Yokoya, J. C. Campuzano, T. Takahashi, M. Randeria, M. R. Norman, T. Mochiku, K. Kadowaki, and J. Giapintzakis, Nature (London) **382,** 51 (1996).

[37] J. M. Harris, Z. X. Shen, P. J. White, D. S. Marshall, M. C. Schabel, J. N. Eckstein, and I. Bozovic, Phys. Rev. B **54,** R15665 (1996).

[38] A. G. Loeser, Z.-X. Shen, D. S. Dessau, D. S. Marshall, C. H. Park, P. Fournier, and A. Kapitulnik, Science **273,** 325 (1996).

[39] F. Schmitt, P. S. Kirchmann, U. Bovensiepen, R. G. Moore, J.-H. Chu, D. H. Lu, L. Rettig, M. Wolf, I. R. Fisher, and Z.-X. Shen, New J. Phys. **13,** 063022 (2011).

[40] G. Stefanucci and R. v. Leeuwen, *Nonequilibrium Many-Body Theory of Quantum Systems: A Modern Introduction* (Cambridge University Press, Cambridge, England, 2013).

[41] M. Schüler, U. De Giovannini, H. Hübener, A. Rubio, M. A. Sentef, T. P. Devereaux, and P. Werner, Phys. Rev. X **10,** 041013 (2020).

[42] M. Schüler, J. C. Budich, and P. Werner, Phys. Rev. B **100**, 041101(R) (2019).

[43] Y. Murakami, M. Schüler, S. Takayoshi, and P. Werner, Phys. Rev. B **101**, 035203 (2020).

[44] R. Tuovinen, D. Golež, M. Eckstein, and M. A. Sentef, Phys. Rev. B **102**, 115157 (2020).

[45] N. Tsuji and P. Werner, Phys. Rev. B **88**, 165115 (2013).

[46] M. Schüler, Y. Murakami, and P. Werner, Phys. Rev. B **97**, 155136 (2018).

[47] G. D. Mahan, *Many-Particle Physics* (Springer Science & Business Media, New York, 2000).

[48] The large energy windows of the ROIs ensure that the total respective band intensities are captured during the relaxation. Thus, the transient intensity change directly reflects quasiparticle scattering.

[49] The full expression of τ_{exp} is given in the Supplemental Material [35].

[50] J. Voit, L. Perfetti, F. Zwick, H. Berger, G. Margaritondo, G. Grüner, H. Höchst, and M. Grioni, Science **290**, 501 (2000).

[51] J. K. Freericks, H. R. Krishnamurthy, and T. Pruschke, Phys. Rev. Lett. **102**, 136401 (2009).

[52] V. V. Baranov and V. V. Kabanov, Phys. Rev. B **89**, 125102 (2014).

[53] A. F. Kemper, M. Sentef, B. Moritz, C. C. Kao, Z. X. Shen, J. K. Freericks, and T. P. Devereaux, Phys. Rev. B **87**, 235139 (2013).

[54] A. F. Kemper, O. Abdurazakov, and J. K. Freericks, Phys. Rev. X **8**, 041009 (2018).

[55] The Hubbard model serves as a generic model to include e-e scattering. Our main conclusions are equally valid for long-range interactions.

[56] P. Lipavský, V. Špička, and B. Velický, Phys. Rev. B **34**, 6933 (1986).

[57] The ROI size is chosen large enough to capture the full band for any value of Δ_{CDW}, thus excluding effects attributed to band shifts that could mask the population dynamics.

[58] Choosing a smaller value of U in the simulations would lead to a better quantitative agreement but requires significantly more computational resources due to the longer timescales. Additional simulations with different values of U and for an additional ROI in the Supplemental Material [35] corroborate the universality of the qualitative behavior.

[59] F. Aryasetiawan and O. Gunnarsson, Rep. Prog. Phys. **61**, 237 (1998).

[60] L. Rettig, R. Cortés, J.-H. Chu, I. R. Fisher, F. Schmitt, R. G. Moore, Z.-X. Shen, P. S. Kirchmann, M. Wolf, and U. Bovensiepen, Nat. Commun. **7**, 10459 (2016).

[61] S. Beaulieu, S. Dong, N. Tancogne-Dejean, M. Dendzik, T. Pincelli, J. Maklar, R. P. Xian, M. A. Sentef, M. Wolf, A. Rubio, L. Rettig, and R. Ernstorfer, Sci. Adv. **7**, 9275 (2021).

[62] U. De Giovannini, H. Hübener, S. A. Sato, and A. Rubio, Phys. Rev. Lett. **125**, 136401 (2020).

[63] P. Hein, S. Jauernik, H. Erk, L. Yang, Y. Qi, Y. Sun, C. Felser, and M. Bauer, Nat. Commun. **11**, 2613 (2020).

[64] Y. Zhang, X. Shi, W. You, Z. Tao, Y. Zhong, F. Cheenicode Kabeer, P. Maldonado, P. M. Oppeneer, M. Bauer, K. Rossnagel, H. Kapteyn, and M. Murnane, Proc. Natl. Acad. Sci. U.S.A. **117**, 8788 (2020).

[65] J. Maklar, Y. W. Windsor, C. Nicholson, M. Puppin, P. Walmsley, V. Esposito, M. Porer, J. Rittmann, D. Leuenberger, M. Kubli, M. Savoini, E. Abreu, S. Johnson, P. Beaud, G. Ingold, U. Staub, I. Fisher, R. Ernstorfer, M. Wolf, and L. Rettig, 10.5281/zenodo .4106272 (2020).

Coherent Modulation of Quasiparticle Scattering Rates in a Photoexcited Charge-Density-Wave System
Supplemental Material

J. Maklar[1], M. Schüler[2], Y. W. Windsor[1], C. W. Nicholson[1], M. Puppin[1], P. Walmsley[2,3],
I. R. Fisher[2,3], M. Wolf[1], R. Ernstorfer[1,4], M. A. Sentef[5], L. Rettig[1]

[1]Fritz-Haber-Institut der Max-Planck-Gesellschaft, Faradayweg 4-6, 14195 Berlin, Germany
[2]Stanford Institute for Materials and Energy Sciences (SIMES), SLAC National
Accelerator Laboratory, Menlo Park, CA 94025, USA
[3]Geballe Laboratory for Advanced Materials and Department of Applied Physics,
Stanford University, CA 94305, USA
[4]Institut für Optik und Atomare Physik, Technische Universität Berlin,
Straße des 17. Juni 135, 10623 Berlin, Germany
[5]Max Planck Institute for the Structure and Dynamics of Matter,
Luruper Chaussee 149, 22761 Hamburg, Germany

December 22, 2021

1   Estimation of the experimental charge-density-wave gap

To determine the experimental transient charge-density-wave (CDW) energy gap Δ_{CDW} near the Fermi level E_{F}, we first extract the energy distribution curves (EDCs) of the gapped momentum region, indicated in Main Fig. 2(b), for different pump-probe delays. Next, we fit the individual EDCs using two Gaussians to describe the peaks below and above E_{F}, respectively. To account for the time-dependent occupation of electronic states due to a transiently varying electronic temperature upon optical excitation, the Gaussians are multiplied by a Fermi-Dirac distribution. The resulting fit function is given by

$$I(E) = \left(A_1 \exp\left(-\frac{(E - E_1)^2}{2\sigma_1^2} \right) + A_2 \exp\left(-\frac{(E - E_2)^2}{2\sigma_2^2} \right) \right) \cdot \frac{1}{\exp\left(E - E_{\mathrm{F}}/k_{\mathrm{B}} T_{\mathrm{e}} \right) + 1} \tag{1}$$

with Gaussian amplitude $A_{1/2}$, peak position $E_{1/2}$, variance $\sigma_{1/2}^2$, transient electronic temperature T_{e} and Boltzmann constant k_{B}. The transient electronic temperature T_{e}, see Fig. S1, and Fermi level E_{F}, which enter the fit function as fixed parameters, are extracted from the metallic part of the Fermi surface, as discussed in detail in Ref. [1]. The Gaussian amplitudes, peak positions and variances are kept as free fit parameters. This model yields an excellent description of the experimental EDCs for time delays, at
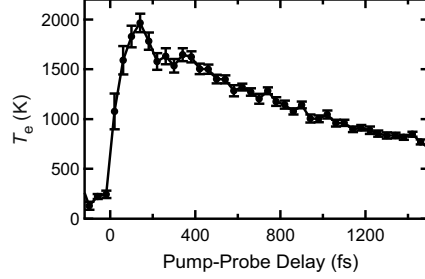
1

Figure S1: Transient electronic temperature T_{e} with one standard deviation as uncertainty extracted from the metallic part of the Fermi surface using a Fermi-Dirac fit.
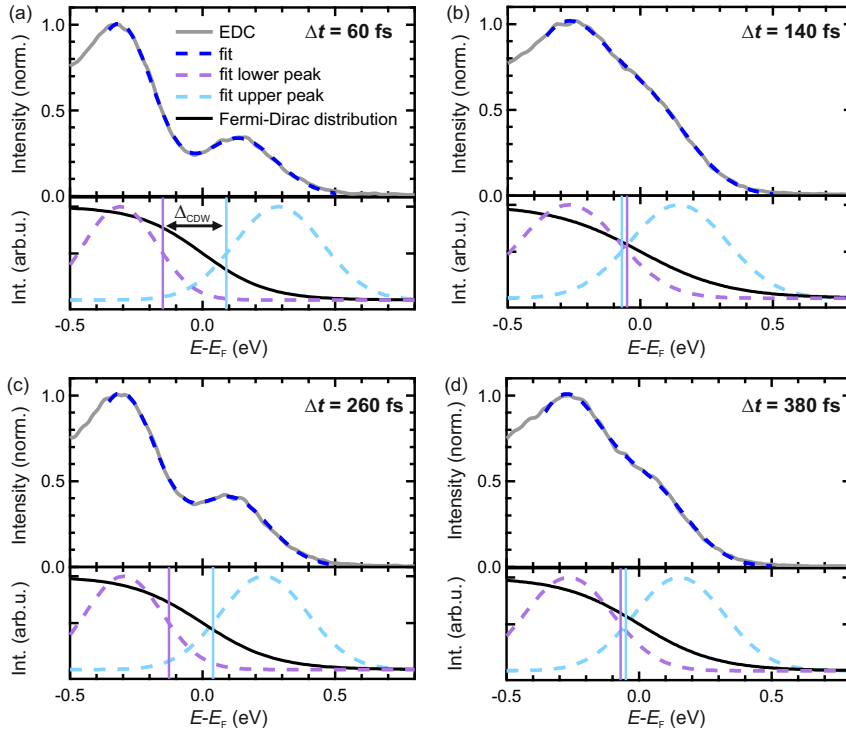

Figure S2: (a-d) Top: EDCs extracted from the momentum region featuring the CDW energy gap (indicated in Main Fig. 2b) for selected pump-probe delays with best fits using Eq. 1. Bottom: Individual components of the best fits (lower/upper Gaussian peak and Fermi-Dirac distribution). The intensities of the individual curves have been rescaled for clarity. Note that the apparent shift of the central positions of the individual Gaussians with respect to the total fit function is caused by the multiplication with the Fermi-Dirac distribution. The purple/blue solid lines mark the midpoint energies of the leading/trailing edges used to approximate Δ_{CDW}.

which the relevant states above E_F are populated (0 fs $< \Delta t <$ 1000 fs). Exemplary fits are shown in Fig. S2.

Finally, we approximate the size of Δ_{CDW} using the difference of the midpoint energies of the leading/trailing edges of the lower/upper peaks, as depicted in Fig. S2. The midpoint energies of the respective edges can be expressed as a shift by the half width at half maximum from the central Gaussian peak positions, with Gaussian 1 describing the peak below and Gaussian 2 the peak above E_F:

$$\Delta_{CDW} = \left(E_2 - \frac{2\sqrt{2\ln 2}\sigma_2}{2} \right) - \left(E_1 + \frac{2\sqrt{2\ln 2}\sigma_1}{2} \right) \tag{2}$$

This edge midpoint approach is a common and reliable method in ARPES to estimate the size of energy gaps, as, e.g., demonstrated for various superconductors [2–4]. The reliability of this approach is further supported by the fact that the initial CDW energy gap near $\Delta t \sim 0$ fs is in excellent agreement with previous studies (400 meV [5]).

To determine the uncertainty of Δ_{CDW}, we sum the individual uncertainties of the parameters entering the edge midpoint approach (Eq. 2). To account for the uncertainty of T_e and E_F entering the initial fit function as constant coefficients (Eq. 1), we calculated the standard deviation of Δ_{CDW} obtained from one thousand successive EDC fits with coefficients T_e and E_F varied randomly around their center values with a normally distributed probability of width σ_{T_e} and σ_{E_F}, respectively. The resulting mean values of Δ_{CDW} with one standard deviation as uncertainty for different pump-probe delays Δt are shown in Fig. S3(a). Note that the large error of Δ_{CDW} near $\Delta t \sim 0$ fs results from the fact that the electrons have not fully reached a thermal distribution yet, leading to a large uncertainty of the electronic temperature.

2 Determination of the experimental transient lifetimes

To model the transient population intensities, we first extract the transient size of the CDW energy gap upon photoexcitation. We describe the CDW gap dynamics using an exponentially damped, absolute sinusoidal fit function with a frequency change over time (chirp) and a linear background with slope a, which is convolved with a Gaussian (FWHM=35 fs) to account for the temporal resolution of the experiment:

$$\Delta_{CDW}(\Delta t) = \left(\Delta_0 \cdot \exp\left(-\Delta t/\tau_{damp}\right) \cdot \left| \sin\left(2\pi\Delta t \left(f + f_{chirp} \cdot \Delta t \right) + \phi \right) \right| + a\Delta t \right) * Gaussian \tag{3}$$

This allows for an excellent description of the experimental data, see Fig. S3(a). The resulting best fit coefficients, i.e., the decay constant of the oscillation amplitude $\tau_{damp} = 450$ fs, the oscillation frequency $f = 2.23$ THz, the frequency chirp $f_{chirp} = -0.36$ THz/ps, and phase $\phi = 0.39\,\pi$, are subsequently used for modeling the transient photoemission intensities.

To describe the transient intensities in the regions of interest (ROIs) 1 and 2 of Main Fig. 2a, we employ a single-exponential decay with amplitude A and lifetime τ_{exp}, convolved with a Gaussian (FWHM=35 fs):

$$I(\Delta t) = A \cdot \exp\left(-\Delta t/\tau_{exp}(\Delta t)\right) * Gaussian \tag{4}$$

3

However, a bare exponential decay with constant lifetime can not reproduce the experimental data, as the photoemission intensities feature a transient modulation of the relaxation rates. These deviations from a single-exponential decay are further emphasized by the derivatives of the transient photoemission intensities with respect to Δt, as shown in Fig. S3(b)–(c), which feature distinct modulations that coincide with the collective CDW dynamics. Whenever the CDW gap at E_F opens, see Fig. S3(a), the relaxation of the high-energy population slows down, indicated by the local minimum of the derivative $|\mathrm{d}I/\mathrm{d}\Delta t|$. Conversely, when the system reaches the metallic state corresponding to $\Delta_{CDW} \sim 0\,\mathrm{eV}$, the high-energy population relaxes faster, indicated by a local maximum of $|\mathrm{d}I/\mathrm{d}\Delta t|$.
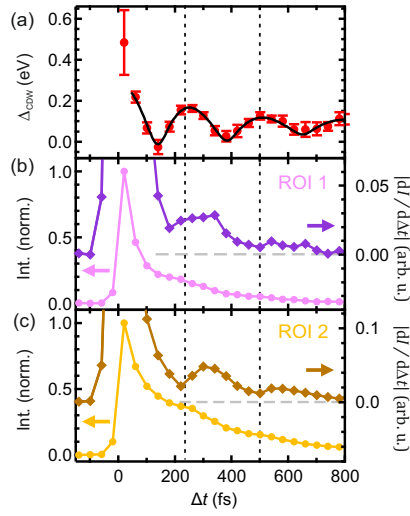

Figure S3: (a) Extracted transient CDW energy gap with one standard deviation as uncertainty. The black solid line marks the best fit using a chirped sinusoidal function (Eq. 3). (b-c) Photoemission intensities versus Δt from the ROIs indicated in Main Fig. 2(a). The derivatives of the photoemission intensities with respect to Δt (purple/brown, right axis, absolute values, numerical differentiation by central differences) emphasize the deviation from an exponential decay with constant lifetime, as they feature distinct modulations that coincide with the oscillations of Δ_{CDW}. The dashed lines serve as guides to the eye.

To account for this oscillatory component of the carrier relaxation rate, we employ a time-dependent lifetime based on the previously extracted parameters of the CDW gap dynamics:

$$\tau_{exp}(\Delta t) = \tau_{metal} + \tau_{CDW} \cdot \exp\left(-\Delta t / \tau_{damp}\right) \cdot \left| \sin\left(2\pi\Delta t \left(f + f_{chirp} \cdot \Delta t\right) + \phi\right)\right| \tag{5}$$

This phenomenological description of the total lifetime comprises the lifetime of the metallic state, τ_{metal}, which serves as a baseline, on top of which an exponentially damped, oscillatory contribution with amplitude τ_{CDW}, corresponding to the observed transient lifetime increase in the CDW state, is added. The functional form of the sine with frequency f, chirp f_{chirp}, the phase offset ϕ, and a damping prefactor with lifetime τ_{damp}, allows us to incorporate the observed dynamics of the CDW gap size Δ_{CDW} into the total lifetime τ_{exp}. We fit the transient photoemission intensities (ROIs 1 and 2) using Eqs. 4 and 5, keeping only τ_{metal}, τ_{CDW} and the amplitude A as variable fit parameters, while keeping the remaining parameters

4

(extracted from the transient CDW gap fit) fixed. This approach yields an excellent description of the experimental data, see Main Fig. 2(e)–(f). The resulting fit coefficients are summarized in Supplementary Table 1.

Finally, this allows us to investigate the dependency of the experimental transient lifetime $\tau_{\mathrm{exp}}(\Delta t)$ as a function of the extracted CDW gap size $\Delta_{\mathrm{CDW}}(\Delta t)$ and a comparison to the theoretical simulations with a static CDW gap, as displayed in Main Fig. 3(c) for ROI 1. The transient lifetime $\tau_{\mathrm{exp}}(\Delta t)$ determined from ROI 2 versus $\Delta_{\mathrm{CDW}}(\Delta t)$ is shown in Fig. S4, which follows a similar trend.
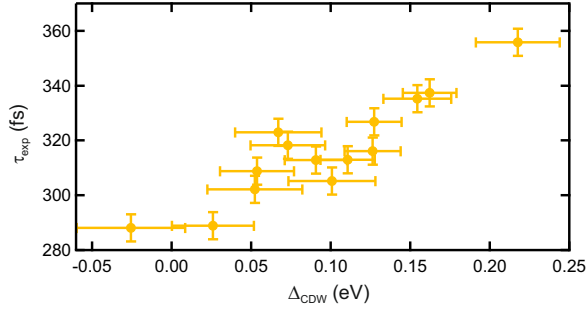

Figure S4: Transient lifetimes $\tau_{\mathrm{exp}}(\Delta t)$ from Main Fig. 2(f), ROI 2, versus the experimentally extracted $\Delta_{\mathrm{CDW}}(\Delta t)$. The error bars correspond to one standard deviation of the respective fits of τ_{exp} and Δ_{CDW}.

Table 1: Best fit coefficients of the decay fits displayed in Main Fig. 2(e)–(f).

Variable	Physical meaning	fixed or free	ROI 1	ROI 2	unit
A	amplitude	free	0.48	0.67	
τ_{metal}	lifetime of metallic phase	free	160	287	fs
τ_{CDW}	lifetime contribution of CDW phase	free	96	91	fs
τ_{damp}	damping prefactor of τ_{CDW}	fixed	450	450	fs
f	oscillation frequency	fixed	2.23	2.23	THz
f_{chirp}	frequency chirp	fixed	-0.36	-0.36	THz/ps
ϕ	phase offset	fixed	0.39	0.39	π

5

3 Details on the simulations

3.1 Tight-binding model

For the simulations we employ the tight-binding (TB) model from Ref. [6] for the quasi-2D Te planes, including the p_x sand p_z orbitals. In absence of any CDW order, the Hamiltonian is defined by

$$\mathbf{h}(\mathbf{k}) = \begin{bmatrix} \varepsilon_x(\mathbf{k}) & V_{xz} \\ V_{xz} & \varepsilon_z(\mathbf{k}) \end{bmatrix} , \tag{6}$$

where

$$\varepsilon_x(\mathbf{k}) = -2t_\parallel \cos[\tfrac{1}{2}(k_x + k_z)a] - 2t_\perp \cos[\tfrac{1}{2}(k_x - k_z)a]$$

$$\varepsilon_z(\mathbf{k}) = -2t_\parallel \cos[\tfrac{1}{2}(k_x - k_z)a] - 2t_\perp \cos[\tfrac{1}{2}(k_x + k_z)a] .$$

The hybridization between the p_x and p_z bands is determined by V_{xz}. For the lattice constants we approximate $a \approx c$. All calculations are performed in the extended 2D Brillouin zone (instead of the reduced 3D Brillouin zone). We will use the labels $m, m' \in \{p_x, p_z\}$ for the orbitals.

Following Ref. [6], the incommensurate CDW with wave-vector $\mathbf{q}_{\text{CDW}}$ can be described by expanding the Hamiltonian (6) in terms of harmonics of $\mathbf{q}_{\text{CDW}}$. Due to the weak intensity of the observed shadow bands, truncating after the first harmonic yields an accurate description. Accordingly the extended Hamiltonian reads

$$\widetilde{\mathbf{h}}(\mathbf{k}) = \begin{bmatrix} \mathbf{h}(\mathbf{k} - \mathbf{q}_{\text{CDW}}) & \mathbf{V} & 0 \\ \mathbf{V} & \mathbf{h}(\mathbf{k}) & \mathbf{V} \\ 0 & \mathbf{V} & \mathbf{h}(\mathbf{k} + \mathbf{q}_{\text{CDW}}) \end{bmatrix} . \tag{7}$$

For simplicity we chose the coupling $\mathbf{V} = V_{\text{CDW}}\mathbf{I}$. The parameter V_{CDW} determines the size of the gap and the intensity of the shadow bands. We chose $t_\parallel = 1.7$ eV, $t_\perp = 0.32$ eV, and $V_{xz} = 0.2$ eV, which best matches the experimental band structure. The coupling strength V_{CDW} is treated as a parameter. We do not include spin-orbit coupling in the model, which is justified by the small spin splittings below the experimental resolution. Optical excitations are not affected in this case.

3.2 Many-body treatment

To obtain a realistic model that includes generic electron-electron (e–e) scattering, we consider the Hubbard model with identical on-site repulsion U for each orbital. For convenience we combine the orbital and the CDW index into a single index $i = (m, N)$ where $N = -1, 0, 1$ denotes the sectors in Eq. (7). We consider the many-body Hamiltonian

$$\hat{H} = \hat{H}_0 + \hat{H}_{\text{e−e}} \equiv \sum_{\mathbf{k}} \sum_{ij,\sigma} \widetilde{h}_{ij}(\mathbf{k})\hat{c}^\dagger_{\mathbf{k}i\sigma}\hat{c}_{\mathbf{k}j\sigma} + U \sum_{\mathbf{k},\mathbf{p},\mathbf{q}} \sum_{ij,\sigma} \hat{c}^\dagger_{\mathbf{k}+\mathbf{q}i\sigma}\hat{c}^\dagger_{\mathbf{p}-\mathbf{q}j\bar{\sigma}}\hat{c}_{\mathbf{p}j\bar{\sigma}}\hat{c}_{\mathbf{k}i\sigma} . \tag{8}$$

Note that the interaction term in Eq. (8) entails an additional simplification, as some combinations of sectors (with respect to Eq. (7)) are excluded. This assumption is justified by the following: (i) scattering

6

processes with small momentum transfer dominate in the experimentally relevant bands (this is particularly pronounced in the more realistic case of a long-range Coulomb interaction); (ii) coupling of different sectors is very weak except for close to the gap region.

To capture the dynamics in presence of e–e interactions, we employ the time-dependent nonequilibrium Green's functions (td-NEGF) framework. To this end we consider the Green's function (GF) on the Kadanoff-Baym contour $\mathcal{C}$ [7],

$$G_{ij\sigma}(\mathbf{k}; t, t') = -i\langle T_C \hat{c}_{\mathbf{k}i\sigma}(t) \hat{c}^{\dagger}_{\mathbf{k}j\sigma}(t') \rangle . \tag{9}$$

Here, T_C denotes the contour ordering symbol. The contour GF (9) contains information on the photoemission spectrum when choosing the location of the contour arguments t, t' accordingly. In particular, the time-resolved photoemission intensity is obtained by the lesser GF $G^{<}_{ij\sigma}(\mathbf{k}; t, t') = i\langle \hat{c}^{\dagger}_{\mathbf{k}j\sigma}(t') \hat{c}_{\mathbf{k}i\sigma}(t)\rangle$ by [8, 9]

$$I(\mathbf{k}, \omega, \Delta t) \propto \text{Im} \sum_{m,\sigma} \int dt \int dt' s(t) s(t') e^{i\omega(t-t')} G^{<}_{(m0)(m0)\sigma}(\mathbf{k}; t, t') . \tag{10}$$

Here we have projected onto the first Brillouin zone containing the main bands (middle sector in Eq. (7)). The energy ω corresponds to the binding energy, while $s(t)$ denotes the shape of the probe pulse, which is delayed with respect to the pump pulse by Δt.

The GF (9) is obtained by solving its equation of motion

$$\left(i\partial_t - \widetilde{\mathbf{h}}(\mathbf{k}, t)\right) \mathbf{G}(\mathbf{k}; t, t') + \int_{\mathcal{C}} d\bar{t} \mathbf{\Sigma}(\mathbf{k}; t, \bar{t}) \mathbf{G}(\mathbf{k}; \bar{t}, t') , \tag{11}$$

where we have employed the compact matrix notation. The self-energy $\mathbf{\Sigma}(\mathbf{k}; t, t')$ captures the many-body effects arising due to e–e scattering. The pump pulse is incorporated by the Peierl's substitution $\widetilde{\mathbf{h}}(\mathbf{k}, t) = \widetilde{\mathbf{h}}(\mathbf{k} - q\mathbf{A}(t))$, where $\mathbf{A}(t)$ stands for the vector potential of the pulse.

Solving the full Kadanoff-Baym equations (11) is a tremendous computational challenge for the resolution with respect to momentum space and reaching relevant time scales. Therefore we employ the generalized Kadanoff-Baym ansatz (GKBA), which transform Eq. (11) into an equation of motion for the single-particle density matrix $\rho(\mathbf{k}, t)$:

$$\frac{d}{dt}\rho(\mathbf{k}, t) + i[\widetilde{\mathbf{h}}(\mathbf{k}, t), \rho(\mathbf{k}, t)] = -(\mathbf{I}(\mathbf{k}, t) + \text{h. c.}) . \tag{12}$$

The quasi-particle scattering effects captured by the self-energy enter the dynamics of the density matrix (12) via the collision integral

$$\mathbf{I}(\mathbf{k}, t) = \int_{-\infty}^{t} d\bar{t} \left(\mathbf{\Sigma}^{<}(\mathbf{k}; t, \bar{t}) \mathbf{G}^{A}(\mathbf{k}; \bar{t}, t) + \mathbf{\Sigma}^{R}(\mathbf{k}; t, \bar{t}) \mathbf{G}^{<}(\mathbf{k}; \bar{t}, t)\right) . \tag{13}$$

Following the same route as in Ref. [10], the correlated equilibrium density matrix $\rho(\mathbf{k}, t)$ is obtained from adiabatically switching on the interactions. Extensive benchmarks [10–13] underpin the accuracy of the GKBA in the relevant regime of weak to moderate interactions.

Eq. (12) is solved with a highly accurate computer code (more details in Ref. [10]). A $N_k = 72 \times 72$ sampling of the Brillouin zone was used, while the time propagation was done in equidistant steps of $h = 0.8$ a.u. and up to $N_t = 7500$ time steps. After obtaining $\rho(\mathbf{k}, t)$ the lesser GF is reconstructed by

$$\mathbf{G}^{<}(\mathbf{k}; t, t') = \mathbf{G}^{R}(\mathbf{k}; t, t')\rho(\mathbf{k}, t') + \rho(\mathbf{k}, t)\mathbf{G}^{A}(\mathbf{k}; t, t') . \tag{14}$$

7

The retarded (advanced) GF $\mathbf{G}^{\mathrm{R}}(\mathbf{k}; t, t')$ ($\mathbf{G}^{\mathrm{A}}(\mathbf{k}; t, t')$) is defined with respect to the mean-field Hamiltonian. Substituting the lesser GF (14) into Eq. (10) then yields the time-resolved photomemission spectra.

3.3 Calculation of the self-energy

The sharply defined bands in the experimental ARPES data and the unusually long lifetime of excited electrons indicate a weak-coupling scenario, in which the e–e interaction can be treated pertubatively. Thus, we employ the second-Born approximation, which defines the self-energy as

$$\Sigma_{ij}^{\mathrm{e-e}, \gtrless}(\mathbf{k}; t, t') = i \frac{U^2}{N_k} \sum_{\mathbf{q}} G_{ij}^{\gtrless}(\mathbf{k} - \mathbf{q}; t, t') P_{ij}^{\gtrless}(\mathbf{q}; t, t') , \tag{15}$$

where

$$P_{ij}^{\gtrless}(\mathbf{q}; t, t') = -\frac{2i}{N_k} \sum_{\mathbf{p}} G_{ij}^{\gtrless}(\mathbf{q} + \mathbf{p}; t, t') G_{ji}^{\lessgtr}(\mathbf{p}; t', t) \tag{16}$$

denotes the electron-hole polarization. For brevity we have dropped the spin index, as all quantities are spin-independent. Eq. (15)–(16) are evaluated numerically and inserted into the collision integral (13). For a qualitative analysis we have also computed the polarization (16) for the equilibrium state, inserting the non-interacting GF. Specifically we calculate the retarded component

$$P_{ij}^{(0),\mathrm{R}}(\mathbf{q}; \omega) = \int_0^\infty dt \, e^{i\omega t} \left[P_{ij}^{(0),>}(\mathbf{q}; t, 0) - P_{ij}^{(0),<}(\mathbf{q}; t, 0) \right] , \tag{17}$$

where the superscript (0) indicates the free GFs entering the definition. For the practical evaluation of the one-shot polarization (17) we insert the time-dependent GFs and perform the integration analytically. Note that a considerably more dense sampling of the Brillouin zone is required to achieve convergence in the real-frequency representation. We include up to $N_k = 300 \times 300$ points to ensure converged results. The average polarization $\bar{P}^{\mathrm{R}}(\omega)$ presented in Fig. 4(d) in the main text is computed from Eq. (17) by

$$\bar{P}^{\mathrm{R}}(\omega) = \frac{1}{\pi q_c^2} \sum_m \int_{|\mathbf{q}| < q_c} d\mathbf{q} \, P_{(m0)(m0)}^{(0),\mathrm{R}}(\mathbf{q}; \omega) , \tag{18}$$

where $q_c = 0.05$ a.u. is a typical value for the scattering processes with small momentum transfer.

4 Simulation of the relaxation dynamics

We have performed simulations within the GKBA formalism to discern the scattering channels and explain the slow-down of the relaxation dynamics observed in the experiments. The calculations are agnostic with respect to the origin of the CDW; we focus on the dynamics of highly excited carriers. As the variation of the photoemission intensity in the gap region – the hallmark of the collective CDW excitation – is slow on the electronic time scale, we keep the CDW frozen in the simulations.

The dynamics is triggered by a short laser pulse, described by the vector potential

$$\mathbf{A}(t) = \mathbf{e} A_0 \sin[\omega_0(t - t_0)] \sin^2 \left(\frac{\pi(t - t_0)}{T_p} \right) , \quad t_0 < t < t_0 + T_p , \tag{19}$$

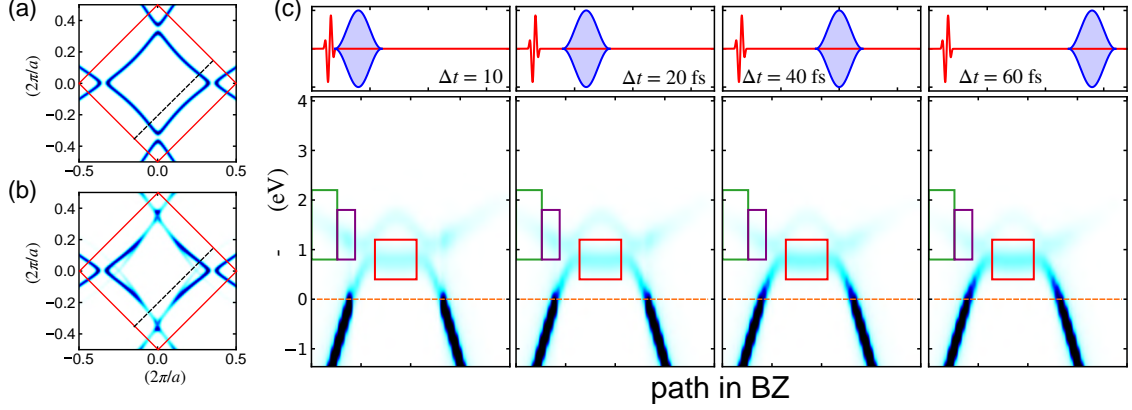Figure S5: Fermi surface calculated from the introduced tight-binding Hamiltonian (7) for $V_{CDW} = 0$ (a), and $V_{CDW} = 0.2$ eV (b). The red square represents the 2D Brillouin zone for the Te plane, while the dashed line illustrates the chosen path in momentum space for which trARPES spectra are presented in (c). (c): Time-resolved photoemission spectra along the path shown in (a), (b) for $U = 1t_{\parallel}$ and $V_{CDW} = 0$ as function of the pump-probe delay Δt. The upper panels show the pump (red) and probe pulse envelope (blue).

where $\mathbf{e}$ is the polarization vector, ω_0 the central frequency, and $T_p = 2\pi n_c/\omega_0$ the duration of a n_c-cycle pulse. We fix $\omega_0 = 1.5$ eV and $\mathbf{e} = (1/\sqrt{2}, 1/\sqrt{2}, 0)^T$. Choosing $n_c = 2$ results in a broad-band pulse which gives rise to a similar excited-state distribution as in the experiments, which we have explicitly confirmed by comparing the experimental spectra to the simulations, optimizing the field strength of the pulse A_0 to match the relative intensity shortly after the pulse in the high-energy ROI in Fig. 2(a) and close to E_F. Note that the TB model does not include deeper bands from which direct transitions to ROI 2 in Fig. 2(a) occur. Therefore, we focus on the higher-energy region. The conclusions are however generic.

While the simulations are performed in the entire Brillouin zone, we focus on the experimentally relevant region cutting through the CDW gap. Fig. S5(a)–(b) illustrates the path in the Brillouin zone (chosen as in the experiments) along which the time-resolved photoemission spectra (10) are calculated. For the evaluation of Eq. (10) we insert the shape function

$$s(t) = \sin^2\left(\frac{\pi(t - \Delta t)}{T_{pr}}\right) , \quad \Delta t \leq t \leq \Delta t + T_{pr} , \tag{20}$$

where $T_{pr} = 20$ fs is chosen as good compromise between energy resolution and attainable time scales.

4.1 Electron-electron scattering dynamics

To investigate the thermalization dynamics in the presence e–e scattering, we simulated the dynamics including the self-energy (15) (and with the Hartree-Fock contribution). Since the time scale of e–e scattering depends on the amount of injected energy [14, 15], we calculated the absorbed energy as a function of A_0 for various values of the CDW state, characterized by V_{CDW}. Comparison to experimental spectra shortly after the pulse corresponds to $V_{CDW} \approx 0.2$ eV, which is chosen as a reference. We fix
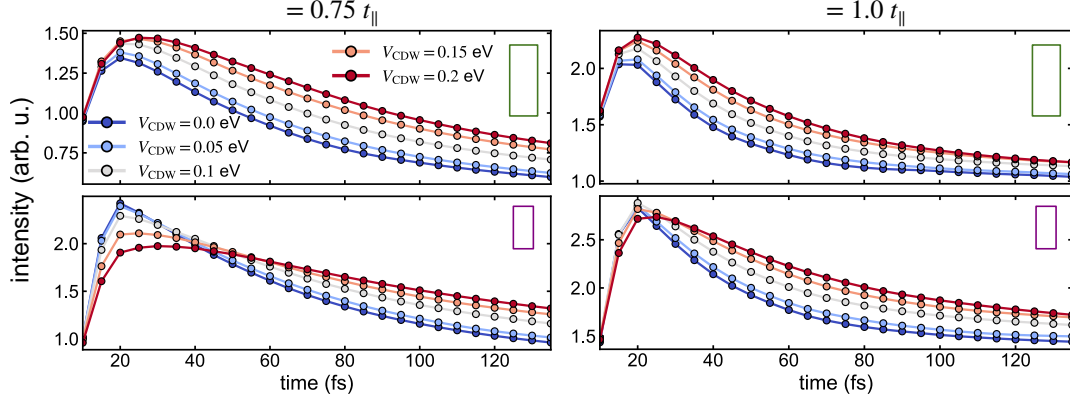
9

Figure S6: Integrated intensity over the relevant ROIs (illustrated by the green and the purple box in Fig. S5(c), respectively) as function of the pump-probe delay Δt. Left panels: $U = 0.75 t_\parallel$, right panels: $U = 1.0 t_\parallel$.

A_0 to fit the excited-state carrier distribution in the experiment for the CDW phase. For other values of V_{CDW}, A_0 is determined by requiring that the same amount of energy has been absorbed.

Fig. S5(c) shows the time-resolved spectra for the metallic phase ($V_{\text{CDW}} = 0$). The pump pulse promotes electrons to the upper bands, in particular in the region indicated by the green and purple boxes, which are connected to the occupied bands by the vertical transitions (see $\Delta t = 10$ fs). Apart from these resonant transitions, the occupation is broadly distributed. This is due to the short pulse and due to ultrafast e–e interactions. The latter effect gives rise to significantly increased absorption compared to the noninteracting case [10]. Furthermore, ultrafast scattering also facilitates additional intra-band transitions [9]. The time-resolved spectra for larger Δt show the thermalization dynamics, characterized by a relaxation towards a high-temperature thermal state. In particular, the initially sharply defined Fermi surface gets smeared as the population accumulates above the Fermi energy E_{F}, while the intensity in the bands at higher energy declines. While the total energy is conserved in the presence of e–e scattering only, the carriers' mean excess energy above E_{F} decays.

Note that the excited-state distribution observed in the experiments is similar, albeit the presence of additional bands at $E - E_{\text{F}} \approx -0.5$ eV modifies the population, specifically in the region indicated by the red boxes in Fig. S5(c). A direct comparison between theory and experiment is difficult in this region of the energy and momentum space, especially on the attainable time scales in the simulations. We will thus restrict the analysis on the region indicated by the purple and the green box in Fig. S5(c). The scattering dynamics discussed below is however generic.

For a quantitative analysis we have calculated time traces by integrating over regions in energy and momentum space, in analogy to the analysis of the experimental spectra. Fig. S6 shows the relaxation dynamics of the highly excited states for various values of the CDW parameter V_{CDW}. We also compare the dynamics for $U = 0.75 t_\parallel$ to $U = 1.0 t_\parallel$ to confirm that the observed behavior is generic. Since U^2 is the scaling factor for the self-energy (15), the relaxation time scale is approximately twice as long for $U = 0.75 t_\parallel$ compared to $U = 1.0 t_\parallel$. The qualitative behavior is very similar in both simulations. Note that, for the simulations presented in the main text, $U = 1.0 t_\parallel$ was used.
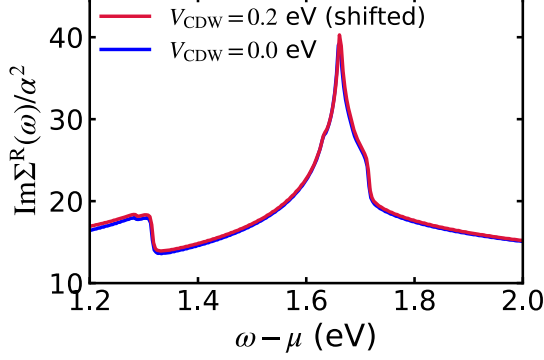
10

Figure S7: Imaginary part of the retarded electron-phonon self-energy $\Sigma^{e-ph,R}(\omega)$ of the conduction band (projected onto the first BZ) for $V_{CDW} = 0$ and $V_{CDW} = 0.2$ eV. We shifted the frequency dependence for $V_{CDW} = 0.2$ eV to compensate for the small shift of the conduction band upon switching on V_{CDW}. A $N_k = 4000 \times 4000$ was required to achieve convergence.

4.2 Effects of electron-phonon coupling

To contrast the scattering channels, we also consider electron-phonon (e–ph) coupling. As confirmed experimentally, the dominant phonon mode is an inter-plane mode perpendicular to the Te plane, with a frequency of $\omega_{ph} \approx 15$ meV. This scenario is captured by including Holstein-type coupling:

$$\hat{H}_{e-ph} = \frac{\alpha}{\sqrt{2N}} \sum_{\mathbf{k},\mathbf{q}} \sum_{i,\sigma} \hat{c}^{\dagger}_{\mathbf{k}i\sigma} \hat{c}_{\mathbf{k}-\mathbf{q}i\sigma}(\hat{b}_{\mathbf{q}} + \hat{b}^{\dagger}_{-\mathbf{q}}) \,, \tag{21}$$

where $\hat{b}_{\mathbf{q}}$ denotes the phonon annihilation operator, while N is the number of points sampling the Brillouin zone.

Here we treat the electron-phonon (e–ph) coupling within the Migdal approximation [16]:

$$\Sigma^{\gtrless}_{ij}(\mathbf{k}; t, t') = i\alpha^2 G^{loc,\gtrless}_{ij}(t, t') D^{\gtrless}_0(t, t') \,, \tag{22}$$

where $G^{loc}_{ij}(t, t') = \frac{1}{N_k} \sum_{\mathbf{k}} G_{ij}(\mathbf{k}; t, t')$ denotes the local GF, while $D_0(t, t')$ represents the free phonon propagator. The e–ph coupling strength is denoted by α. Since we consider a single Einstein mode, the phonon propagator $D^{\gtrless}_0(t, t')$ does not exhibit a momentum dependence. For this reason, the self-energy (22) is momentum independent.

To assess the effects of e–ph scattering, we calculated the retarded component of the self-energy (22)

$$\Sigma^{R}_{ij}(\omega) = \int_0^{\infty} dt \, e^{i\omega t} \left[\Sigma^{>}_{ij}(t, t') - \Sigma^{<}_{ij}(t, t') \right] \,. \tag{23}$$

In Fig. S7 we compare the imaginary part for the metallic and the CDW phase over a range of ω corresponding to the relevant conduction band. Note that the bare conduction band is shifted by 18 meV to higher energy in the CDW phase. For a one-to-one comparison we shifted the self-energy in the CDW

11

phase in Fig. S7 accordingly. As Fig. S7 demonstrates, the self-energy of the conduction band shows practically no dependence on V_{CDW}. Hence, the relaxation dynamics for the same pulse-induced population – if only e–ph coupling is present – is identical in the metallic and the CDW phase. This is consistent with the discussion of the scattering phase space in the main text. In contrast to e–e scattering, the relaxation of highly-excited electrons within the top band is always possible upon emitting a phonon. The presence of an electron gap at the Fermi level does not influence the probability of this process.
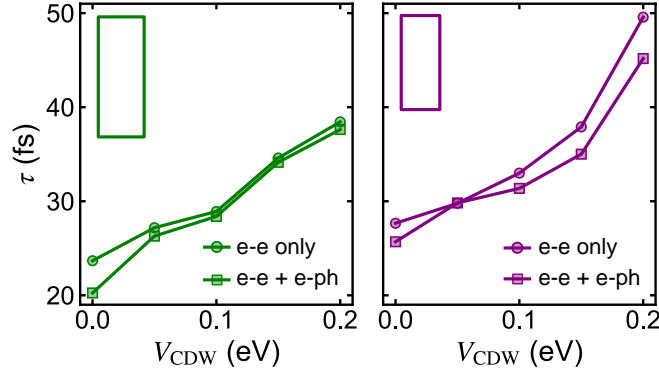

Figure S8: Relaxation time extracted in the regions of interest (analogous to Fig. 3(c) in the main text). Circles represent the case of e–e scattering only, while squares show the relaxation times for the Hubbard-Holstein model with $\alpha = 10^{-3}$.

To confirm this picture we have performed additional GKBA simulations where we included both the e–e self-energy (15) and the e–ph self-energy (22). The simulations were carried out analogously to the case of e–e scattering only. After computing the trARPES spectrum via Eq. (10), we analyzed the ROIs as the main text and extracted the corresponding relaxation time τ, which is shown in Fig. S8. The e–ph coupling strength can be estimated by matching the quasi-particle lifetime determined by the imaginary part of the e–ph self-energy (Fig. S7) to the long-time relaxation behavior in the experiments ($t > 500$ fs).

In contrast to the case of e–e scattering only, in Fig. S8 we compare the extracted relaxation times with and without e–ph scattering. As Fig. S8 demonstrates, the scattering time is slightly reduced by introducing the e–ph coupling. The monotonic dependence of V_{CDW} is retained. This analysis underpins that e–ph scattering can not give rise to a significant dependence of the scattering dynamics on the CDW state.

References

[1] J. Maklar, Y. W. Windsor, C. W. Nicholson, M. Puppin, P. Walmsley, V. Esposito, M. Porer, J. Rittmann, D. Leuenberger, M. Kubli, M. Savoini, E. Abreu, S. L. Johnson, P. Beaud, G. Ingold, U. Staub, I. R. Fisher, R. Ernstorfer, M. Wolf, and L. Rettig, Nat. Commun. **12**, 2499 (2021).

[2] H. Ding, T. Yokoya, J. C. Campuzano, T. Takahashi, M. Randeria, M. R. Norman, T. Mochiku, K. Kadowaki, and J. Giapintzakis, Nature **382**, 51 (1996).

[3] J. M. Harris, Z. X. Shen, P. J. White, D. S. Marshall, M. C. Schabel, J. N. Eckstein, and I. Bozovic, Phys. Rev. B **54**, R15665 (1996).

[4] A. G. Loeser, Z.-X. Shen, D. S. Dessau, D. S. Marshall, C. H. Park, P. Fournier, and A. Kapitulnik, Science **273**, 325 (1996).

[5] F. Schmitt, P. S. Kirchmann, U. Bovensiepen, R. G. Moore, J.-H. Chu, D. H. Lu, L. Rettig, M. Wolf, I. R. Fisher, and Z.-X. Shen, New J. Phys. **13**, 063022 (2011).

[6] V. Brouet, W. L. Yang, X. J. Zhou, Z. Hussain, R. G. Moore, R. He, D. H. Lu, Z. X. Shen, J. Laverock, S. B. Dugdale, N. Ru, and I. R. Fisher, Phys. Rev. B **77**, 235104 (2008).

[7] G. Stefanucci and R. v. Leeuwen, *Nonequilibrium Many-Body Theory of Quantum Systems: A Modern Introduction* (Cambridge University Press, 2013).

[8] J. Freericks, H. Krishnamurthy, and T. Pruschke, Phys. Rev. Lett. **102**, 136401 (2009).

[9] M. Sentef, A. F. Kemper, B. Moritz, J. K. Freericks, Z.-X. Shen, and T. P. Devereaux, Phys. Rev. X **3**, 041033 (2013).

[10] M. Schüler, U. De Giovannini, H. Hübener, A. Rubio, M. A. Sentef, T. P. Devereaux, and P. Werner, Phys. Rev. X **10**, 041013 (2020).

[11] M. Schüler, J. C. Budich, and P. Werner, Phys. Rev. B **100**, 041101 (2019).

[12] Y. Murakami, M. Schüler, S. Takayoshi, and P. Werner, Phys. Rev. B **101**, 035203 (2020).

[13] R. Tuovinen, D. Golež, M. Eckstein, and M. A. Sentef, Phys. Rev. B **102**, 115157 (2020).

[14] N. Tsuji and P. Werner, Phys. Rev. B **88**, 165115 (2013).

[15] M. Schüler, Y. Murakami, and P. Werner, Phys. Rev. B **97**, 155136 (2018).

[16] G. D. Mahan, *Many-Particle Physics* (Springer Science & Business Media, 2000).

4.4 Nano Lett. 22, 5420 — 5426 (2022): Ultrafast momentum-resolved hot electron dynamics in the two-dimensional topological insulator bismuthene

J. Maklar, R. Stühler, M. Dendzik, T. Pincelli, S. Dong, S. Beaulieu, A. Neef, G. Li, M. Wolf, R. Ernstorfer, R. Claessen, and L. Rettig

The publication Maklar et al., Nano Lett. 22, 5420 — 5426 (2022) reports on the ultrafast electron dynamics of the 2D QSH insulator bismuthene upon photoexcitation. The associated supplementary information is reprinted below the main article. The associated raw data is publicly available at the Zenodo data repository, doi 10.5281/zenodo.5512069.

Author contributions

J.M., M.D., R.S., S.D., S.B., T.P., A.N. and L.R. carried out the trARPES experiments; **J.M.** analyzed the trARPES data with support from R.S.; R.S. prepared and characterized the samples and analyzed the STM data; G.L. performed the DFT calculations; **J.M.** wrote the manuscript with support from L.R., R.S., R.E. and R.C.; L.R., R.E., M.W. and R.C. provided the experimental infrastructure; all authors commented on the paper.

Letter

Ultrafast Momentum-Resolved Hot Electron Dynamics in the Two-Dimensional Topological Insulator Bismuthene

Julian Maklar, Raúl Stühler, Maciej Dendzik, Tommaso Pincelli, Shuo Dong, Samuel Beaulieu, Alexander Neef, Gang Li, Martin Wolf, Ralph Ernstorfer, Ralph Claessen, and Laurenz Rettig*

Read Online

| ACCESS | | Metrics & More | | Article Recommendations | | Supporting Information |

ABSTRACT: Two-dimensional quantum spin Hall (QSH) insulators are a promising material class for spintronic applications based on topologically protected spin currents in their edges. Yet, they have not lived up to their technological potential, as experimental realizations are scarce and limited to cryogenic temperatures. These constraints have also severely restricted characterization of their dynamical properties. Here, we report on the electron dynamics of the novel room-temperature QSH candidate bismuthene after photoexcitation using time- and angle-resolved photo-emission spectroscopy. We map the transiently occupied conduction band and track the full relaxation pathway of hot photocarriers. Intriguingly, we observe photocarrier lifetimes much shorter than those in conventional semiconductors. This is ascribed to the presence of topological in-gap states already established by local probes. Indeed, we find spectral signatures consistent with these earlier findings. Demonstration of the large band gap and the view into photoelectron dynamics mark a critical step toward optical control of QSH functionalities.

KEYWORDS: Topological insulators, quantum spin Hall effect, bismuthene, time- and angle-resolved photoemission spectroscopy, trARPES, ultrafast carrier dynamics
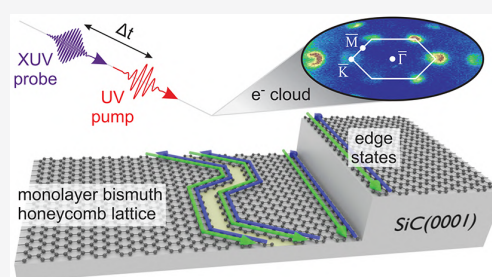
A promising platform for spintronic devices are two-dimensional (2D) topological insulators (TIs).[1] Based on the quantum spin Hall (QSH) effect, 2D TIs feature an insulating band structure in their interior (here referred to as 2D bulk) surrounded by metallic states at their edges. These helical edge states (ESs) are characterized by spin-momentum locking, allowing for spin currents with opposite polarization for forward- and backward-moving electrons. As they are topologically protected by time-reversal symmetry against single-particle backscattering, they also enable dissipationless transport.[2,3] However, any practical application based on helical ESs requires a large bulk band gap preventing interference with thermally excited bulk carriers at room temperature. Thus, in addition to a thorough characterization of the ES properties, also mapping out the bulk valence and conduction bands is critical. Yet, so far band structure investigations of 2D TIs are scarce[4−6] and an understanding of their dynamical properties and microscopic interactions, imperative for controlling QSH functionalities, is lacking.

A suitable approach to tackle these questions is time- and angle-resolved photoemission spectroscopy (trARPES), which has been pivotal for characterizing the electronic structure and fundamental interactions of 3D TIs, the 3D analogs of QSH insulators.[7−13] This method grants direct access to the energy- and momentum-dependent electron dynamics after femto-second optical excitation and to states that are not occupied in equilibrium. Thus, trARPES allows for mapping of the transiently populated states above the Fermi level, which has been essential for a clear separation of semiconducting bulk and metallic topological in-gap states in 3D TIs. Gaining a similar understanding of the electronic structure and elementary scattering processes of 2D TIs is of strong interest from both scientific and application perspectives.

A novel platform to address this knowledge gap is the room temperature QSH candidate bismuthene, that is, a monolayer of bismuth atoms arranged in a planar honeycomb geometry on a semiconducting silicon carbide SiC(0001) substrate.[14] Spatially resolved scanning tunneling spectroscopy (STS) measurements have demonstrated a large band gap of ∼0.8 eV in bulk areas, far greater than in any other QSH system,[4−6,15−20] and conductive 1D states at exposed sample edges near substrate terrace steps,[14,21] as illustrated in Figure 1a. Intriguingly, in topologically nontrivial materials, additional pairs of coupled ESs can arise within the bulk areas at extended 1D defects,[22,23] recently observed within the 2D bulk of
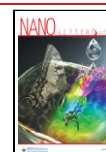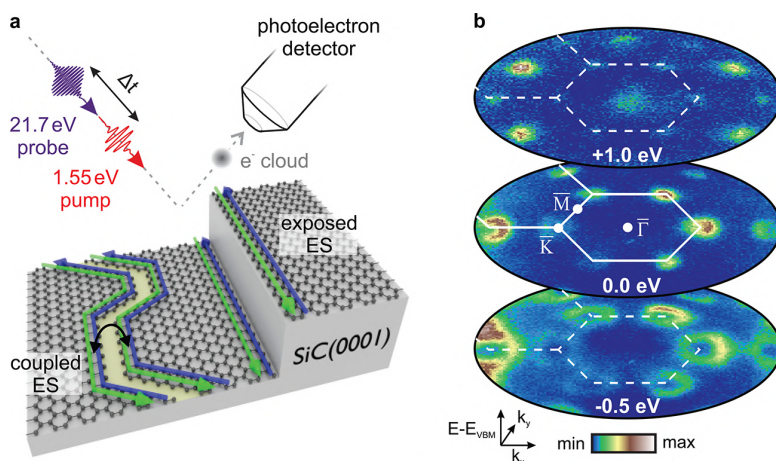
Figure 1. Experimental scheme and photoelectron constant-energy contours. (a) Illustration of the trARPES experiment. An optical pump pulse excites the bismuthene sample, followed by an XUV pulse that probes the electronic distribution after a time delay, Δt. The green and blue arrows represent the two spin channels of the coupled ESs at a domain boundary and of the exposed ESs at a substrate step edge. (b) Constant-energy contours with radius $k_{\parallel} \approx 2$ Å^{-1} of bismuthene after photoexcitation ($h\nu = 1.55$ eV, $\Delta t = -75$ to $+75$ fs). Two exemplary BZs and high-symmetry points are indicated.
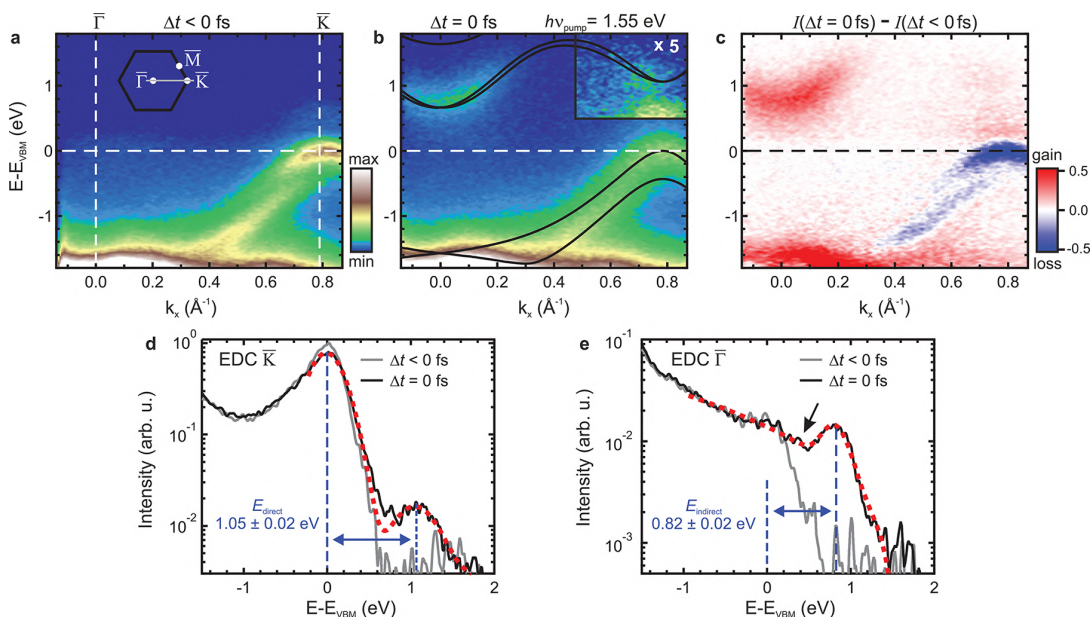
Figure 2. Electronic band-structure maps. (a) False-color plots of the trARPES measurements of bismuthene along the $\overline{\Gamma}-\overline{K}$ direction (gray line in inset) in equilibrium and (b) after optical excitation ($h\nu = 1.55$ eV, incident fluence $F = 0.50$ mJ cm^{-2}, $\Delta t = -40$ to $+40$ fs). The intensity in the inset is enhanced by a factor of 5. DFT band structure calculations (black) are adopted from Reis et al.[14] (c) Differential photoemission intensity (pre-excitation signal subtracted) at $\Delta t = 0$ fs. (d, e) Energy distribution curves (EDCs) (d) at $\overline{K}$ and (e) at $\overline{\Gamma}$ in equilibrium and after weak excitation ($F = 0.14$ mJ cm^{-2}, $\Delta t = -40$ to $+40$ fs, momentum-integration ± 0.05 Å^{-1}). The red dashed curves mark best fits as described in the text. The black arrow indicates the in-gap intensity extending into the conduction band upon photoexcitation (see discussion). The direct and indirect band gaps are marked in blue.

bismuthene along structure-induced domain boundaries.[24] However, a demonstration of the elusive ESs using a momentum-resolved probe has proven challenging, as they constitute only a marginal fraction of the total surface area. Furthermore, confirmation of the theoretically predicted large indirect bulk band gap of bismuthene and characterization of microscopic carrier scattering processes are still missing, as previous studies largely relied on momentum-integrating local probes.[14,21,24]

Here, we investigate the ultrafast electron dynamics of photoexcited bismuthene at room temperature using trARPES, as illustrated in Figure 1a, allowing us to access the microscopic scattering channels from the dynamics of the nonequilibrium state prepared by optical excitation. Combining a hemispherical analyzer and a time-of-flight momentum microscope for photoelectron detection,[25,26] we map the transiently populated conduction band structure and confirm the existence of a wide indirect bulk band gap of ∼0.82 eV. In addition, we identify faint gap-filling spectral weight that
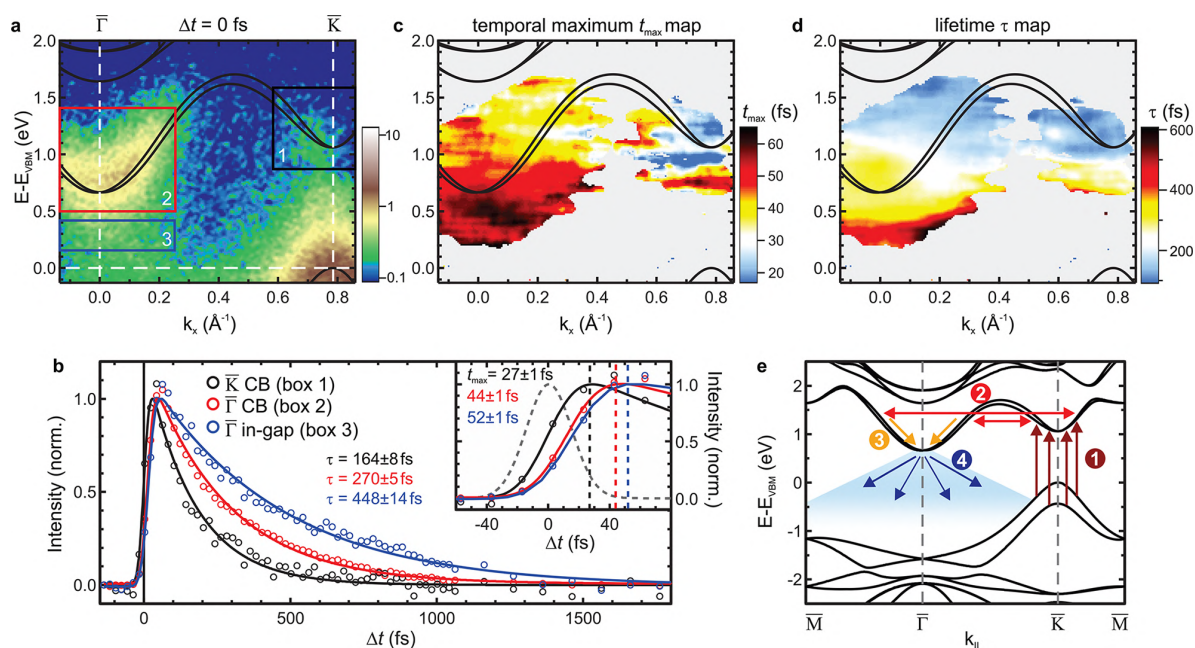
Figure 3. Carrier relaxation dynamics. (a) Excited-state band dispersion after 1.55 eV optical excitation ($F = 0.50$ mJ cm^{-2}). (b) Normalized photoemission intensities corresponding to boxes 1−3 indicated in panel a as a function of pump−probe delay. The solid lines show best fits using a single-exponential decay convolved with a Gaussian (Gaussian width as free parameter). The fit parameters t_{max} (temporal intensity maximum) and τ ($1/e$ decay constant) are given with one standard deviation as uncertainty. Inset: dynamics near $\Delta t = 0$ fs. The gray dashed line indicates the temporal profile of the pump-laser pulse. (c) Temporal maximum t_{max} and (d) carrier lifetimes τ from bin-wise energy- and momentum-dependent decay fits. For this, the transient photoemission intensities are extracted across the energy-momentum region shown in panel a using a sliding-window integration ($\Delta E = 0.1$ eV, $\Delta k_x = 0.15$ Å^{-1}) and fitted using the function described above. Regions with low photoemission intensity or large fit uncertainties ($\sigma_{t_{max}} > 10$ fs, $\sigma_{\tau} > 40$ fs) are masked in gray. (e) Schematic scattering processes within the DFT band structure (see text). The in-gap states are indicated in blue.

connects bulk valence and conduction bands, which we attribute largely to the topological ESs located at the structural domain boundaries of bismuthene.[24] Tracking the full relaxation pathway of hot photocarriers across the entire first Brillouin zone (BZ) reveals a fast depletion of the transient conduction band population within ∼1 ps, as the in-gap states enable a highly efficient relaxation of excited carriers, incompatible with the slow recombination observed in topologically trivial indirect semiconductors.

Bismuthene was epitaxially grown on SiC(0001) substrates (see Methods). High-quality sample surfaces with low defect rates were confirmed using scanning tunneling microscopy (STM) and low-energy electron diffraction (LEED), see Supplementary Figure S1.

We begin by mapping the electronic band structure of bismuthene upon photoexcitation, as shown in Figure 1b. Strong spin−orbit coupling in combination with covalent bonding of the Bi atoms with the substrate opens a large band gap in the Dirac-like crossing at the $\overline{K}$ points of the hexagonal BZ.[27] Excitation with near-infrared optical pulses lifts charge carriers across the bulk band gap and transiently populates conduction band states localized at $\overline{K}$ and, more pronounced, at the $\overline{\Gamma}$ points of the first and second BZs 1 eV above the valence-band maximum (VBM). Next, we focus on a momentum cut along the $\overline{\Gamma}-\overline{K}$ direction, which features the region of the direct optical interband transition near $\overline{K}$ and the conduction-band minimum (CBM) at $\overline{\Gamma}$. Consistent with previous studies,[14] the equilibrium band structure of bismuthene features sharp spin−orbit split low-energy valence

bands at $\overline{K}$ (Figure 2a). Upon optical excitation, a weak excited carrier population at $\overline{K}$ and a distinct dispersive band at the CBM at $\overline{\Gamma}$ emerge (Figures 2b,c). Concurrently, the valence bands at $\overline{K}$ are depleted by the optical transition (blue colored region in Figure 2c), and their bandwidth broadens due to scattering of the photoholes with excited quasiparticles.[28,29]

Band-gap renormalization by photodoping is particularly pronounced in 2D materials due to reduced charge carrier screening.[30,31] To minimize this effect, we extract the direct and indirect band gaps at temporal pump−probe overlap using a low incident fluence of 0.14 mJ cm^{-2}, as shown in Figures 2d,e. At $\overline{K}$, we find a direct band gap of 1.05 ± 0.02 eV, extracted from the peak positions of Gaussian fits to the upper spin−orbit split band at the VBM and to the lowest-lying CB, which is in excellent agreement with density functional theory (DFT) calculations (1.07 eV[14]). The indirect band gap between the VBM at $\overline{K}$ and the CBM at $\overline{\Gamma}$, extracted using a Gaussian fit with an exponentially decaying background, amounts to 0.82 ± 0.02 eV, which is in reasonable correspondence with the DFT value of 0.67 eV.[14] Further-more, the experimental value also perfectly agrees with the momentum-integrated bulk band gap of ∼0.8 eV obtained from STS measurements.[14] We note that already at a low fluence of 0.14 mJ cm^{-2}, the indirect quasiparticle band gap is weakly renormalized by ∼40 meV within 100 fs, resulting from the increased screening by quasi-free photocarriers (Supple-mentary Figure S2). For moderate fluences, we observe a significant initial band gap reduction by ∼150 meV, followed by a transient recovery, in agreement with previous studies of
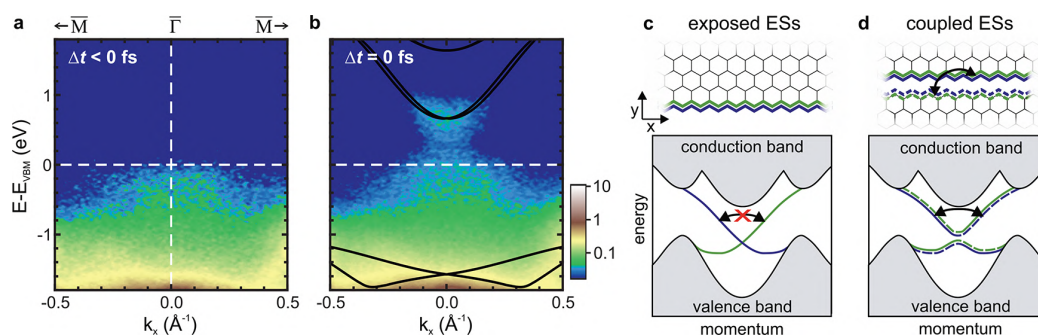
Figure 4. In-gap intensity. (a) Photoemission spectra at $\bar{\Gamma}$ in equilibrium and (b) after optical excitation ($h\nu$ = 1.55 eV, F = 0.32 mJ cm^{-2}). Faint spectral weight is located between the band gap predicted by bulk DFT calculations (black), connecting the valence and conduction states. Visibility of the in-gap states is enhanced by a logarithmic color scale. (c, d) (top) Sketch of helical ESs (blue, green) at an exposed sample edge with zigzag termination and of coupled ESs at a domain boundary, respectively. (bottom) Schematic dispersion of infinitely extended exposed and coupled 1D ESs, respectively. The projected bulk band structure is indicated in gray. The hybridization of coupled ES pairs opens an energy gap and lifts spin-momentum locking, enabling single-particle backscattering, indicated by the black arrow. The size of the gap opening at the crossing of the ES dispersion, however, is expected to be significantly lower than our experimental energy resolution of ~150 meV. Adopted from refs 14 and 24.

2D semiconductors.[30,31] Additional measurements using 3.1 eV optical excitation, providing a larger view into the dispersion of the lowest-energy conduction band, are shown in Supplementary Figure S3.

Next, to elucidate the quasiparticle scattering channels in the photocarrier relaxation processes of bismuthene, we investigate the excited-state population dynamics after 1.55 eV optical excitation along the $\bar{\Gamma}-\bar{K}$ direction (Figure 3a). As the transient photoemission intensities in Figure 3b show, a CB population builds up first near $\bar{K}$ (box 1 in Figure 3a), reaching its maximum intensity at 27 fs. The apparent delay with respect to temporal pump–probe overlap is due to a buildup of the excited-state population at the $\bar{K}$ valley until the end of the pump laser pulse, see the inset in Figure 3b. Subsequently, carriers appear at $\bar{\Gamma}$ (box 2) with a delay of ~40 fs, and last a faint intensity within the bulk band gap at $\bar{\Gamma}$ (box 3) builds up, followed by a complete recovery on a time scale of ~1 ps. We quantify these dynamics by employing single-exponential decay fits, characterized by the time delay at which the excited-state population reaches the maximum, t_{max}, and the $1/e$ lifetime, τ. To establish the full energy- and momentum-dependent scattering pathway, we extend this evaluation of three exemplary areas by fitting the transient intensity of each energy–momentum bin across Figure 3a using a sliding integration window. The resulting energy–momentum maps of the fit parameters t_{max} and τ allow us to track the arrival time of excited carriers in energy–momentum space (Figure 3c) and provide a concise overview of the lifetimes associated with particular states (Figure 3d).

Combining the results of both maps yields a detailed picture of the complete carrier relaxation pathway, schematically depicted in Figure 3e: (1) Carriers are initially injected by a vertical interband transition into the CB near $\bar{K}$ using 1.55 eV radiation. (2) The hot electrons redistribute by intervalley scattering, which spreads the carriers over an extended momentum region into the $\bar{\Gamma}$ valley on a 10 fs time scale, a phenomenon commonly observed in photoexcited semiconductors.[32−35] (3) Subsequently, hot carriers relax toward the CBM at $\bar{\Gamma}$ via electron–electron and electron–phonon scattering within ~50 fs. Although bulk bismuthene exhibits an indirect band gap of nearly 1 eV, the lifetime of the conduction band population is only on the order of few 100 fs, an orders of

magnitude faster relaxation than in conventional indirect semiconductors.[32,36−39] (4) These ultrashort lifetimes indicate a highly efficient carrier relaxation. The question naturally arises which states other than the insulating 2D bulk states in bismuthene could mediate the observed fast decay. Intriguingly, we observe faint gap-filling spectral weight reaching up to the CBM for several 100 fs after photoexcitation (Supplementary Figure S4), which we discuss below. A relaxation of the conduction band population through these in-gap states is supported by the fact that they are populated last and feature the longest lifetimes. Finally, within ~1.5 ps, also the in-gap states above the VBM are fully depleted. Note that the extracted population lifetimes are distinct from single-particle lifetimes that are directly encoded in the electron self-energy, and thus only represent an upper limit for the time scale of scattering processes.[40,41]

Lastly, we examine the in-gap spectral weight, and we discuss its origin. We find that already in equilibrium a faint intensity is located at $\bar{\Gamma}$ reaching up to E_{VBM} (Figure 4a). Upon optical excitation, the in-gap intensity extends into the CBM (Figure 4b), resulting in the absence of an explicit gap between bulk conduction and valence bands (black arrow in Figure 2e). While it may seem obvious to assign the in-gap feature to the topological ESs that were directly probed in previous STM/STS studies,[14,21,24] a careful examination is required.

For that, we compare the relaxation dynamics and the in-gap feature for bismuthene grown on two different substrate types, that is, intentionally miscut and planar SiC substrates (Supplementary Figure S1). Using a miscut substrate yields a high density of unidirectional, topologically protected exposed ES along the parallel substrate step edges, as illustrated in Figure 4c, while bismuthene prepared on a planar substrate features only a negligible density of (randomly oriented) substrate steps with exposed ESs. Yet, for both substrate types, additional topological ESs arise at structural phase-slip domain boundaries within the 2D bulk of bismuthene. These domain boundaries result from the fact that the $(\sqrt{3} \times \sqrt{3})$ Bi honeycombs can have three distinct registries with respect to the substrate lattice, causing the growth of domains. Pairs of helical ESs emerge at the zigzag edges on either side of these boundaries, see Figure 4d, lifting the topological protection through mutual hybridization and leading to a mixing of

different helicities, as confirmed by local tunneling spectroscopy.[24]

The presented characterization of the in-gap feature and relaxation dynamics was conducted on bismuthene prepared on a miscut substrate. However, in bismuthene prepared on a planar substrate featuring only a negligible density of exposed ESs, equivalent relaxation dynamics (Supplementary Figure S5) and a similar in-gap feature (Supplementary Figures S4 and S6) are observed. This leads us to the conclusion that the in-gap intensity primarily originates from topological ESs that arise at structural domain boundaries, which are present in both planar and miscut samples. The faint intensity of the in-gap states on the order of a few percent of the bismuthene bulk bands at $\bar{K}$ is consistent with the assignment to coupled ESs, as the domain boundaries constitute only a fraction of the probed surface. We further conclude that the relaxation of excited-state charge carriers must be strongly facilitated by the quasi-metallic density of states observed at such domain boundaries, enabling the rapid depletion of the conduction band population, analogous to the depletion of conduction band populations by topological surface states in photoexcited 3D TIs.[8] Since we do not observe large deviations for the decay times in the case of the bismuthene sample grown on a miscut substrate (Supplementary Figure S5), any definite conclusion on the additional role of the exposed topological ESs is difficult to draw at this point. Future developments in (time-resolved) nano-ARPES featuring a nanometer spatial resolution may allow isolation of the spectral features of exposed ESs at substrate terrace steps and individual pairs of coupled ESs at domain boundaries.

While the coupled ESs at domain boundaries consistently explain the in-gap spectral weight and short photocarrier lifetimes, several alternative scenarios can potentially induce a continuous in-gap intensity. First, impurities and defects may provide additional states within the bulk band gap. However, STM/STS studies show that only domain boundaries and exposed sample edges host in-gap states, while all other sample regions remain fully gapped.[14,21,24] In addition, the observed confinement of the in-gap intensity to the momentum-region near $\bar{\Gamma}$ speaks against impurities as primary origin, as such defect states typically lack a clear momentum dependence.[42] Second, a large energy line-width of the bismuthene bulk valence band may lead to a metal-like extension of intensity up to the Fermi level. However, analogous to the first line of argument, spatially resolved STS measurements unambiguously demonstrate insulating behavior in bulk regions,[14] indicating that the observed continuous in-gap intensity is not connected to bulk bismuthene but rather to ESs. Thus, by excluding alternative interpretations and consistent with earlier local tunneling spectroscopy results,[24] we assign the in-gap spectral weight largely to coupled ESs at domain boundaries. As ESs forming along extended 1D defects critically limit the lifetime of excited carriers and may also pose challenges for applications utilizing the spin-selective transport along exposed sample edges,[23,43] our study underlines the need for high-quality sample surfaces.

In conclusion, we experimentally mapped the electronic band structure of the quantum spin Hall insulator bismuthene after near-infrared photoexcitation and determined the direct and indirect band gaps of ~1.1 eV and ~0.8 eV, respectively. Analysis of the microscopic scattering pathway of hot photocarriers revealed exceptionally fast carrier relaxation dynamics governed by faint in-gap states located within the indirect band gap, which correspond with the topological edge states arising at bismuthene domain boundaries. The demonstration of a large fundamental band gap and the in-gap spectral weight persisting at room temperature and under strong optical excitation highlight the promising role of bismuthene as an ambient-condition quantum spin Hall candidate. Additionally, due to the exceptionally large band gap, bismuthene serves as a unique platform for optically addressing novel functionalities based on the topological edge states and for studying excitons in a topologically nontrivial system. Our insights gained on quasiparticle scattering processes lay the basis for future studies of sub-band gap excitations and optical control schemes of edge-state currents.[44,45]

◼ METHODS

Sample Preparation and STM Measurements. Bismuthene was epitaxially grown on n-doped 4H-SiC(0001) substrates (0.01−0.03 Ω·cm, carrier concentration ~10^{18}–10^{19} cm^{-3}, planar and 4° miscut) in ultrahigh vacuum <10^{-10} mbar. Prior to growth, a smooth H-terminated SiC surface was prepared by hydrogen-based dry-etching. Growth was performed at ~600 °C to thermally desorb the surface H-termination, while simultaneously offering Bi atoms from a commercial effusion cell.[14] Successful growth of low-defect bismuthene samples was verified using low-energy electron diffraction and scanning tunneling microscopy.

Time-Resolved ARPES Measurements. After characterization, the samples were transferred to the trARPES setup using an UHV suitcase at $p < 10^{-10}$ mbar. All measurements were performed at room temperature using a laser-based high-harmonic-generation trARPES setup (p-polarized probe at $h\nu_{\text{probe}} = 21.7$ eV, s-polarized pump at $h\nu_{\text{pump}} = 1.55$, 3.10 eV, 500 kHz repetition rate, $\Delta E \approx 150$ meV, $\Delta t \approx 40$ fs) with a 6-axis manipulator (SPECS Carving).[25] Photoelectrons were detected with either a hemispherical analyzer (SPECS Phoibos 150) or a time-of-flight momentum microscope (SPECS METIS 1000).[26] The momentum microscope allows for parallel acquisition of the 3D photoelectron distribution $I(E_{\text{kin}}, k_x, k_y)$ across a large energy and momentum range and was thus utilized for overview measurements of the electronic band structure (Figure 1). In contrast, the hemispherical analyzer allows for fast data acquisition within a limited energy-momentum window, and was thus used to map selected high-symmetry directions (Figures 2–4). The data presented in Figure 1 were acquired on a planar substrate and that in Figures 2–4 on a miscut substrate. The extreme ultraviolet (XUV) probe spot size (fwhm) was ~80×80 μm^2. The pump spot sizes were ~260×200 μm^2 ($h\nu = 1.55$ eV) and ~510×475 μm^2 ($h\nu = 3.10$ eV). All fluences stated in the text correspond to incident fluences. Temporal pump−probe overlap was determined from the pump-laser-induced depletion of the valence band population, as shown in Supplementary Figure S7.

◼ ASSOCIATED CONTENT

Ⓢ Supporting Information

The Supporting Information is available free of charge at https://pubs.acs.org/doi/10.1021/acs.nanolett.2c01462.

> STM and LEED surface characterization of the bismuthene samples, characterization of the time-dependent quasiparticle band gap, mapping of the

conduction-band dispersion after 3 eV optical excitation, additional trARPES characterization of the in-gap spectral weight, and determination of temporal pump–probe overlap (PDF)

AUTHOR INFORMATION

Corresponding Author

Laurenz Rettig − *Fritz-Haber-Institut der Max-Planck-Gesellschaft, D-14195 Berlin, Germany*; Email: rettig@fhi-berlin.mpg.de

Authors

Julian Maklar − *Fritz-Haber-Institut der Max-Planck-Gesellschaft, D-14195 Berlin, Germany;* ⊙ orcid.org/0000-0003-4123-4455

Raúl Stühler − *Physikalisches Institut and Würzburg-Dresden Cluster of Excellence ct.qmat, University of Würzburg, D-97070 Würzburg, Germany*

Maciej Dendzik − *Fritz-Haber-Institut der Max-Planck-Gesellschaft, D-14195 Berlin, Germany;* Present Address: Department of Applied Physics, KTH Royal Institute of Technology, Hannes Alfvns vg 12, 114 19 Stockholm, Sweden

Tommaso Pincelli − *Fritz-Haber-Institut der Max-Planck-Gesellschaft, D-14195 Berlin, Germany*

Shuo Dong − *Fritz-Haber-Institut der Max-Planck-Gesellschaft, D-14195 Berlin, Germany*

Samuel Beaulieu − *Fritz-Haber-Institut der Max-Planck-Gesellschaft, D-14195 Berlin, Germany;* Present Address: Université de Bordeaux, CNRS, CEA, CELIA, UMR5107, F33405, Talence, France.

Alexander Neef − *Fritz-Haber-Institut der Max-Planck-Gesellschaft, D-14195 Berlin, Germany*

Gang Li − *School of Physical Science and Technology, ShanghaiTech University, Shanghai 200031, China*

Martin Wolf − *Fritz-Haber-Institut der Max-Planck-Gesellschaft, D-14195 Berlin, Germany*

Ralph Ernstorfer − *Fritz-Haber-Institut der Max-Planck-Gesellschaft, D-14195 Berlin, Germany; Institut für Optik und Atomare Physik, Technische Universität Berlin, 10623 Berlin, Germany;* ⊙ orcid.org/0000-0001-6665-3520

Ralph Claessen − *Physikalisches Institut and Würzburg-Dresden Cluster of Excellence ct.qmat, University of Würzburg, D-97070 Würzburg, Germany*

Complete contact information is available at:
https://pubs.acs.org/10.1021/acs.nanolett.2c01462

Author Contributions

J.M., M.D., R.S., S.D., S.B., T.P., A.N., and L.R. carried out the trARPES experiments; J.M. analyzed the trARPES data with support from R.S.; R.S. prepared and characterized the samples and analyzed the STM data; G.L. performed the DFT calculations; J.M. wrote the manuscript with support from L.R., R.S., R.E., and R.C.; L.R., R.E., M.W., and R.C. provided the experimental infrastructure; all authors commented on the paper.

Notes

The authors declare no competing financial interest.

All data that support the findings of this study are publicly available at the Zenodo data repository, 10.5281/zenodo.5512069.

REFERENCES

(1) Avsar, A.; Ochoa, H.; Guinea, F.; Özyilmaz, B.; van Wees, B.; Vera-Marun, I. J. Colloquium: Spintronics in graphene and other two-dimensional materials. *Rev. Mod. Phys.* **2020**, *92*, 021003.

(2) Hasan, M. Z.; Kane, C. L. Colloquium: topological insulators. *Rev. Mod. Phys.* **2010**, *82*, 3045.

(3) Kane, C. L.; Mele, E. J. Quantum spin Hall effect in graphene. *Phys. Rev. Lett.* **2005**, *95*, 226801.

(4) Tang, S.; Zhang, C.; Wong, D.; Pedramrazi, Z.; Tsai, H.-Z.; Jia, C.; Moritz, B.; Claassen, M.; Ryu, H.; Kahn, S.; et al. Quantum spin Hall state in monolayer 1T'-WTe$_2$. *Nat. Phys.* **2017**, *13*, 683−687.

(5) Chen, P.; Pai, W. W.; Chan, Y.-H.; Sun, W.-L.; Xu, C.-Z.; Lin, D.-S.; Chou, M.; Fedorov, A.-V.; Chiang, T.-C. Large quantum-spin-Hall gap in single-layer 1-T' WSe$_2$. *Nat. Commun.* **2018**, *9*, 2003.

(6) Wu, R.; Ma, J.-Z.; Nie, S.-M.; Zhao, L.-X.; Huang, X.; Yin, J.-X.; Fu, B.-B.; Richard, P.; Chen, G.-F.; Fang, Z.; et al. Evidence for topological edge states in a large energy gap near the step edges on the surface of ZrTe$_5$. *Phys. Rev. X* **2016**, *6*, 021017.

(7) Wang, Y.; Hsieh, D.; Sie, E.; Steinberg, H.; Gardner, D.; Lee, Y.; Jarillo-Herrero, P.; Gedik, N. Measurement of intrinsic Dirac fermion cooling on the surface of the topological insulator Bi$_2$Se$_3$ using time-resolved and angle-resolved photoemission spectroscopy. *Phys. Rev. Lett.* **2012**, *109*, 127401.

(8) Sobota, J. A.; Yang, S.; Analytis, J. G.; Chen, Y.; Fisher, I. R.; Kirchmann, P. S.; Shen, Z.-X. Ultrafast optical excitation of a persistent surface-state population in the topological insulator Bi$_2$Se$_3$. *Phys. Rev. Lett.* **2012**, *108*, 117403.

(9) Sobota, J. A.; Yang, S.-L.; Leuenberger, D.; Kemper, A. F.; Analytis, J. G.; Fisher, I. R.; Kirchmann, P. S.; Devereaux, T. P.; Shen, Z.-X. Distinguishing bulk and surface electron-phonon coupling in the topological insulator Bi$_2$Se$_3$ using time-resolved photoemission spectroscopy. *Phys. Rev. Lett.* **2014**, *113*, 157401.

(10) Cacho, C.; Crepaldi, A.; Battiato, M.; Braun, J.; Cilento, F.; Zacchigna, M.; Richter, M.; Heckmann, O.; Springate, E.; Liu, Y.; et al. Momentum-resolved spin dynamics of bulk and surface excited states in the topological insulator Bi$_2$Se$_3$. *Phys. Rev. Lett.* **2015**, *114*, 097401.

(11) Neupane, M.; Xu, S.-Y.; Ishida, Y.; Jia, S.; Fregoso, B. M.; Liu, C.; Belopolski, I.; Bian, G.; Alidoust, N.; Durakiewicz, T.; et al. Gigantic surface lifetime of an intrinsic topological insulator. *Phys. Rev. Lett.* **2015**, *115*, 116801.

(12) Sumida, K.; Kakoki, M.; Reimann, J.; Nurmamat, M.; Goto, S.; Takeda, Y.; Saitoh, Y.; Kokh, K.; Tereshchenko, O.; Güdde, J.; et al. Magnetic-impurity-induced modifications to ultrafast carrier dynamics in the ferromagnetic topological insulators $Sb_{2-x}V_xTe_3$. *New J. Phys.* **2019**, *21*, 093006.

(13) Reimann, J.; Schlauderer, S.; Schmid, C.; Langer, F.; Baierl, S.; Kokh, K.; Tereshchenko, O.; Kimura, A.; Lange, C.; Güdde, J.; et al. Subcycle observation of lightwave-driven Dirac currents in a topological surface band. *Nature* **2018**, *562*, 396−400.

(14) Reis, F.; Li, G.; Dudy, L.; Bauernfeind, M.; Glass, S.; Hanke, W.; Thomale, R.; Schaefer, J.; Claessen, R. Bismuthene on a SiC substrate: A candidate for a high-temperature quantum spin Hall material. *Science* **2017**, *357*, 287−290.

(15) König, M.; Wiedmann, S.; Brüne, C.; Roth, A.; Buhmann, H.; Molenkamp, L. W.; Qi, X.-L.; Zhang, S.-C. Quantum spin Hall insulator state in HgTe quantum wells. *Science* **2007**, *318*, 766−770.

(16) Knez, I.; Du, R.-R.; Sullivan, G. Evidence for Helical Edge Modes in Inverted InAs/GaSb Quantum Wells. *Phys. Rev. Lett.* **2011**, *107*, 136603.

(17) Leubner, P.; Lunczer, L.; Brüne, C.; Buhmann, H.; Molenkamp, L. W. Strain engineering of the band gap of HgTe quantum wells using superlattice virtual substrates. *Phys. Rev. Lett.* **2016**, *117*, 086403.

(18) Fei, Z.; Palomaki, T.; Wu, S.; Zhao, W.; Cai, X.; Sun, B.; Nguyen, P.; Finney, J.; Xu, X.; Cobden, D. H. Edge conduction in monolayer WTe_2. *Nat. Phys.* **2017**, *13*, 677−682.

(19) Wu, S.; Fatemi, V.; Gibson, Q. D.; Watanabe, K.; Taniguchi, T.; Cava, R. J.; Jarillo-Herrero, P. Observation of the quantum spin Hall effect up to 100 K in a monolayer crystal. *Science* **2018**, *359*, 76−79.

(20) Sun, S.; et al. Epitaxial Growth of Ultraflat Bismuthene with Large Topological Band Inversion Enabled by Substrate-Orbital-Filtering Effect. *ACS Nano* **2022**, *16*, 1436−1443.

(21) Stühler, R.; Reis, F.; Müller, T.; Helbig, T.; Schwemmer, T.; Thomale, R.; Schäfer, J.; Claessen, R. Tomonaga−Luttinger liquid in the edge channels of a quantum spin Hall insulator. *Nat. Phys.* **2020**, *16*, 47−51.

(22) Lima, E. N.; Schmidt, T. M.; Nunes, R. W. Topologically protected metallic states induced by a one-dimensional extended defect in the bulk of a 2D topological insulator. *Nano Lett.* **2016**, *16*, 4025−4031.

(23) Pezo, A.; Focassio, B.; Schleder, G. R.; Costa, M.; Lewenkopf, C.; Fazzio, A. Disorder effects of vacancies on the electronic transport properties of realistic topological insulator nanoribbons: The case of bismuthene. *Phys. Rev. Mater.* **2021**, *5*, 014204.

(24) Stühler, R.; Kowalewski, A.; Reis, F.; Jungblut, D.; Dominguez, F.; Scharf, B.; Li, G.; Schäfer, J.; Hankiewicz, E. M.; Claessen, R. Lifting topological protection in a quantum spin Hall insulator by edge coupling. *arXiv* 2021, 2111.04348, https://arxiv.org/abs/2111.04348 (accessed June 11, 2022).

(25) Puppin, M.; Deng, Y.; Nicholson, C.; Feldl, J.; Schröter, N.; Vita, H.; Kirchmann, P.; Monney, C.; Rettig, L.; Wolf, M.; et al. Time- and angle-resolved photoemission spectroscopy of solids in the extreme ultraviolet at 500 kHz repetition rate. *Rev. Sci. Instrum.* **2019**, *90*, 023104.

(26) Maklar, J.; Dong, S.; Beaulieu, S.; Pincelli, T.; Dendzik, M.; Windsor, Y.; Xian, R.; Wolf, M.; Ernstorfer, R.; Rettig, L. A quantitative comparison of time-of-flight momentum microscopes and hemispherical analyzers for time-and angle-resolved photo-emission spectroscopy experiments. *Rev. Sci. Instrum.* **2020**, *91*, 123112.

(27) Li, G.; Hanke, W.; Hankiewicz, E. M.; Reis, F.; Schäfer, J.; Claessen, R.; Wu, C.; Thomale, R. Theoretical paradigm for the quantum spin Hall effect at high temperatures. *Phys. Rev. B* **2018**, *98*, 165146.

(28) Kanasaki, J.; Tanimura, H.; Tanimura, K.; Ries, P.; Heckel, W.; Biedermann, K.; Fauster, T. Ultrafast dynamics in photoexcited valence-band states of Si studied by time-and angle-resolved photoemission spectroscopy of bulk direct transitions. *Phys. Rev. B* **2018**, *97*, 035201.

(29) Dendzik, M.; et al. Observation of an Excitonic Mott Transition through Ultrafast Core-cum-Conduction Photoemission Spectrosco-py. *Phys. Rev. Lett.* **2020**, *125*, 096401.

(30) Liu, F.; Ziffer, M. E.; Hansen, K. R.; Wang, J.; Zhu, X. Direct determination of band-gap renormalization in the photoexcited monolayer MoS_2. *Phys. Rev. Lett.* **2019**, *122*, 246803.

(31) Ulstrup, S.; Čabo, A. G.; Miwa, J. A.; Riley, J. M.; Grønborg, S. S.; Johannsen, J. C.; Cacho, C.; Alexander, O.; Chapman, R. T.; Springate, E.; Bianchi, M.; Dendzik, M.; Lauritsen, J. V.; King, P. D. C.; Hofmann, P. Ultrafast Band Structure Control of a Two-Dimensional Heterostructure. *ACS Nano* **2016**, *10*, 6315−6322.

(32) Bertoni, R.; Nicholson, C. W.; Waldecker, L.; Hübener, H.; Monney, C.; De Giovannini, U.; Puppin, M.; Hoesch, M.; Springate, E.; Chapman, R. T.; et al. Generation and evolution of spin-, valley-, and layer-polarized excited carriers in inversion-symmetric WSe_2. *Phys. Rev. Lett.* **2016**, *117*, 277201.

(33) Hein, P.; Stange, A.; Hanff, K.; Yang, L.; Rohde, G.; Rossnagel, K.; Bauer, M. Momentum-resolved hot electron dynamics at the 2H-MoS_2 surface. *Phys. Rev. B* **2016**, *94*, 205406.

(34) Madéo, J.; Man, M. K.; Sahoo, C.; Campbell, M.; Pareek, V.; Wong, E. L.; Al- Mahboob, A.; Chan, N. S.; Karmakar, A.; Mariserla, B. M. K.; et al. Directly visualizing the momentum-forbidden dark excitons and their dynamics in atomically thin semiconductors. *Science* **2020**, *370*, 1199−1204.

(35) Dong, S.; et al. Direct measurement of key exciton properties: Energy, dynamics, and spatial distribution of the wave function. *Nat. Sci.* **2021**, *1*, e10010.

(36) Schroder, D. K. *Semiconductor Material and Device Character-ization*; John Wiley & Sons, Ltd: Hoboken, NJ, 2005.

(37) Wang, H.; Zhang, C.; Rana, F. Surface recombination limited lifetimes of photoexcited carriers in few-layer transition metal dichalcogenide MoS_2. *Nano Lett.* **2015**, *15*, 8204−8210.

(38) Li, J.; Goryca, M.; Yumigeta, K.; Li, H.; Tongay, S.; Crooker, S. A. Valley relaxation of resident electrons and holes in a monolayer semiconductor: Dependence on carrier density and the role of substrate-induced disorder. *Phys. Rev. Mater.* **2021**, *5*, 044001.

(39) Lee, W.; Lin, Y.; Lu, L.-S.; Chueh, W.-C.; Liu, M.; Li, X.; Chang, W.-H.; Kaindl, R. A.; Shih, C.-K. Time-resolved ARPES Determination of a Quasi-Particle Band Gap and Hot Electron Dynamics in Monolayer MoS_2. *Nano Lett.* **2021**, *21*, 7363−7370.

(40) Yang, S.-L.; Sobota, J. A.; Leuenberger, D.; He, Y.; Hashimoto, M.; Lu, D. H.; Eisaki, H.; Kirchmann, P. S.; Shen, Z.-X. Inequivalence of Single-Particle and Population Lifetimes in a Cuprate Super-conductor. *Phys. Rev. Lett.* **2015**, *114*, 247001.

(41) Kemper, A. F.; Abdurazakov, O.; Freericks, J. K. General Principles for the Nonequilibrium Relaxation of Populations in Quantum Materials. *Phys. Rev. X* **2018**, *8*, 041009.

(42) Strocov, V. N.; Lev, L. L.; Kobayashi, M.; Cancellieri, C.; Husanu, M.-A.; Chikina, A.; Schröter, N. B. M.; Wang, X.; Krieger, J. A.; Salman, Z. k-resolved electronic structure of buried hetero-structure and impurity systems by soft-X-ray ARPES. *J. Electron Spectrosc. Relat. Phenom.* **2019**, *236*, 1−8.

(43) Tiwari, S.; Van de Put, M. L.; Sorée, B.; Vandenberghe, W. G. Carrier transport in two-dimensional topological insulator nanorib-bons in the presence of vacancy defects. *2D Mater.* **2019**, *6*, 025011.

(44) McIver, J. W.; Hsieh, D.; Steinberg, H.; Jarillo-Herrero, P.; Gedik, N. Control over topological insulator photocurrents with light polarization. *Nat. Nanotechnol.* **2012**, *7*, 96−100.

(45) Kuroda, K.; Reimann, J.; Kokh, K. A.; Tereshchenko, O. E.; Kimura, A.; Güdde, J.; Höfer, U. Ultrafast energy- and momentum-resolved surface Dirac photocurrents in the topological insulator Sb_2Te_3. *Phys. Rev. B* **2017**, *95*, 081103.

Supporting Information for "Ultrafast Momentum-resolved Hot Electron Dynamics in the Two-dimensional Topological Insulator Bismuthene"

Julian Maklar[1], Raúl Stühler[2], Maciej Dendzik[1,3], Tommaso Pincelli[1], Shuo Dong[1], Samuel Beaulieu[1,4], Alexander Neef[1], Gang Li[5], Martin Wolf[1], Ralph Ernstorfer[1,6], Ralph Claessen[2], and Laurenz Rettig[1]

[1] *Fritz-Haber-Institut der Max-Planck-Gesellschaft, Faradayweg 4-6, D-14195 Berlin, Germany*
[2] *Physikalisches Institut and Würzburg-Dresden Cluster of Excellence ct.qmat, University of Würzburg, D-97070 Würzburg, Germany*
[3] *Current address: Department of Applied Physics, KTH Royal Institute of Technology, Hannes Alfvéns väg 12, 114 19 Stockholm, Sweden*
[4] *Current address: Université de Bordeaux - CNRS - CEA, CELIA, UMR5107, F33405, Talence, France*
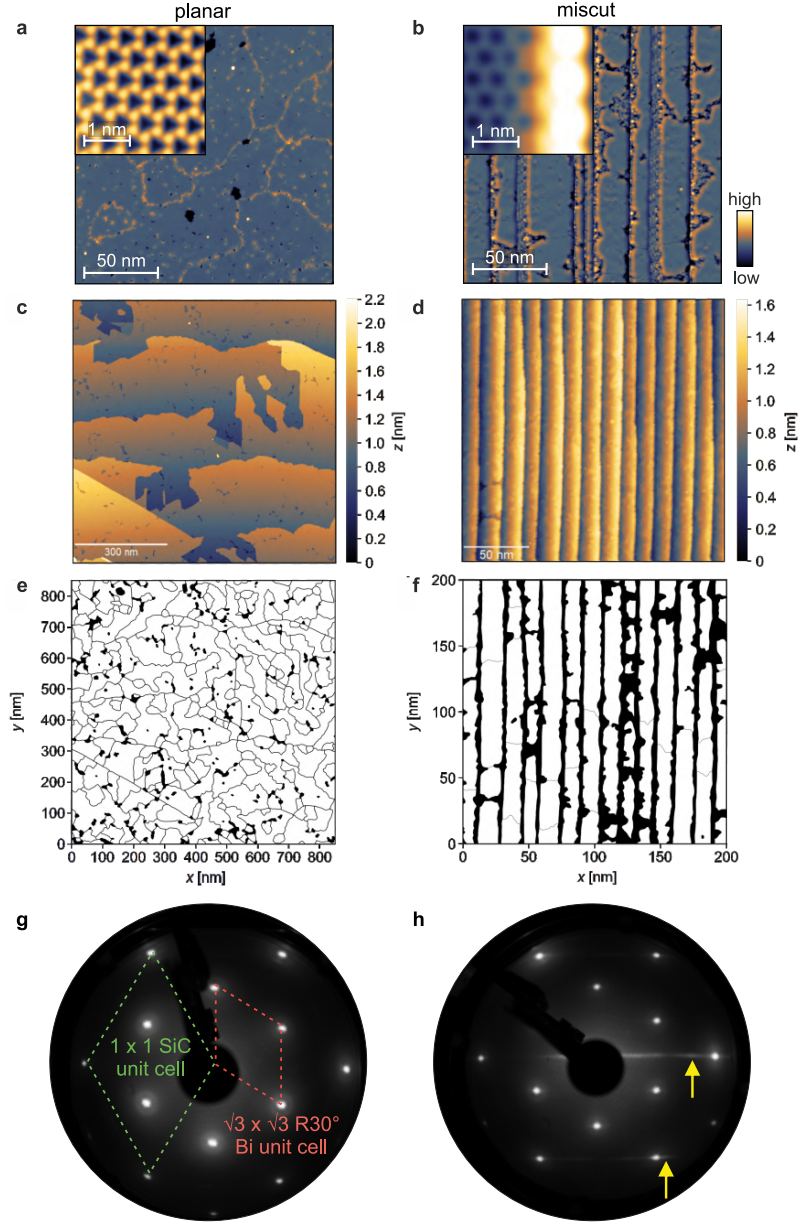[5] *School of Physical Science and Technology, ShanghaiTech University, Shanghai 200031, China*
[6] *Institut für Optik und Atomare Physik, Technische Universität Berlin, Straße des 17. Juni 135, 10623 Berlin, Germany*

June 11, 2022

Supplementary Figures

Supplementary Fig. S1: Surface characterization of bismuthene samples. (a) STM constant-current image of bismuthene on a planar SiC substrate. A meandering network of domain boundary segments (bright ridges) intersects the bismuthene film into connected domains. Inset: Close-up of the Bi honeycomb lattice. (b) STM image of bismuthene on a 4° miscut substrate featuring unidirectional SiC terrace steps every $\sim 15\,\mathrm{nm}$ that induce exposed bismuthene edges. Inset: Bi honeycombs near a step edge. While both the morphology of the planar and the miscut bismuthene samples feature domain boundaries, the miscut bismuthene sample exhibits a significantly larger exposed edge density. Scan parameters: $V_{\mathrm{set}} = 3.0\,\mathrm{V}$, $I_{\mathrm{set}} = 50\,\mathrm{pA}$, $T = 4.35\,\mathrm{K}$; insets: $V_{\mathrm{set}} = -0.8\,\mathrm{V}$, $I_{\mathrm{set}} = 100\,\mathrm{pA}$, $T = 4.35\,\mathrm{K}$. (c and d) Overview STM constant current images of bismuthene on a planar and a miscut substrate, respectively. Scan parameters: (c) $V_{\mathrm{set}} = 3.0\,\mathrm{V}$, $I_{\mathrm{set}} = 50\,\mathrm{pA}$, $T = 4.35\,\mathrm{K}$; (d) $V_{\mathrm{set}} = 2.6\,\mathrm{V}$, $I_{\mathrm{set}} = 30\,\mathrm{pA}$, $T = 4.35\,\mathrm{K}$. (e and f) Binary masks marking domain boundaries and defective areas on the planar and miscut samples from (c) and (d), respectively. (g) Low-energy electron diffraction of bismuthene on a planar SiC substrate recorded at an energy of $48\,\mathrm{eV}$ and (h) on a miscut substrate at $50\,\mathrm{eV}$. Sharp, intense diffraction spots and a weak diffuse background signal indicate high-quality sample surfaces. The yellow arrows in (h) mark stripe-like elongations of the SiC spots corresponding to unidirectional substrate step edges. Exemplary SiC 1x1 and Bi $\sqrt{3}$x$\sqrt{3}$ R30° reciprocal unit cells are indicated.
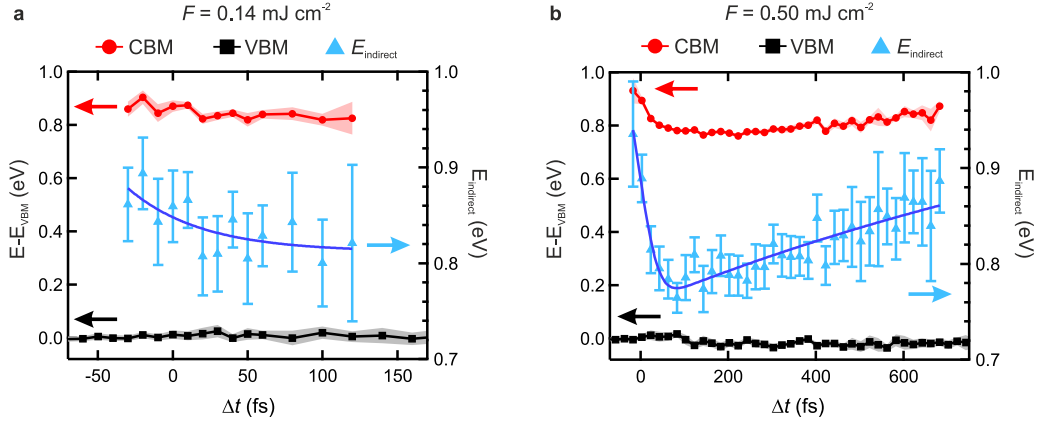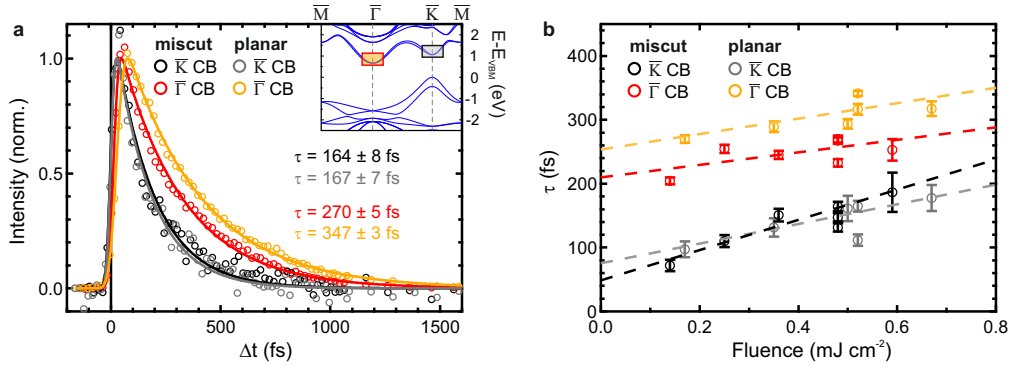
Supplementary Fig. S2: Renormalization of the quasiparticle band gap. Position of the CBM and VBM (left axis) and extracted indirect band gap (CBM-VBM difference, right axis) as a function of pump-probe delay for (a) low and (b) moderate incident fluence. When applying a low fluence of $F = 0.14\,\text{mJ}\,\text{cm}^{-2}$ (panel a), the VBM position remains approximately constant while the CBM position shifts slightly downwards within 100 fs, resulting in a reduction of the indirect band gap by ~ 40 meV. However, in this fluence regime, the limited number of hot carriers in combination with their fast relaxation allows for reliable tracking of the CBM only up to ~ 120 fs. For a moderate fluence of $F = 0.50\,\text{mJ}\,\text{cm}^{-2}$ (panel b), we observe a pronounced time-dependent band-gap renormalization, as the CBM undergoes a significant shift while also the position of the VBM changes with Δt. The photoexcited quasi-free carriers initially increase the screening of the Coulomb interactions, transiently reducing the effective band-gap size by ~ 150 meV. As the system relaxes to equilibrium, the band gap recovers with increasing Δt. The solid blue lines in (a) and (b) serve as guides to the eye. The band positions were extracted using Gaussian fits as discussed in the main text. The error bands and bars correspond to one standard deviation resulting from the Gaussian fits.
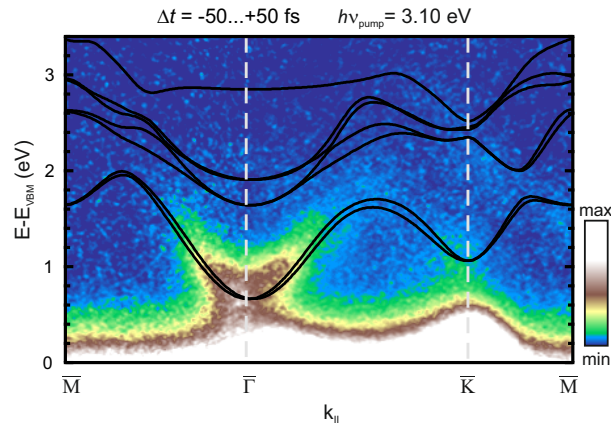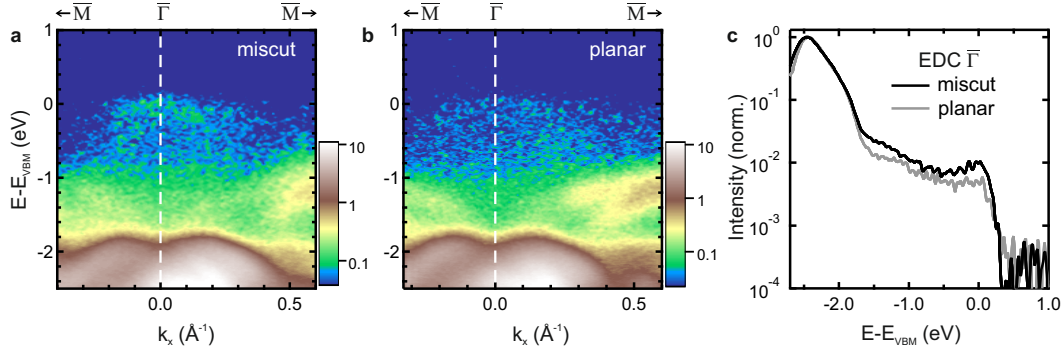

Supplementary Fig. S3: Conduction band dispersion after photoexcitation. Photoemission intensity along the high-symmetry momentum directions after 3.1 eV optical excitation ($F=0.03\,\text{mJ}\,\text{cm}^{-2}$) at temporal pump-probe overlap. DFT calculations are shown in black.

3
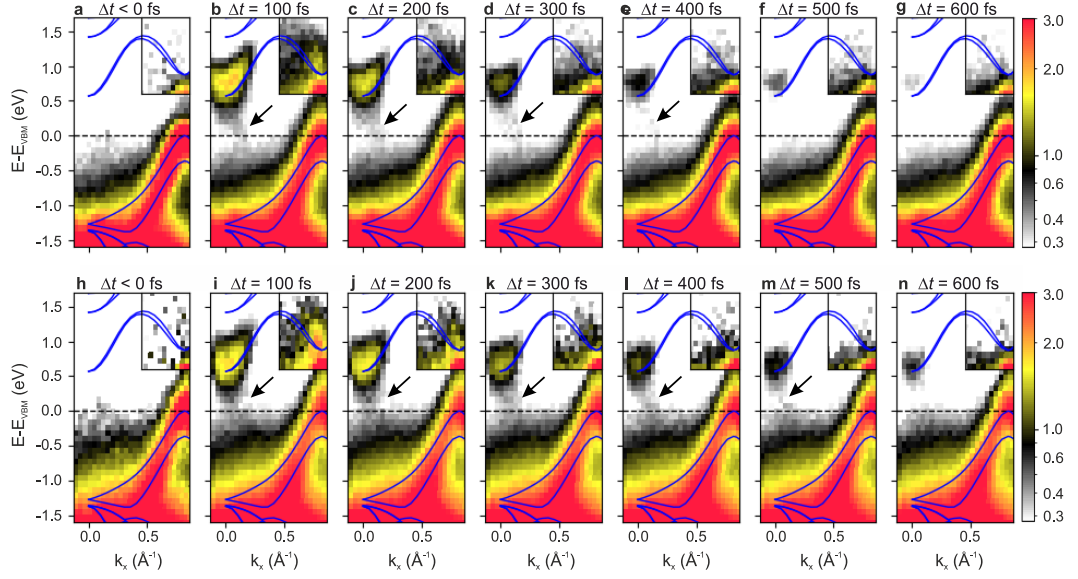
Supplementary Fig. S4: Dynamic band-structure maps. (a-g) False-colour plots of the trARPES measurements of bismuthene on a miscut substrate along the $\overline{\Gamma}$-$\overline{K}$ direction for selected time delays (time integration window of 200 fs, $h\nu = 1.55\,\mathrm{eV}$, $F=0.50\,\mathrm{mJ\,cm^{-2}}$). (h-n) Equivalent measurements for bismuthene on a planar substrate. The black arrows indicate the in-gap intensity near $\overline{\Gamma}$. The intensity in the insets at $\overline{K}$ is enhanced. DFT band structure calculations are shown in blue.


Supplementary Fig. S5: Photocarrier lifetimes. (a) Normalized photoemission intensities of the conduction band populations at $\overline{K}$ and $\overline{\Gamma}$ for bismuthene on miscut and planar substrates ($F=0.50\,\mathrm{mJ\,cm^{-2}}$) versus pump-probe delay. The inset indicates the energy-momentum regions of interest within the DFT band structure of the respective time traces (equivalent to boxes 1 and 2 in Fig. 3a). Single-exponential decay fits reveal similar $1/e$ lifetimes of the populations at $\overline{K}$ for both substrate types, and slightly increased lifetimes at $\overline{\Gamma}$ for the planar substrate. (b) Extracted lifetimes for both substrate types as function of incident fluence. The dashed lines serve as guides to the eye. While the overall lifetime increases with fluence, the lifetime at $\overline{\Gamma}$ for the planar substrate is systematically higher with respect to the miscut substrate for all applied fluences. The error bars correspond to one standard deviation of the fit parameter τ.

4

Supplementary Fig. S6: In-gap feature at $\overline{\Gamma}$. (a) Equilibrium band dispersion of bismuthene on a miscut substrate. A faint feature near the VBM is identified, which we assign to topological ESs. (b) Band dispersion of bismuthene on a planar substrate, exhibiting a similar, slightly less pronounced feature at $\overline{\Gamma}$. (c) Corresponding EDCs at $\overline{\Gamma}$. Both samples show a faint but distinct intensity up to E_{VBM}, which is roughly a factor 2 more intense for the miscut substrate.

Determination of temporal pump-probe overlap

To determine the temporal pump-probe overlap $\Delta t = 0\,\mathrm{fs}$, we extract the initial depletion of the valence band population at $\overline{\mathrm{K}}$ (red box in Supplementary Fig. S7a) resulting from the vertical optical transition. The extracted photoemission intensity as function of pump-probe delay is fitted using an error-function, see Supplementary Fig. S7b. Here, the central position of the error function corresponds to the temporal peak of the optical pump pulse, t_0. For all measurements presented in this manuscript, we calibrate the pump-probe delay such that $\Delta t = 0\,\mathrm{fs}$ corresponds to t_0.
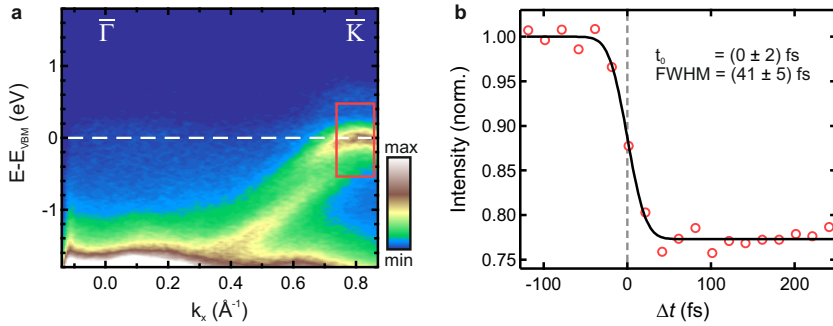

Supplementary Fig. S7: Arrival time of the optical excitation pulse. (a) Equilibrium ARPES measurement of the $\overline{\Gamma}$-$\overline{\mathrm{K}}$ direction. (b) Normalized photoemission intensity extracted from the red box in panel (a) as function of pump-probe delay (red circles, $h\nu_{\mathrm{pump}} = 1.55\,\mathrm{eV}$, incident fluence $F = 0.50\,\mathrm{mJ\,cm^{-2}}$). The black solid line marks the best fit using an error function. Fit coefficient values of the temporal peak t_0 and full width at half maximum of the pump pulse are stated in the figure, respectively. One standard deviation is given as uncertainty.

5

Discussion of publications

Time-resolved ARPES is a highly versatile method as it provides access to the photoemission matrix elements, the occupation function, and the spectral function with time resolution. Thus, it allows addressing a wide array of research questions in materials sciences. Fig. 5.1 summarizes the areas we explore in this thesis, ranging from method development – benchmarking a MM for trARPES experiments – to studying the thermally unoccupied band structure, microscopic interactions, and photoinduced phase transitions in various quantum materials. The material systems under investigation include strongly correlated materials, CDW systems, 2D TIs, and 2D atom lattices on semiconductor substrates, underlining the diversity of quantum materials and their emergent phases. In this chapter, we summarize the four central publications reprinted in the previous chapter, discuss their connection, examine their implications, and put them into context with additional work presented in Appendices A and B.

Momentum microscopy for trARPES experiments. Recent advancements in time-of-flight-based MMs have led to a growing presence of this novel detection scheme in photoemission studies, as it enables a highly parallelized and simultaneous acquisition of the full 3-dimensional momentum- and energy-resolved photoelectron distribution [113–115]. Combining such instruments with modern high-repetition-rate extreme ultraviolet (XUV) laser sources for ultrafast pump-probe photoemission experiments seems like an ideal match and is followed by several groups worldwide [102, 107, 116, 117]. However, several factors such as space-charge effects, electro-optic lens aberrations, and experimental acquisition times require careful examination. In Ref. [I] we present a quantitative benchmark comparison of MMs and the current standard spectrometers used in photoelectron spectroscopy, HAs, with a focus on XUV trARPES experiments. We discuss advantages, limitations, and their complementary nature in the context of common trARPES scenarios.

While the working principle of the time-of-flight MM is highly efficient, as all photoelectrons are guided into the detector, it poses several challenges for trARPES experiments. (i) The electro-optical lens column introduces chromatic aberrations, which limit, depending on the effective photoelectron source size, the energy window that can be acquired at high momentum resolution. For trARPES experiments with a typical XUV probe spot size on the order of $100 \times 100\,\mu m$ (FWHM), a reduction of the effective source size by use of field apertures in the real-space image plane of the MM is required, blocking the majority of emitted photoelectrons. (ii) While state-of-the-art laser systems gen-
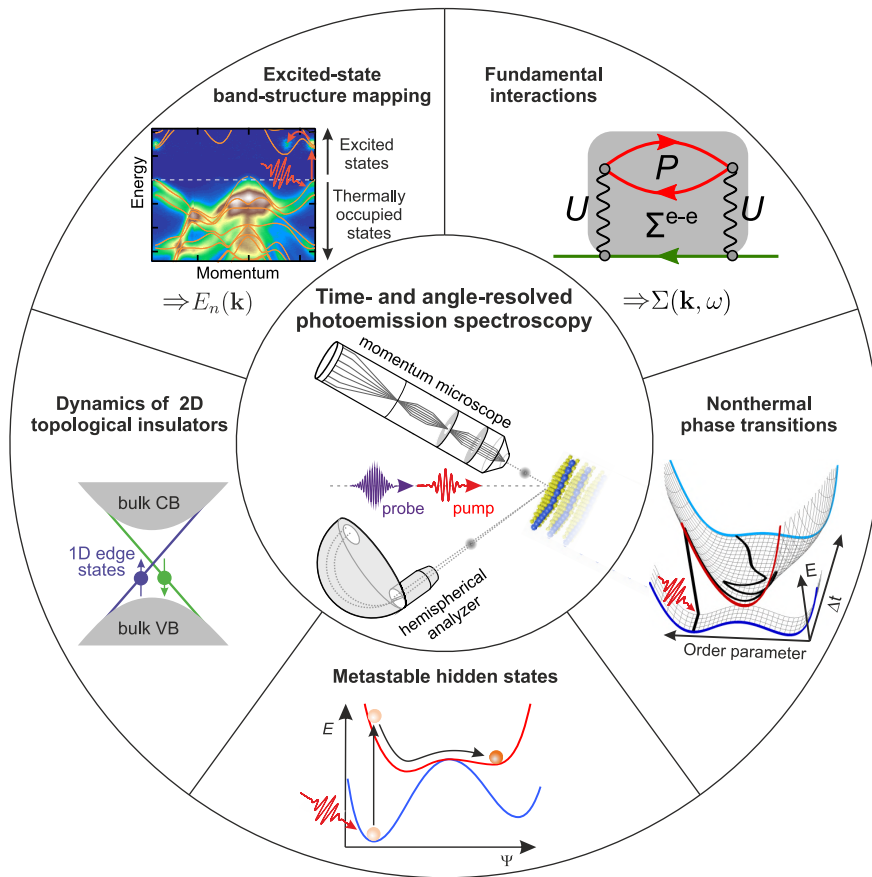
Figure 5.1: Areas covered in this thesis. Illustration of the various facets of the investigation of quantum materials discussed in this thesis.

erate sufficient XUV flux at MHz repetition rates to compensate for these transmission losses, space-charge effects, that is, the modification of the electron's angular and energy distribution due to Coulomb repulsion within a dense photoelectron cloud, limit the applicable XUV flux. As the full photoelectron cloud is accelerated into the lens system by applying a high positive voltage to an electrostatic extractor lens placed close to the sample surface, detrimental space-charge effects arise at significantly lower photoelectron currents as compared to HAs. (iii) The pump laser may also emit low-energy electrons from the sample, which are subsequently guided into the MM. Thus, space-charge effects resulting from the interaction of probe- and pump-emitted electrons are amplified in the MM. (iv) Lastly, the working principle of the photoelectron detection unit consisting of an MCP combined with a position-sensitive delay-line detector limits the detection rate of MMs to approximately a single event per pulse, as multi-hits can only be detected in certain instances. As in each MM measurement the entire photoelectron distribution from the secondary tail to excited states is mapped, while typically only the region near E_{F} is of interest, extended acquisition times are required to achieve statistics comparable to the HA within specific energy-momentum regions.

We find that the bottleneck when using the MM for XUV trARPES experiments at typical acquisition parameters is space charge. Aperture transmission losses and a low quantum efficiency of the detection unit lead to a situation where we reach the limit for tolerable space-charge distortions already at an XUV flux yielding ~0.3 detected events per pulse. Hence, increasing the transmission by minimizing the XUV spot size is critical to reach the detector saturation of 1 cts/pulse at negligible space-charge effects. However, focusing the XUV spot size to a regime where no field apertures are needed ($\lesssim 25{\times}25\,\mu$m) requires the use of advanced optical components such as zone plates or microcapillary lenses.

Recently, Schönhense et al. [118] presented a different route to suppress space-charge effects while obtaining count rates close to detector saturation. Their approach utilizes a retarding electrostatic field to direct secondary electrons and pump-laser-emitted electrons back to the sample surface before they can deteriorate the energy- and momentum resolution of high-energy photoelectrons. This retarding configuration strongly suppresses space-charge effects and greatly extends the range of applicable pump-laser fluences. Additionally, as slow secondary electrons are filtered out, the acquisition rate of energetically relevant regions of the photoelectron distribution can be increased. Yet, so far this retarding configuration of the MM has only been demonstrated for probe energies of ~ 100 eV up to few keV using accelerator-based light sources. As the suppression of space charge critically depends on the ratio of primary electrons to slow secondaries, applying this approach to table-top XUV trARPES experiments with photon energies in the range of few tens of eV is challenging. To utilize the MM in the retarding configuration in table-top setups, further development is required to push HHG-based MHz light sources to higher photon energies.

While time-resolved momentum microscopy exhibits several technical challenges, accessing the full photoelectron distribution bears great potential. Firstly, it allows for efficient characterization of the (thermally unoccupied) band structure of novel materials. Particularly for capturing time-resolved processes, the MM represents an ideal tool, as various photoinduced electronic processes can occur simultaneously and spread over a large energy—momentum range. Secondly, obtaining the full momentum distribution within a fixed measurement geometry is critical to access information encoded in the matrix elements [V, VIII, 119], to reconstruct excitonic wave functions [120, 121], and to map the orbitals of molecular crystals [IX, 116, 122]. Yet, even at a repetition rate of 500 kHz, MM measurements require acquisition times of 20 hours and more for 4D datasets (3D photoelectron distribution + time). Thus, after identifying the most critical energy-momentum regions, the HA serves as an efficient tool to map narrow energy-momentum windows at high statistics – approximately 2 orders of magnitude faster within a limited 2D energy-momentum window. This allows for a systematic variation of experimental parameters during trARPES studies, such as pump-laser fluence or temperature, within reasonable acquisition times. Combining both detection schemes in a single setup grants the highest flexibility for trARPES experiments and has been essential for investigating the electron dynamics in the 2D TI bismuthene [IV] and for characterizing the nonequilibrium hidden phase in the TMD 1T-TaS$_2$ [XI].

Photoelectron spectroscopy with time, spatial, and momentum resolution. A fur-

ther exciting feature of the MM is that it grants direct access to the spatially-resolved photoelectron distribution on the µm scale, termed photoemission electron microscopy (PEEM). In analogy to optical microscopy, a reciprocal and a real-space image are generated in the MM that can be selectively projected on the detector. Thus, simply by choice of lens voltages, the MM allows switching between momentum- and real-space measurements. Furthermore, by employing a pump-probe scheme, PEEM can be readily extended to the time domain. Combining trARPES and time-resolved PEEM (trPEEM) facilitates the investigation of spatial inhomogeneities, their electronic band structure, and associated dynamics. To demonstrate both detection modes of the MM, we study a buried defect in the CDW material $TbTe_3$, see Appendix A.1. Inserting a field aperture in the real-space image plane of the MM permits high spatial selectivity during band-structure measurements, allowing us to track the CDW suppression on the µm-sized defect. In contrast, inserting an aperture in the reciprocal image plane allows for high momentum-selectivity in PEEM measurements, so-called dark-field PEEM imaging. By centering the aperture on the momentum region associated with the CDW-gap, we find that the spatially-resolved photoelectron distribution at E_F directly reflects the footprint of the metallic defect, as only the normal metallic phase hosts electronic states at this particular energy-momentum region. In other words, the MM allows separating complex symmetry-broken phases in real space by their characteristic momentum signature and allows studying their transient evolution upon photoexcitation. This approach is particularly promising for the investigation of quantum materials that feature inhomogeneities, for example, in the form of a macroscopic phase coexistence [123–127].

In sum, combining a MM and HA with a high-repetition-rate XUV source yields an extremely versatile experimental setup and allows us to address a vast array of scientific questions. The setup is particularly suited to investigate low-dimensional quantum materials, as we demonstrate in the following.

Electron dynamics in a 2D topological insulator. In Ref. [IV] we report on the ultrafast electron dynamics of the novel 2D TI bismuthene. So far, time-resolved measurements of monolayer 2D TIs and a demonstration of the elusive topological edge states using a momentum-resolved probe had been missing. Here, to characterize the excited-state band structure and electronic relaxation processes of bismuthene, our dual-detector approach has proven invaluable. Using the MM, we first map the band structure within the full first BZ after near-infrared photoexcitation, which reveals gapped Dirac-cones at $\overline{K}$ and a pronounced excited-state population at $\overline{\Gamma}$. Having identified the most critical high-symmetry direction, we turn to the HA to perform a fluence-dependent study of the direct and indirect bulk quasiparticle band gaps and carrier dynamics. We confirm the large theoretically-predicted indirect bulk band gap of $\sim 0.8\,\text{eV}$ and capture the complete inter- and intravalley relaxation pathway of hot electrons. We find that the charge-carrier population at the conduction-band minimum relaxes on a timescale of $\sim 1\,\text{ps}$ – orders of magnitude faster than in topologically trivial indirect semiconductors – which we assign to the presence of topological metallic edge states. Intriguingly, we identify faint signatures of the topological in-gap states within the bulk band gap, in correspondence with previous (momentum-integrating) STM studies [57, 128, 129].

A special feature of 2D TIs is the formation of topological edge states not only at exposed sample edges but also along extended 1D defects such as domain boundaries [130]. Recently, such topological edge states have been observed along structural domain boundaries of bismuthene [129]. As pairs of counterpropagating states emerge on either side of the domain boundaries in direct proximity to each other, they hybridize, effectively lifting the topological protection due to the mixing of different helicities. To investigate the role of topologically protected edge states at exposed sample edges and of coupled edge states arising at domain boundaries, we study bismuthene samples with different densities of the respective edge-state types. This reveals that the in-gap signal is dominated by coupled edge states at domain boundaries. The edge-state coupling may also speed up the relaxation of the excited edge-state population. The lifted topological protection enables elastic single-particle momentum- and spin backscattering between opposite ESs by nonmagnetic defects and extends the phase-space for inelastic scattering events such as electron-hole creation and interband scattering. As the domain walls in bismuthene feature a plenitude of irregularities and kinks, emerging defect-induced states in combination with the lifted topological protection might explain the short population lifetimes in bismuthene.

The scattering pathway in bismuthene is reminiscent of the processes observed in photoexcited 3D TIs [131–134]. First, carriers are lifted from bulk valence to conduction states, followed by electron-electron interlayer scattering and subsequent relaxation to the bottom of the conduction band mediated by electron-phonon scattering. Finally, the carriers scatter into the topological in-gap states and relax to the valence band, likely via energy transfer to the lattice. However, differences between 2D and 3D TIs arise from their distinct dimensionality. While the 1D topological edge states of bismuthene are only faintly visible, as they cover a small fraction of the total surface area, the topological states of 3D TIs extend over the entire surface, yielding a pronounced photoemission signal. Furthermore, in 3D TIs, the overlap between bulk states and topological surface states is independent of the specific position on the surface. In contrast, in 2D QSH insulators, relaxation of excited carriers requires transport from bulk regions to metallic topological states at the edges of the bismuthene film. As in the investigated bismuthene samples the average spatial distance to a border that hosts metallic edge states is only on the order of a few nm, carrier relaxation on the ps timescale is in general agreement with diffusive transport of photocarriers on the surface [135]. Optimizing sample growth conditions to increase the size of bismuthene domains may thus allow enhancing the excited-state population lifetimes.

Addressing QSH functionalities with light. The demonstration of the large fundamental bulk band gap and observation of signatures of edge states at room temperature pave the way for more elaborate optical-control experiments. In 3D TIs, circularly-polarized light pulses have been used to control the spin polarization of topological surface states and to induce helical Dirac photocurrents [136–140]. Moreover, terahertz light waves have been employed to accelerate Dirac fermions, thereby driving transient surface currents [109]. While it is challenging to apply such control schemes to most 2D TIs due to their small bulk band gaps $\lesssim 150\,\text{meV}$ [8, 55, 56, 141, 142], the wide band gap of bismuthene opens up the possibility to apply all-optical control concepts to QSH

functionalities. Furthermore, our results open the way for studying nonequilibrium excitons in a topologically nontrivial material, which has attracted significant interest following the recent observation of exciton condensation in the QSH insulator monolayer WTe_2 [143, 144]. Having established the quasiparticle band gaps using trARPES, we provide a starting point for the investigation of excitons in bismuthene upon resonant optical excitation.

We demonstrated how trARPES with a dual-detector approach can be utilized for an extensive electronic characterization of a novel 2D quantum material. In the following, we return to topologically trivial systems to investigate symmetry-breaking phase transitions under nonequilibrium conditions. In particular, we focus on photoinduced CDW-to-metal transitions, investigate the driving forces of nonthermal transition pathways, and reveal how ultrafast phase transitions affect microscopic interactions.

Surfing on the energy landscape: collective excitations of CDW order. In Ref. [II] we present a comprehensive study of an ultrafast CDW-to-metal transition in the prototypical CDW compound $TbTe_3$. By combining trARPES and time-resolved X-ray diffraction (trXRD), we track the electronic and lattice dynamics of the CDW and the transient electronic temperature after optical excitation throughout the full melting and recovery cycle. This reveals a surprising reformation of CDW order at electronic temperatures far greater than the equilibrium transition temperature, which we ascribe to transiently suppressed lattice fluctuations in the nonthermal scenario of hot electrons coupled to an initially cold lattice. Additionally, we map the collective CDW excitations over a large fluence range, which allows us to reconstruct the underlying transient energy landscape using time-dependent Ginzburg-Landau theory.

While in equilibrium only the phase corresponding to the global minimum of the free energy surface can be accessed, a *sudden* perturbation by an ultrashort light pulse can modify the energy landscape and trigger a collective dynamic response of the system's order. Upon excitation of $TbTe_3$ at a fluence far above the threshold of CDW melting, we observe a collective quench of the electronic and structural CDW order within $\sim 100\,\mathrm{fs}$, followed by several cycles of coherent reemergence and melting of CDW order. After $\sim 1\,\mathrm{ps}$, the damped, coherent order-parameter oscillations subside, giving rise to the normal high-temperature state, until, after $\sim 2\,\mathrm{ps}$, an incoherent recovery of the CDW order sets in. By extending Ginzburg-Landau theory to the time domain, we link the observed order-parameter dynamics to the temporal evolution of the transient energy surface. We find that the optical excitation transforms the double-well ground-state potential into a high-symmetry single-well shape with a new minimum position that corresponds to the metallic phase. This launches a high-frequency coherent oscillation of the CDW order parameter around this new minimum, as evidenced by the collective switching between the CDW and normal metallic phase. As the system equilibrates and cools down, the potential shape relaxes back to the double-well ground state and the order parameter follows the evolution of the global minimum toward the CDW state. Intriguingly, we achieve an excellent quantitative description of the extracted order-parameter dynamics over a large fluence range using a model based on a simplistic 1D energy surface. This implies a marginal coupling of the CDW excitation to other lattice modes, which

is further supported by the long coherence time of the order-parameter dynamics. The confined dimensionality of the system[4] may facilitate such a coherent response, as it strongly restricts the phase-space for scattering. Similar coherent CDW excitations have been observed in other low-dimensional systems such as the prototypical Peierls system $K_{0.3}MoO_3$ [81]. The weak coupling of the CDW mode to other phonons further results in slow heating of the effective lattice temperature, giving rise to an unusual nonthermal CDW recovery.

Nonthermal CDW recovery. We show that our understanding of equilibrium phase transitions can be adapted to an out-of-equilibrium description by a captivatingly simple extension of Ginzburg-Landau theory. Yet, in contrast to phase transitions under equilibrium conditions, the critical temperature might not provide a valid description in a system exhibiting strong nonequilibrium between different coupled degrees of freedom such as electrons and lattice in CDW materials. Indeed, we observe that the CDW state in photoexcited $TbTe_3$ recovers while the electronic subsystem is still at elevated temperatures far above the equilibrium critical temperature. We attribute the premature CDW recovery to the suppression of lattice fluctuations in the transient nonthermal phonon distribution. After few ps, the electrons are still at elevated temperatures and only certain optical phonons are strongly excited, while the overall vibrational phonon population is still close to the value before excitation – the lattice is effectively still cold. Thus, thermal lattice fluctuations, which counteract CDW formation, are strongly suppressed, facilitating CDW order at electronic temperatures above thermal T_c. Hence, to capture the experimental order-parameter dynamics on a quantitative level, we adapt time-dependent Ginzburg-Landau theory employing a time-dependent nonequilibrium critical temperature, which converges to the equilibrium critical temperature on the time scale of lattice equilibration.

Accessing microscopic interactions during an ultrafast phase transition. The question arises how the ultrafast collective switching between metallic and CDW phases affects microscopic interactions such as electron-electron and electron-phonon scattering. Indeed, concomitant with the CDW oscillation, we observe a modulation of the relaxation rate of hot quasiparticles far above E_F, as reported in Ref. [III]. We find that, once the CDW energy gap at E_F opens, the relaxation of the high-energy quasiparticle population slows down, while, in the normal metallic state, the relaxation speeds up. To gain a microscopic view of the interplay of quasiparticle scattering and the transiently modified electronic band structure, we employ simulations based on nonequilibrium Green's functions. We demonstrate how the spectral-weight oscillations at E_F modulate the available electron-electron scattering partners of high-energy quasiparticles, while electron-phonon scattering remains unaffected in the considered energy region.

The electron self-energy encodes all interactions with the electronic quasiparticle and thus a detailed understanding is highly desirable. To investigate the electron self-

---

[4]The CDW physics of the tritellurides are governed by 2D Te square nets, which are weakly coupled to neighboring TbTe slabs. In the CDW phase, the square nets become distorted and form quasi-1D polytelluride oligomers with an approximately 7-fold superstructure with respect to the normal lattice constant along the c-axis [145, 146].

energy, typically a variation of external parameters such as temperature, pressure, or doping is required. However, the order-parameter oscillations in photoexcited TbTe$_3$ allow us to employ a *coherent lock-in* approach to identify changes associated with the phase switching. By tracking the spectral features that modulate at the frequency of the order-parameter oscillations, we can assess the effect of the CDW and metallic phases on the electron self-energy under similar experimental conditions – in contrast to studies relying on the variation of external parameters. While we utilize a rather specific scenario of a collective CDW excitation to demonstrate this lock-in approach, a variety of modes such as coherent phonons [X, 13, 25, 87, 88, 147] and collective excitations of certain symmetry-broken states [148, 149], can be imprinted on the electronic band structure. Furthermore, our main conclusion – the impact of the scattering phase space on the electron self-energy – is independent of the particular CDW physics and is relevant for a large range of materials featuring metal-to-insulator transitions or modifications of the Fermi surface geometry.

Linking experimentally accessible metrics to microscopic interactions. The complexity of interpreting trARPES spectra lies in the fact that the observed relaxation dynamics reflect population lifetimes, which are generally inequivalent to single-particle lifetimes directly encoded in the electron self-energy [150, 151]. We solve this problem by complementing our experimental trARPES results with a combined theoretical ansatz. Based on a time-dependent nonequilibrium Green's function formalism, we first simulate the population lifetimes allowing for a direct comparison to the experimental relaxation dynamics, which reproduces the observed scaling of the population lifetimes with the CDW energy-gap opening. Subsequently, to gain a microscopic understanding of the relevant interactions, we perform a detailed analysis of the self-energy and show that the opening of the CDW-gap strongly reduces the phase-space for electron-electron scattering processes, slowing down the relaxation of hot quasiparticles.

To conclude, we investigated a photoinduced CDW-to-metal transition and the associated change of the electron self-energy. Moreover, we demonstrated how the gradient of the transient energy landscape governs the nonthermal evolution of the CDW order. We found that, in the regime of strong perturbation, the energy landscape transforms into a single-well potential, which triggers an overshoot of the CDW order parameter beyond the new minimum (corresponding to the metallic state) to the other side of the potential. Owing to the 1D CDW pattern of the tritellurides [145, 146], reversing the sign of the order parameter only introduces a phase shift with respect to the original CDW pattern, as the *inverted* CDW configuration is geometrically equivalent to the initial ordering. In fact, for many CDW compounds such as K$_{0.3}$MoO$_3$ [81] and TiSe$_2$ [152] inversion of the CDW amplitude results in a state that is geometrically equivalent to the original CDW pattern. The question naturally arises whether a CDW pattern that gives rise to a novel geometry upon inversion exists in real materials and how such systems respond to an ultrafast optical perturbation. Intriguingly, such a CDW pattern can be found in the low-temperature ground state of 1T-TaS$_2$, which we examine in the following.

Uncovering the transition pathway to a metastable hidden phase. In Ref. [XI] we

investigate the dynamical pathway to the metastable *hidden* quantum state of bulk $1T$-TaS$_2$. The layered TMD TaS$_2$ features multiple competing phases based on various arrangements of star-shaped CDW clusters, which are often described as polarons, as the atoms at the edges of the star pattern contract to screen an unbound charge localized at the center. The commensurate CDW ground state of TaS$_2$ consists of commensurately ordered star-shaped clusters with a $\sqrt{13} \times \sqrt{13}$ supercell. Excitation of this insulating commensurate CDW state by an optical or voltage pulse triggers a transition to the hidden phase. The hidden phase is a metallic long-lived nonequilibrium state that can only be realized by a strong sudden perturbation and that features properties distinct from any phase present in the equilibrium phase diagram [24]. While the atomic structure of the hidden phase has been studied extensively [153–156], the fundamental processes governing the trajectory to the hidden phase have remained elusive so far. Combining our dual-detector approach with additional high-energy-resolution ARPES measurements, we provide an exhaustive characterization of the electronic band structure of the hidden phase, which reveals a global collapse of the Mott-insulating ground state. Next, using trARPES, we investigate the dynamical transition from the commensurate ground state to the hidden phase and observe a surprisingly fast transition timescale of a few hundred fs, suggesting a highly efficient nonthermal switching pathway governed by a collective CDW excitation. Lastly, employing a multi-pulse optical excitation scheme, we demonstrate a high degree of coherent control over the switching process to the hidden phase, providing strong evidence for the key role of the collective CDW excitation driving the transition.

Analogous to TbTe$_3$, the dynamics of the commensurate CDW ground state of TaS$_2$ upon photoexcitation are dictated by the transient free energy surface. However, there are two crucial differences with respect to the tritellurides. First, the inversion of the star-shaped $\sqrt{13} \times \sqrt{13}$ CDW distortion results in a novel CDW pattern that is geometrically inequivalent to the original pattern and exhibits a distinct lattice and electronic structure. Thus, a collective overshoot induces a novel, inverted CDW order, which has recently been observed in the related CDW compound $1T$-TaSe$_2$ [157]. Second, to capture the transition to the hidden phase, the previously employed 1D energy surface does not suffice. In TaS$_2$, in addition to the commensurate in-plane CDW order, the out-of-plane CDW order between neighboring TaS$_2$ sheets also plays a critical role. The hidden phase is characterized by commensurate CDW domains which are intersected by a multitude of domain walls. These irregular domain-wall networks in each layer shift the CDW clusters by one or more atomic lattice vectors in different directions, thus breaking long-range order along the out-of-plane direction. Hence, a description by a high-dimensional corrugated energy surface accounting for in-plane and out-of-plane order and featuring a local minimum corresponding to the metastable hidden phase is required.

Upon single-pulse optical excitation above the critical fluence for switching to the hidden phase, we observe signatures for an overshoot of the CDW pattern to an inverted geometry, followed by the formation of the hidden phase within ~ 800 fs. The rapid transition suggests a collective pathway from the inverted geometry to the local minimum corresponding to the metastable hidden phase. This implies that the gradient of the transient energy surface connects the inverted CDW configuration rather to the hid-

den phase than to the global minimum corresponding to the commensurate ground state. As trARPES provides only indirect hints for the discussed processes, theoretical modeling of the temporal evolution of the free energy surface and an investigation of the lattice dynamics are required to underpin the proposed transition pathway. Furthermore, it remains to be answered whether the proposed CDW overshoot also governs the transition to the metastable amorphous phase of TaS_2, which is a glassy electronic quantum state that can be realized by strong optical perturbation of the commensurate ground state at fluences far above the threshold of switching to the hidden phase [158].

Strong correlations in nonequilibrium: atom lattices as Mott-Hubbard toy models. The ground state of TaS_2 has long served as a Mott-Hubbard model system and has been investigated extensively by trARPES [83, 85, 159–163]. Yet, given the intertwined nature of the Mott-insulating ground state and CDW order, the recently established critical role of the interlayer stacking order on the low-energy states [11, 12], and the transient optical switching to various long-lived metallic states [164], TaS_2 may not serve as an ideal system to study strong correlations under nonequilibrium conditions. In contrast, dilute atom lattices on insulating substrates represent a captivatingly simple platform to realize many-body condensates and to test our understanding of strong correlations in a controllable 2D environment. As the degree of correlations is highly tunable by choice of atomic species and substrate, and since 2D atomic lattices represent close realizations of well-studied elementary theoretical models such as the spin-$1/2$ triangular antiferromagnetic Heisenberg model [43, 165], they provide an optimal platform to investigate Mott physics far from equilibrium. In Appendix A.2 we present first trARPES results of the adatomic Mott insulator Sn/Si(111)-($\sqrt{3} \times \sqrt{3}$), that is, a dilute monolayer of Sn atoms arranged in a triangular geometry on a Si(111) substrate. We uncover the transiently populated UHB and track its ultrafast quench within $\sim 50\,fs$, as the UHB peak transforms into a hot-electron continuum. Interestingly, the observed dynamics are reminiscent of the evolution of the UHB of TaS_2 after weak photoexcitation [161], suggesting universality of the dynamical behavior. By demonstrating the feasibility of accessing Mott-Hubbard physics in Sn/Si(111)-($\sqrt{3} \times \sqrt{3}$) far from equilibrium, our results pave the way for studying the dynamics of further strongly-correlated adatom systems using trARPES. In particular, we propose an experimental investigation of the fundamental nonequilibrium processes in photoexcited adatomic Mott insulators – relaxation of doubly-occupied sites, ultrafast heating and cooling, and the effect of photodoping. Furthermore, we suggest a time- and momentum-resolved investigation of the quasi-particle peak observed in modulation-doped atomic lattices [166].

6

Conclusions and outlook

In conclusion, we studied the ultrafast dynamics of a variety of monolayer and layered quasi-2D quantum materials after optical excitation, investigated nonthermal phase transitions and nonequilibrium states, and examined the microscopic interactions between elementary degrees of freedom. We established the large fundamental bulk band gap of a novel 2D quantum spin Hall material, observed topological edge states with momentum resolution, and examined the scattering pathways of excited photocarriers. Furthermore, we significantly advanced the understanding of photoinduced CDW-to-metal transitions and observed collective order-parameter excitations in unprecedented detail. This allowed us to reconstruct the transient free energy surface during the full CDW melting- and recovery cycle and to gain insights into the interplay of fundamental interactions with the electronic band structure. Moreover, we showed how the coupling between electrons and lattice in a highly nonthermal setting can lead to a situation where the equilibrium transition temperature of a many-body phase loses its validity. Lastly, we realized a nonequilibrium hidden phase by steering the configuration of a prototypical quantum material into a local minimum on the corrugated energy landscape and demonstrated how a tailored sequence of optical pulses can be used to uncover the driving forces of phase transitions. Our results vividly demonstrate the possibility of understanding and controlling many-body phases of quantum materials by ultrashort light pulses.

Novel approaches enabled by time-resolved momentum microscopy. In addition, we provided an exhaustive characterization of the MM for trARPES experiments. In the following, we summarize five developments enabled by time-resolved momentum microscopy, which may be transformative for the investigation of quantum materials.

(i) Full in-plane momentum mapping: Parallel acquisition of the full photoelectron distribution yields unprecedented insights into the electronic structure and allows, in combination with novel analysis methods, extracting the full (excited-state) band structure [167]. This provides an exhaustive basis to benchmark theoretical band-structure calculation methods and allows determining the total (valence-band) electronic energy, a highly desired quantity for assessing the energetics of phase transitions. Furthermore, utilizing free-electron lasers as light sources facilitates a simultaneous acquisition of core-level dynamics, providing a full characterization of the electronic structure over an extremely large energy and momentum range [104, 168, 169].

(ii) Orbital wave-function imaging: Acquisition of the full photoelectron distribu-

tion in a fixed geometry is critical to fully utilize the information encoded in the photoemission matrix elements. Matrix elements manifest in an emission-angle-dependent modulation of the photoemission signal and strongly depend on the polarization of the incoming probe beam with respect to the sample orientation. The difference in the photoemission signal for varying probe polarizations is known as dichroism of the angular photoelectron distribution. Studying such dichroic signals allows reconstructing fundamental quantities encoded in the electronic wave function such as the orbital texture [V, VIII, 170, 171]. As the orbital texture is intimately linked to the Berry curvature, a momentum-dependent vector field whose integral over the full BZ defines the topological index, the MM represents an ideal tool for the characterization of topologically nontrivial materials [119, 172–176].

(iii) High-dimensional photoemission spectroscopy: The single-event detection of the MM combined with high-repetition-rate light sources facilitates the concept of high-dimensional photoemission spectroscopy, where in addition to energy and parallel momentum a large parameter space is sampled. The fundamental idea is that each detected electron becomes a high-dimensional object associated with a multitude of parameters such as energy, parallel momentum, pump-probe delay, polarization, fluence, and wavelength of the pump and probe pulses, sample orientation, et cetera. Only later during the analysis, the parameter set is reduced to the ones most relevant for the observables under investigation. While in this work we focused on the 4D parameter set $I(k_x, k_y, E, \Delta t)$, utilizing sample rotation or probe-beam polarization as additional parameters can be used to investigate, for example, photoemission dichroism [V, VIII, 119].

(iv) Frequency-domain ARPES: A variety of collective phenomena such as CDW excitations and coherent phonons can be imprinted on the electronic band structure, manifesting as a periodic modulation of certain strongly-coupled electronic states. Fourier-transforming trARPES data along the time axis, termed frequency-domain ARPES (ωARPES), allows for identifying energy-momentum regions that respond strongly to such excitations [88, 177]. When complemented by measurements of the atomic displacement, ωARPES also facilitates a quantitative determination of band- and momentum-resolved electron-phonon matrix elements [25]. This approach is particularly powerful when combined with the MM, as it allows to determine the global band renormalization by collective phenomena, which has been restricted so far mostly to the region near E_F.

(v) Aperture-based measurement configurations: The MM allows for convenient switching between the acquisition of photoelectrons in reciprocal and real space by choice of electro-optical lens voltages. Combining these measurement configurations with apertures in the respective image planes of the MM allows to perform trARPES experiments at a spatial resolution down to the μm scale, facilitating the study of small samples [VII, 107, 121], and to investigate spatial inhomogeneities with high momentum selectivity by dark-field PEEM imaging, as demonstrated in Appendix A.1. As many quantum materials and their transient nonequilibrium states feature inhomogeneities resulting from intertwined and macroscopically coexisting states [123–127], time-resolved momentum microscopy represents an ideal match.

A

Supplementary results

In this chapter, we present additional unpublished results demonstrating the real- and reciprocal-space configurations of the MM and show first trARPES measurements of the Mott-insulating adatom system $Sn/Si(111)$-$(\sqrt{3} \times \sqrt{3})\,R30°$.

A.1 Measurement configurations of the momentum microscope

The MM enables conceptually new measurement configurations as real- and momentum-space image planes are generated within the detector. The use of field apertures in the real-space image plane permits spatial selectivity in band structure measurements down to the μm scale, while the use of so-called contrast apertures in the reciprocal image plane enables momentum selectivity for measurements of the real-space photoelectron distribution when using the PEEM configuration of the MM. Combining these approaches provides access to the dynamics of spatial inhomogeneities on the order of 10s of fs, at few μm spatial resolution, $\sim 150\,meV$ energy resolution, and at high momentum selectivity. Exemplary measurements of the CDW compound $TbTe_3$ in the vicinity of a crystal defect demonstrate real- and reciprocal-space configurations combined with a pump-probe approach.

Time- and spatially-resolved ARPES. To demonstrate spatial selectivity in trARPES measurements using the MM, we first identify an inhomogeneity on the $TbTe_3$ sample surface. For that, we employ the MM in the PEEM configuration. As inhomogeneities such as crystal defects typically reduce the work function, we utilize the multi-photon photoemission signal generated by 1.5 eV laser pulses in the search for a suitable defect. Due to the non-linearity of multi-photon photoemission, the reduced work function locally increases the photoemission signal, resulting in a stark intensity contrast between defects and pristine sample regions, as the horizontally traversing defect in $TbTe_3$ presented in Fig. A.1a) shows. Having identified a spatial inhomogeneity, we first perform trARPES measurements on the defect-free area by inserting a field aperture in the real-space image plane (indicated in orange). In equilibrium, the photoemission intensity at

E_F is strongly reduced within the CDW gapped areas[5], see Fig. A.1c). Ultrafast optical excitation transiently melts the CDW [78], evident from the intensity gain in the previously gapped regions within a few hundred fs, see panel d). Interestingly, when selecting photoelectrons originating only from the defect region by inserting a small field aperture (indicated in red in panel a), we observe a fully metallic, ungapped FS in equilibrium, see panel b). As the band structure features sharp, undistorted bands, we speculate that the crystal defect may be buried below the surface, straining the topmost crystal layer and thus suppressing CDW formation.
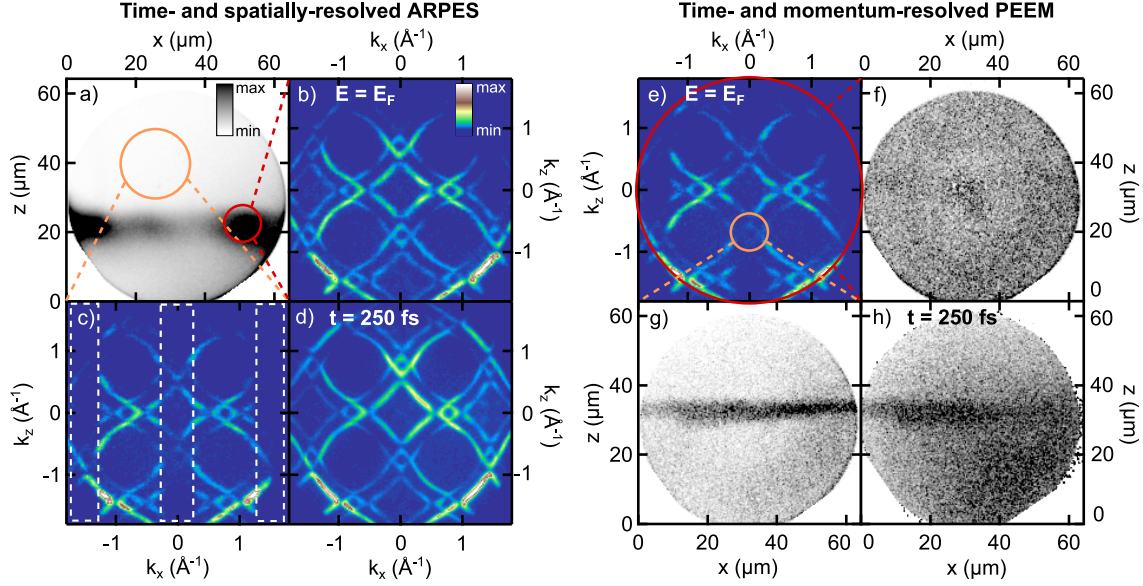
Figure A.1: Measurement configurations of the MM using apertures. a) Energy-integrated PEEM image of pump-laser-induced photoemission signal from a crystal defect in TbTe$_3$ ($h\nu = 1.55$ eV, absorbed fluence $F_{abs} = 140\,\mu J\,cm^{-2}$). **b)** Static FS of the defect region of TbTe$_3$ ($E_F \pm 50$ meV, field aperture diameter $d_{FA} = 100\,\mu m$). **c)** Static FS of the defect-free sample area ($d_{FA} = 200\,\mu m$). White boxes mark the CDW-gapped regions. **d)** FS of the defect-free sample region after photoexcitation ($h\nu_{pump} = 1.55$ eV, $F_{abs} = 30\,\mu J\,cm^{-2}$, $\Delta t = 250$ fs). **e)** Static FS, same as panel c. **f)** Static XUV PEEM image at E_F of the sample spot characterized in panel a without a contrast aperture and **g)** with a contrast aperture ($d_{CA} = 200\,\mu m$) focused on the CDW-gapped area. **h)** PEEM image with contrast aperture after photoexcitation ($h\nu_{pump} = 1.55$ eV, $F_{abs} = 90\,\mu J\,cm^{-2}$, $\Delta t = 250$ fs). All measurements were performed at $T = 80$ K.

Time- and momentum-resolved PEEM. In Fig. A.1e-h), we present time- and momentum-resolved PEEM measurements of the identified defect. When no contrast aperture is inserted in the reciprocal image plane, the spatial distribution of photoelec-

---

[5]In the rare-earth tritelluride TbTe$_3$, strongly wave-vector dependent electron-phonon coupling [35], in conjunction with a moderately well-nested Fermi surface [178], lead to the formation of a unidirectional CDW below $T_c = 336$ K [179] in which some portions of the Fermi surface are gapped while others remain metallic [180]. Thus, only momentum-stripes along the k_z direction feature an energy gap opening at E_F. Note that, by convention, the in-plane crystal directions are along the x and z (k_x and k_z) axes.

trons emitted by the XUV probe is averaged over all momenta across the photoemission horizon. Since the CDW only partially gaps the FS, also CDW-gapped sample regions host electrons up to E_F. Therefore, the real-space electron distribution at E_F is largely homogeneous, as shown in panel f). However, focusing the contrast aperture on the CDW-gapped region of the FS (orange circle in panel e) results in a clear contrast between the defect, which hosts metallic states in the selected energy-momentum region, and the surrounding CDW-gapped area. Hence, the signal at E_F in the selected momentum area originates exclusively from sample regions where CDW formation is hindered, corresponding to the footprint of the defect. Lastly, we combine momentum-selective PEEM with a pump-probe approach, which reveals a partial metallization in sample regions next to the defect, as shown in panel h).

A.2 Doublon dynamics in a prototypical Mott-insulating adatom system

Gaining a full understanding of prototypical Mott insulators such as cuprates, iron-based superconductors, and organic charge salts remains an ongoing challenge despite several decades of research due to their complex elemental compositions, crystal structures, and intricate phase diagrams [28, 181, 182]. In contrast, epitaxially grown dilute atom lattices on insulating substrates represent a captivatingly simple platform to realize and control many-body condensates [41, 183]. An exciting feature of this material class is the tunability of correlations by choice of adatom species and substrate. As the 2D character leads to reduced dielectric screening in the adatom layers, strong electronic correlations govern the electronic properties, resulting in a Mott insulating ground state in a variety of adatom-substrate combinations [38, 39, 42, 184, 185]. In particular, these structurally simple systems provide an ideal playground for studying the dynamics of strongly-excited correlated systems and for testing our theoretical understanding of correlations far from equilibrium [186–188]. Yet, while the equilibrium properties of adatom systems have been studied extensively by ARPES, STM, and scanning tunneling spectroscopy (STS), characterization of their nonequilibrium properties is missing.

Here, we investigate the Mott-insulating ground state of a dilute triangular lattice of Sn atoms on a silicon (111) substrate surface, Sn/Si(111)-($\sqrt{3} \times \sqrt{3}$) R30°, henceforth $\sqrt{3}$-Sn/Si(111). Using trARPES, we unambiguously demonstrate the UHB – the spectroscopic signature of doubly occupied sites, so-called doublons – and track its occupation dynamics upon optical excitation. At pump-probe overlap before thermal equilibration of the electronic system, we observe a pronounced UHB peak within the substrate band gap and determine the Mott energy gap to ~ 0.8 eV, in general agreement with STM studies [39, 166]. Furthermore, we find that the UHB peak vanishes within $\sim$50 fs and a metallic hot-electron continuum builds up, suggesting a quench of the Mott state. Our measurements validate state-of-the-art spectral-weight calculations of $\sqrt{3}$-Sn/Si(111) [44] and serve as a starting point for a momentum-resolved investigation of the nonequilibrium properties of a range of adatom systems.
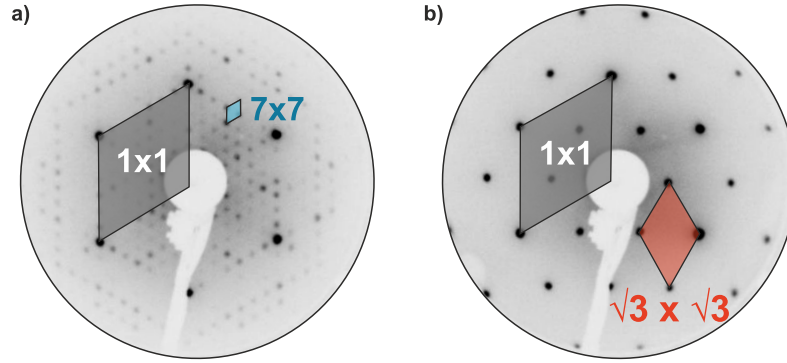
The $\sqrt{3}$-Sn/Si(111) surface reconstruction. $\sqrt{3}$-Sn/Si(111) consists of a triangular
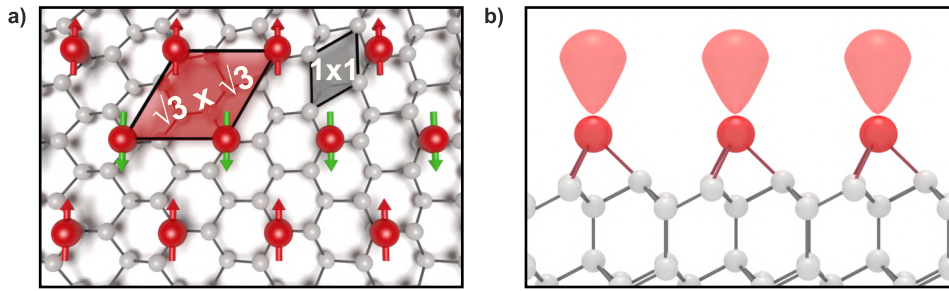
Figure A.2: Schematic of the $\sqrt{3}$-Sn/Si(111) surface reconstruction. a) Illustration of the $\sqrt{3} \times \sqrt{3}$ Sn reconstruction (red spheres) on a Si(111) surface (gray spheres). The geometrically frustrated triangular spin-1/2 lattice gives rise to a row-wise antiferromagnetic ordering [43, 165], indicated by colored arrows. The unit cells of the adatom layer and the substrate are shaded in red and gray, respectively. **b)** Side view the $\sqrt{3}$-Sn/Si(111) sample surface illustrating the protruding dangling-bond p_z states of the Sn atoms (light red).

array of Sn atoms residing at the T_4 sites of the Si(111) surface, see Fig. A.2a). The adatom unit cell is enlarged by $\sqrt{3}$ and rotated by 30° with respect to the (1×1) unit cell of the substrate. In this configuration, three of four Sn valence orbitals form covalent back-bonds with the substrate, while the out-of-plane p_z-orbital remains half-filled, see Fig. A.2b), giving rise to a rich phase diagram [38, 189, 190]. Without any inclusion of correlation effects, the unsaturated Sn $5p_z$ states yield a narrow metallic surface band at half-filling [191], which is in strong contrast to experimental data. The reduced screening due to the confined dimensionality of the adatom layer and the localization of unpaired electrons at each Sn lattice site resulting from the large nearest-neighbor distance lead to a situation where the on-site Coulomb energy exceeds the kinetic energy term. Hence, $\sqrt{3}$-Sn/Si(111) is a Mott insulator.

Preparation of $\sqrt{3}$-Sn/Si(111). The preparation routine of $\sqrt{3}$-Sn/Si(111) has been developed in the group of Prof. Ralph Claessen at the University of Würzburg, utilizing STM and low-energy electron diffraction (LEED) to verify a high sample quality. The description of the routine closely follows Refs. [41, 183]. The boron-doped p-type silicon wafers ($R \approx 1 - 20 \, \text{Ohm cm}$) used in this study were cut along the (111) plane at a thickness of $\approx 0.3 - 0.5 \, \text{mm}$. After cleaning the substrates in an acetone and isopropanol bath, they are mounted in a sample holder for direct current heating and placed in the heating stage of the UHV preparation chamber. Passing a current through the substrate results in resistive heating and provides direct control of the sample temperature, which is monitored using a pyrometer. After degassing the sample for several hours at 600 °C, the substrate is flashed close to the melting point at ≈ 1380 °C, which yields a highly ordered (7×7) surface reconstruction, see Fig. A.3a). The prepared clean Si(111)-(7×7) surface reconstruction serves as substrate for the Sn adatom layer. A 1/3 monolayer of Sn (99.99 % purity) is evaporated from a Knudsen cell onto the substrate, which is kept at RT. A subsequent anneal at ≈ 650 °C for 150 s triggers the adatom surface diffusion and long-range ordering. Successful growth of the $(\sqrt{3} \times \sqrt{3})$ adlayer is confirmed by LEED, see Fig. A.3b).

Figure A.3: LEED images of the silicon substrate and the √3-Sn/Si(111) sample. a) LEED image of the Si(111)-(7 × 7) surface reconstruction. Surface and bulk reciprocal unit cells are indicated in blue and gray, respectively. **b)** LEED image of the √3-Sn/Si(111) reconstruction. The reciprocal unit cell of the Sn layer is marked in red. Both LEED patterns were acquired at a beam energy of 44 eV.

Band-structure mapping. We start by mapping the band structure of √3-Sn/Si(111) upon 1.5 eV optical excitation at 20 K, far below the critical temperature of the Mott-metal-insulator transition, see Fig. A.4a-b). Before arrival of the optical pump pulse, we observe the weakly dispersive LHB near E_F associated with the half-filled p_z orbitals of the Sn atoms, in agreement with previous studies [39, 43]. Note that, due to our limited energy resolution, we do not observe a clear gap opening at E_F. Upon optical excitation, a faint transient population builds up at Γ approximately 0.50 eV above E_F and we observe a broad Fermi-edge resulting from the optical heating of the electronic subsystem. We ascribe the excited-state feature at Γ to the UHB based on the following arguments:

(i) The feature can be unequivocally assigned to the Sn adlayer, as it is located within the band gap of the semiconducting substrate. The energy distribution curve (EDC) at the M point of the 1 × 1 reciprocal unit cell features the conduction band minimum (CBM) of the Si substrate, see Fig. A.4d), which is located ∼ 0.25 eV above the excited-state feature at Γ. (ii) The energetic position of the excited-state feature, which is situated ∼ 0.80 eV above the LHB at Γ, is in agreement with momentum-integrating STS measurements of the UHB [39, 166]. Furthermore, the observed feature is in excellent agreement with theoretical calculations of the spectral-weight distribution of the UHB, see Fig. A.4c), which predict a similar energy gap and the most pronounced UHB spectral weight at Γ. (iii) Last, the excited-state feature exhibits ultrashort lifetimes, as expected for doubly occupied UHB states [161]. Thus, we conclude that the excited-state feature can be assigned to the UHB.

Ultrafast doublon dynamics. Tracking the transient photoemission intensity within the energy-momentum region of the UHB reveals a rapid exponential decay with a $1/e$ lifetime of 123 ± 7 fs, see Fig. A.4e). However, as the selected ROI also captures the tail of the broad Fermi-Dirac distribution reflecting the strongly-heated electron system, the transient intensity only provides an upper limit of the lifetime of the UHB. To gain a better understanding of the temporal evolution of the doublon occupation, we inves-
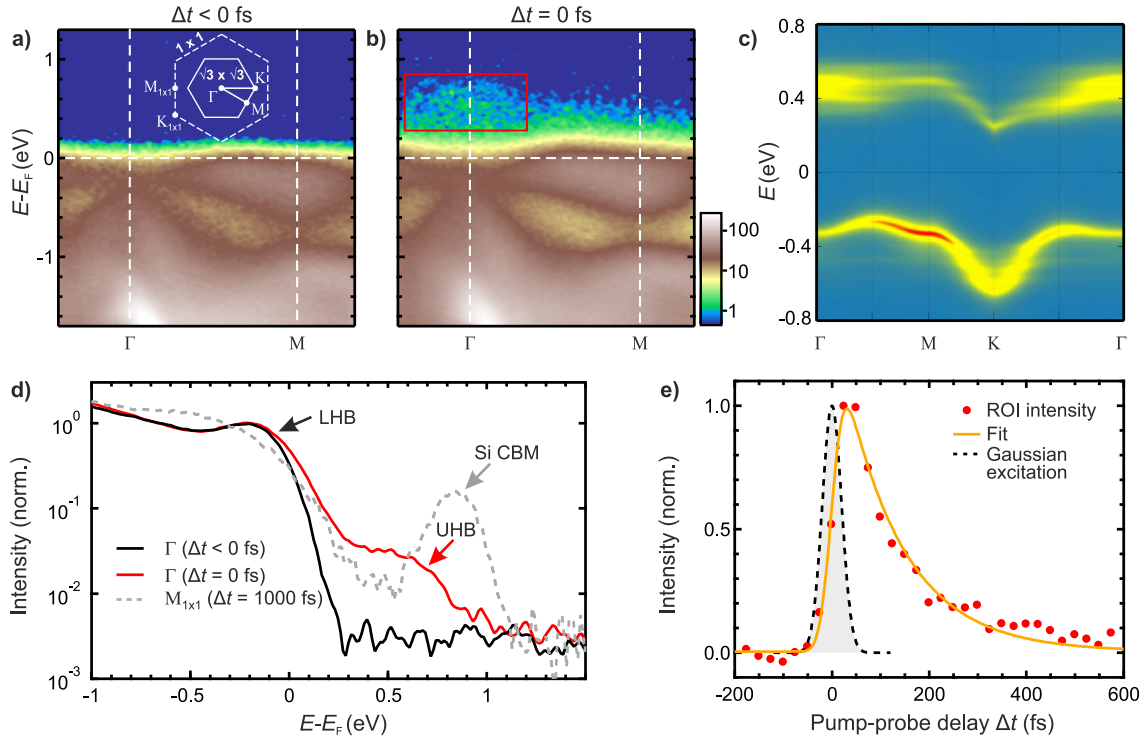
Figure A.4: Band-structure mapping. a) trARPES energy-momentum cuts along the $\Gamma - M$ direction before and **b)** at temporal pump-probe overlap using the HA for photoelectron detection ($T = 20$ K, incident fluence $F_{\text{inc}} = 0.35$ mJ cm^{-2}). The surface BZs of the Sn adlayer (solid lines) and the substrate (dashed lines) are indicated in panel a. **c)** False-color plot of the single-particle spectral function of $\sqrt{3}$-Sn/Si(111) calculated by an extended variational cluster approach, see Ref. [44]. **d)** EDCs at Γ and $M_{1\times1}$ at selected pump-probe delays Δt. **e)** Transient photoemission intensity extracted from the red box in panel b with an exponential decay fit. The shaded gray area indicates the temporal profile of the pump pulse. *Panel c reprinted with permission from Ref. [44]. Copyright 2019 American Physical Society.*

tigate the EDCs at Γ for selected pump-probe delays, see Fig. A.5. Upon photoexcitation, the UHB is transiently populated and a clear excited-state peak is visible up to $\Delta t = 50$ fs. Subsequently, the peak vanishes and is replaced by a hot-electron continuum. The short lifetime of the UHB is in general agreement with previous studies of the Mott-insulating ground state of TaS$_2$ [161]. Ligges et al. assign the short lifetimes to doublon-hole recombination, which occurs on the timescales of electronic hopping. An estimate of the hopping timescale of $\sqrt{3}$-Sn/Si(111), considering only nearest-neighbor hopping ($t = 0.0522$ eV [44]), yields $\hbar/t \approx 13$ fs, in overall agreement with the observed rapid doublon decay. Yet, photoexcitation also strongly heats the electronic subsystem, which thermalizes on a similar timescale, destabilizing the Mott-insulating ground state and inducing a transient metallization. Thus, further studies are required to disentangle concurrent processes such as heating of the electrons and doublon-hole recombination. In addition, also the role of photodoping of the Hubbard bands through optical depop-
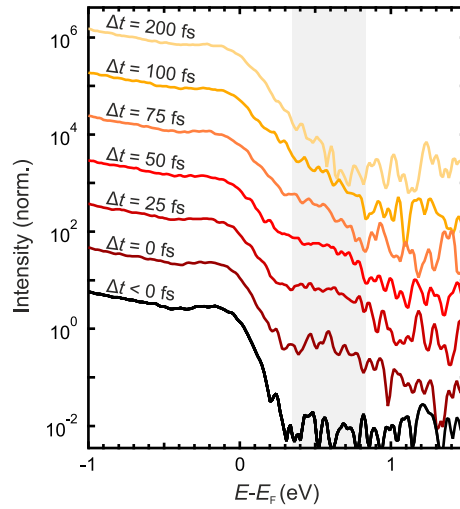
Figure A.5: EDCs at Γ for various pump-probe delays. The curves are vertically offset for clarity. The shaded gray area highlights the energy region of the UHB. The data was acquired at $T = 20$ K and $F_{inc} = 0.35$ mJ cm^{-2}.

ulation of the LHB and population of the UHB by vertical transitions from lower-lying substrate states and its effect on the Mott-insulating ground state has to be evaluated.

In conclusion, we demonstrated the UHB of the Mott-insulator $\sqrt{3}$-Sn/Si(111) with momentum resolution and tracked its temporal evolution upon photoexcitation. Our results demonstrate the feasibility of investigating Mott physics of dilute atom lattices using trARPES, paving the way for further studies of related adatom systems.

B

Preprint: arXiv:2206.03788 (2022): Coherent light control of a metastable hidden phase

In this chapter, the preprint of Ref. [XI], which is currently under review, is reproduced.

J. Maklar, S. Dong, J. Sarkar, Y.A. Gerasimenko, T. Pincelli, S. Beaulieu, P.S. Kirchmann, J.A. Sobota, S.-L. Yang, D. Leuenberger, R.G. Moore, Z.-X. Shen, M. Wolf, D. Mihailovic, R. Ernstorfer, and L. Rettig

The preprint of the manuscript is available at arXiv:2206.03788 (2022). The manuscript reports on the ultrafast light-induced formation dynamics of the long-lived metastable hidden phase in the layered dichalcogenide $1T$-TaS$_2$. The associated supplementary information is reprinted below the main article.

Author contributions

L.R., D.M., and **J.M.** conceived the experiment; **J.M.**, S.D., J.S., T.P., S.B., and L.R. carried out the XUV trARPES experiments; P.S.K., J.A.S., S.-L.Y., D.L., and R.G.M. carried out the 6 eV-laser-ARPES experiments; Y.A.G. conducted and analyzed the STM experiments; **J.M.** analyzed the trARPES data with support from L.R and J.S.; **J.M.** wrote the manuscript with support from L.R., Y.A.G., and D.M.; L.R., R.E., M.W., and Z.-X.S. provided the experimental infrastructure; all authors commented on the paper.

Coherent Light Control of a Metastable Hidden Phase

J. Maklar[1], S. Dong[1], J. Sarkar[1], Y.A. Gerasimenko[2,3], T. Pincelli[1], S. Beaulieu[1,*], P.S. Kirchmann[4], J.A. Sobota[4], S.-L. Yang[4,5,†], D. Leuenberger[4,5], R.G. Moore[4,‡], Z.-X. Shen[4,5], M. Wolf[1], D. Mihailovic[2,3], R. Ernstorfer[1,6], and L. Rettig[1]

[1] *Fritz-Haber-Institut der Max-Planck-Gesellschaft, Faradayweg 4-6, D-14195 Berlin, Germany*
[2] *Dept. of Complex Matter, Jožef Stefan Institute, Jamova 39, SI-1000 Ljubljana, Slovenia*
[3] *Center of Excellence on Nanoscience and Nanotechnology – Nanocenter (CENN Nanocenter), Jamova 39, SI-1000 Ljubljana, Slovenia*
[4] *Stanford Institute for Materials and Energy Sciences, SLAC National Accelerator Laboratory, 2575 Sand Hill Road, Menlo Park, California 94025, USA*
[5] *Geballe Laboratory for Advanced Materials, Departments of Physics and Applied Physics, Stanford University, Stanford, California 94305, USA*
[6] *Institut für Optik und Atomare Physik, Technische Universität Berlin, Straße des 17. Juni 135, 10623 Berlin, Germany*
[*] *Present address: Université de Bordeaux - CNRS - CEA, CELIA, UMR5107, F33405, Talence, France*
[†] *Present address: University of Chicago, Pritzker School of Molecular Engineering, Chicago, IL 60637, USA*
[‡] *Present address: Materials Science and Technology Division, Oak Ridge National Laboratory, Oak Ridge, TN 37831, USA*

June 9, 2022

Metastable phases present a promising route to expand the functionality of complex materials. Of particular interest are light-induced metastable phases that are inaccessible under equilibrium conditions, as they often host new, emergent properties switchable on ultrafast timescales. However, the processes governing the trajectories to such hidden phases remain largely unexplored. Here, using time- and angle-resolved photoemission spectroscopy, we investigate the ultrafast dynamics of the formation of a hidden quantum state in the layered dichalcogenide $1T\text{-}TaS_2$ upon photoexcitation. Our results reveal the nonthermal character of the transition governed by a collective charge-density-wave excitation. Utilizing a double-pulse excitation of the structural mode, we show vibrational coherent control of the phase-transition efficiency. Our demonstration of exceptional control, switching speed, and stability of the hidden phase are key for device applications.

Controlling material properties on demand remains a long-standing challenge in condensed-matter physics. Inspired by femtochemistry, the illumination by ultrashort light pulses poses a promising route to understanding and actively manipulating the macroscopic properties of quantum materials. Multiple optical control pathways have been established based on a transient modification of the free-energy landscape, ultrafast heating, and Floquet engineering [1]. These control schemes allow, for example, triggering electronic phase transitions on femto- to picosecond timescales [2] and steering intricate structural transitions by excitation of specific lattice modes [3]. Remarkably, in materials with multiple competing orders, ultrashort light pulses can also induce metastable states that feature properties inaccessible under thermodynamic equilibrium conditions, so-called hidden phases. As hidden phases expand emergent functionalities of complex solids, are often switchable on ultrafast timescales, and provide insights into fundamental interactions and phase competition, they are of high interest from a scientific and an application perspective. Prominent examples include optical switching to hidden metallic states in strongly correlated materials [4, 5] and possible photoinduced superconductivity at temperatures far above T_c [6]. Yet, the microscopic processes governing the transition to metastable states often lack a clear understanding, resulting in unspecific empirical switching protocols with

non-optimal efficiencies and limited control over stability. Furthermore, most hidden phases persist only transiently on a ps timescale, precluding any practical application in switchable devices.

A particularly interesting metastable state is the metallic hidden (H) phase of $1T$-$\mathrm{TaS_2}$, as it can be reversibly induced by optical or electrical pulses and is accompanied by an insulator-to-metal transition with an orders-of-magnitude drop in resistivity [7–15]. Additionally, the H phase is exceptionally long-lived and thus represents a promising platform for device functionality [16]. In equilibrium, the layered transition-metal dichalcogenide $1T$-$\mathrm{TaS_2}$ features multiple competing ground states resulting from the interplay of Coulomb repulsion, Fermi-surface nesting, and interlayer interaction. At the heart of the various orderings lies the formation of star-shaped polaron clusters, i.e., clusters of ions that are inwards radially displaced toward an unbound charge localized at the cluster centers (Fig. 1A). The polaron formation gives rise to a metallic nearly commensurate (NC) phase below 350 K that consists of patches of ordered polaron clusters separated by smooth periodic domain walls (Fig. 1B). Cooling below 180 K leads to a hysteretic first-order transition to a Mott-insulating commensurate (C) phase with long-range intralayer polaron order [17] (Fig. 1C), also discussed in terms of a charge density wave (CDW). Additionally, in the C phase, an interlayer alignment of polarons leads to a unit cell doubling along the out-of-plane direction, referred to as interlayer stacking order, which is suspected to strongly affect the low-energy electronic states [9, 18–21].

Optical or electrical excitation of the C ground state triggers a transition to the metallic metastable H phase, which consists of microscopic commensurate domains intersected by a large number of irregular domain walls that induce an abrupt CDW phase slip between neighboring domains (Fig. 1D). While the atomic structure of the H phase has been studied extensively [9–12], the origin of the metallization is still under debate [7, 10, 12, 18] as measurements of the electronic band structure have been missing. Furthermore, even though an electron-hole imbalance following the excitation has been suggested as driver of the transition to the H phase [7], a microscopic understanding of the switching mechanism – imperative for improving the switching energy and speed of memory devices based on metastable configurations [16] – has remained elusive. Particularly the role of coherences, which have been exploited to boost the switching efficiency in other systems [3], has remained largely unexplored.

Here, we use time- and angle-resolved photoemission spectroscopy (trARPES) to probe the electronic band structure and formation dynamics of the metastable H quantum state in bulk $1T$-$\mathrm{TaS_2}$ upon near-infrared femtosecond optical excitation. Employing a combination of XUV and UV trARPES, we map out the band structure of the H phase within the full first Brillouin zone and at high energy resolution. We observe a global collapse of the Mott-insulating state, providing further hints for the critical role of the interlayer stacking order. Tracking the electron dynamics during the photoinduced phase transition from C ground state to H phase reveals a surprisingly fast timescale of a few hundred fs, suggesting a highly efficient nonthermal switching pathway governed by a collective CDW excitation. Using a two-pump-pulse excitation scheme, we demonstrate vibrational coherent control of the transition to the H phase, evident from pump-pump-delay-dependent oscillations of the switching efficiency at the CDW amplitude mode frequency. Based on the observed band-structure dynamics, we discuss an ultrafast microscopic switching pathway from C to H phase. Our study demonstrates exceptional control over the properties of complex solids by utilizing tailored optical multi-pulse excitations of ordered states and highlights a promising route in the search for new hidden states.

Results

Band-structure mapping. First, we map out the static band structure along the high-symmetry directions for the different phases (Fig. 1). In the NC phase at room temperature, Ta $5d$ states give rise to a metallic low-energy band that reaches up to the Fermi level (E_F) at $\overline{\Gamma}$. Upon cooling, the gapped C phase emerges, as the polaron clusters become commensurate with the atomic lattice. This periodic charge- and lattice distortion leads to a splitting of the Ta $5d$ band into subbands due to the formation of CDW energy gaps Δ_CDW, with d electrons of the 12 outer Ta atoms of the star-shaped clusters occupying the subbands up to $E - E_\mathrm{F} \sim -0.4$ eV. The
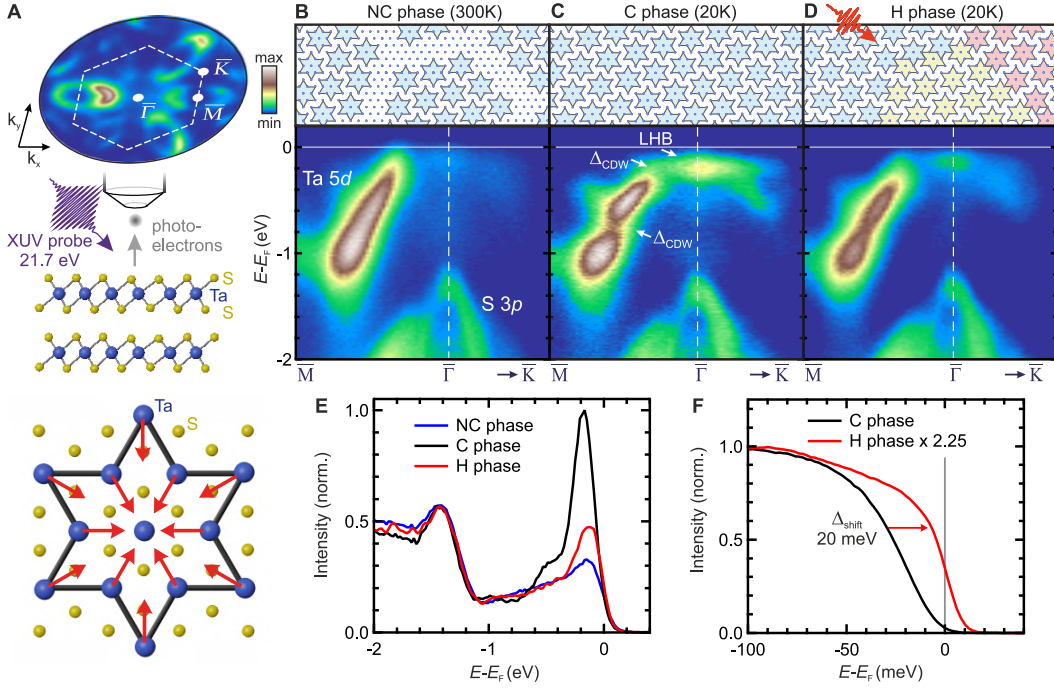
Fig. 1: **Band-structure mapping.** (**A**) Top: Schematic of the static XUV ARPES measurements and the layered $1T$-TaS$_2$ sample. An exemplary isoenergy surface of the NC phase ($E - E_{\mathrm{F}} = -0.5$ eV, momentum radius $k_{\parallel} \sim 2$ Å^{-1}) with hexagonal surface Brillouin zone and high symmetry points is shown. Bottom: Illustration of the star-shaped polaron cluster. (**B** to **D**) Top: Schematic intralayer polaron order of the NC, C and H phases (domains indicated by different colors). Bottom: ARPES energy-momentum cuts along the high-symmetry directions of the respective phases. Switching to the H phase was achieved by a single optical pulse at $h\nu = 1.55$ eV at an absorbed fluence $> F_{\mathrm{crit}} \sim 0.5$ mJ·cm^{-2}. (**E**) EDCs of the examined phases at $\overline{\Gamma}$. (**F**) EDCs of C and H phase at $\overline{\Gamma}$ near E_{F} (gray line), obtained with a laser-ARPES setup with high energy resolution (see methods).

remaining 13th electron remains localized on the central Ta atom due to strong on-site Coulomb repulsion, giving rise to a narrow lower Hubbard band (LHB) at -0.2 eV and the opening of a small Mott gap at E_{F}, in agreement with previous observations [22]. Strikingly, switching from the C ground state to the persistent H phase at 20 K by a single optical pulse induces a drastic modification of the low-energy states. Most notably, the LHB intensity is strongly suppressed, as evinced by the energy distribution curves (EDCs) at $\overline{\Gamma}$ (Fig. 1E), accompanied by a suppression of the Mott gap (Fig. 1F and Supplementary Fig. S1). While, strictly speaking, the low-energy band in the H phase is a strongly-correlated metallic band, we refer to it as LHB across all phases.

Since ARPES is only sensitive to short-range order and averages over a macroscopic surface area due to the μm-sized probe beam, the drastic spectral change upon switching from C to H phase is remarkable, as both phases consist predominantly of commensurately ordered polaron clusters, with only a fraction of the H phase consisting of domain walls (Supplementary Fig. S2). However, recent studies demonstrated a strong influence of the interlayer polaron stacking order on the low-energy electronic states [9, 18–21]. As Ta $5d_{z^2}$ orbitals with strong out-of-plane character are located at the cluster centers, the interlayer orbital overlap is highly sensitive to the interlayer polaron alignment. While, in the C ground state, two neighboring layers dimerize, switching to the H phase induces a multitude of irregular domain wall networks in each layer which shift the central cluster atoms by one or more atomic lattice vectors in different directions [11]. These irregular phase shifts of the intralayer polaron order within each layer induce disorder along the out-of-plane direction, breaking long-range order of the interlayer dimerization [12] and thus reducing interlayer hopping. This external restacking may induce

3

metallization, as the subtle balance of on-site Coulomb repulsion, intra- and interlayer hopping is perturbed, quenching the fragile Mott state [9, 18]. Our measurements directly support this scenario, as we observe suppression of the LHB and closing of the Mott gap despite only minimal changes in the intralayer ordering. The metallization of a Mott insulator upon reducing inter-layer hopping is consistent with a simple bilayer Hubbard model [23], although a more realistic theoretical treatment is required to capture the respective phases of TaS_2.
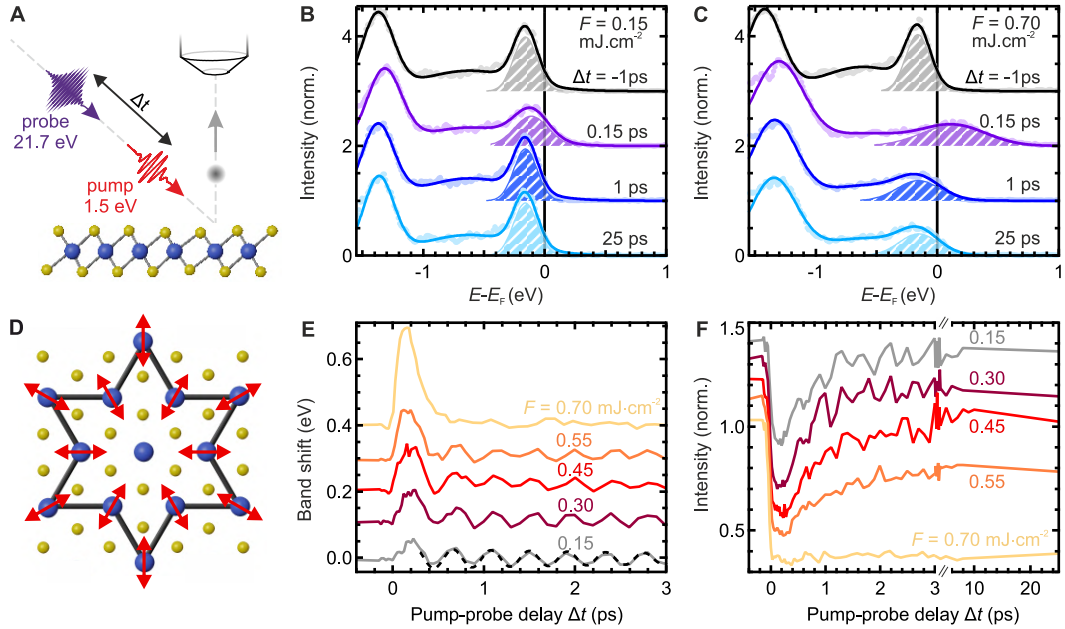
Fig. 2: Dynamical transition to H phase. (**A**) Sketch of the trARPES experiment with pump-probe delay Δt. (**B**) EDCs (dots) at $\bar{\Gamma}$ for selected delays after excitation at fluences below and (**C**) above the threshold fluence of the H phase ($T = 160$ K, rep. rate = 10 kHz). The solid lines mark best fits using 3 Gaussian peaks as described in Supplementary Sec. A. The shaded areas indicate the Gaussian peak capturing the LHB. (**D**) Illustration of the collective oscillation of the star-shaped lattice distortion (CDW AM). (**E**) Band shift of the LHB versus Δt for various fluences, extracted from the corresponding Gaussian center position. The dashed black line marks a sinusoidal fit ($f = 2.4$ THz). (**F**) Peak intensity of the LHB versus Δt for various fluences, extracted from the Gaussian fits. Curves are vertically offset for clarity.

Dynamical phase transition. Having established the spectral fingerprints of the H phase, we next investigate the dynamical transition from C to H phase. Stroboscopic pump-probe trARPES measurements of the electronic switching dynamics (Fig. 2A) require relaxation to the C ground state between successive pump-probe cycles – not feasible at very low temperatures due to the exceptionally long lifetime of the H phase [8]. Thus, we increase the sample temperature to 160 K, which reduces the lifetime to < 100 µs and allows us to study the transition of the unperturbed C ground state to the H phase in a pump-probe experiment at a repetition rate of 10 kHz. We focus on the dynamics of the LHB at $\bar{\Gamma}$ for various pump-laser fluences ranging from the weak-response regime to above the switching threshold (see exemplary EDCs in Fig. 2, B and C). Using Gaussian fits of the EDCs (see Supplementary Sec. A), we extract the dynamical evolution of the LHB peak intensity, the key feature to identify the H phase, as well as the transient shift of the LHB energy position.

For an absorbed fluence of 0.15 mJ·cm^{-2}, far below the switching threshold, optical excitation launches a collective, coherent oscillation of the periodic charge- and lattice distortion, termed amplitude mode (AM), corresponding to an expansion-contraction motion of the polaron clusters (Fig. 2D) at 2.4 THz [24]. Due to strong electron-phonon coupling, this causes a modulation of the LHB energy at the frequency of the AM (grey curve in Fig. 2E). While several bands across the full Brillouin zone are transiently renormalized by the CDW modulation, the energetic position of the LHB at $\bar{\Gamma}$ couples most strongly to the CDW, and can thus be used as a measure of

the CDW lattice displacement [25, 26]. Additionally, within 50 fs after the excitation, the LHB intensity is reduced by ∼40%, resulting from an initial quench of the Mott state by transient heating and depopulation of the LHB by electron-hole excitations into higher-lying states [27], followed by a full recovery within a few ps (grey curve in Fig. 2F).

With increasing fluence, the initial band shift grows while the AM oscillations become less pronounced, and the LHB intensity only partially recovers within the examined time range. Finally, for the highest applied fluence of 0.7 mJ·cm^{-2}, the system undergoes a transition from C to H phase, evidenced by a strong persistent quench of the LHB intensity that shows no onset of recovery within tens of ps. Concomitantly, within 250 fs, the LHB undergoes a colossal transient metallization, shifting upwards by ∼300 meV, far above the equilibrium E_{F}, followed by a damped exponential recovery. This dramatic shift indicates a pronounced cooperative lattice motion counteracting the CDW distortion, and, as the band shifts significantly above the band position of the metallic high-temperature phases [28], hints toward an overshoot of the displacement beyond the symmetric undistorted state, which has also been observed in the related compound 1T-TaSe$_2$ [29]. The absence of AM modulations further supports the scenario of a strong disruption of the CDW order during the phase transition. Within ∼800 fs, the LHB position relaxes to the new quasi-equilibrium position and the transition is completed, in general agreement with switching times reported by optical studies [13–15].

Since the transition from C to H phase involves a major reorganization of the lattice, the observed switching time is surprisingly short – far below the timescale of electron-lattice equilibration [16] – suggesting a highly efficient nonthermal collective transition pathway. The question naturally arises which mode facilitates such a coupled electronic and structural transition. The AM appears to be the most likely driver of such a concerted transition, as it connects electronic and structural orders and evolves, with increasing fluence, from an oscillatory motion into an unusually large band shift associated with a significant cooperative lattice response.
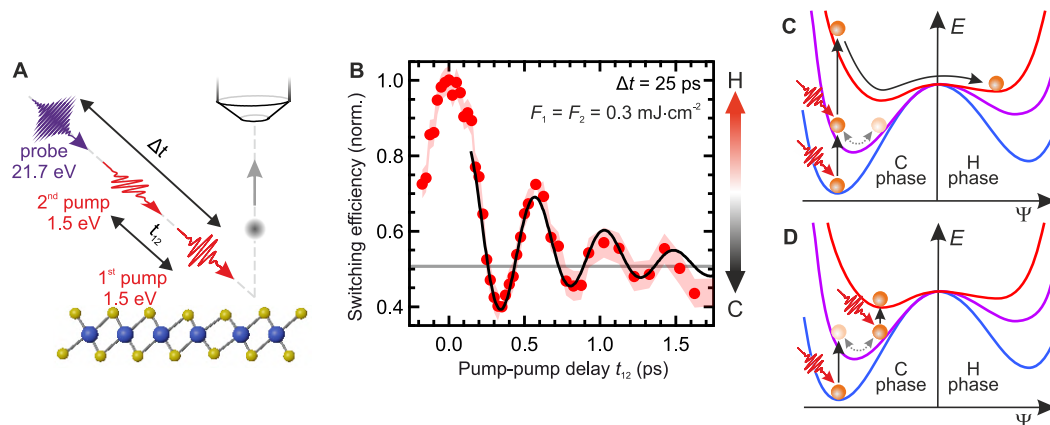
Fig. 3: Coherent control of the transition to the H phase. (**A**) Schematic of the trARPES experiment with two successive optical excitation pulses with pump-pump delay t_{12} and pump-probe delay Δt. To avoid interference artifacts during the cross-correlation, the pump pulses are linearly cross-polarized. (**B**) Switching efficiency (red dots) versus t_{12}, derived from the LHB intensity, with sinusoidal fit (black curve, f = 2.2 THz). An efficiency of 1 corresponds to the H phase, derived from the LHB intensity at t_{12}=0 ps, while an efficiency of 0 corresponds to the LHB intensity of the unperturbed C ground state at 160 K (see Supplementary Sec. C for details of the parametrization). The solid gray line indicates the asymptotic behavior for large pump-pump delays. The red shaded area indicates an uncertainty of one standard deviation derived from the Gaussian fits. (**C**) Schematic energy surfaces in equilibrium (blue) and after excitation by a first (purple) and second (red) optical pulse. The system's order is parametrized by the order parameter Ψ along the AM coordinate. Depending on the pump-pump delay, the excitation leads to an efficient pathway to the H phase or (**D**) to a halt of the dynamics, suppressing the transition.

Vibrational coherent control of the phase transition. To map out the role of the collective CDW excitation in the transition to the H phase, we perform trARPES measurements with two time-delayed optical pump pulses. The aim is to coherently control the AM (Fig. 3A).

5

The initial pulse excites the AM, whereas the oscillation amplitude is either amplified (in-phase excitation) or suppressed (out-of-phase excitation) by the time-delayed second pulse [30, 31]. We first demonstrate coherent control of the AM in the C phase in the weak-response regime with both pump pulses at equal fluence far below F_{crit} (Supplementary Sec. B). Utilizing again the transient LHB position at $\overline{\Gamma}$ as a proxy of the CDW symmetry breaking, we observe, upon two-pulse excitation, a strong modulation of the AM oscillation amplitude as a function of pump-pump delay t_{12} with the period of the AM – indicating effective coherent control.

Next, we increase the fluence to $F_1 = F_2 = 0.3$ mJ·cm^{-2}, staying below the critical fluence of the H phase for each individual pulse, but crossing the threshold in combination. By monitoring the LHB at a fixed pump$_1$-probe delay of 25 ps, we probe the system after the new quasi-equilibrium is formed. Varying the pump-pump delay, we track whether the system has been switched to the H phase (strongly reduced LHB intensity) or remains in the C ground state (only minor reduction). Strikingly, the LHB intensity and position feature a pronounced modulation with pump-pump delay, as evinced by the strongly t_{12}-dependent EDCs at $\overline{\Gamma}$ (Supplementary Fig. S3). This dependence is highlighted by the phase transition efficiency, a parametrization of the t_{12}-dependent LHB intensity (Fig. 3B). The coherent modulation of the switching efficiency with t_{12} at 2.2 THz, close to the AM frequency in the weak-response regime [24], provides direct evidence for the decisive role of the collective CDW excitation in the photoinduced transition and demonstrates exceptional control over the phase transition using a multi-pulse excitation protocol. The distinct dependence of the switching efficiency rules out a temperature-driven transition from C to H phase, since, in a thermal switching scenario, the efficiency would only depend on the total deposited energy and would show no strong dependence on t_{12} within the studied range.

Inspecting the phase of the switching efficiency reveals that its local maxima approximately coincide with constructive amplification of the AM by the second optical pulse, while minima coincide with suppression of the AM by the subsequent pulse (Supplementary Fig. S4). This indicates that, upon constructive amplification of the CDW excitation beyond a certain threshold, the transition to the H phase commences, while suppression impedes switching. Already at a fluence of 0.3 mJ·cm^{-2}, a faint suppression of the LHB is observed by a single pulse, resulting in a switching efficiency of ~ 0.5 for two individual pulses with large pump-pump delay (grey line in Fig. 3B). Remarkably, within the first oscillation cycle, coherent control of the AM allows suppressing the switching efficiency below the level of two individual pulses, demonstrating an effective suppression of the phase transition by the pulse sequence. Coherent amplification and suppression pathways within transient energy surfaces are sketched in Fig. 3, C and D. Note that the one-dimensional energy landscape only serves as a schematic illustration. The offset of the local extrema of the switching efficiency from optimal amplification and suppression of the AM in the low-fluence regime by few 10 fs suggests that the transition is governed by a more complex multi-dimensional energy landscape defined by intra- and interlayer CDW order (Supplementary Fig. S4).

Discussion

Our results demonstrate the ultrafast timescale and vibrational coherent control of the transition from C to H phase and expose the collective CDW excitation as an integral part of the optical switching mechanism. The colossal upwards band shift of the LHB in the strong-response regime, the rapid transition within a few hundred fs, and the control of the switching efficiency through the AM imply a nonthermal, cooperative transition pathway dictated by a transient energy landscape. Based on the observed band-structure dynamics, we propose a microscopic pathway for the photoinduced phase transition (Fig. 4): Initially, the system is in the Mott-insulating polaronic C phase. The optical pump pulse is absorbed by the electronic system, which thermalizes within tens of fs, reaching a maximum temperature far beyond 1000 K [7, 25] and melting the Mott energy gap. Simultaneously, the strong electronic perturbation displaces the ionic coordinates from their CDW ground-state positions toward the high-temperature symmetric positions, launching a delayed outwards motion towards these new quasi-equilibrium coordinates. Concomitantly, the commensurate CDW energy gaps close and the LHB is renormalized toward higher
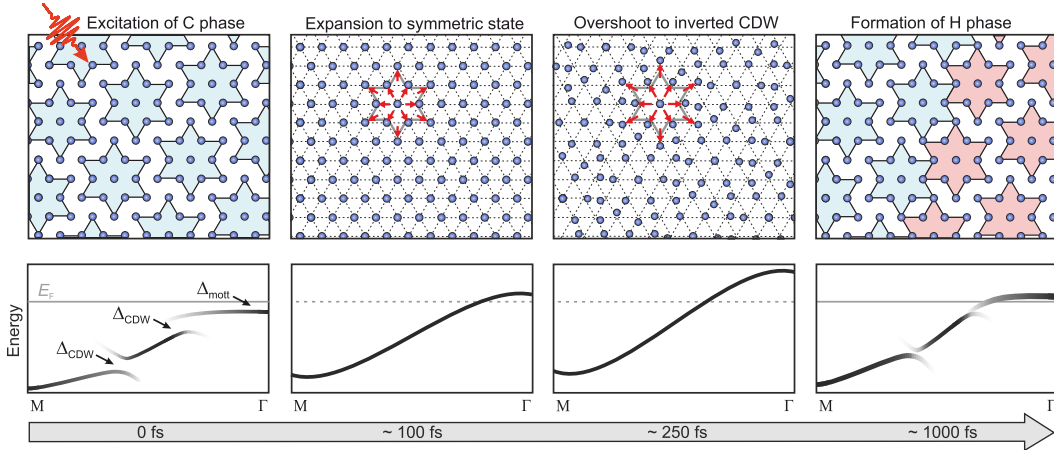
Fig. 4: Illustration of the transition to the H state. Top: Illustration of the intralayer lattice structure during the phase transition from C to H phase following a collective CDW excitation (see text). Bottom: Corresponding schematic dispersion of the Ta $5d$ band. The grey horizontal line marks the equilibrium E_{F}. In the highly out-of-equilibrium state after photoexcitation, the position of E_{F} is not well-defined, indicated by the dashed line.

energies. Intriguingly, strong optical perturbation can lead to an overshoot of the ionic displacement beyond the undistorted high-symmetry positions. While for most CDW materials such an overshoot leads to a CDW pattern that is geometrically equivalent to the initial CDW [32, 33], over-driving the star-shaped polaron clusters leads to the formation of a new (inverted) CDW geometry. In the compound $1T$-TaSe$_2$, which features a similar star-shaped CDW, the formation of an inverted CDW state – shifting the lattice and charge density from the cluster center to the peripheral – was observed, associated with a pronounced upwards shift of the low-energy band at $\bar{\Gamma}$ [29]. Similarly in TaS$_2$, the observed colossal shift of the LHB position within 250 fs suggests a CDW overshoot to an inverted pattern. Subsequently, on a timescale of a few hundred fs, the LHB position relaxes, which we assign to the reemergence of polaron clusters. However, the persistent collapse of the Mott-insulating state indicates a transition to the H phase, in which the formation of a network of irregular domain boundaries in each TaS$_2$ layer breaks the interlayer polaron stacking order, quenching the delicate Mott gap of the C phase.

The question arises whether the formation of the H phase plays out through an incoherent formation process or a collective pathway connected to the inverted CDW pattern. The ultrafast switching time suggests the latter, likely facilitated by strong coupling of the over-driven CDW state to other vibrational modes [34, 35] that enable efficient reformation of polaron clusters. Interestingly, as the CDW order in $1T$-TaS$_2$ is rotated by $\sim 13°$ with respect to the atomic lattice, previous studies showed that optical excitation of the room-temperature NC phase, which transiently completely suppresses the NC order, leads to the reformation of the NC phase in patches of two degenerate (clockwise and counter-clockwise rotated) CDW domains [36]. However, in the H phase, only a single rotational orientation similar to the initial CDW rotation in the C phase is observed [11], suggesting that a nonthermal transition pathway, which preserves the orientation, connects C and H phases. Yet, the large number of irregular domain walls also indicates a high degree of disorder during the recovery. The formation of domain walls is attributed to an effective charge injection by the photoexcitation [7, 16]. During the recovery of order, the additional charges are accommodated in domain walls within the commensurate structure, effectively increasing the polaron density as neighboring stars within the domain walls share corners [11]. Local fluctuations and aggregation of excess charges may thus interplay with a cooperative recovery of CDW order, resulting in the formation of the H phase. Additional studies of the ultrafast lattice dynamics are required to elucidate the microscopic details during the reformation of short-range CDW order.

Intriguingly, the H phase can also be induced by optical or voltage pulses with pulse lengths that significantly exceed the period of the AM [7, 16], precluding any collective CDW response.

However, the switching by an incoherent charge-carrier injection by ps to ns pulses requires drastically higher switching energy densities. This demonstrates that, while the H phase can also be stabilized by an incoherent excitation, the collective switching pathway enables a more rapid and efficient transition.

Conclusion

Using time- and angle-resolved photoemission spectroscopy, we provide a detailed characterization of the electronic band structure and switching dynamics of the metastable hidden state of $1T$-TaS_2 upon femtosecond optical excitation, thereby revealing the key role of a collective charge-density-wave excitation in the nonthermal transition pathway. The exceptional speed and high degree of control over the phase transition in combination with the remarkable stability of the hidden phase underline its unique functionality for memory device applications [16]. Furthermore, we envision that collective excitations of complex symmetry-broken ground states may reveal hidden orders in a variety of materials [37]. Particularly resonant (multi-pulse) excitations of coherences, minimizing detrimental heating of the electrons and lattice, represent a promising route to realizing and understanding new emergent phases in quantum materials.

Acknowledgements

References

[1] A. de la Torre et al., "Colloquium: Nonthermal pathways to ultrafast control in quantum materials", Rev. Mod. Phys. **93**, 041002 (2021).

[2] C. L. Smallwood et al., "Tracking cooper pairs in a cuprate superconductor by ultrafast angle-resolved photoemission", Science **336**, 1137–1139 (2012).

[3] J. G. Horstmann et al., "Coherent control of a surface structural phase transition", Nature **583**, 232–236 (2020).

[4] V. R. Morrison et al., "A photoinduced metal-like phase of monoclinic VO_2 revealed by ultrafast electron diffraction", Science **346**, 445–448 (2014).

[5] J. Zhang et al., "Cooperative photoinduced metastable phase control in strained manganite films", Nat. Mater. **15**, 956–960 (2016).

[6]M. Budden et al., "Evidence for metastable photo-induced superconductivity in K_3C_{60}", Nat. Phys. **17**, 611–618 (2021).

[7]L. Stojchevska et al., "Ultrafast switching to a stable hidden quantum state in an electronic crystal", Science **344**, 177–180 (2014).

[8]I. Vaskivskyi et al., "Controlling the metal-to-insulator relaxation of the metastable hidden quantum state in $1T$-TaS_2", Sci. Adv. **1**, e1500168 (2015).

[9]L. Ma et al., "A metallic mosaic phase and the origin of Mott-insulating state in $1T$-TaS_2", Nat. Commun. **7**, 10956 (2016).

[10]D. Cho et al., "Nanoscale manipulation of the Mott insulating state coupled to charge order in $1T$-TaS_2", Nat. Commun. **7**, 10453 (2016).

[11]Y. A. Gerasimenko, P. Karpov, I. Vaskivskyi, S. Brazovskii, and D. Mihailovic, "Intertwined chiral charge orders and topological stabilization of the light-induced state of a prototypical transition metal dichalcogenide", npj Quantum Mater. **4**, 32 (2019).

[12]Q. Stahl et al., "Collapse of layer dimerization in the photo-induced hidden state of $1T$-TaS_2", Nat. Commun. **11**, 1247 (2020).

[13]J. Ravnik et al., "A time-domain phase diagram of metastable states in a charge ordered quantum material", Nat. Commun. **12**, 2323 (2021).

[14]J. Ravnik, I. Vaskivskyi, T. Mertelj, and D. Mihailovic, "Real-time observation of the coherent transition to a metastable emergent state in $1T$-TaS_2", Phys. Rev. B **97**, 075304 (2018).

[15]F. Y. Gao et al., "Snapshots of a light-induced metastable hidden phase driven by the collapse of charge order", Preprint at https://arxiv.org/abs/2112.11015v1 (2021).

[16]D. Mihailovic et al., "Ultrafast non-thermal and thermal switching in charge configuration memory devices based on $1T$-TaS_2", Appl. Phys. Lett. **119**, 013106 (2021).

[17]R. E. Thomson, B. Burk, A. Zettl, and J. Clarke, "Scanning tunneling microscopy of the charge-density-wave structure in $1T$-TaS_2", Phys. Rev. B **49**, 16899–16916 (1994).

[18]C. J. Butler, M. Yoshida, T. Hanaguri, and Y. Iwasa, "Mottness versus unit-cell doubling as the driver of the insulating state in $1T$-TaS_2", Nat. Commun. **11**, 2477 (2020).

[19]T. Ritschel et al., "Orbital textures and charge density waves in transition metal dichalcogenides", Nat. Phys. **11**, 328–331 (2015).

[20]S.-H. Lee, J. S. Goh, and D. Cho, "Origin of the insulating phase and first-order metal-insulator transition in $1T$-TaS_2", Phys. Rev. Lett. **122**, 106404 (2019).

[21]C. W. Nicholson et al., "Modified interlayer stacking and insulator to correlated-metal transition driven by uniaxial strain in $1T$-TaS_2", Preprint at https://arxiv.org/abs/2204.05598v1 (2022).

[22]L. Perfetti, T. A. Gloor, F. Mila, H. Berger, and M. Grioni, "Unexpected periodicity in the quasi-two-dimensional mott insulator $1T$-TaS_2 revealed by angle-resolved photoemission", Phys. Rev. B **71**, 153101 (2005).

[23]A. Fuhrmann, D. Heilmann, and H. Monien, "From mott insulator to band insulator: a dynamical mean-field theory study", Phys. Rev. B **73**, 245118 (2006).

[24]J. Demsar, L. Forró, H. Berger, and D. Mihailovic, "Femtosecond snapshots of gap-forming charge-density-wave correlations in quasi-two-dimensional dichalcogenides 1T-TaS_2 and 2H-$TaSe_2$", Phys. Rev. B **66**, 041101 (2002).

[25]L. Perfetti et al., "Time evolution of the electronic structure of 1T-TaS_2 through the insulator-metal transition", Phys. Rev. Lett. **97**, 067402 (2006).

[26]S. Hellmann et al., "Time-domain classification of charge-density-wave insulators", Nat. Commun. **3**, 1069 (2012).

[27]M. Ligges et al., "Ultrafast doublon dynamics in photoexcited $1T$-TaS_2", Phys. Rev. Lett. **120**, 166401 (2018).

[28]C. Sohrt, A. Stange, M. Bauer, and K. Rossnagel, "How fast can a peierls–mott insulator be melted?", Faraday Discuss. **171**, 243–257 (2014).

[29]Y. Zhang et al., "Creation of a novel inverted charge density wave state", Struct. Dyn. **9**, 014501 (2022).

[30]D. Mihailovic et al., "Femtosecond data storage, processing, and search using collective excitations of a macroscopic quantum state", Appl. Phys. Lett. **80**, 871–873 (2002).

[31]L. Rettig, J.-H. Chu, I. R. Fisher, U. Bovensiepen, and M. Wolf, "Coherent dynamics of the charge density wave gap in tritellurides", Faraday Discuss. **171**, 299–310 (2014).

[32]T. Huber et al., "Coherent structural dynamics of a prototypical charge-density-wave-to-metal transition", Phys. Rev. Lett. **113**, 026401 (2014).

[33]J. Maklar et al., "Nonequilibrium charge-density-wave order beyond the thermal limit", Nat. Commun. **12**, 2499 (2021).

[34]E. S. Zijlstra, L. L. Tatarinova, and M. E. Garcia, "Laser-induced phonon-phonon interactions in bismuth", Phys. Rev. B **74**, 220301 (2006).

[35]G. Sciaini et al., "Electronic acceleration of atomic motions and disordering in bismuth", Nature **458**, 56–59 (2009).

[36]A. Zong et al., "Ultrafast manipulation of mirror domain walls in a charge density wave", Sci. Adv. **4**, eaau5501 (2018).

[37]N. Yoshikawa et al., "Ultrafast switching to an insulating-like metastable state by amplitudon excitation of a charge density wave", Nat. Phys. **17**, 909–914 (2021).

[38]M. Puppin et al., "Time- and angle-resolved photoemission spectroscopy of solids in the extreme ultraviolet at 500 kHz repetition rate", Rev. Sci. Instrum. **90**, 023104 (2019).

[39]J. Maklar et al., "A quantitative comparison of time-of-flight momentum microscopes and hemispherical analyzers for time- and angle-resolved photoemission spectroscopy experiments", Rev. Sci. Instrum. **91**, 123112 (2020).

[40]A. S. Ngankeu et al., "Quasi-one-dimensional metallic band dispersion in the commensurate charge density wave of $1T$-TaS$_2$", Phys. Rev. B **96**, 195147 (2017).

[41]A. Gauthier et al., "Tuning time and energy resolution in time-resolved photoemission spectroscopy with nonlinear crystals", J. Appl. Phys. **128**, 093101 (2020).

Supplementary Information for "Coherent Light Control of a Metastable Hidden Phase"

Materials and Methods

<u>XUV-trARPES</u>

Crystals of $1T$-TaS$_2$ were grown by chemical transport method with iodine as a transport agent. The ARPES measurements were performed in ultra-high vacuum $< 1 \times 10^{-10}$ mbar (samples cleaved in-situ), using a table-top high-harmonic-generation trARPES setup [38, 39] ($h\nu_{\mathrm{probe}}$=21.7 eV, $h\nu_{\mathrm{pump}}$=1.55 eV, $\Delta E \approx 150$ meV, $\Delta t \approx 35$ fs) with a pulse picker to vary the repetition rate (from single pulses up to 500 kHz). The samples are positioned with a 6-axis manipulator with cryogenic temperature control (SPECS Carving). Photoelectrons are collected either by a SPECS Phoibos 150 hemispherical analyzer or a SPECS METIS 1000 time-of-flight momentum microscope. The momentum microscope allows parallel acquisition of the 3D photoelectron distribution across a large energy- and in-plane momentum range, advantageous for static band-structure mapping (Figs. 1A to E, S6, S7C and D, S8), while the hemispherical analyzer allows for fast data acquisition of 2D energy-momentum cuts, ideal for time-resolved measurements within a limited energy-momentum range at low repetition rates (Figs. 2, 3, S3, S4, S5, S7A and B).

The EDCs extracted from momentum-microscopy data were integrated over a momentum area of 0.2×0.2 Å^{-2}. The EDCs extracted from hemispherical-analyzer data were integrated along the momentum-resolved direction over 0.35 Å^{-1}. For the applied probe energy of 21.7 eV, an inner potential $V_0 = 20$ eV and work function $\Psi = 4.5$ eV of $1T$-TaS$_2$ [40], we estimate that, within the 3D Brillouin zone, we map the band structure approximately at the Brillouin-zone center with respect to the out-of-plane k_z direction.

The pump and probe spot sizes (FWHM) are $\approx 150 \times 150$ μm^2 and $\approx 70 \times 60$ μm^2, respectively. All discussed fluences refer to the absorbed fluence, estimated using a complex refractive index of n=3.2 and k=2.9 at λ=800 nm. Temporal pump-probe overlap ($\Delta t = 0$ fs) was determined from the transient pump-laser-induced population of high-energy states ($E > E_{\mathrm{F}} + 0.5$ eV).

Switching to the H phase has been achieved using optical pulses at 800 nm and an absorbed fluence $> F_{\mathrm{crit}} \approx 0.5$ mJ·cm^{-2} at a pulse length of $t_{\mathrm{FWHM}} = 35$ fs.

<u>UV-trARPES</u>

Additional static measurements (Figs. 1F, S1) with increased energy resolution ($\Delta E < 22$ meV) were obtained using a 6 eV-laser-ARPES setup with a Scienta R4000 hemispherical analyzer [41]. For the 6eV-laser-ARPES experiments, we used a regenerative amplifier operating at 10 kHz to switch the sample with 10 ms long bursts consisting of 100 p-polarized 830 nm pulses at an absorbed fluence of 1 mJ·cm^{-2}. The pump beam profile (FWHM) was 363×390 μm^2. 6eV-laser-ARPES was acquired with the frequency-quadrupled output of an oscillator operating at 80 MHz repetition rate. The probe beam profile (FWHM) was 41×35 μm^2. During the 6-eV ARPES experiments, the sample was kept at 11 K.

Supplementary Figures
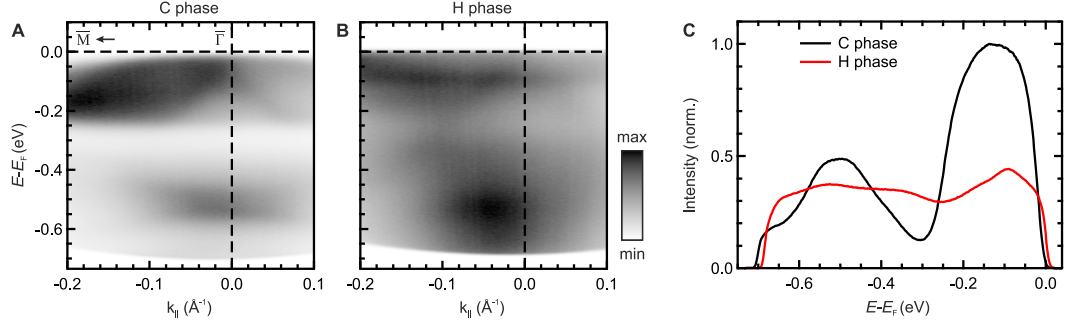
Fig. S1: Static high-energy-resolution ARPES measurements. (**A**) Energy-momentum distribution of the pristine C phase and (**B**) of the photoinduced H phase at a sample temperature of $T = 11$ K obtained using a 6 eV laser-based ARPES setup (see methods). (**C**) EDCs of the respective phases at $\overline{\Gamma}$.
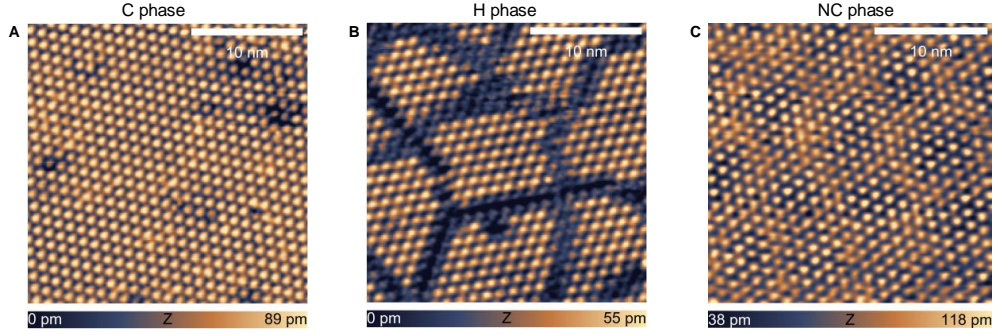
Fig. S2: STM images of the C, H and NC phases of $1T$-TaS$_2$. (**A** and **B**) The images are taken at $V = -800$ mV at 5 K and (**C**) at 300 K. Switching from C to H phase was performed in-situ at 5 K with a single optical pulse at the fluence of 1 mJ·cm^{-2}, 800 nm central wavelength and 60 fs duration.
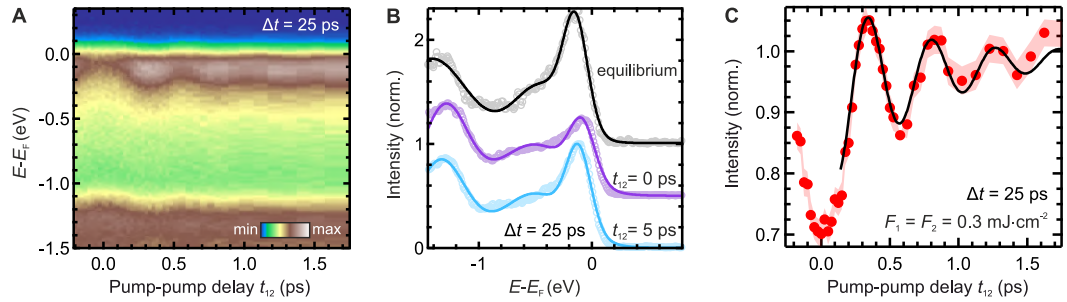
Fig. S3: Coherent control of the H phase using two successive pump pulses. (**A**) EDCs at $\overline{\Gamma}$ as function of t_{12} for a fixed pump-probe delay of $\Delta t = 25$ ps ($T = 160$ K, $F_1 = F_2 = 0.3$ mJ·cm^{-2}, rep. rate = 10 kHz). (**B**) Exemplary EDCs (circles) with Gaussian fits (solid lines) at $\overline{\Gamma}$ in equilibrium and for selected pump-pump delays t_{12} at $\Delta t = 25$ ps ($T = 160$ K, $F_1 = F_2 = 0.3$ mJ·cm^{-2}, rep. rate of 10 kHz, curves vertically offset). (**C**) LHB peak intensity (red dots) as a function of t_{12} for a fixed pump-probe delay of $\Delta t = 25$ ps, extracted from panel **A**. The intensity is normalized to the value obtained for $t_{12} = 5$ ps. The black line marks a damped sinusoidal fit with frequency $f = 2.2$ THz.
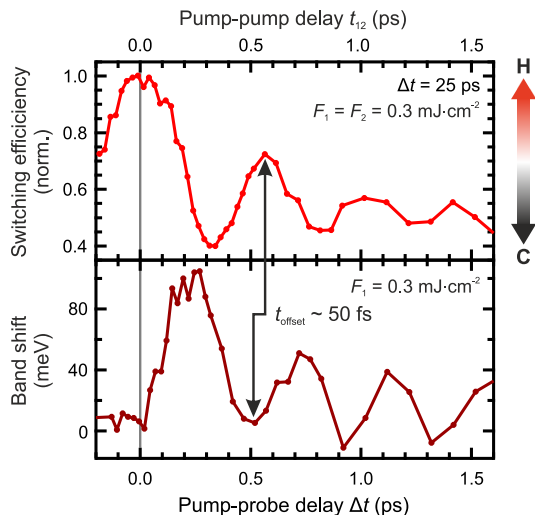
Fig. S4: Comparison of the 2-pulse switching efficiency and the single-pulse AM band oscillation. Top: Switching efficiency as function of pump-pump delay t_{12} (as presented in Fig. 3) at fixed Δt following 2-pulse excitation. Bottom: LHB shift as function of pump-probe delay Δt after single-pulse excitation (as presented in Fig. 2). The two curves show approximately inverse behavior, with an offset of only few ten fs between respective maxima/minima. The direct comparison of the two curves shows that approximately in-phase excitation (constructive amplification of AM; arrival of second pulse when band shift is at local minimum) leads to efficient switching to the H phase (maximum of switching efficiency). In contrast, when the second pulse arrives approximately out-of-phase (suppression of AM; arrival of second pulse when band shift is at local maximum), switching is inhibited.

Supplementary Text

A   Extracting Energy Position and Peak Intensity of the LHB

To quantify the (dynamic) energy shift and intensity change of the LHB, we employ a phenomenological description of the experimental EDCs at $\overline{\Gamma}$ using a sum of three Gaussian functions, which yields an excellent description of the data (Fig. 2, B and C). For the fit of the time-resolved data, the FWHM and the position of the central Gaussian located at $E - E_{\mathrm{F}} \approx -0.7$ eV are kept fixed at the pre-excitation value, while its peak intensity and the remaining parameters of the Gaussian functions describing the LHB at -0.15 eV and the valence band at -1.3 eV are kept as free fit parameters. This fit procedure has been used to extract the modulation of the energetic position and peak intensity of the LHB from time-resolved pump-probe and coherent control data, and has also been applied to evaluate the static temperature ramp (Supplementary Fig. S8).

B   Coherent Control of the CDW Amplitude Mode in the Weak-response Regime

Using trARPES, we demonstrate coherent control of the CDW AM of $1T$-TaS$_2$ in the C phase in the low-fluence (weak-response) regime. The AM excitation leads to a transient modulation of the energetic position of several bands near the Fermi level. Particularly the LHB energy at $\overline{\Gamma}$ undergoes a very pronounced transient oscillation. Therefore, we track the AM by extracting the LHB energy position at $\overline{\Gamma}$, employing the Gaussian fitting procedure discussed above. Upon excitation by a single pump pulse (see grey and black curves in Supplementary Fig. S5A), a sinusoidal oscillation of the LHB position at a frequency of ~ 2.4 THz is launched. When exciting the AM by a second pulse (see colored curves), the initial oscillation is either amplified (in-phase
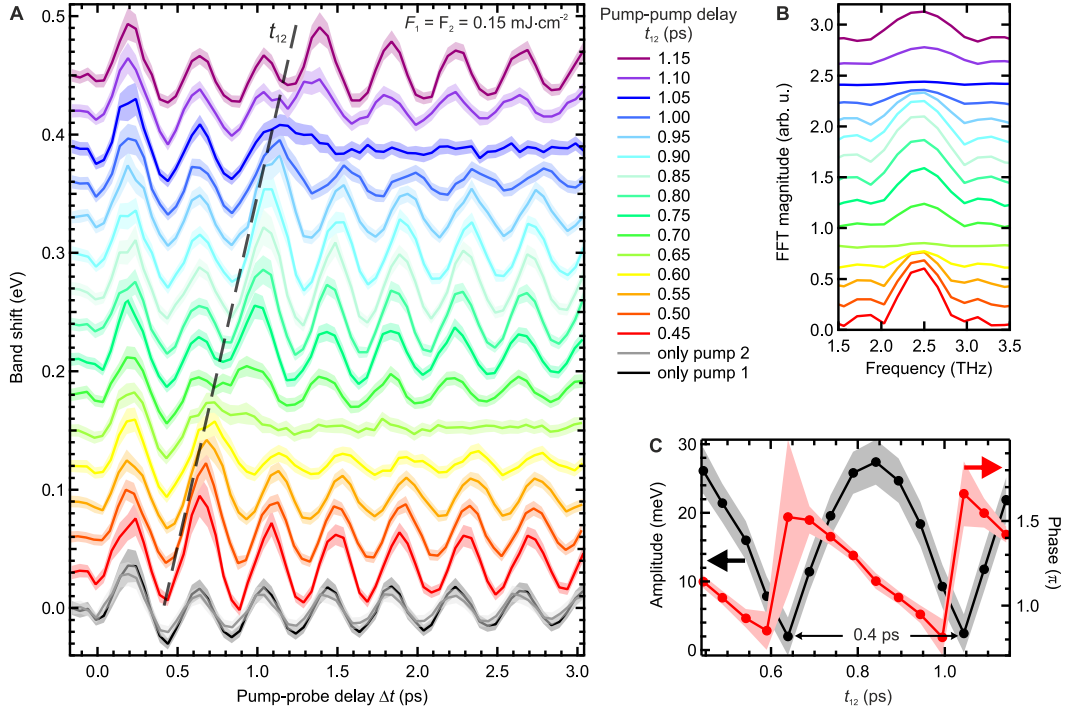
Fig. S5: Coherent control of the CDW AM using two optical pump pulses. (**A**) Band shift (solid lines) of the LHB as a function of pump-probe delay Δt for various pump-pump delays t_{12} for fluences $F_1 = F_2 = 0.15$ mJ·cm^{-2} far below the switching threshold of the H phase (rep. rate 500 kHz, $T = 20$ K, curves vertically offset for clarity). The dashed black line indicates the arrival time of the second pump pulse. The black and grey curves mark the reference band shifts induced by the individual pump pulses. The shaded areas correspond to an uncertainty of one standard deviation resulting from the Gaussian fit. (**B**) Fast Fourier transform magnitude of the band shifts in panel **A** for $\Delta t > 1.5$ ps. (**C**) Oscillation amplitude (black, left axis) and phase (red, right axis) extracted from sinusoidal fits of the band shifts in **A** as a function of pump-pump delay t_{12}. The shaded areas mark an uncertainty of one standard deviation resulting from the sinusoidal fits.

excitation) or suppressed (out-of-phase excitation), depending on the pump-pump delay t_{12}. This is captured by the Fourier transform magnitudes for various pump-pump delays (Supplementary Fig. S5B), featuring pronounced peaks at 2.4 THz for in-phase excitation ($t_{12} \sim n/2.4$ THz, with positive integer n) and a flat curve for out-of-phase excitation ($t_{12} \sim (n+0.5)/2.4$ THz). Lastly, we also fit the band shift using a sine function to extract the oscillation amplitude and phase as a function of t_{12} (Supplementary Fig. S5C). The periodicity of amplitude and phase directly reflects the frequency of the AM.

C   Parametrization of the Switching Efficiency

To parametrize the phase transition efficiency from C to H phase upon excitation by two successive optical pulses, we fit the t_{12}-dependent EDCs at $\overline{\Gamma}$ (Supplementary Fig. S3A) using Gaussian functions as discussed above (exemplary EDCs shown in Supplementary Fig. S3B). From the Gaussian fits, we extract the peak intensity of the LHB as a function of pump-pump delay (Supplementary Fig. S3C). For the parametrization of the switching efficiency (Fig. 3B), the LHB peak intensity at $t_{12} \sim 0$ ps is defined as an efficiency of 1 (full switching, H phase), whereas the LHB intensity in the static C ground state is defined as 0 (no switching, C phase). Intensity values between the two extrema are parametrized accordingly to intermediate (partial) switching efficiencies.

D   Partial Suppression of CDW gaps in the Hidden Phase

In addition to the modification of the LHB, we observe a partial suppression of the commensurate CDW gaps in the H phase (Supplementary Fig. S6). The partial CDW-gap suppression is likely connected to the breaking of interlayer dimerization, as density functional theory calculations predict a strong dependence of the CDW gaps on interlayer stacking order [19, 20]. In the H phase, averaging over a large number of microscopic domains with random interlayer arrangements may lead to a blurring of individual, energetically displaced CDW gaps, while also the absolute size of the gaps may be reduced as compared to the bilayer-stacked C phase [10].
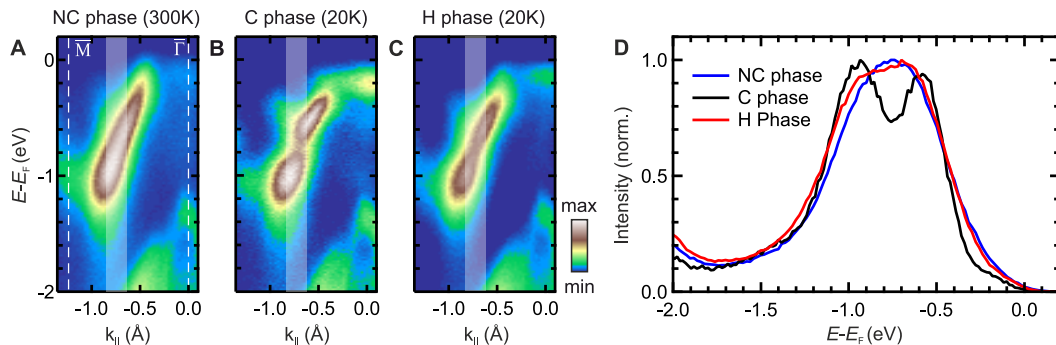
Fig. S6: CDW energy gap. (**A** to **C**) Static energy-momentum cuts along the $\overline{M} - \overline{\Gamma}$ direction for NC, C and H phases. (**D**) EDCs of the shaded momentum regions in panels **A** to **C**, highlighting a partial suppression of the CDW energy gap in the H phase.

E   Details of the Optical Switching

Optical switching from C to H phase and optical erasing, i.e., melting the metastable H phase by laser-heating to restore the C ground state, are highly reproducible over many switching cycles. During the optical erasing procedure, the previously switched sample area is exposed to the pump laser at a repetition rate of 500 kHz at a fluence of a few hundred µJ·cm^{-2}, resulting in strong average heating, thus reducing the lifetime of the H phase [7]. Exemplary spectra of the pristine C phase, photoinduced H phase, and C phase after optical erasure reveal that the ground state is fully restored by the erasing procedure (Supplementary Fig. S7, A and B).

For a pump-pulse length of FWHM=35 fs, we find a critical fluence of $F_{\mathrm{crit}} = 0.5$ mJ·cm^{-2} at $h\nu = 1.55$ eV, as determined from the LHB peak intensity (Supplementary Fig. S7C). Interestingly, we observe a sharp fluence threshold, as the fluence range of intermediate switching between C and H phase amounts to only few ten µJ·cm^{-2}. Note, however, that F_{crit} critically depends on the pulse length [7]. Furthermore, we find that the full transition to the H phase is induced by a single optical pulse, whereas subsequent pulses show no effect (Supplementary Fig. S7D).

The critical fluence observed at 20 K during this characterization using the momentum microscope is slightly lower than for the experiments performed at increased temperatures using the hemispherical analyzer (Fig. 2), which may originate from a weak temperature-dependence of the threshold fluence or may stem from a slight inaccuracy of the fluence calibration between different experimental geometries.

The recovery of the metastable H phase is well described by a thermally activated Arrhenius-like behavior [8]. At 20 K, we observe no recovery of the H phase within the course of 24 hours. However, with increasing temperatures the lifetime strongly decreases, reducing to a few ten seconds at ∼50 K [8]. Thus, heating the sample at a rate of 1 K per minute after optical switching to the H phase at 20 K reveals a relaxation to the C phase at ∼45 K, evident from the recovery of the LHB intensity (Supplementary Fig. S8).
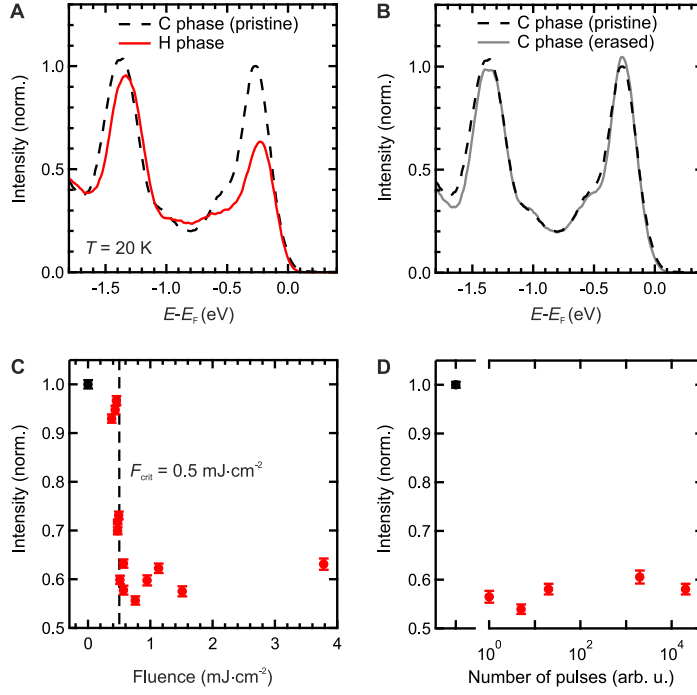
Fig. S7: Characterization of optical switching. (A) EDCs at $\overline{\Gamma}$ at 20 K of the pristine C phase and after optically inducing the H phase using few optical pulses at $F = 2.5$ mJ·cm^{-2}. **(B)** EDCs at $\overline{\Gamma}$ of the pristine C phase and after erasing the H phase by laser-based average heating (exposure to the pump laser for 1 s at 500 kHz and $F = 0.3$ mJ·cm^{-2}). **(C)** Peak intensity of the LHB extracted from Gaussian fits as a function of pump fluence (exposure for 1 s at 20 Hz). The dashed line marks the critical threshold fluence of $F_{\rm crit} = 0.5$ mJ·cm^{-2}. After each individual measurement, an optical erase has been performed to revert the system to the C ground state. **(D)** Intensity of the LHB as a function of number of pump pulses applied to the sample ($F = 3.5$ mJ·cm^{-2}). In panels **C** to **D**, the error bars correspond to one standard deviation resulting from the Gaussian fit as described above. The black data points mark the peak intensities of the pristine C phase.
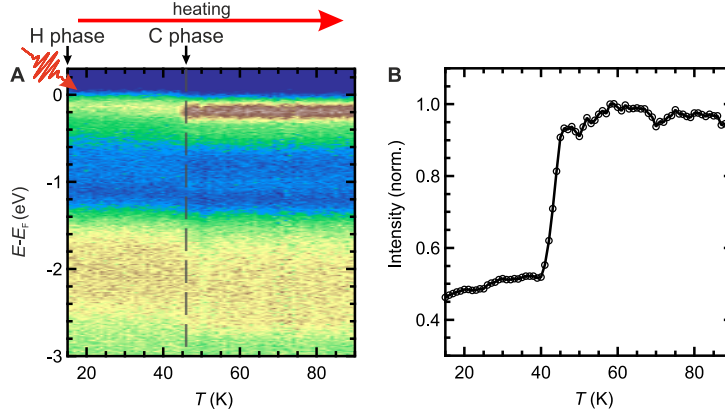
Fig. S8: Stability of the H phase. (A) EDCs at $\overline{\Gamma}$ with increasing sample temperature T (rate of 1 K per minute) after switching to the H phase at 20 K. **(B)** Corresponding LHB peak intensity versus T.

16

F Mottness Collapse in the Absence of Intralayer Domain walls

Mapping the electronic band structure of the H phase revealed a metallization due to a collapse of the Mott-insulating ground state, which we link to the loss of long-range order along the out-of-plane direction. Here, we present further evidence for the critical role of the stacking order by investigating a buried domain wall in $1T$-TaS$_2$ using scanning tunneling microscopy (STM), as presented in Supplementary Fig. S9. After applying a voltage pulse at the position marked by the red cross, we observe the metallization of a patch on the sample surface (indicated by 'hidden') despite the absence of any domain walls in the topmost layer. The STM contrast at the edges of the metallic patch despite the lack of a CDW phase shift indicates buried domain walls in the layer underneath, which further corroborates the strong impact of the stacking order on the low-energy electronic states.
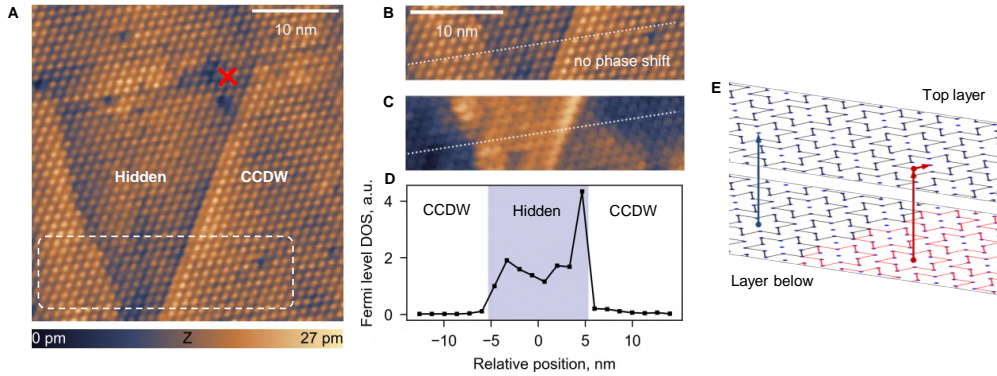
Fig. S9: Mottness collapse in the absence of intralayer domain walls. (A) Pseudo-topographic STM image of a $1T$-TaS$_2$ surface ($V = -800$ mV, $I = 1$ nA) after applying a 3 V voltage pulse in the top right corner (red cross). (B) Close-up inspection of the irregular triangle in A demonstrates the absence of any CDW phase shifts despite the different appearance. (C) In-gap STM image ($V = -50$ mV, $I = 300$ pA) of the area in B demonstrates an enhanced low-energy contrast. Note the bright edge indicating the presence of domain wall states underneath. (D) Spectral weight at the Fermi level extracted from dI/dV measurements along the dotted line in B and C, confirming the Mottness collapse in the absence of intralayer domain walls. Note that the in-gap spectral weight is present both at the boundaries and in the middle of the switched area (shaded blue). This confirms the involvement of the coupling between the layers in the Mottness collapse. (E) Speculative arrangement of the Star of David clusters in the top layer and the layer beneath. Red clusters are phase-shifted within the plane with respect to the blue ones. The arrows indicate the inter- and intra-layer shifts respectively.

References

[1] B. Keimer and J. E. Moore, "The physics of quantum materials", Nat. Phys. **13**, 1045–1055 (2017).

[2] C. Broholm et al., "Basic Research Needs Workshop on Quantum Materials for Energy Relevant Technology", Office of Science, US Department of Energy (2016).

[3] Y. Tokura, M. Kawasaki, and N. Nagaosa, "Emergent functions of quantum materials", Nat. Phys. **13**, 1056–1068 (2017).

[4] J. A. Sobota, Y. He, and Z.-X. Shen, "Angle-resolved photoemission studies of quantum materials", Rev. Mod. Phys. **93**, 025006 (2021).

[5] P. Narang, C. A. C. Garcia, and C. Felser, "The topology of electronic band structures", Nat. Mater. **20**, 293–300 (2021).

[6] K. S. Novoselov et al., "Two-dimensional gas of massless Dirac fermions in graphene", Nature **438**, 197–200 (2005).

[7] C. L. Kane and E. J. Mele, "Quantum spin Hall effect in graphene", Phys. Rev. Lett. **95**, 226801 (2005).

[8] X. Qian, J. Liu, L. Fu, and J. Li, "Quantum spin Hall effect in two-dimensional transition metal dichalcogenides", Science **346**, 1344–1347 (2014).

[9] G. Gruner, *Density waves in solids* (CRC press, 1994).

[10] B. Sipos et al., "From Mott state to superconductivity in 1T-TaS$_2$", Nat. Mater. **7**, 960–965 (2008).

[11] C. J. Butler, M. Yoshida, T. Hanaguri, and Y. Iwasa, "Mottness versus unit-cell doubling as the driver of the insulating state in 1T-TaS$_2$", Nat. Commun. **11**, 2477 (2020).

[12] Y. D. Wang et al., "Band insulator to Mott insulator transition in 1T-TaS2", Nat. Commun. **11**, 4215 (2020).

[13] S. Gerber et al., "Femtosecond electron-phonon lock-in by photoemission and x-ray free-electron laser", Science **357**, 71–75 (2017).

[14] S. Hellmann et al., "Time-domain classification of charge-density-wave insulators", Nat. Commun. **3**, 1069 (2012).

[15] S. Dal Conte et al., "Disentangling the Electronic and Phononic Glue in a High-T$_c$ Superconductor", Science **335**, 1600–1603 (2012).

[16] S. Wandel et al., "Enhanced charge density wave coherence in a light-quenched, high-temperature superconductor", Science **376**, 860–864 (2022).

[17] A. Kogar et al., "Light-induced charge density wave in LaTe$_3$", Nat. Phys. **16**, 159–163 (2020).

[18]D. N. Basov, R. D. Averitt, and D. Hsieh, "Towards properties on demand in quantum materials", Nat. Mater. **16**, 1077–1088 (2017).

[19]A. de la Torre et al., "Colloquium: Nonthermal pathways to ultrafast control in quantum materials", Rev. Mod. Phys. **93**, 041002 (2021).

[20]D. Mihailovic et al., "Ultrafast non-thermal and thermal switching in charge configuration memory devices based on 1T-TaS2", Appl. Phys. Lett. **119**, 013106 (2021).

[21]A. Mraz et al., "Charge Configuration Memory Devices: Energy Efficiency and Switching Speed", Nano Lett. **22**, 4814–4821 (2022).

[22]M. Mitrano et al., "Possible light-induced superconductivity in K_3C_{60} at high temperature", Nature **530**, 461–464 (2016).

[23]M. Budden et al., "Evidence for metastable photo-induced superconductivity in K_3C_{60}", Nat. Phys. **17**, 611–618 (2021).

[24]L. Stojchevska et al., "Ultrafast switching to a stable hidden quantum state in an electronic crystal", Science **344**, 177–180 (2014).

[25]U. De Giovannini, H. Hübener, S. A. Sato, and A. Rubio, "Direct Measurement of Electron-Phonon Coupling with Time-Resolved ARPES", Phys. Rev. Lett. **125**, 136401 (2020).

[26]X. Zhu, J. Guo, J. Zhang, and E. W. Plummer, "Misconceptions associated with the origin of charge density waves", Adv. Phys. X **2**, 622–640 (2017).

[27]P. Fazekas, *Lecture Notes on Electron Correlation and Magnetism | Series in Modern Condensed Matter Physics*, Vol. 5 (World Scientific Publishing Company, 1999).

[28]M. Imada, A. Fujimori, and Y. Tokura, "Metal-insulator transitions", Rev. Mod. Phys. **70**, 1039–1263 (1998).

[29]B. A. Bernevig, *Topological Insulators and Topological Superconductors* (Princeton University Press, 2013).

[30]M. Z. Hasan and C. L. Kane, "Colloquium: Topological insulators", Rev. Mod. Phys. **82**, 3045–3067 (2010).

[31]X.-L. Qi and S.-C. Zhang, "Topological insulators and superconductors", Rev. Mod. Phys. **83**, 1057–1110 (2011).

[32]A. Zong, "Charge density waves", in *Emergent states in photoinduced charge-density-wave transitions* (Springer International Publishing, 2021), pp. 37–68.

[33]M. D. Johannes and I. I. Mazin, "Fermi surface nesting and the origin of charge density waves in metals", Phys. Rev. B **77**, 165135 (2008).

[34]H.-M. Eiter et al., "Alternative route to charge density wave formation in multiband systems", Proc. Natl. Acad. Sci. USA **110**, 64–69 (2013).

[35]M. Maschek et al., "Wave-vector-dependent electron-phonon coupling and the charge-density-wave transition in $TbTe_3$", Phys. Rev. B **91**, 235146 (2015).

[36]K. Rossnagel, "On the origin of charge-density waves in select layered transition-metal dichalcogenides", J. Phys.: Condens. Matter **23**, 213001 (2011).

[37] P. Fazekas and E. Tosatti, "Charge carrier localization in pure and doped 1T-TaS$_2$", Physica B+C **99**, 183–187 (1980).

[38] G. Profeta and E. Tosatti, "Triangular mott-hubbard insulator phases of Sn/Si(111) and Sn/Ge(111) surfaces", Phys. Rev. Lett. **98**, 086401 (2007).

[39] S. Modesti et al., "Insulating ground state of Sn/Si(111)-($\sqrt{3} \times \sqrt{3}$)R30°", Phys. Rev. Lett. **98**, 126401 (2007).

[40] G. Kotliar and D. Vollhardt, "Strongly correlated materials: insights from dynamical mean-field theory", Phys. Today **57**, 53–59 (2004).

[41] J. Maklar, "Doping of a triangular Sn atom lattice on a semiconductor substrate", MA thesis (Julius-Maximilians-Universität Würzburg, 2018).

[42] H. H. Weitering et al., "Mott insulating ground state on a triangular surface lattice", Phys. Rev. Lett. **78**, 1331–1334 (1997).

[43] G. Li et al., "Magnetic order in a frustrated two-dimensional atom lattice at a semiconductor surface", Nat. Commun. **4**, 1620 (2013).

[44] F. Adler et al., "Correlation-driven charge order in a frustrated two-dimensional atom lattice", Phys. Rev. Lett. **123**, 086401 (2019).

[45] M. Fruchart and D. Carpentier, "An introduction to topological insulators", C. R. Phys. **14**, 779–815 (2013).

[46] J. Wang and S.-C. Zhang, "Topological states of condensed matter", Nat. Mater. **16**, 1062–1067 (2017).

[47] N. Nagaosa, "A new state of quantum matter", Science **318**, 758–759 (2007).

[48] J. E. Moore and L. Balents, "Topological invariants of time-reversal-invariant band structures", Phys. Rev. B **75**, 121306 (2007).

[49] L. Fu, C. L. Kane, and E. J. Mele, "Topological Insulators in Three Dimensions", Phys. Rev. Lett. **98**, 106803 (2007).

[50] M. Z. Hasan and J. E. Moore, "Three-Dimensional Topological Insulators", Annu. Rev. Condens. Matter Phys. **2**, 55–78 (2011).

[51] C. L. Kane and E. J. Mele, "Z_2 Topological Order and the Quantum Spin Hall Effect", Phys. Rev. Lett. **95**, 146802 (2005).

[52] H. Min et al., "Intrinsic and Rashba spin-orbit interactions in graphene sheets", Phys. Rev. B **74**, 165310 (2006).

[53] M. König et al., "Quantum Spin Hall Insulator State in HgTe Quantum Wells", Science **318**, 766–770 (2007).

[54] B. A. Bernevig and S.-C. Zhang, "Quantum Spin Hall Effect", Phys. Rev. Lett. **96**, 106802 (2006).

[55] S. Tang et al., "Quantum spin hall state in monolayer 1T'-WTe$_2$", Nat. Phys. **13**, 683–687 (2017).

[56] Z. Fei et al., "Edge conduction in monolayer WTe$_2$", Nat. Phys. **13**, 677–682 (2017).

[57] F. Reis et al., "Bismuthene on a sic substrate: a candidate for a high-temperature quantum spin hall material", Science **357**, 287–290 (2017).

[58] G. Li et al., "Theoretical paradigm for the quantum spin hall effect at high temperatures", Phys. Rev. B **98**, 165146 (2018).

[59] S. Hüfner, *Photoelectron spectroscopy: principles and applications* (Springer Science & Business Media, 2003).

[60] R. Comin and A. Damascelli, "ARPES: A Probe of Electronic Correlations", in *Strongly Correlated Systems: Experimental Techniques* (Springer, 2015), pp. 31–71.

[61] U. Bovensiepen and P. S. Kirchmann, "Elementary relaxation processes investigated by femtosecond photoelectron spectroscopy of two-dimensional materials", Laser Photonics Rev. **6**, 589–606 (2012).

[62] C. L. Smallwood, R. A. Kaindl, and A. Lanzara, "Ultrafast angle-resolved photoemission spectroscopy of quantum materials", Europhys. Lett. **115**, 27001 (2016).

[63] X. Zhou et al., "New developments in laser-based photoemission spectroscopy and its scientific applications: a key issues review", Rep. Prog. Phys. **81**, 062101 (2018).

[64] S. Moser, "An experimentalist's guide to the matrix element in angle resolved photoemission", J. Electron Spectrosc. Relat. Phenom. **214**, 29–52 (2017).

[65] F. Boschini et al., "Role of matrix elements in the time-resolved photoemission signal", New J. Phys. **22**, 023031 (2020).

[66] J. K. Freericks and H. R. Krishnamurthy, "Constant Matrix Element Approximation to Time-Resolved Angle-Resolved Photoemission Spectroscopy", Photonics **3**, 58 (2016).

[67] R. Haight et al., "Picosecond Time-Resolved Photoemission Study of the InP(110) Surface", Phys. Rev. Lett. **54**, 1302–1305 (1985).

[68] J. A. Sobota et al., "Direct optical coupling to an unoccupied dirac surface state in the topological insulator Bi_2Se_3", Phys. Rev. Lett. **111**, 136802 (2013).

[69] S. Ulstrup et al., "Ultrafast Band Structure Control of a Two-Dimensional Heterostructure", ACS Nano **10**, 6315–6322 (2016).

[70] F. Liu, M. E. Ziffer, K. R. Hansen, J. Wang, and X. Zhu, "Direct determination of band-gap renormalization in the photoexcited monolayer MoS_2", Phys. Rev. Lett. **122**, 246803 (2019).

[71] C. W. Nicholson et al., "Excited-state band mapping and momentum-resolved ultrafast population dynamics in In/Si (111) nanowires investigated with XUV-based time- and angle-resolved photoemission spectroscopy", Phys. Rev. B **99**, 155107 (2019).

[72] M. Puppin et al., "Excited-state band structure mapping", Phys. Rev. B **105**, 075417 (2022).

[73] R. Haight, "Electron dynamics at surfaces", Surf. Sci. Rep. **21**, 275–325 (1995).

[74] H. Petek and S. Ogawa, "Femtosecond time-resolved two-photon photoemission studies of electron dynamics in metals", Prog. Surf. Sci. **56**, 239–310 (1997).

[75] M. Weinelt, "Time-resolved two-photon photoemission from metal surfaces", J. Phys.: Condens. Matter **14**, R1099–R1141 (2002).

[76] J. D. Rameau et al., "Energy dissipation from a correlated system driven out of equilibrium", Nat. Commun. **7**, 13761 (2016).

[77] M. X. Na et al., "Direct determination of mode-projected electron-phonon coupling in the time domain", Science **366**, 1231–1236 (2019).

[78] F. Schmitt et al., "Transient electronic structure and melting of a charge density wave in $TbTe_3$", Science **321**, 1649–1652 (2008).

[79] R. Cortés et al., "Momentum-Resolved Ultrafast Electron Dynamics in Superconducting $Bi_2Sr_2CaCu_2O_{8+\delta}$", Phys. Rev. Lett. **107**, 097002 (2011).

[80] T. Rohwer et al., "Collapse of long-range charge order tracked by time-resolved photoemission at high momenta", Nature **471**, 490–493 (2011).

[81] T. Huber et al., "Coherent structural dynamics of a prototypical charge-density-wave-to-metal transition", Phys. Rev. Lett. **113**, 026401 (2014).

[82] P. Beaud et al., "A time-dependent order parameter for ultrafast photoinduced phase transitions", Nat. Mater. **13**, 923–927 (2014).

[83] C. Sohrt, A. Stange, M. Bauer, and K. Rossnagel, "How fast can a Peierls–Mott insulator be melted?", Faraday Discuss. **171**, 243–257 (2014).

[84] C. W. Nicholson et al., "Beyond the molecular movie: dynamics of bands and bonds during a photoinduced phase transition", Science **362**, 821–825 (2018).

[85] L. Perfetti et al., "Time evolution of the electronic structure of $1T\text{-}TaS_2$ through the insulator-metal transition", Phys. Rev. Lett. **97**, 067402 (2006).

[86] E. Papalazarou et al., "Coherent Phonon Coupling to Individual Bloch States in Photoexcited Bismuth", Phys. Rev. Lett. **108**, 256808 (2012).

[87] S.-L. Yang et al., "Mode-Selective Coupling of Coherent Phonons to the Bi2212 Electronic Band Structure", Phys. Rev. Lett. **122**, 176403 (2019).

[88] P. Hein et al., "Mode-resolved reciprocal space mapping of electron-phonon interaction in the Weyl semimetal candidate $Td\text{-}WTe_2$", Nat. Commun. **11**, 2613 (2020).

[89] Y. H. Wang, H. Steinberg, P. Jarillo-Herrero, and N. Gedik, "Observation of Floquet-Bloch States on the Surface of a Topological Insulator", Science **342**, 453–457 (2013).

[90] T. Oka and S. Kitamura, "Floquet Engineering of Quantum Materials", Annu. Rev. Condens. Matter Phys. **10**, 387–408 (2019).

[91] J. Faure et al., "Full characterization and optimization of a femtosecond ultraviolet laser source for time and angle-resolved photoemission on solid surfaces", Rev. Sci. Instrum. **83**, 043109 (2012).

[92] C. L. Smallwood, C. Jozwiak, W. Zhang, and A. Lanzara, "An ultrafast angle-resolved photoemission apparatus for measuring complex materials", Rev. Sci. Instrum. **83**, 123904 (2012).

[93] F. Boschini et al., "An innovative Yb-based ultrafast deep ultraviolet source for time-resolved photoemission experiments", Rev. Sci. Instrum. **85**, 123903 (2014).

[94] Y. Yang et al., "A time- and angle-resolved photoemission spectroscopy with probe photon energy up to 6.7 eV", Rev. Sci. Instrum. **90**, 063905 (2019).

[95] A. Gauthier et al., "Tuning time and energy resolution in time-resolved photoemission spectroscopy with nonlinear crystals", J. Appl. Phys. **128**, 093101 (2020).

[96] B. Frietsch et al., "A high-order harmonic generation apparatus for time- and angle-resolved photoelectron spectroscopy", Rev. Sci. Instrum. **84**, 075106 (2013).

[97] S. Eich et al., "Time- and angle-resolved photoemission spectroscopy with optimized high-harmonic pulses using frequency-doubled Ti:Sapphire lasers", J. Electron Spectrosc. Relat. Phenom. **195**, 231–236 (2014).

[98] F. Cilento et al., "Advancing non-equilibrium ARPES experiments by a 9.3 eV coherent ultrafast photon source", Journal of Electron Spectroscopy and Related Phenomena **207**, 7–13 (2016).

[99] E. J. Sie, T. Rohwer, C. Lee, and N. Gedik, "Time-resolved XUV ARPES with tunable 24–33 eV laser pulses at 30 meV resolution", Nat. Commun. **10**, 3535 (2019).

[100] J. H. Buss et al., "A setup for extreme-ultraviolet ultrafast angle-resolved photoelectron spectroscopy at 50-kHz repetition rate", Rev. Sci. Instrum. **90**, 023105 (2019).

[101] M. Puppin et al., "Time-and angle-resolved photoemission spectroscopy of solids in the extreme ultraviolet at 500 khz repetition rate", Rev. Sci. Instrum. **90**, 023104 (2019).

[102] M. Keunecke et al., "Time-resolved momentum microscopy with a 1 MHz high-harmonic extreme ultraviolet beamline", Rev. Sci. Instrum. **91**, 063905 (2020).

[103] R. Cucini et al., "Coherent narrowband light source for ultrafast photoelectron spectroscopy in the 17–31 eV photon energy range", Struct. Dyn. **7**, 014303 (2020).

[104] D. Kutnyakhov et al., "Time- and momentum-resolved photoemission studies using time-of-flight momentum microscopy at a free-electron laser", Rev. Sci. Instrum. **91**, 013109 (2020).

[105] C. Corder et al., "Ultrafast extreme ultraviolet photoemission without space charge", Struct. Dyn. **5**, 054301 (2018).

[106] A. K. Mills et al., "Cavity-enhanced high harmonic generation for extreme ultraviolet time- and angle-resolved photoemission spectroscopy", Rev. Sci. Instrum. **90**, 083001 (2019).

[107] J. Madéo et al., "Directly visualizing the momentum-forbidden dark excitons and their dynamics in atomically thin semiconductors", Science **370**, 1199–1204 (2020).

[108] R. Wallauer et al., "Momentum-Resolved Observation of Exciton Formation Dynamics in Monolayer WS_2", Nano Lett. **21**, 5867–5873 (2021).

[109] J. Reimann et al., "Subcycle observation of lightwave-driven dirac currents in a topological surface band", Nature **562**, 396–400 (2018).

[110] M. Puppin et al., "500 kHz OPCPA delivering tunable sub-20 fs pulses with 15 W average power based on an all-ytterbium laser", Opt. Express **23**, 1491–1497 (2015).

[111] R. P. Xian, L. Rettig, and R. Ernstorfer, "Symmetry-guided nonrigid registration: The case for distortion correction in multidimensional photoemission spectroscopy", Ultramicroscopy **202**, 133–139 (2019).

[112] R. P. Xian et al., "An open-source, end-to-end workflow for multidimensional photoemission spectroscopy", Sci. Data **7**, 442 (2020).

[113] C. Tusche, A. Krasyuk, and J. Kirschner, "Spin resolved bandstructure imaging with a high resolution momentum microscope", Ultramicroscopy **159**, 520–529 (2015).

[114] G. Schönhense, K. Medjanik, and H.-J. Elmers, "Space-, time- and spin-resolved photoemission", J. Electron Spectrosc. Relat. Phenom. **200**, 94–118 (2015).

[115] K. Medjanik et al., "Direct 3D mapping of the Fermi surface and Fermi velocity - Nature Materials", Nat. Mater. **16**, 615–621 (2017).

[116] R. Wallauer et al., "Tracing orbital images on ultrafast time scales", Science **371**, 1056–1059 (2021).

[117] A. Kunin et al., "Momentum-Resolved Exciton Coupling and Valley Polarization Dynamics in Monolayer WS_2", arXiv:2203.02419 (2022).

[118] G. Schönhense et al., "Suppression of the vacuum space-charge effect in fs-photoemission by a retarding electrostatic front lens", Rev. Sci. Instrum. **92**, 053703 (2021).

[119] M. Schüler et al., "Polarization-Modulated Angle-Resolved Photoemission Spectroscopy: Toward Circular Dichroism without Circular Photons and Bloch Wavefunction Reconstruction", Phys. Rev. X **12**, 011019 (2022).

[120] S. Dong et al., "Direct measurement of key exciton properties: Energy, dynamics, and spatial distribution of the wave function", Nat. Sci. **1**, e10010 (2021).

[121] M. K. L. Man et al., "Experimental measurement of the intrinsic excitonic wave function", Sci. Adv. **7**, eabg0192 (2021).

[122] K. Baumgärtner et al., "Ultrafast orbital tomography of a pentacene film using time-resolved momentum microscopy at a FEL", Nat. Commun. **13**, 2741 (2022).

[123] A. Singer et al., "Nonequilibrium Phase Precursors during a Photoexcited Insulator-to-Metal Transition in V_2O_3", Phys. Rev. Lett. **120**, 207601 (2018).

[124] A. Ronchi et al., "Early-stage dynamics of metallic droplets embedded in the nanotextured Mott insulating phase of V_2O_3", Phys. Rev. B **100**, 075111 (2019).

[125] A. Ronchi et al., "Nanoscale self-organization and metastable non-thermal metallicity in Mott insulators", Nat. Commun. **13**, 3730 (2022).

[126] A. S. McLeod et al., "Nanotextured phase coexistence in the correlated insulator V_2O_3", Nat. Phys. **13**, 80–86 (2017).

[127] A. Zong et al., "Ultrafast manipulation of mirror domain walls in a charge density wave", Sci. Adv. **4**, eaau5501 (2018).

[128] R. Stühler et al., "Tomonaga–Luttinger liquid in the edge channels of a quantum spin Hall insulator", Nat. Phys. **16**, 47–51 (2020).

[129] R. Stühler et al., "Effective lifting of the topological protection of quantum spin Hall edge states by edge coupling", Nat. Commun. **13**, 3480 (2022).

[130] E. N. Lima, T. M. Schmidt, and R. W. Nunes, "Topologically Protected Metallic States Induced by a One-Dimensional Extended Defect in the Bulk of a 2D Topological Insulator", Nano Lett. **16**, 4025–4031 (2016).

[131] J. A. Sobota et al., "Ultrafast optical excitation of a persistent surface-state population in the topological insulator Bi_2Se_3", Phys. Rev. Lett. **108**, 117403 (2012).

[132] Y. Wang et al., "Measurement of intrinsic dirac fermion cooling on the surface of the topological insulator Bi_2Se_3 using time-resolved and angle-resolved photoemission spectroscopy", Phys. Rev. Lett. **109**, 127401 (2012).

[133] M. Neupane et al., "Gigantic surface lifetime of an intrinsic topological insulator", Phys. Rev. Lett. **115**, 116801 (2015).

[134] S. Zhu et al., "Ultrafast electron dynamics at the Dirac node of the topological insulator Sb_2Te_3", Sci. Rep. **5**, 13213 (2015).

[135] S. Das Sarma, S. Adam, E. H. Hwang, and E. Rossi, "Electronic transport in two-dimensional graphene", Rev. Mod. Phys. **83**, 407–470 (2011).

[136] J. W. McIver, D. Hsieh, H. Steinberg, P. Jarillo-Herrero, and N. Gedik, "Control over topological insulator photocurrents with light polarization", Nat. Nanotechnol. **7**, 96–100 (2012).

[137] K. Kuroda, J. Reimann, J. Güdde, and U. Höfer, "Generation of transient photocurrents in the topological surface state of Sb_2Te_3 by direct optical excitation with mid-infrared pulses", Phys. Rev. Lett. **116**, 076801 (2016).

[138] K. Kuroda et al., "Ultrafast energy- and momentum-resolved surface Dirac photocurrents in the topological insulator Sb_2Te_3", Phys. Rev. B **95**, 081103 (2017).

[139] J. Sánchez-Barriga et al., "Ultrafast spin-polarization control of Dirac fermions in topological insulators", Phys. Rev. B **93**, 155426 (2016).

[140] J. Güdde and U. Höfer, "Ultrafast Dynamics of Photocurrents in Surface States of Three-Dimensional Topological Insulators", Phys. Status Solidi B **258**, 2000521 (2021).

[141] S. Wu et al., "Observation of the quantum spin hall effect up to 100 Kelvin in a monolayer crystal", Science **359**, 76–79 (2018).

[142] P. Chen et al., "Large quantum-spin-hall gap in single-layer 1-T' WSe_2", Nat. Commun. **9**, 2003 (2018).

[143] B. Sun et al., "Evidence for equilibrium exciton condensation in monolayer WTe_2", Nat. Phys. **18**, 94–99 (2022).

[144] Y. Jia et al., "Evidence for a monolayer excitonic insulator", Nat. Phys. **18**, 87–93 (2022).

[145]E. DiMasi, M. C. Aronson, J. F. Mansfield, B. Foran, and S. Lee, "Chemical pressure and charge-density waves in rare-earth tritellurides", Phys. Rev. B **52**, 14516–14525 (1995).

[146]C. Malliakas, S. J. L. Billinge, H. J. Kim, and M. G. Kanatzidis, "Square Nets of Tellurium: Rare-Earth Dependent Variation in the Charge-Density Wave of RETe$_3$ (RE = Rare-Earth Element)", J. Am. Chem. Soc. **127**, 6510–6511 (2005).

[147]I. Avigo et al., "Coherent excitations and electron–phonon coupling in Ba/EuFe$_2$As$_2$ compounds investigated by femtosecond time- and angle-resolved photoemission spectroscopy", J. Phys.: Condens. Matter **25**, 094003 (2013).

[148]A. F. Kemper, M. A. Sentef, B. Moritz, J. K. Freericks, and T. P. Devereaux, "Direct observation of Higgs mode oscillations in the pump-probe photoemission spectra of electron-phonon mediated superconductors", Phys. Rev. B **92**, 224517 (2015).

[149]Y. Murakami, D. Goležl, M. Eckstein, and P. Werner, "Photoinduced Enhancement of Excitonic Order", Phys. Rev. Lett. **119**, 247601 (2017).

[150]S.-L. Yang et al., "Inequivalence of single-particle and population lifetimes in a cuprate superconductor", Phys. Rev. Lett. **114**, 247001 (2015).

[151]A. F. Kemper, O. Abdurazakov, and J. K. Freericks, "General principles for the nonequilibrium relaxation of populations in quantum materials", Phys. Rev. X **8**, 041009 (2018).

[152]S. Duan et al., "Optical manipulation of electronic dimensionality in a quantum material", Nature **595**, 239–244 (2021).

[153]L. Ma et al., "A metallic mosaic phase and the origin of Mott-insulating state in $1T$-TaS$_2$", Nat. Commun. **7**, 10956 (2016).

[154]D. Cho et al., "Nanoscale manipulation of the Mott insulating state coupled to charge order in 1T-TaS$_2$", Nat. Commun. **7**, 10453 (2016).

[155]Y. A. Gerasimenko, P. Karpov, I. Vaskivskyi, S. Brazovskii, and D. Mihailovic, "Intertwined chiral charge orders and topological stabilization of the light-induced state of a prototypical transition metal dichalcogenide", npj Quantum Mater. **4**, 32 (2019).

[156]Q. Stahl et al., "Collapse of layer dimerization in the photo-induced hidden state of 1T-TaS$_2$", Nat. Commun. **11**, 1247 (2020).

[157]Y. Zhang et al., "Creation of a novel inverted charge density wave state", Struct. Dyn. **9**, 014501 (2022).

[158]Y. A. Gerasimenko et al., "Quantum jamming transition to a correlated electron glass in 1T-TaS$_2$", Nat. Mater. **18**, 1078–1083 (2019).

[159]L. Perfetti et al., "Femtosecond dynamics of electronic states in the Mott insulator 1T-TaS$_2$ by time resolved photoelectron spectroscopy", New J. Phys. **10**, 053019 (2008).

[160]J. C. Petersen et al., "Clocking the melting transition of charge and lattice order in 1T-TaS$_2$ with ultrafast extreme-ultraviolet angle-resolved photoemission spectroscopy", Phys. Rev. Lett. **107**, 177402 (2011).

[161] M. Ligges et al., "Ultrafast doublon dynamics in photoexcited 1T-TaS$_2$", Phys. Rev. Lett. **120**, 166401 (2018).

[162] I. Avigo et al., "Doublon bottleneck in the ultrafast relaxation dynamics of hot electrons in 1T-TaS$_2$", Phys. Rev. Research **2**, 022046 (2020).

[163] A. Simoncig et al., "Dissecting Mott and charge-density wave dynamics in the photoinduced phase of $1T-$TaS$_2$", Phys. Rev. B **103**, 155120 (2021).

[164] J. Ravnik et al., "A time-domain phase diagram of metastable states in a charge ordered quantum material", Nat. Commun. **12**, 2323 (2021).

[165] G. Li, M. Laubach, A. Fleszar, and W. Hanke, "Geometrical frustration and the competing phases of the Sn/Si(111) $\sqrt{3} \times \sqrt{3}R$30° surface systems", Phys. Rev. B **83**, 041104 (2011).

[166] F. Ming et al., "Realization of a hole-doped mott insulator on a triangular silicon lattice", Phys. Rev. Lett. **119**, 266802 (2017).

[167] R. P. Xian et al., "A machine learning route between band mapping and band structure", arXiv:2005.10210 (2020).

[168] M. Dendzik et al., "Observation of an excitonic mott transition through ultrafast core-cum-conduction photoemission spectroscopy", Phys. Rev. Lett. **125**, 096401 (2020).

[169] D. Curcio et al., "Ultrafast electronic linewidth broadening in the C $1s$ core level of graphene", Phys. Rev. B **104**, L161104 (2021).

[170] Y. Cao et al., "Mapping the orbital wavefunction of the surface states in three-dimensional topological insulators", Nat. Phys. **9**, 499–504 (2013).

[171] O. Fedchenko et al., "4D texture of circular dichroism in soft-x-ray photoemission from tungsten", New J. Phys. **21**, 013017 (2019).

[172] Y. Liu, G. Bian, T. Miller, and T.-C. Chiang, "Visualizing Electronic Chirality and Berry Phases in Graphene Systems Using Photoemission with Circularly Polarized Light", Phys. Rev. Lett. **107**, 166803 (2011).

[173] C. Hwang et al., "Direct measurement of quantum phases in graphene via photoemission spectroscopy", Phys. Rev. B **84**, 125422 (2011).

[174] R. Takahashi and N. Nagaosa, "Berry curvature and orbital angular momentum of electrons in angle-resolved photoemission spectroscopy", Phys. Rev. B **91**, 245133 (2015).

[175] S. Cho et al., "Experimental Observation of Hidden Berry Curvature in Inversion-Symmetric Bulk $2H-$WSe$_2$", Phys. Rev. Lett. **121**, 186401 (2018).

[176] M. Schüler et al., "Local Berry curvature signatures in dichroic angle-resolved photoelectron spectroscopy from two-dimensional materials", Sci. Adv. **6**, eaay2730 (2020).

[177] T. Suzuki et al., "Detecting electron-phonon coupling during photoinduced phase transition", Phys. Rev. B **103**, L121105 (2021).

[178] J. Laverock et al., "Fermi surface nesting and charge-density wave formation in rare-earth tritellurides", Phys. Rev. B **71**, 085114 (2005).

[179] N. Ru et al., "Effect of chemical pressure on the charge density wave transition in rare-earth tritellurides RTe$_3$", Phys. Rev. B **77**, 035114 (2008).

[180] V. Brouet et al., "Angle-resolved photoemission study of the evolution of band structure and charge density wave properties in RTe$_3$ (R= Y, La, Ce, Sm, Gd, Tb, and Dy)", Phys. Rev. B **77**, 235104 (2008).

[181] A. Damascelli, Z. Hussain, and Z.-X. Shen, "Angle-resolved photoemission studies of the cuprate superconductors", Rev. Mod. Phys. **75**, 473–541 (2003).

[182] B. J. Powell and R. H. McKenzie, "Quantum frustration in organic Mott insulators: from spin liquids to unconventional superconductors", Rep. Prog. Phys. **74**, 056501 (2011).

[183] P. A. Höpfner, "Two-Dimensional Electron Systems at Surfaces – Spin-Orbit Interaction and Electronic Correlations", Doctoral thesis (Universität Würzburg, 2012).

[184] M. Rohlfing and J. Pollmann, "U Parameter of the Mott-Hubbard Insulator $6H$-SiC(0001) - ($\sqrt{3} \times \sqrt{3}$)R30°: An Ab Initio Calculation", Phys. Rev. Lett. **84**, 135–138 (2000).

[185] V. Ramachandran and R. M. Feenstra, "Scanning Tunneling Spectroscopy of Mott-Hubbard States on the $6H$-SiC(0001) $\sqrt{3} \times \sqrt{3}$ Surface", Phys. Rev. Lett. **82**, 1000–1003 (1999).

[186] H. Aoki et al., "Nonequilibrium dynamical mean-field theory and its applications", Rev. Mod. Phys. **86**, 779–837 (2014).

[187] M. Eckstein and P. Werner, "Photoinduced States in a Mott Insulator", Phys. Rev. Lett. **110**, 126401 (2013).

[188] J. Li, D. Golez, P. Werner, and M. Eckstein, "η-paired superconducting hidden phase in photodoped Mott insulators", Phys. Rev. B **102**, 165136 (2020).

[189] X. Cao et al., "Chiral d-wave superconductivity in a triangular surface lattice mediated by long-range interaction", Phys. Rev. B **97**, 155145 (2018).

[190] S. Wolf, D. Di Sante, T. Schwemmer, R. Thomale, and S. Rachel, "Triplet Superconductivity from Nonlocal Coulomb Repulsion in an Atomic Sn Layer Deposited onto a Si(111) Substrate", Phys. Rev. Lett. **128**, 167002 (2022).

[191] S. Schuwalow, D. Grieger, and F. Lechermann, "Realistic modeling of the electronic structure and the effect of correlations for Sn/Si(111) and Sn/Ge(111) surfaces", Phys. Rev. B **82**, 035116 (2010).

Publications

[I] J. Maklar et al., "A quantitative comparison of time-of-flight momentum microscopes and hemispherical analyzers for time- and angle-resolved photoemission spectroscopy experiments", Rev. Sci. Instrum. **91**, 123112 (2020).

[II] J. Maklar et al., "Nonequilibrium charge-density-wave order beyond the thermal limit", Nat. Commun. **12**, 2499 (2021).

[III] J. Maklar et al., "Coherent modulation of quasiparticle scattering rates in a photoexcited charge-density-wave system", Phys. Rev. Lett. **128**, 026406 (2022).

[IV] J. Maklar et al., "Ultrafast Momentum-Resolved Hot Electron Dynamics in the Two-Dimensional Topological Insulator Bismuthene", Nano Lett. **22**, 5420–5426 (2022).

[V] S. Beaulieu et al., "Revealing Hidden Orbital Pseudospin Texture with Time-Reversal Dichroism in Photoelectron Angular Distributions", Phys. Rev. Lett. **125**, 216404 (2020).

[VI] S. Beaulieu et al., "Ultrafast dynamical Lifshitz transition", Sci. Adv. **7**, eabd9275 (2021).

[VII] S. Dong et al., "Observation of ultrafast interfacial Meitner-Auger energy transfer in a van der Waals heterostructure", arXiv:2108.06803 (2021).

[VIII] S. Beaulieu et al., "Unveiling the orbital texture of 1T-TiTe$_2$ using intrinsic linear dichroism in multidimensional photoemission spectroscopy", npj Quantum Mater. **6**, 93 (2021).

[IX] A. Neef et al., "Orbital-resolved Observation of Singlet Fission", arXiv:2204.06824 (2022).

[X] G. Kremer et al., "Field-induced ultrafast modulation of Rashba coupling at room temperature in ferroelectric α-GeTe(111)", arXiv:2204.11630 (2022).

[XI] J. Maklar et al., "Coherent Light Control of a Metastable Hidden Phase", arXiv:2206.03788 (2022).

Acknowledgments

Selbstständigkeitserklärung

Ich, Julian Maklar, erkläre gegenüber der Freien Universität Berlin, dass ich die vorliegende Dissertation selbstständig und ohne Benutzung anderer als der angegebenen Quellen und Hilfsmittel angefertigt habe. Die vorliegende Arbeit ist frei von Plagiaten. Alle Ausführungen, die wörtlich oder inhaltlich aus anderen Schriften entnommen sind, habe ich als solche kenntlich gemacht. Diese Dissertation wurde in gleicher oder ähnlicher Form noch in keinem früheren Promotionsverfahren eingereicht.

Mit einer Prüfung meiner Arbeit durch ein Plagiatsprüfungsprogramm erkläre ich mich einverstanden.

<div align="right">

_____

Datum, Unterschrift

</div>